Copyright Undertaking

STUDY OF COLOR CHANGE IN SEED-MEDIATED GROWTH OF GOLD NANOPARTICLES AND INSIGHTS INTO TURKEVICH METHOD

HE QIJIN

PhD

The Hong Kong Polytechnic University

2019

The Hong Kong Polytechnic University

Department of Biomedical Engineering

Study of Color Change in Seed-Mediated Growth of Gold Nanoparticles and Insights into Turkevich Method

HE Qijin

A thesis submitted in partial fulfillment of the requirements for the degree of Doctor of Philosophy

August 2018

Certificate of Originality

I hereby declare that this thesis is my own work and that, to the best of my knowledge and belief, it reproduces no material previously published or written, nor material that has been accepted for the award of any other degree or diploma, except where due acknowledgement has been made in the text.

____________________ (Signed)

HE Qijin (Name of Student)

Abstract

Gold nanomaterials have received great attention within the scientific community mostly due to their unique optical properties. Many forms of gold nanomaterials have been developed for various applications. The simplest form of gold nanomaterials is spherical in shape and known as gold nanoparticles (AuNPs), whose dispersion is ruby red in color (for widely used AuNPs of diameter ~13 nm). The widely adopted synthesis methods of AuNPs include Turkevich and seed-mediated growth. For the two methods with citrate as reducing agent, a purple/blue intermediate stage has been reported by some literatures. However, no consensus has been reached on the underlying reason for such coloration. There are five main schools of thoughts proposed in the literature: (i) formation of fluffy large aggregates from AuNPs which are spherical in shape; (ii) formation of solid polycrystalline nanowires via aggregation from AuNPs or deposition of gold along certain facet of AuNP seeds; (iii) formation of spherical aggregates from "glue" particles (liquid globules or Au(I)/sodium acetone dicarboxylate (SAD) complex) within which AuNPs nucleate and grow, without AuNPs directly interacting with each other; (iv) kinetic intermediate from closely spaced gold clusters/particles before compacting into AuNPs without any aggregates formation; (v) attachment of gold ions at electric double layer of the AuNPs without any aggregates formation. This study closely examined the seed-mediated growth of 5 nm citrate-capped AuNPs at room temperature. By close monitoring of the different color stages and manipulation of the colors, the purple/blue color appearance and disappearance have been proposed in this thesis to result from the formation and disintegration of chain-like structures which form from AuNPs interconnected by some liquid "glue". Key components within such liquid

“glue” include Au(III) complex ions (in the form of $[AuCl_3(OH)]^-$) and SAD (oxidation product of sodium citrate), cross-linking probably via hydrogen bonds and ligand replacement of chloride ions within $[AuCl_3(OH)]^-$ by the carboxylate groups of SAD. The close proximity of the connected AuNPs results in red shift of the localized surface plasmon resonance peak and increase in the near-infrared absorption for the red-to-purple/blue color change. With complete consumption of Au(III) complex ions by reducing agents (e.g., citrate, SAD, and acetone), the “glue” is depleted and such chain-like structures can no longer maintain, redispersing AuNPs for purple/blue-to-red color change. The red-to-purple/blue-to-red color reversal can be viewed as the dynamic process between chain-like structure formation (facilitated by liquid “glue” formation from interaction between Au(III) complex ions and SAD; SAD is gradually produced from citrate oxidation) and chain-like structure disintegration (induced by depletion of liquid “glue” from consumption of Au(III) complex ions). This proposed mechanism is also applicable to illustrate the red-to-purple/blue-to-red color reversal in seed-mediated growth of 13 nm citrate-coated AuNPs as well as the purple/blue-to-red color change in Turkevich method, offering new insights into the underlying physicochemical processes for the two widely adopted AuNP synthesis methods.

Acknowledgements

I would like to express my sincere gratitude to my chief supervisor Dr. LEE Ming Hung Thomas for his guidance throughout my PhD study. I have learnt from him the scientific methodology to approach a research question. His curiosity in acquiring new knowledge and positive attitudes have also deeply inspired me as a lifelong mentor.

I would also like to thank my two co-supervisors, Prof. YIP Shea Ping and Dr. LAI Yau Ming Patrick for their great help and instructions. Both of them have taught me abundant useful techniques for my research project.

Besides, I am greatly grateful for the financial support from Hong Kong PhD Fellowship Scheme, our department BME, and Prof. ZHENG Yongping (our department head).

Last but not least, I wouldn’t have learnt so much without the help from the colleagues in S106 (especially Dr. WONG Kwun Fung Jacky, Dr. CHAU Li Yin Blizzard, Dr. QIN Ailin, Ms. WANG Shiyao, and Ms. GAN Maria) and the support from my lovely family. Big thanks to all of them who have been encouraging me over the past six years.

Table of Contents

List of Figures

List of Tables

List of Abbreviations

AAO	anodic aluminum oxide
AFM	atomic force microscopy
$AgNO_3$	silver nitrate
APTES	3-aminopropyltriethoxysilane
AR	aspect ratio
AuNC	gold nanocluster
AuNP	gold nanoparticle
AuNR	gold nanorod
AuNS	gold nanoshell
CTAB	cetyltrimethylammonium bromide
DLS	dynamic light scattering
EPR	enhanced permeability and retention
EF	enhancement factor
FITC	fluorescein isothiocyanate
FRET	Förster resonant energy transfer
$HAuCl_4$	chloroauric acid
HCl	hydrogen chloride
HRTEM	high-resolution TEM
LSPR	localized surface plasmon resonance
MMP	metalloprotease
MSEF	metal surface enhanced fluorescence
$NaAuCl_4$	sodium tetrachloroaurate

$NaBH_4$	sodium borohydride
NaCl	sodium chloride
Na_3Ct	trisodium citrate
NaOH	sodium hydroxide
NIR	near-infrared
PAT	photoacoustic tomography
PDT	photodynamic therapy
PEI	polyethylenimine
PTT	photothermal therapy
QD	quantum dot
R	sodium citrate to $AuCl_4^-$ concentration ratio
SAD	sodium acetone dicarboxylate
SAXS	small angle X-ray scattering
SERS	surface-enhanced Raman scattering
siRNA	small interfering RNA
TEM	transmission electron microscopy
TOAB	tetraoctylammonium bromide
Tris	tris(hydroxymethyl) aminomethane
UV–vis	ultraviolet–visible
XANES	X-ray absorption near edge spectroscopy

Chapter 1. Introduction

1.1. Nanomaterials

Nanomaterials, generally accepted as materials with at least one dimension in 1–100 nm, have been under intense research over the past decades. With distinct properties from their bulk counterparts, nanomaterials have sparkled in a multitude of areas including but not limited to catalysis and energy storage [1-4], *in vitro* diagnostics and sensing [5-8], *in vivo* disease diagnosis and treatment [9-12].

Intense research effort has been put into this field to synthesize and study both organic (polymeric nanoparticles [13-16], liposomes [17-18], dendrimers [19-21], fullerene [22-24], carbon nanotubes [25-28], graphene [29-31], peptide and protein nanoparticle conjugates [32], etc.) and inorganic (gold nanomaterials [33-34], silica nanoparticles [35], quantum dots [36], magnetic nanoparticles [37], etc.) nanomaterials. Some examples of nanomaterials are depicted in Figure 1.1.

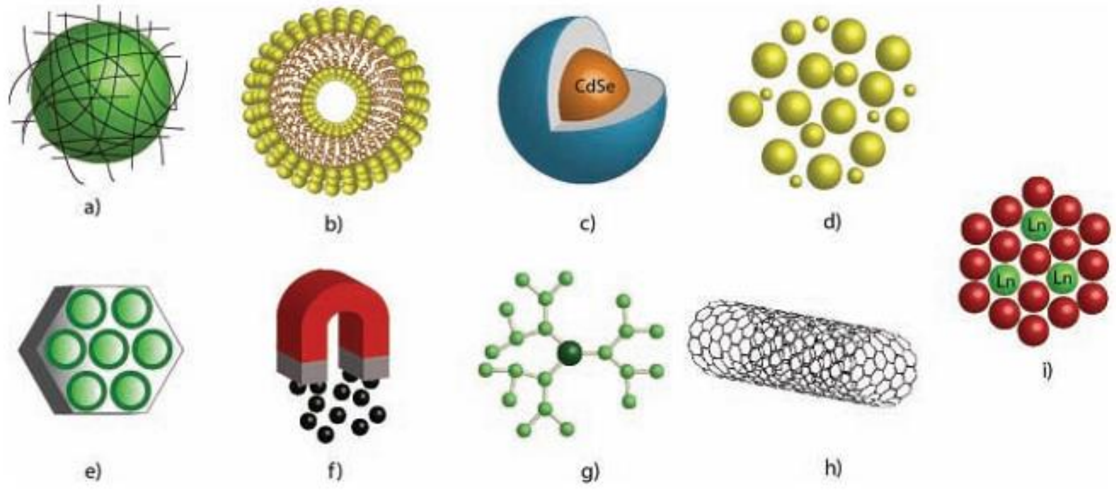

Figure 1.1. Examples of nanomaterials. (a) polymeric nanoparticles, (b) liposomes, (c) quantum dots, (d) spherical gold nanomaterials, (e) zeolite L, (f) magnetic nanoparticles, (g) dendrimers, (h) carbon nanotubes, (i) upconverting nanophosphors. Adapted from [12].

1.2. Gold nanomaterials

Gold has long been valued as coinage and jewelry in human history largely due to its extremely low abundance and extraordinary stability [38]. In the nano regime, which is billionth of 1 meter, the gold nanomaterials (or colloids) have also been employed for various applications. One famous example is the Lycurgus Cup which was crafted in the 4th century. The existence of gold nanomaterials endows this piece of art with different colors when light was shined from different directions through it. In the 6th to 15th centuries, gold nanomaterials were incorporated into glass windows in many European cathedrals to create vibrant colors. Besides, gold nanomaterials were even prescribed by doctors for treatment of many diseases including heart diseases and tumors, and many books were published on their curative functions in the 17th century

[39]. The scientific study of gold nanomaterial synthesis was pioneered by Michael Faraday in 1857, who also found the ruby red color of the synthesized gold materials could be varied by changing their size [40]. Huge progress has been made afterwards, and more thorough understanding of their properties and applications has been achieved.

1.2.1. Optical properties

1.2.1.1. Localized surface plasmon resonance (LSPR)

The striking color of the gold nanomaterials was attributed to their extinction (sum of absorption and scattering) of light by Gustav Mie in 1908 via solving the Maxwell equations for spherical gold nanomaterials [41]. The extinction peak of gold nanomaterials corresponds to the resonant collective oscillation of the gold surface free electrons with the incident electromagnetic fields, which is also referred to as the localized surface plasmon resonance (LSPR, Figure 1.2). Two types of light–matter interactions can occur: absorption (the incident light can be converted to heat via phonon–phonon relaxation) and scattering (the light is re-radiated to all directions with no change in the photon frequency) [38, 42-43]. Apart from the properties of the dispersing medium, the size, shape, and interparticle distance of the gold nanomaterials can all affect the LSPR and thus tune their extinction spectra and colloidal colors.

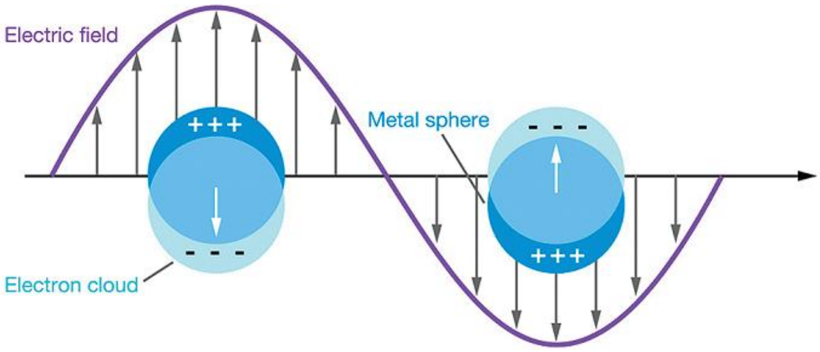

Figure 1.2. Schematic diagram for LSPR. Adapted from [44].

1.2.1.2. Size-dependent optical properties

Although Faraday documented the first hypothesis that the color of his prepared gold colloid depends on its size [40], Mie established the mathematical explanation of the size-dependence of extinction coefficients of spherical gold nanomaterials [41]. As illustrated in Figure 1.3A, an increase in the diameter can shift the LSPR peak to a longer wavelength, corresponding to red-to-purple/blue change of the colloid color. Another trend worth noting is a larger scattering portion with an increase in particle size. This is due to the faster increase of scattering cross section relative to the absorption cross section. For 150 nm spheres (which is beyond the size range of being defined as nanomaterials), scattering accounts for most part of their extinction (Figure 1.3B). Such size-dependent optical properties are also apparent in other shapes of gold nanomaterials (Figure 1.3C–H).

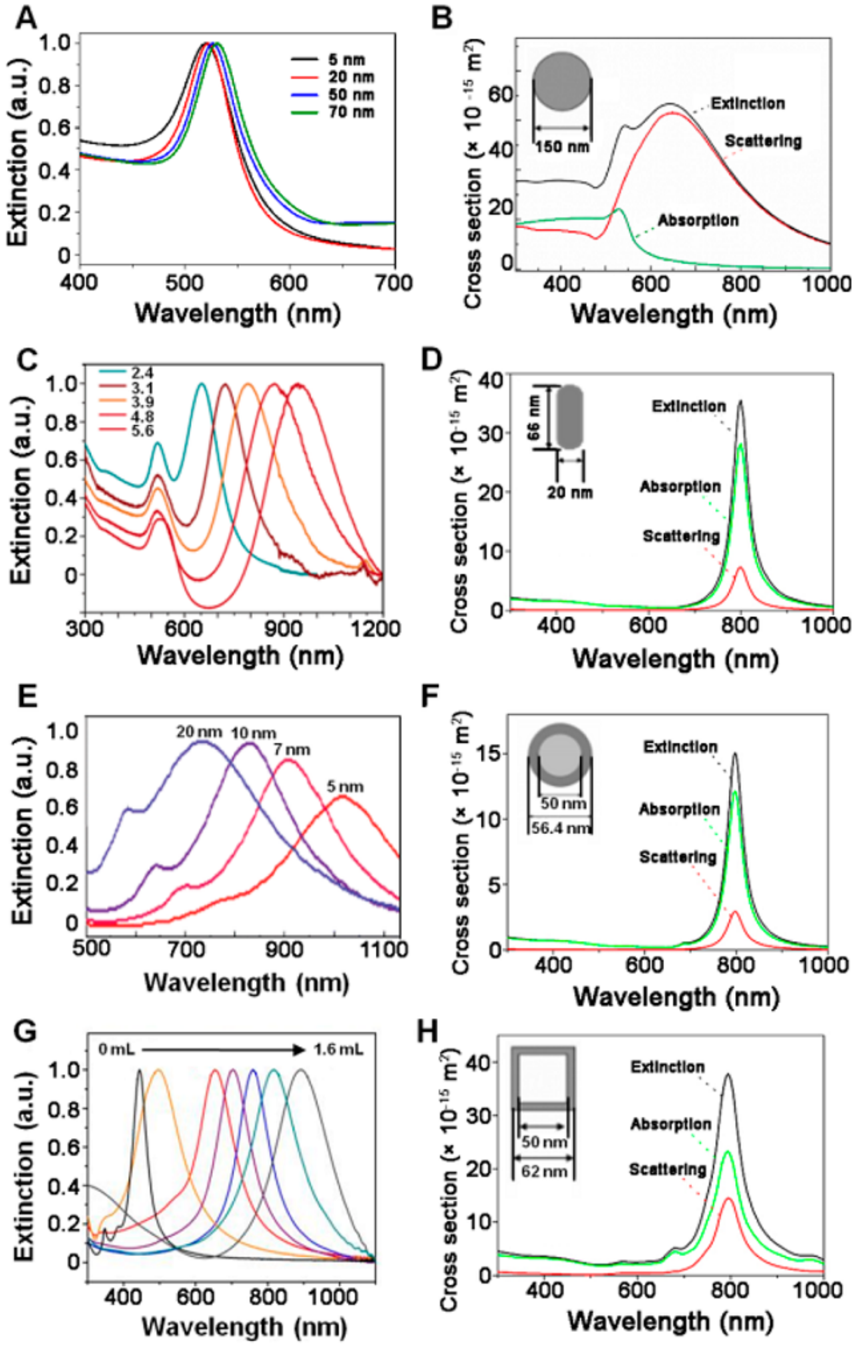

Figure 1.3. Measured size-dependent extinction of spherical gold nanomaterials–AuNPs (A), gold nanorods–AuNRs (C), gold nanoshells–AuNSs (E), gold nanocages (G), and calculated scattering and absorption portion of the extinction cross section of one specific size of AuNPs (B), AuNRs (D), AuNSs (F), and gold nanocages (H). Adapted from [38].

1.2.1.3. Shape-dependent optical properties

Since tuning the LSPR of the spherical form of gold nanomaterials, or gold nanoparticles (AuNPs), from 5 to 70 nm, does not vary the extinction spectrum significantly, research efforts have explored synthesizing other shapes of gold nanomaterials including gold nanorods (AuNRs) [45-46], gold nanoshells (typically with a silica core, AuNSs) [47-48], gold nanocages [49], etc. Their optical properties can be well tuned over a large wavelength range, as depicted in Figure 1.3. The underlying mechanism for their special optical extinction is their unique LSPR modes with the incoming electromagnetic radiation from the case of AuNPs [44, 50].

1.2.1.4. Interparticle distance-dependent optical properties

One striking feature of surface plasmons is their ability to couple with each other. When two individual plasmonic materials are in close proximity, within nanometers, their oscillating plasmons interfere to create new mode of LSPR [51-52]. As one example, Mirkin et al. employed oligonucleotides to cross-link individual AuNPs and observed a red-to-purple/blue color change (Figure 1.4). The color can be reversed back to red by heating to denature the formed duplex and dissociate the linked AuNPs [53]. A seminal work studied the LSPR peak shift dependence on interparticle distance and found an exponential decay. Such LSPR coupling would vanish when the particle distance is 2.5 times larger than the particle size [51]. Actually the coupling of LSPR can also create extremely high local electric fields or “hot spots”. This phenomenon is very useful in the area of surface-enhanced Raman scattering (SERS) and other spectroscopic methods, enabling great improvement in their detection limits and even the detection of a single molecule [44, 50, 54-55].

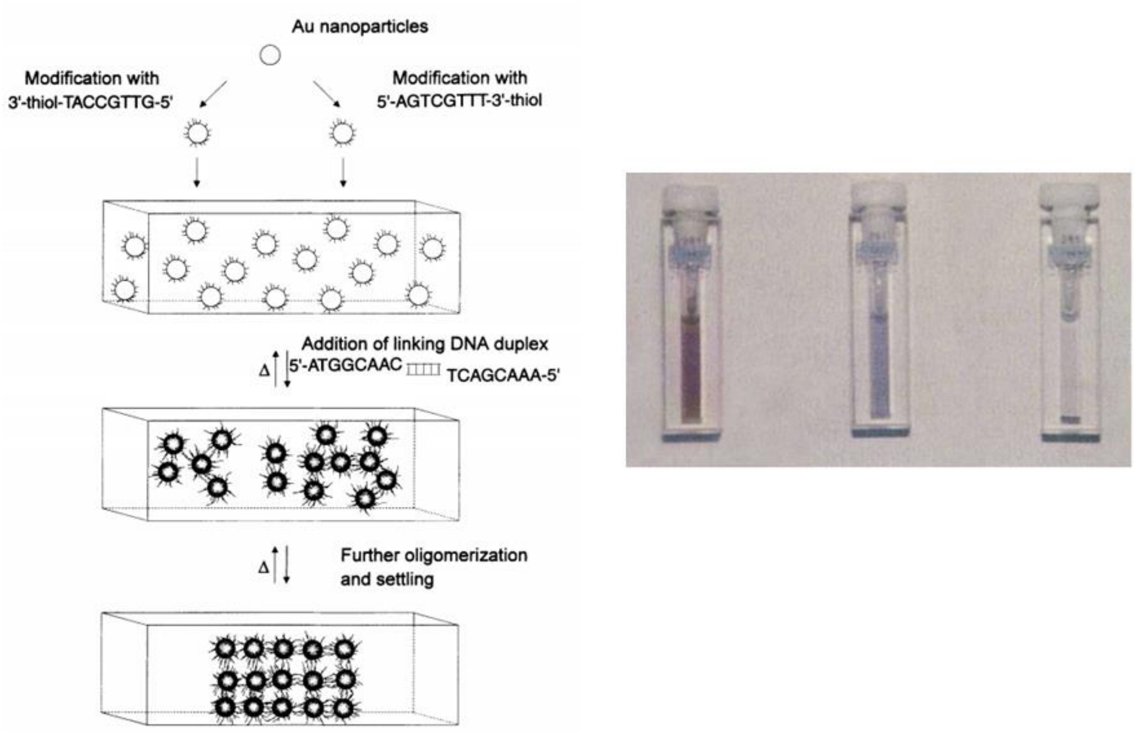

Figure 1.4. An example of manipulating the color of AuNPs via a linking DNA duplex to cross-link two individual particles. The color images show the red-to-purple/blue color change after cross-linking. The blue dispersion will even settle to form precipitates. Both the blue and precipitated samples can be reversed back to the red state via heating to dissociate the linked AuNPs. Adapted from [53].

1.2.1.5. Applications

The LSPR extinction of gold nanomaterials results from the light–matter interactions. Plentiful applications of gold nanomaterials in various fields, exploiting their LSPR, have been achieved. This section will briefly introduce some of them.

(a) Photocatalysts

It was proposed that LSPR can donate electrons to the adsorbed reactants, therefore gold nanomaterials have been studied in photocatalysis [56]. To name a few, Fenton reaction [57], reduction of nitroaromatic compounds [58-59], and oxidation of organic contaminants in air [60], have proven their photocatalytic capability, which is most efficient at the LSPR wavelength [61]. Even more research has been carried out on synthesizing gold/semiconductor nanostructures because LSPR can also donate electrons to the semiconductor and enhance the charge carriers' stability [56]. Thus, gold nanomaterials were exploited actively for harvesting solar energy.

(b) SERS substrates

The collective oscillation of free electrons creates a high localized electric field on the particle surface, which can enhance Raman signal by an enhancement factor (EF) of 10^5~10^6 [62-63]. SERS is useful in both molecule detection and *in vivo* imaging (after localizing the Raman-active vehicles to the target site) [64]. As mentioned in Section 1.2.1.4 on their interparticle distance-dependent optical properties, such enhancement can further be improved when two discrete particles are placed in close proximity to form "hot spots".

(c) Metal surface-enhanced fluorescence (MSEF) substrates

Similarly, the strong electric field is also capable of increasing the fluorescence yield of adsorbed fluorophores by changing their relaxation pathway from their excited state [65-66]. The MSEF effect can be optimized after careful consideration of the particle size (changing scattering over absorption ratio) and fluorophore location to minimize quenching effect of gold nanomaterials [67-68]. AuNPs of 200 nm diameter were found to outperform the 40 nm ones and increased the fluorescence yield to 2.5 times over the control [69].

(d) Förster resonant energy transfer (FRET) acceptors for analyte detection

Due to the large extinction cross section of gold nanomaterials, gold nanomaterials are promising acceptors for many donor fluorophores to construct the FRET system [70-72], where the photoluminescence from the donor molecules are effectively quenched. Their quenching capabilities were utilized to construct fluorescent probes for various targets. Figure 1.5 shows one example by Xia et al. which used gold nanocage as the quencher. When the target matrix metalloprotease-2 (MMP-2) was present, the linking peptide was cleaved and the bound fluorescein isothiocyanate (FITC) was released to the solution, restoring the quenched fluorescence [73].

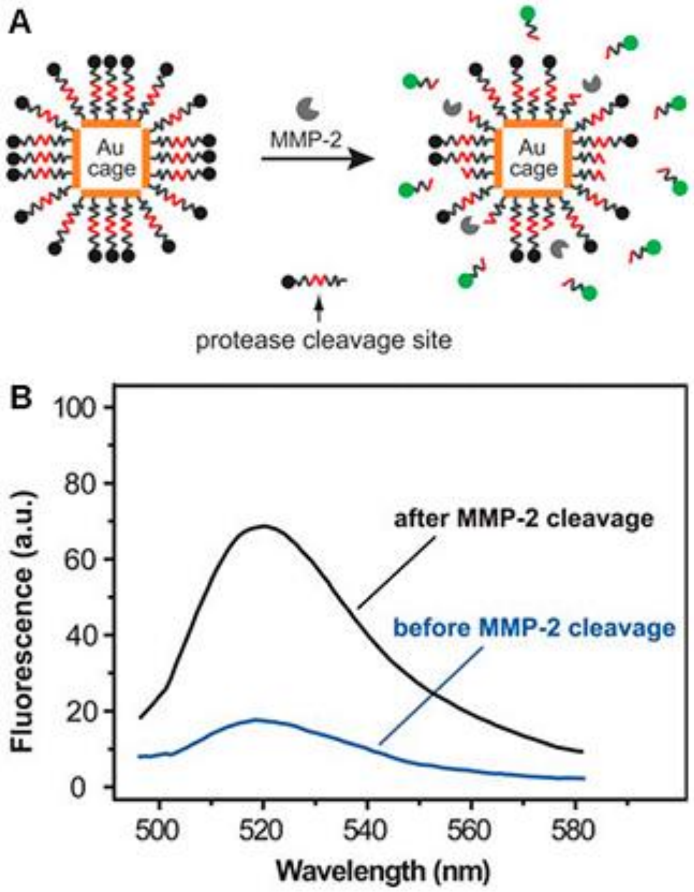

Figure 1.5. (A) Schematic diagram showing the detection platform for the target MMP-2 via FRET. (B) Fluorescence signal of the solution before and after MMP-2 cleavage. Adapted from [73].

(e) Colorimetric probes for analyte detection

Since LSPR can be tuned by medium properties and the interparticle distance, detection platforms for analytes (metal ions, small molecules, large biomolecules, etc.) have been developed via the manipulation of the two parameters, especially the interparticle distance. Generally, when the distance between two particles is less than 2.5 times their size [51], coupling of LSPR would red shift the extinction curve to longer wavelength. Blue shift would occur when the closely spaced particles separate from each other.

Mirkin et al. pioneered this area in 1997 and developed a method to detect a target polynucleotide utilizing AuNPs, which were surface modified with the target's complementary strands (probes). With the presence of the single-stranded target, the dispersed AuNPs were cross-linked, changing the color of the spot test result (Figure 1.6A). Another striking finding from this study was the sharp transition temperature of the oligonucleotide-modified AuNPs (Figure 1.6B and 1.6C), enabling the discrimination of mismatched targets [74].

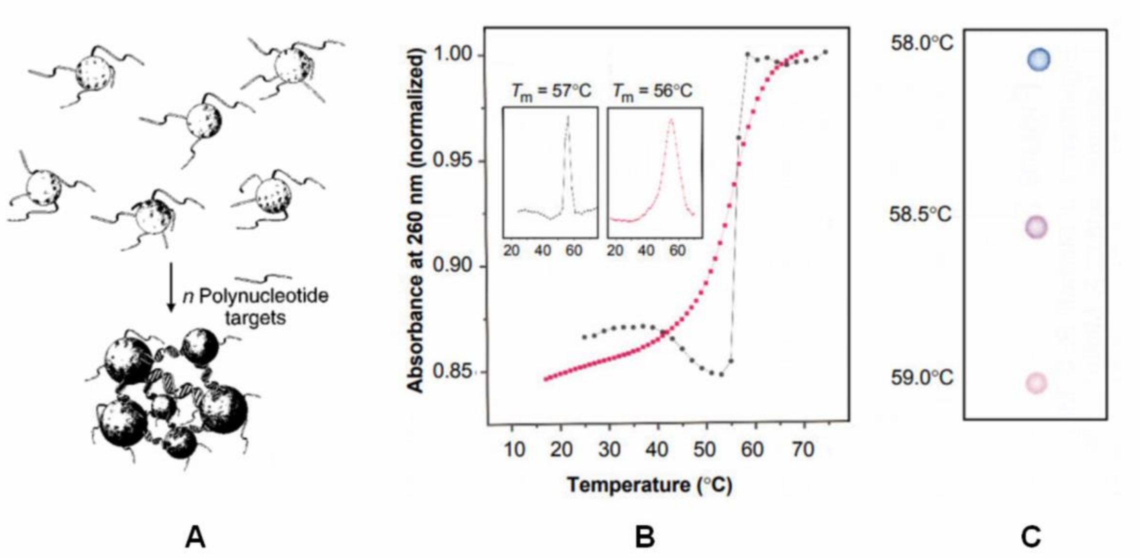

Figure 1.6. (A) The first detection scheme using AuNPs for colorimetric detection of single-stranded polynucleotide. (B) Thermal dissociation curves of the complementary duplex (hybridization product of the target and probe), with (black circles) and without (red squares) AuNPs. (C) The spot test result of the duplex with AuNPs, confirming the sharp transition temperature at 58.5 ℃. Adapted from [74].

Another seminal work by Li and Rothberg identified different propensities of single- and double-stranded oligonucleotides (ssDNA and dsDNA) to adsorb onto citrate-coated AuNPs, and designed a hybridization assay for target ssDNA detection based on the findings (Figure 1.7). When the target ssDNA coexisted with the probe ssDNA, they would form dsDNA, which shielded the bases and wouldn't adsorb onto the negatively charged AuNPs due to strong electrostatic repulsion between gold surface and negatively charged phosphate backbone of dsDNA. Without the target, the probe ssDNA could however favorably interact with the gold surface by uncoiling and exposing its bases, which could stick to the particle via van der Waals attraction. The adsorbed probe ssDNA could stabilize the citrate-AuNPs against salt-induced aggregation, whereas the sample with the target would aggregate to a bluish color [75].

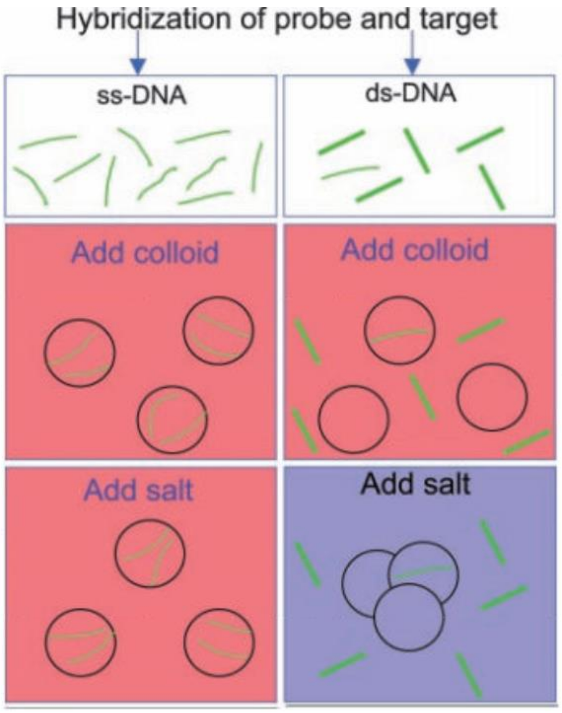

Figure 1.7. Schematic diagram illustrating ssDNA target detection via the different salt stabilities of AuNPs in the absence/presence of the target strand. Adapted from [75].

Aptamers, which are single-stranded nucleic acids and have strong affinity for many analytes (e.g., metal ions, small molecules, and proteins) with high specificity, can also be incorporated to the aforementioned systems. Thus, colorimetric assays based on AuNPs have been extended successfully for the detection of a large pool of targets [76-78]. A lot of efforts have been made on increasing the detection sensitivity by combining with target amplification or signal amplification pathways, and designing new assay schemes via the manipulation of the interparticle distances.

(f) Photothermal therapy (PTT) agents

Gold nanomaterials are burgeoning as PTT agents compared to their traditional counterparts (e.g., indocyanine green) due to their superior absorption coefficients and photostabilities. After absorption of the incident photons, the energy can be dissipated efficiently by coupling to atomic lattice vibrations (phonons). The following phonon–phonon relaxation can then result in significant heat generation, increasing the local temperature [79-80]. Photothermal therapy is feasible in anticancer treatment because tumor cells are more prone to destruction at elevated temperature. Based on the mode of the applied laser, continuous or pulsed wave, cell death is induced in either apoptotic or necrotic pathways. For *in vivo* applications, to minimize the tissue absorption and maximize penetration depth, near-infrared (NIR) laser is employed. Therefore, gold nanomaterials with LSPR in the “NIR window” are more suitable for this application [81]. AuNSs [82-83], AuNRs [84], gold nanocages [85], and self-assembled small AuNPs [86], with their high photothermal conversion efficiency, have been proven as excellent PTT agents [87].

(g) Photoacoustic tomography (PAT) contrast agents

The nonradiative energy relaxation of gold nanomaterials, as mentioned in the previous section, would result in great heat dissipation. When a pulsed laser with wavelength at the LSPR is applied, such dissipation would cause a drastic local temperature increase. The local pressure would then build up in the confined area and produce ultrasound waves [88]. This light to ultrasound energy conversion enables the construction of photoacoustic imaging modalities, which encompass both the high spatial resolution of light-based techniques and the deep penetration of ultrasound [89]. The feasibility of AuNPs [90], AuNSs [91], and gold nanocages [92] as PAT contrast agents has been established. Figure 1.8 shows that the injected AuNSs and gold nanocages increased the blood absorption (at wavelength ~800 nm) by 63% and 81%, respectively. The gold nanocages have slight advantages here due to their higher absorption vs. scattering [91-92].

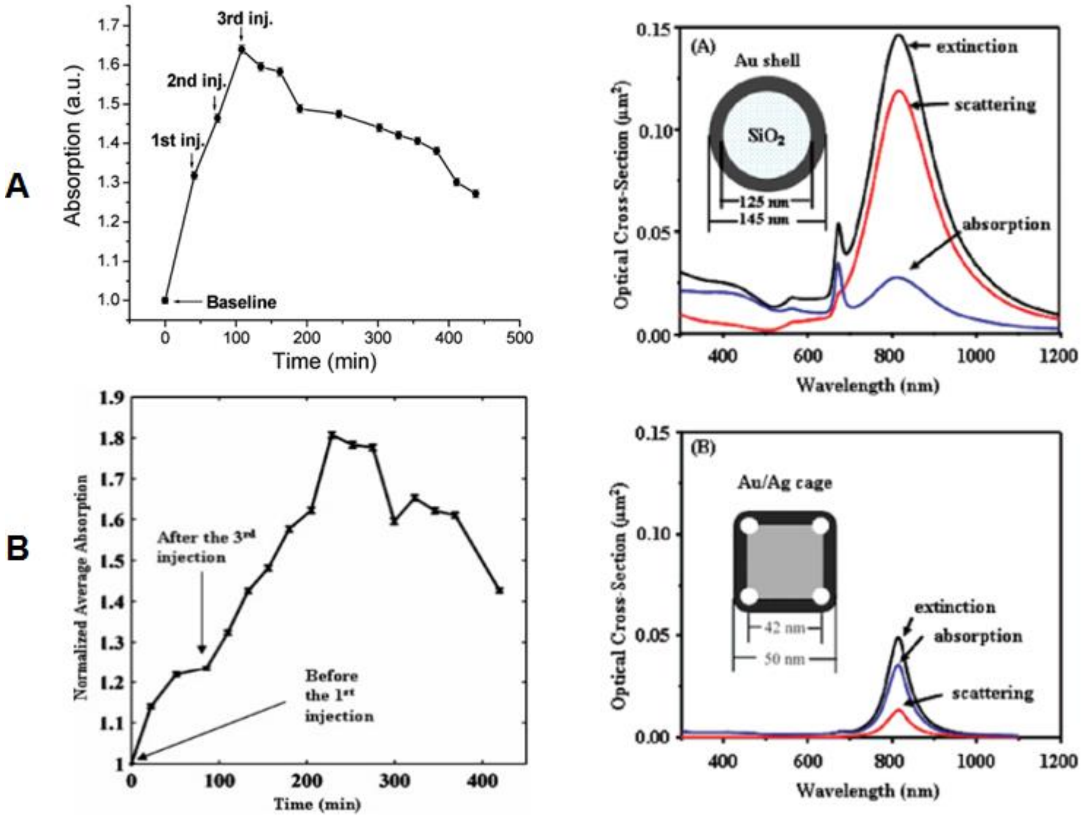

Figure 1.8. (A) Optical absorption of the rat's blood after 3 injections of AuNSs, and the calculated extinction. Adapted from [91]. (B) Optical absorption of the rat's blood after 3 injections of gold nanocages, and the calculated extinction. Adapted from [92].

1.2.2. Other properties

Apart from their fascinating optical properties due to LSPR, gold nanomaterials also possess other properties which further help pave their way in the biomedical field.

1.2.2.1. X-ray contrast

X-ray-based imaging is one of the most widely used imaging modalities in hospital. The conventional X-ray contrast agents are iodine-based. Gold nanomaterials can serve as superior X-ray contrast agents because gold has higher atomic number and thus higher electron density than iodine, allowing even stronger attenuation of X-ray. The first demonstration of using gold nanomaterials as X-ray contrast agent dated back to 2004, when Hainfeld et al. injected 1.9 nm gold nanoclusters (AuNCs) into Balb/c mice and clearly visualized the tiny vasculature (~100 μm diameter) around the tumor region [93]. Later in 2006, the same group compared the 1.9 nm AuNCs and a commercial iodine-based contrast agent, and achieved better image for the AuNCs [94]. Besides, the traditional small molecule contrast agents generally do not have targeting capabilities due to short blood circulation time, which is another drawback compared with the gold nanomaterials.

1.2.2.2. Radiosensitization

Gold nanomaterials are also capable of absorbing and concentrating X-ray to where they are localized, largely increasing the radiotherapy efficacy [93, 95]. By distributing the radiosensitizers to the diseased site, selective treatment can be achieved without damaging the healthy tissue.

1.2.2.3. Enhanced biodistribution

The enhanced permeability and retention effect (EPR effect) results from the abnormalities of the vasculature and lymphatic drainage around solid tumor region [96-97]. This allows the preferred biodistribution of nanomaterials at the tumor sites compared with small molecules. Although the pharmacokinetics is always complicated by other factors (e.g., protein corona formation, clearance by reticuloendothelial system), gold nanomaterials were proved to show better accumulation at tumor sites [98-99]. Due to the advantages of facile surface modification and remarkable biocompatibility, gold nanomaterials can serve as a delivery vehicle and be functionalized with different functional moieties, e.g., cancer drugs, small interfering RNA (siRNA), and photosensitizer, for drug delivery, gene therapy, and photodynamic therapy (PDT), respectively [79].

Some of the aforementioned applications can be smartly combined to achieve on-demand drug delivery using NIR lasers, and even create a single multimodal platform with both the therapeutic and diagnostic functions [38].

1.3. Synthesis of gold nanomaterials

1.3.1. Synthesis of different forms of gold nanomaterials

This section briefly introduces the syntheses of some extensively studied gold nanomaterials, excluding AuNPs, which will be discussed separately in Section 1.3.2.

1.3.1.1. Gold nanoclusters (AuNCs)

Gold nanoclusters, AuNCs, were not included in the previous sections because of their unique optical properties. This special set of gold nanomaterials contains only a few to several hundred gold atoms, with a size below 2 nm. In this size range, the LSPR would vanish due to the spatial confinement of the free electrons, and instead AuNCs exhibit strong and size-dependent photoluminescence properties [100-101].

AuNCs were previously synthesized via the sputtering of a gold target by some ions in rare gas matrices [102-103]. However, this method generally produces a mixture of different clusters and the cluster stability is low without any capping ligands. Solution-based syntheses of AuNCs are more preferable, which can be surface-protected by ligands (e.g., phosphines, thiols, and amines). Such syntheses can be divided into two pathways: “bottom-up” and “top-down”.

(a) “Bottom-up” approach

A seminal work was done by Schmid et al. to synthesize phosphine-stabilized Au_{55} clusters by the reduction of a gold precursor with diborane gas in benzene [104]. The formed clusters were difficult to isolate and not very stable. Brust–Schiffrin method is the pioneering work of producing ultrastable monolayer-protected AuNCs in two-phase liquid–liquid system [105], inspired by Faraday's two-phase preparation of gold colloid in 1857 [40]. Briefly, the gold precursor $AuCl_4^-$ was transferred from aqueous phase to the organic toluene phase by a phase-transfer agent tetraoctylammonium bromide (TOAB), where the precursor was reduced by aqueous sodium borohydride ($NaBH_4$, a strong reducing agent) and capped by dodecanethiol ($C_{12}H_{25}SH$). The formed thiol-stabilized AuNCs were extremely stable and the size could be adjusted by varying the thiol-to-gold ratio. Later, the same group developed a one-phase method to produce another thiol-capped AuNCs by *p*-mercaptophenol [106]. The Brust–Schffrin method has been modified by many studies to produce thiolated AuNCs with different sizes and surface chemistries [107-109].

(b) "Top-down" approach

AuNCs can also be prepared via precursor- or ligand-induced etching of the larger AuNPs. Figure 1.9 shows one example of etching 6 nm dodecylthiol-capped AuNPs to obtain Au_3 clusters induced by the excess thiol ligands. The etching reaction was completed after 50 min of thermal reflux at ~300 ℃ [110]. Multivalent coordinating polymer polyethylenimine (PEI) [111] and gold precursors [112] were also proven to successfully etch AuNPs to prepare luminescent AuNCs.

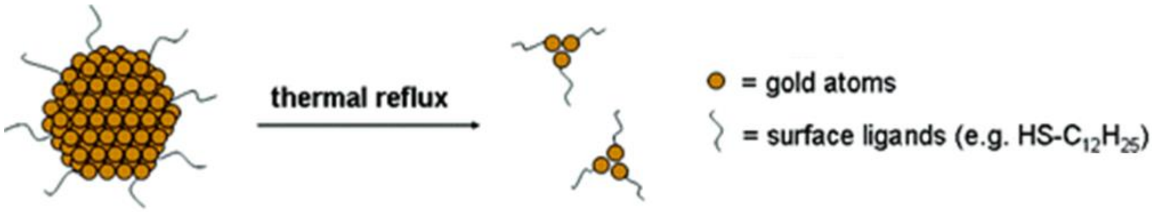

Figure 1.9. Schematic diagram showing the ligand-induced etching of larger thiol-capped AuNPs to form Au_3 nanoclusters induced by excess dodecylthiol under thermal reflux. Modified from [110].

1.3.1.2. Gold nanorods (AuNRs)

Rod-shaped gold nanomaterials, or AuNRs, were first electrochemically template-synthesized by hard anodic aluminum oxide (AAO) membrane [113] or soft cetyltrimethylammonium bromide (CTAB) surfactants [114]. Seed-mediated growth is the most widely used method for AuNR synthesis and was developed by the groups of Murphy and El-Sayed [115-118]. Typically, as depicted in Figure 1.10, CTAB-coated gold seeds (< 3 nm; produced by $NaBH_4$ reduction of chloroauric acid $HAuCl_4$) were introduced to a growth solution of gold precursor, reducing agent ascorbic acid, surfactant CTAB, and silver nitrate ($AgNO_3$). Ascorbic acid would only reduce Au(III) to Au(I) without the presence of seeds. Once the seeds were introduced, anisotropic growth would occur to produce AuNRs via either surfactant-preferential-binding-directed [119] or electric-field-directed [120] mechanism. No consensus has been achieved on the underlying mechanism though. Varying the concentration of the added silver ions was able to control the AuNR size [118]. Another valuable work for AuNR synthesis was performed by Jana et al. to synthesize the gold seeds *in situ*. This modification enabled the synthesis of smaller rods than the conventional procedure but maintaining the aspect ratio (AR, ratio of length over diameter) [121]. Since smaller AuNRs have larger absorption portion of the extinction cross section (more preferable for photothermal conversion), the modified protocol may find more potential use in PTT applications [122].

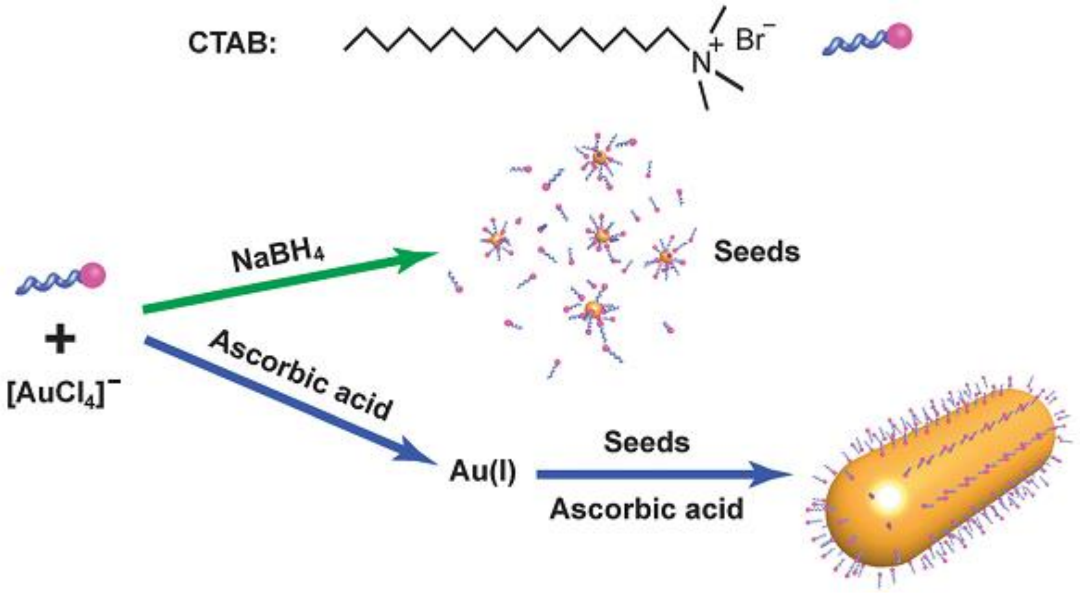

Figure 1.10. Schematic diagram illustrating seed-mediated growth of AuNRs. Adapted from [123].

1.3.1.3. Gold nanoshells (AuNSs)

AuNS, consisting of a spherical dielectric/semiconductor core and a thin outer layer of uniform gold, exhibits highly tunable LSPR. Thus, abundant protocols were developed to obtain AuNSs with different core materials including but not limited to silica [124-125], quantum dots (QDs) [126], liposomes [127], and polymeric nanoparticles [128]. The first silica@gold core-shell AuNSs were experimentally produced by Halas et al. in 1998, which also provided the insights for synthesizing other AuNS structures [124]. In this pioneering work, monodisperse silica nanoparticles were grown by Stöber method [129] and functionalized with amine groups using 3-aminopropyltriethoxysilane (APTES). Then, 1–2 nm AuNCs [130] were introduced and bound to the silica surface via gold–amine linkage [131]. Subsequent addition of gold precursor and reducing agent deposited atomic gold around the AuNCs at the silica surface, increasing gold coverage to form a complete shell (Figure 1.11).

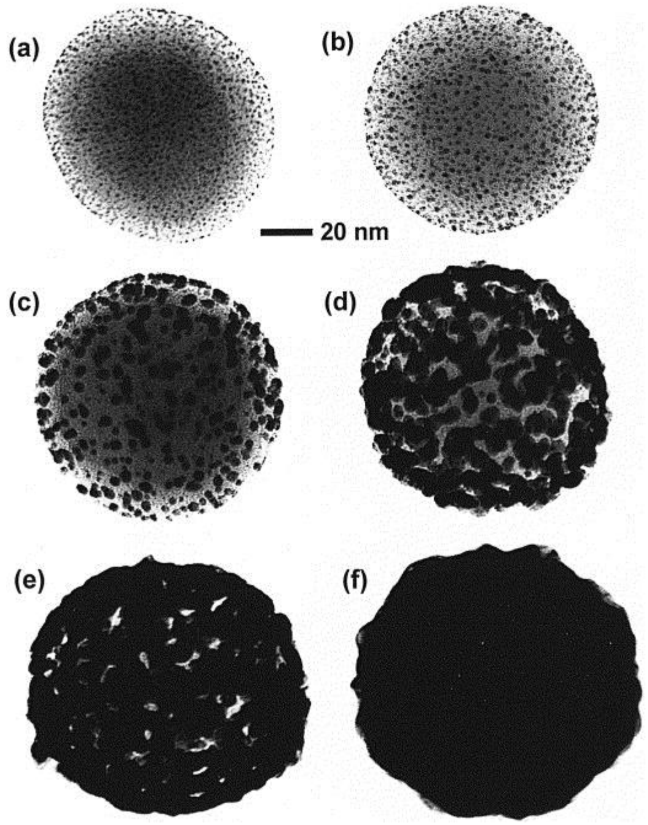

Figure 1.11. Transmission electron microscopy (TEM) images of the silica@gold core-shell formation process. Adapted from [124].

1.3.1.4. Gold nanocages

Gold nanocages have similar optical properties as AuNSs, but with hollow interior and porous walls. This set of gold nanomaterials was developed by Xia's group in 2002 [132]. Since elemental silver can be oxidized by Au(III), adding $HAuCl_4$ to silver nanocubes can dissolute the silver atoms while depositing elemental gold at the cube surface. Due to the 3:1 stoichiometry between displaced silver and the deposited gold, void spaces would form after the alloying and dealloying processes [133]. Using silver nanocubes as the sacrificial template, different shapes of gold nanocages have been obtained by varying the synthesis parameters [134].

1.3.2. Synthesis of gold nanoparticles (AuNPs)

Synthesis of spherical forms of gold nanomaterials, AuNPs, has been documented by a large amount of literature and is thoroughly summarized in a review written by Astruc et al. [135], but the three methods presented below are the most intensely utilized. Most of the published protocols can be considered as modifications from these methods.

1.3.2.1. Turkevich method

Turkevich method, simply adding sodium citrate to boiling $HAuCl_4$ under rapid stirring, is the most popular synthesis protocol for AuNPs [136]. Despite the fact that this method was not firstly reported by Turkevich et al., they systematically studied the reaction under different temperatures (70, 80, and 100 ℃), different concentrations of sodium citrate, and different dilutions of the reaction mixture. The produced citrate-capped AuNPs were about 20 nm in diameter. An "organizer" model was proposed in this pioneering work to explain the nucleation and growth mechanism of AuNPs. Frens then manipulated the citrate to $HAuCl_4$ ratio to achieve control over the particle size in the range of 16 to 147 nm, although the monodispersity of the produced AuNPs larger than 41 nm was poor [137]. Better size and shape control on this method has been achieved via tuning the reaction pH [138-145], temperature [140, 146-147], order of reactants addition [142, 148], citrate to $HAuCl_4$ ratio R [141, 144, 146, 148-149], addition of silver ions [138], etc. These parameters can affect the redox reaction between sodium citrate and gold precursor, thus the supersaturation of gold atoms, which determines the nucleation rate and size as predicted in the classical nucleation theory [150]. Some parameters can have complex influences on the nucleation and growth of AuNPs (e.g., mixing rate can affect both the reaction mixture pH and the reactant concentration).

Chemical reactions involved in this popular method have been revealed as follows [136, 151-153]. Gold precursor (in the form of Au(III) complex ions complexing with Cl^- or OH^-) gains electrons and is reduced to Au(I) complex ions, while sodium citrate is reduced to sodium acetone dicarboxylate (SAD). Then the Au(I) complex ions are bridged together by SAD, disproportionating to form Au(III) and gold atoms for AuNP nucleation and growth. Such disproportionation reaction can be catalyzed by the presence of gold surface, enabling surface-catalyzed particle growth. For full reduction of Au(III) by sodium citrate, the citrate to $HAuCl_4$ ratio R should be larger than their stoichiometric ratio of 1.5. However, full depletion of Au(III) was reported by Frens when R was ~0.4 [137]. This is rationalized by some authors that the degradation product of SAD, acetone [154-155], is able to reduce $HAuCl_4$ to produce stable AuNPs [136, 153, 156]. Besides, acid form of SAD (acetone dicarboxylic acid) was also reported to react with $HAuCl_4$ for AuNP formation [136, 157], with final oxidation products of formic acid and acetic acid. Therefore, even though only two reactants (sodium citrate and $HAuCl_4$) are added in this method, there are many species involved in the physicochemical processes of AuNP formation, not to mention the hydroxylation of Au(III) complex ions and the protonation/deprotonation of citrate.

1.3.2.2. Brust–Schiffrin method

The Brust–Schiffrin method was originally developed for the synthesis of AuNCs (introduced in Section 1.3.1.1). Modifications of this method (e.g., varying thiol-to-gold ratio [158]) enabled the synthesis of thiol-capped AuNPs of smaller size, which is not attainable via the Turkevich method. Generally, $NaBH_4$ is used as the reducing agent due to its strong reducing strength.

1.3.2.3. Seed-mediated growth method

Seed-mediated growth method was briefly introduced in Section 1.3.1 for the synthesis of AuNRs and AuNSs. In the AuNP synthesis, this strategy is able to address the low monodispersity issue of Turkevich method when producing larger (> 40 nm) particles. Seed-mediated growth of AuNPs was modified and intensively employed by Natan et al. at the end of the 20th century [159-161]. Their protocol started with synthesizing 12 nm citrate-AuNPs as seeds, then using citrate/hydroxylamine to reduce $HAuCl_4$ onto the seeds without inducing further nucleation. Their syntheses yielded small portion of undesired AuNRs. Murphy’s group obtained high-quality AuNPs in the range of 5–40 nm, wherein 3.5 nm citrate-AuNPs (produced by $NaBH_4$ reduction) were grown with ascorbic acid and CTAB as particle stabilizer [162]. In 2006, Liz-Marzán et al. successfully produced even larger monodisperse AuNPs by increasing the reaction temperature to 35 °C and including a filtration step in the procedure [163]. Further modifications of seed-mediated approach are available to improve the product quality [164-167].

1.3.3. Color change in the synthesis of AuNPs

1.3.3.1. Turkevich method

In a typical Turkevich synthesis, once sodium citrate is added to the boiling gold precursor $HAuCl_4$ solution, the light yellow color would disappear, and the whole mixture would then turn from colorless to purple/blue before the final ruby red colloid is formed. Since purple/blue color generally indicates a larger particle size compared with the final red product (refer to Section 1.2.1.2), such color change phenomenon contradicts the widely accepted LaMer nucleation and growth mechanism for nanoparticle formation. This classical mechanism consists of two separate steps: a burst nucleation and then nuclei growth by diffusion [168-169], resulting in an increasing size of the formed nanoparticles. Therefore, great research effort was made to understand the purple/blue-to-red color change and illustrated below in chronological order. There are in total 12 key papers studying such color change in Turkevich method (p. 27–63) and five possible mechanisms were proposed: (i) formation of fluffy large aggregates from AuNPs which are spherical in shape; (ii) formation of solid polycrystalline nanowires via aggregation from AuNPs or deposition of gold along certain facet of AuNP seeds; (iii) formation of spherical aggregates from “glue” particles (liquid globules or Au(I)/sodium acetone dicarboxylate (SAD) complex) within which AuNPs nucleate and grow, without AuNPs directly interacting with each other; (iv) kinetic intermediate from closely spaced gold clusters/particles before compacting into AuNPs without any aggregates formation; (v) attachment of gold ions at electric double layer of the AuNPs without any aggregates formation. A tabulated summary of these 12 papers and the other 4 key papers studying on color change of seed-mediated growth of AuNPs (with citrate as reducing agent; Section 1.3.3.2; p. 64–71) is given at Section 1.3.3.3.

(1) Both Turkevich et al. and Frens reported such color change in their work, but didn’t explore the phenomenon [136-137]. Chow and Zukoski attributed the intermediate purple/blue color to the formation of fluffy large particles (> 100 nm), which shrank over time to produce the final particles of around 20 nm (mechanism (i)) [170]. In this study, they found the final particle sizes were weakly dependent on the reaction temperature, in agreement with Turkevich et al. [136]. At boiling condition, the color change was too fast to allow detailed analysis. Therefore, three lower temperatures (60, 70, and 80 ℃) were adopted. The evolution of the reaction extinction spectrum in the ultraviolet–visible (UV–vis) range at a reaction temperature of 70 ℃ was recorded, as shown in Figure 1.12A. The peak extinction wavelength changes of the reactions at the three temperatures were depicted in Figure 1.12B. Using Mie’s theory to convert the peak location to particle size, the researchers estimated the existence of larger particles with 110 to 120 nm size in the purple/blue state.

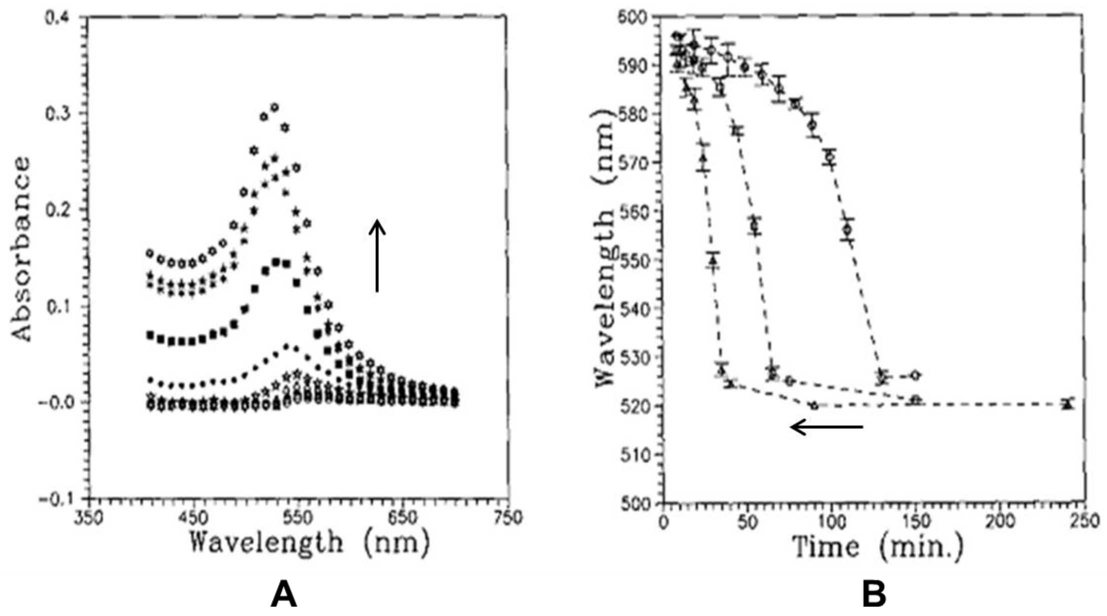

Figure 1.12. (A) Evolution of extinction spectra of Turkevich reaction under 70 ℃. The concentration of sodium citrate and $HAuCl_4$ were 1.6 mM and 0.24 mM, respectively (R = 6.67). (B) Evolution of extinction peak wavelengths of reactions under 60, 70, and 80 ℃. Higher temperature corresponded to faster wavelength change. Adapted from [170].

Iodometric titration was employed to quantify Au(III) complex ions in the course of the reaction. It was found that the isolated structures giving rise to the purple/blue color only contained little Au(III). A trend was noted that ~30% consumption of the total Au(III) correlated with the abrupt color change [170]. Dynamic light scattering (DLS; measuring the hydrodynamic diameter of the nanostructures) also suggested the existence of larger particles in the purple/blue stage (Figure 1.13). Similar evidence was visualized under TEM. For the reaction under 60 ℃ as a typical representative, fluffy large particles coexisted with smaller electron dense particles (5–15 nm) until 120 min after mixing of the reagents (Figure 1.14a–d). Final particles were 15 nm and monodisperse (Figure 1.14e).

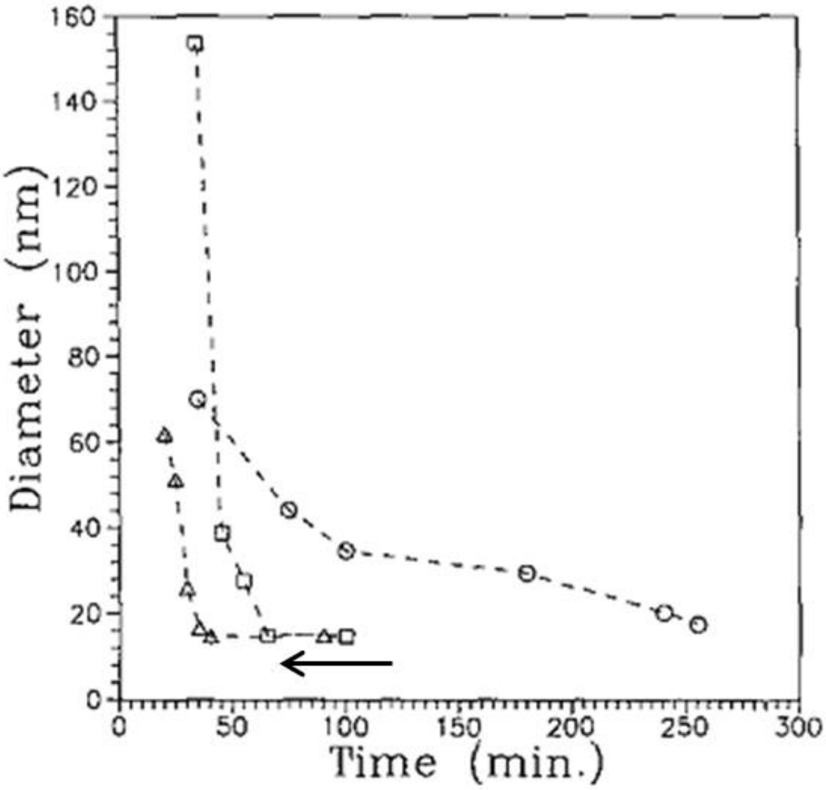

Figure 1.13. Measured hydrodynamic diameter of the nanostructures in the reaction mixture at 60, 70, and 80 ℃ (R = 6.67). The arrow indicated higher temperature. Adapted from [170].

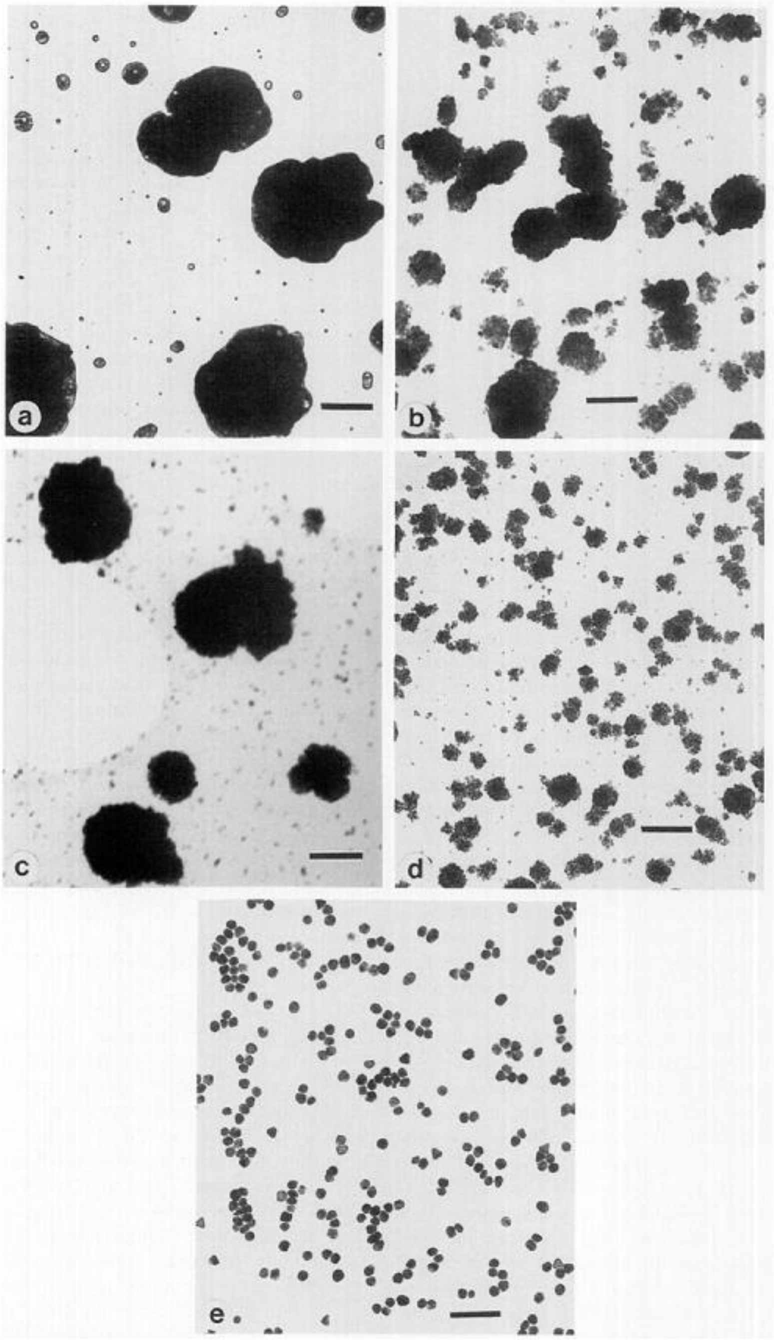

Figure 1.14. TEM images of reaction mixture under 60 ℃ (R = 6.67) collected at (a) 10 min, (b) 30 min, (c) 60 min, and (d) 120 min after mixing, and (e) final particles. Scale bar of 100 nm. Adapted from [170].

Although the size change during the purple/blue-to-red color change determined from UV–vis, DLS, and TEM didn't agree well, a general trend with shrinking particle size was consistent across the three characterization techniques [170]. Such size change and associated color change were rationalized by colloidal stability that: (a) the surface of the formed primary particles was firstly adsorbed by $AuCl_4^-$ ions, which endowed a low surface potential and aggregated the particles to from the fluffy large particles (the preferential adsorption of $AuCl_4^-$ ions over citrate onto gold surface was confirmed by atomic force microscopy studies of this group [171-172]); (b) irreversible aggregation was limited by the steric barrier formed by adsorbed ions; (c) with the consumption of the $AuCl_4^-$ ions, citrate ions bound onto the particles and increased the surface potential, the agglomerates falling apart to individual particles; (d) once the particles were separated, reduction went faster due to greater availability of reactive surfaces.

(2) To further verify the possible mechanism for the aggregation and dispersion of fluffy large particles, this group optimized their experimental setup and performed atomic force microscopy (AFM) again to monitor possible chemical reactions at the gold/solution interface under room temperature [173]. A gold-coated silica sphere (5 or 20 μm) was mounted to the AFM cantilever tip. The substrate was also coated with gold, and various solutions were introduced between these two gold surfaces. The deflection profile of the cantilever was converted to force curve (Figure 1.15A), based on which the electrostatic diffuse layer potential was calculated via DLVO theory (Figure 1.15B). Initially, 0.33 mM sodium citrate with pH 6.3 was added to the fluid cell and allowed to equilibrate for 17 h. Then, 0.1 mM $HAuCl_4$ in 0.33 mM sodium citrate (R = 3.3) was introduced, decreasing the repulsive interaction and endowing an attractive force within

15 min. The authors attributed this force change and corresponding potential drop to the preferential binding of monovalent $AuCl_4^-$ ions over trivalent/divalent citrate ions. With the reduction of $AuCl_4^-$ ions at room temperature, more citrate ions adsorbed onto the two gold surfaces and restored the repulsive force, which was also consistent with the increase in the diffuse layer potential with time. When analyzing the short-range force profile for the system after adding the reaction mixture for 15 min, the authors identified a non-linear compression behavior indicating a deformable surface (Figure 1.16). Despite the preferential binding of $AuCl_4^-$ ions, the labelled ~0.5 nm jumps were well correlated with the size of a citrate ion, suggesting a multilayer adsorption of citrate ions. This observation contradicted the potential drop in Figure 1.15B, since citrate ions were highly charged at the studied pH. They rationalized these findings by proposing the pairing of citrate ions with counterions and the formation of a neutral deformable network onto the gold surfaces. They also speculated that $AuCl_4^-$ ions didn't bind in their charged form either.

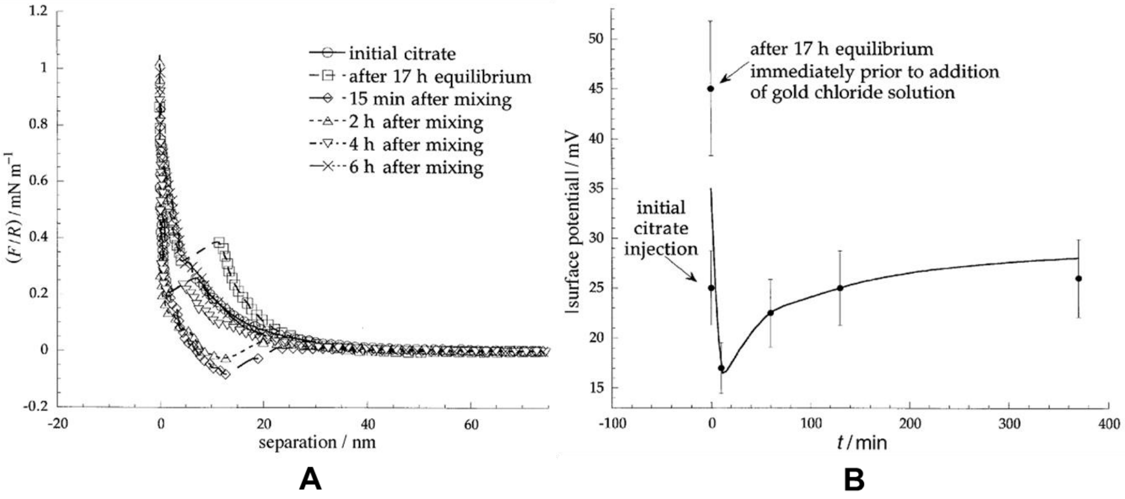

Figure 1.15. (A) Force–separation profile for the gold-coated silica sphere–gold-coated substrate interaction in the presence of 0.1 mM $HAuCl_4$ and 0.33 mM sodium citrate (R = 3.3) at pH 6.3 under room temperature. (B) The calculated evolving electrostatic diffuse layer potential based on (A). Adapted from [173].

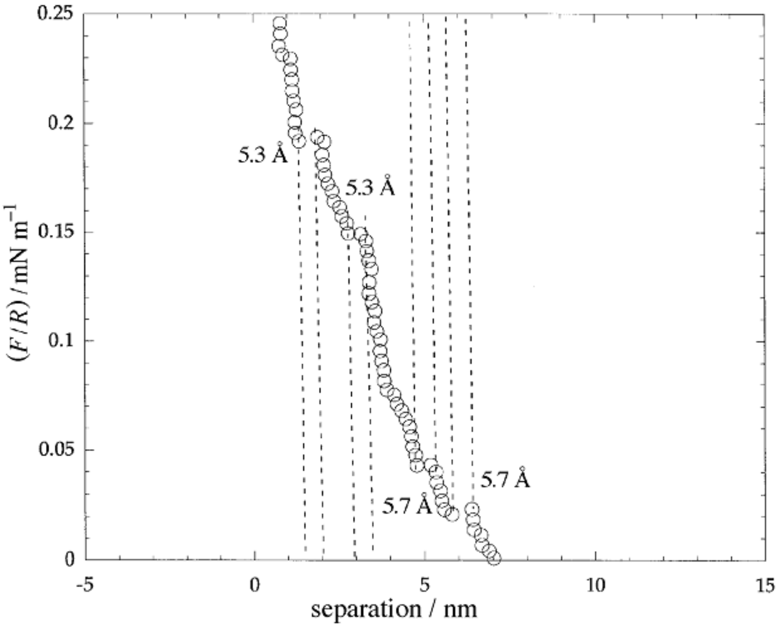

Figure 1.16. Short-range force–separation profile for the two gold surfaces 15 min after the introduction of 0.1 mM $HAuCl_4$ and 0.33 mM sodium citrate (R = 3.3) mixture. Adapted from [173].

(3) In another study, reducing the sodium salt of $HAuCl_4$ ($NaAuCl_4$) with sodium citrate at 80 ℃, with low R values to form nanowires, yielded another possible explanation for the color change (mechanism (ii)) [174]. When R was in the range of 0.4–2.7, the mixture would go through yellow, colorless, light blue, dark blue, and then red, whereas R within 0.1–0.3 range stopped at blue as the final color. Figure 1.17 shows the color changes for R = 0.4, and the UV–vis absorption spectra profiles for R = 0.4 and R = 0.3.

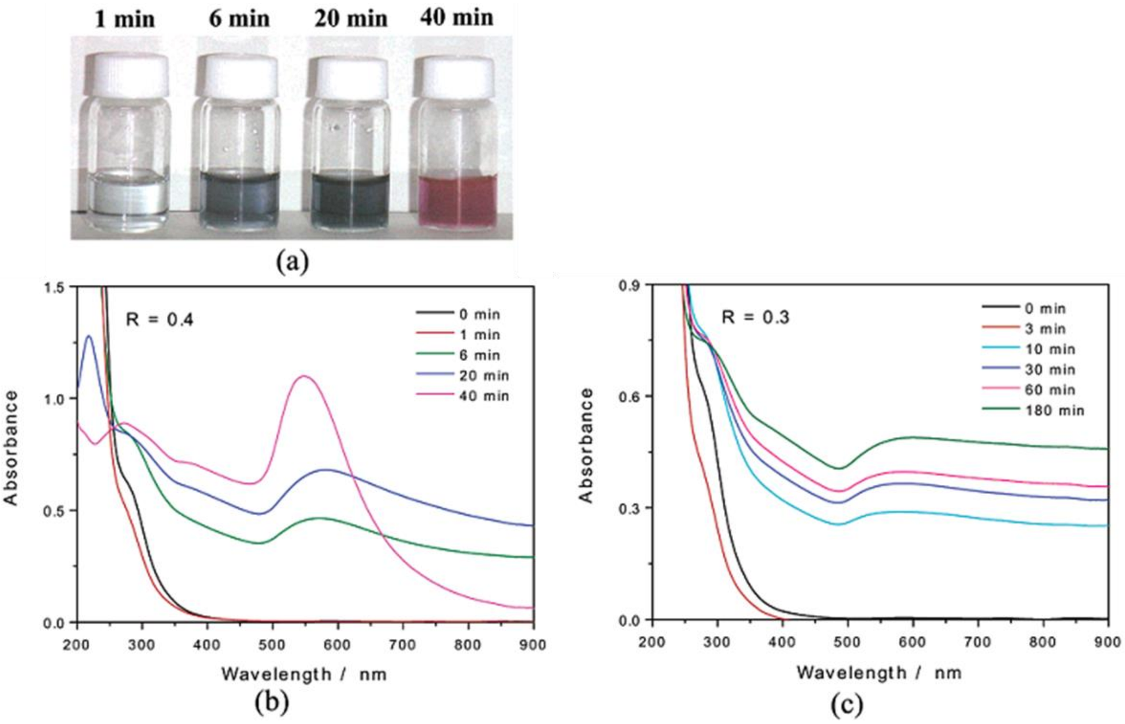

Figure 1.17. (a) Color change profile for R = 0.4. (b) UV–vis absorption of reaction with R = 0.4, consistent with the color change. (c) UV–vis absorption of reaction with R = 0.3. The blue color still persisted till 180 min after mixing. Adapted from [174].

The researchers attributed the blue color appearance to the existence of solid polycrystalline nanowires observed under TEM [174]. For R = 0.4, the nanowires were visible at 6 min, and disappeared at 40 min after the start of reaction (Figure 1.18). However, such structures persisted till 180 min when R was 0.3 (Figure 1.19).

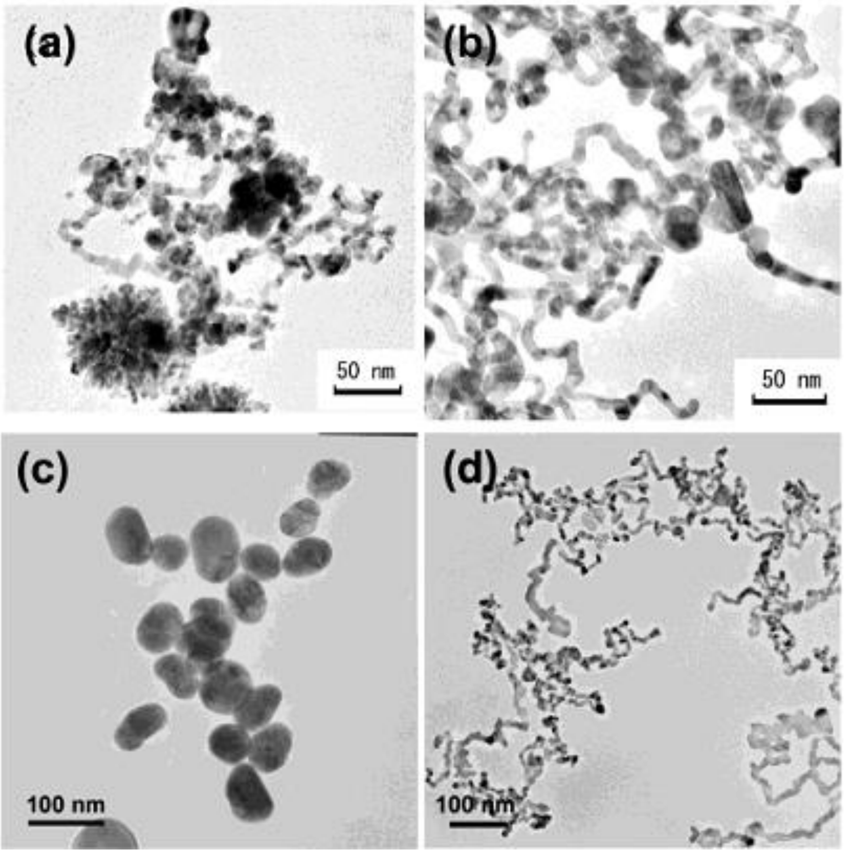

Figure 1.18. TEM images taken for quenched samples aliquoted from reaction mixture with R = 0.4 at (a) 6 min, (b) 20 min, and (c) 40 min after the start of reaction. (d) Washed sample of (a). Fluffy large particles shown in (a) was washed away, showing better image of the formed wires. Adapted from [174].

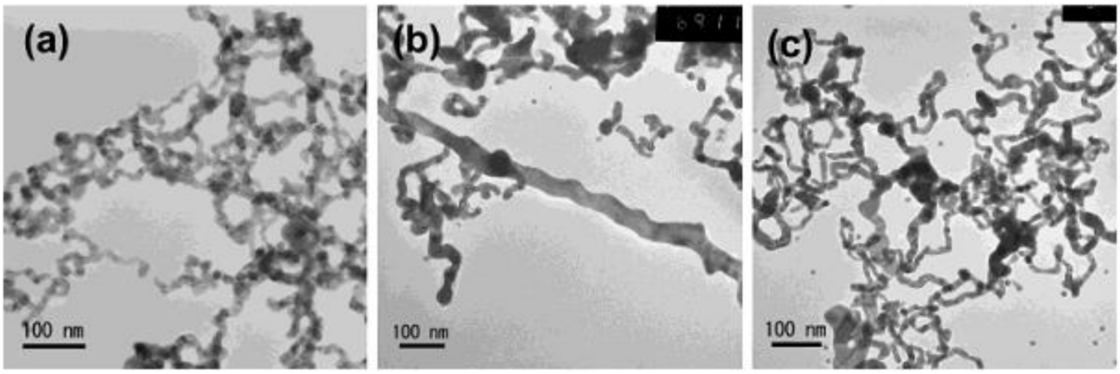

Figure 1.19. TEM images taken for quenched samples aliquoted from reaction mixture with R = 0.3 at (a) 10 min, (b) 60 min, and (c) 180 min after the start of reaction. The wires persisted until 180 min without breaking down to individual particles. Adapted from [174].

In their previous work, the authors found the nanowires were stable against the addition of a water-soluble thiol compound, indicating that the wires were made of tightly fused AuNPs [175]. TEM images were also taken for reaction with R = 0.2 and similar nanowires were observed (Figure 1.20). High-resolution TEM (HRTEM) image showed the deposition of metallic gold at the concave surface formed between two adjacent fused AuNPs. The electron diffraction result revealed the polycrystallinity of the formed nanowires.

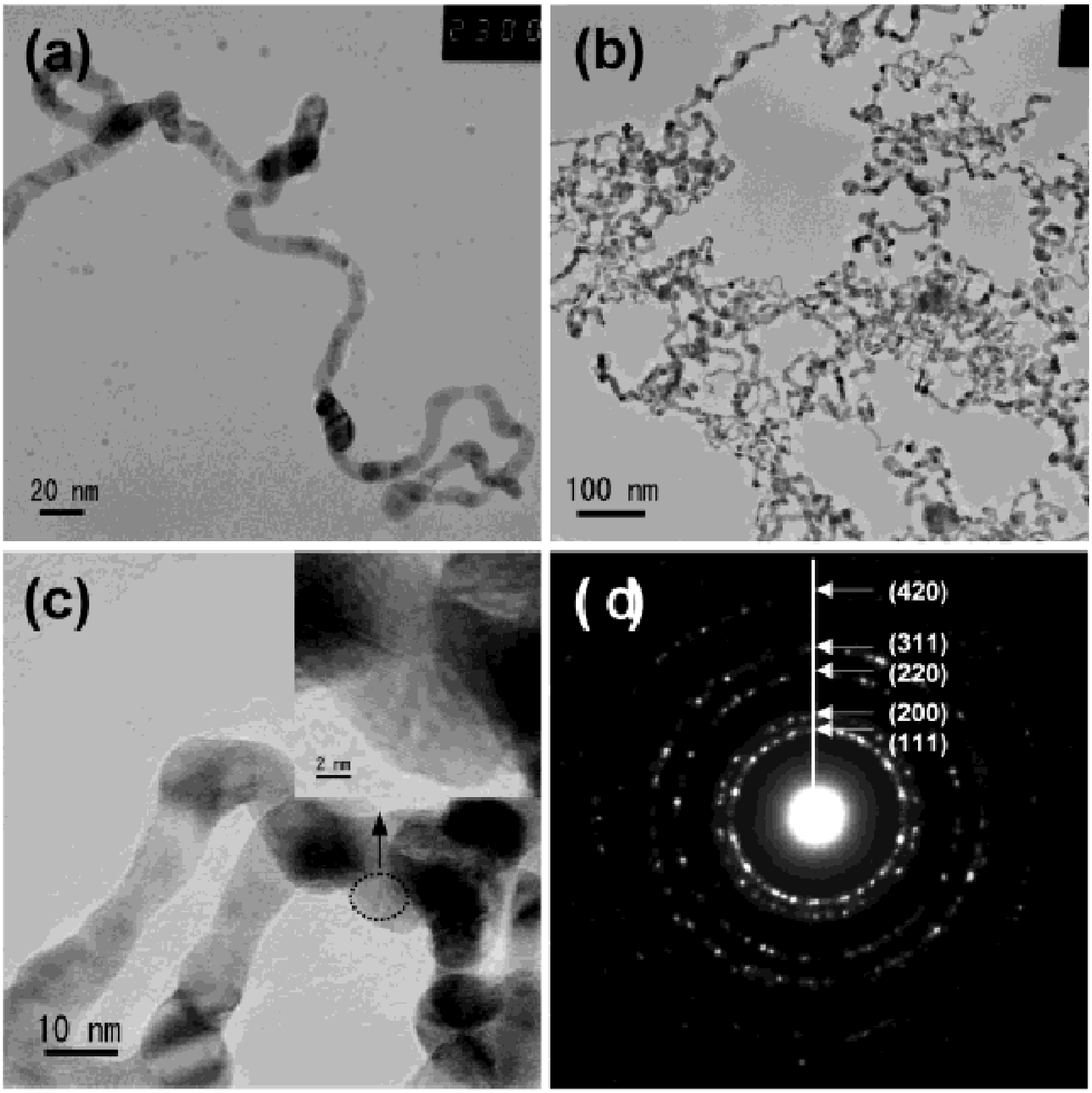

Figure 1.20. TEM images of reaction with R = 0.2 at (a) 30 min and (b) 60 min. (c) HRTEM image of (b) showing the deposition of metallic gold at the concave surface between two tightly fused AuNPs. (d) Electron diffraction of (c) showing the polycrystalline structure of the nanowires. Adapted from [174].

Concentrations of $AuCl_4^-$ and total Au in the solution phase were measured for both reaction conditions, and the metallic gold concentration [Au_0] was calculated by subtracting [Au] with [$AuCl_4^-$]. The normalized results are shown in Figure 1.21. It was proposed in this study that $AuCl_4^-$ played an essential role in the formation and stabilization of the nanowire structures. With the consumption of $AuCl_4^-$, such wire-like structures could no longer be maintained and individual particles would form, causing the blue-to-red color shift [174]. To further substantiate the importance of $AuCl_4^-$ in maintaining the wires, a TEM grid carrying the formed nanowires was treated with hydrogen gas (H_2) for 1 h at room temperature (Figure 1.22). The breakdown of the nanowires to discrete nanoparticles was claimed to result from the reduction of $AuCl_4^-$ by H_2 [174].

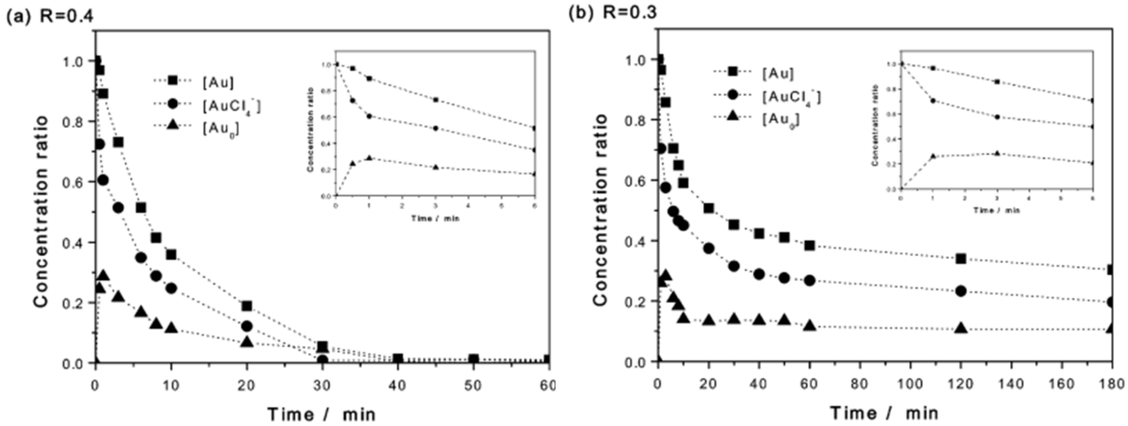

Figure 1.21. Normalized concentration of total gold [Au], precursor gold [$AuCl_4^-$], and metallic gold [Au_0] in solution phase after centrifuging off the nanostructures, under (a) R = 0.4 and (b) R = 0.3 reaction conditions. Adapted from [174].

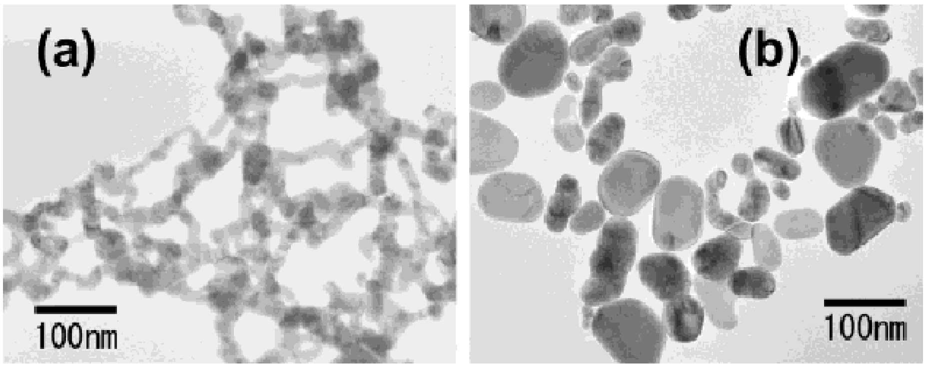

Figure 1.22. (a) TEM image of nanowires prepared at R = 0.3 for 10 min. (b) TEM image showing breakdown of the wires after treating the same TEM grid in hydrogen gas (H_2) for 1 h under room temperature. Adapted from [174].

(4) Kimling et al. investigated Turkevich method with different R (0.67–5) and didn’t find any aggregates in their small angle X-ray scattering (SAXS) results. Thus, they hypothesized that the blue color came from the plasmon excitation delocalization among the closely spaced clusters/particles (< 5 nm) formed at the beginning of the reaction (mechanism (iv)). Such kinetic intermediate of undefined shape only temporarily existed before the clusters agglomerate and compact into AuNPs with distinct LSPR [149].

(5) Pong et al. performed Turkevich synthesis under boiling condition with R = 3.88 [176]. Aliquots were taken during the reaction and were washed before investigation using TEM. Figure 1.23 shows the representative TEM images of different color stages. Basically, colorless stage was populated with 3–5 nm small AuNPs and some wire-like segments. Dark blue stage got extensive nanowire networks with diameter of ~5 nm. Then, the nanowires broke down to smaller network with diameter

of ~8 nm in the purple stage. Individual AuNPs (13–15 nm) would then cleave off the wires to form the final ruby-red dispersion. Similar gold nanowire structures were formed when the reaction temperature was 50 ℃ (Figure 1.24a), and when R was adjusted to 5 (Figure 1.24b) and 2 (Figure 1.24c).

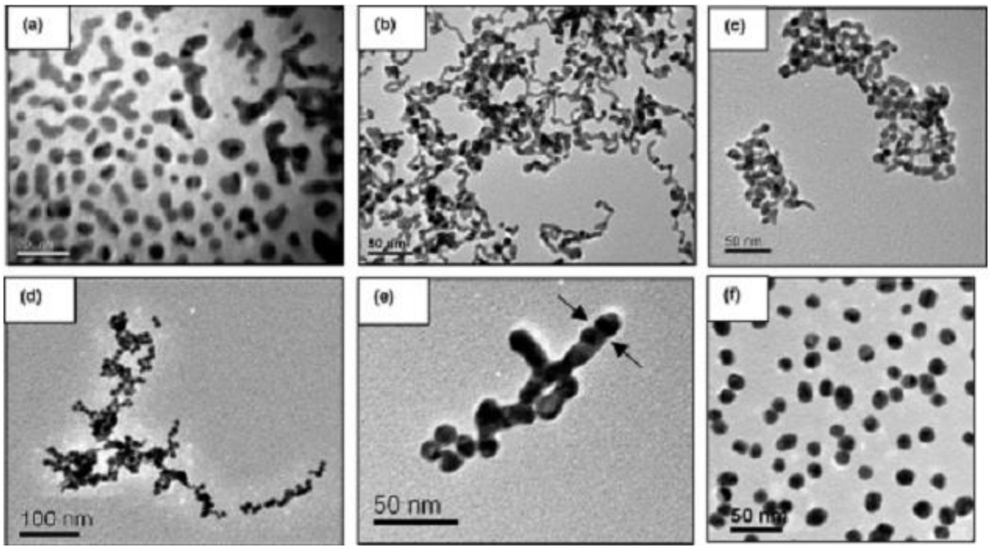

Figure 1.23. TEM images of aliquots taken from AuNP synthesis using Turkevich method. (a) Colorless phase with 3–5 nm small AuNPs and some wire-like segments. (b) Dark blue phase with extensive network of nanowires with diameter of ~5 nm. (c) Dark purple phase with small segments of nanowires with diameter of ~8 nm. (d) Purple-to-red transition phase where spherical AuNPs in the range of 10–13 nm were cleaved off the wires. (e) Constriction and cleavage site. (f) Final ruby-red phase with individual 13–15 nm AuNPs. Adapted from [176].

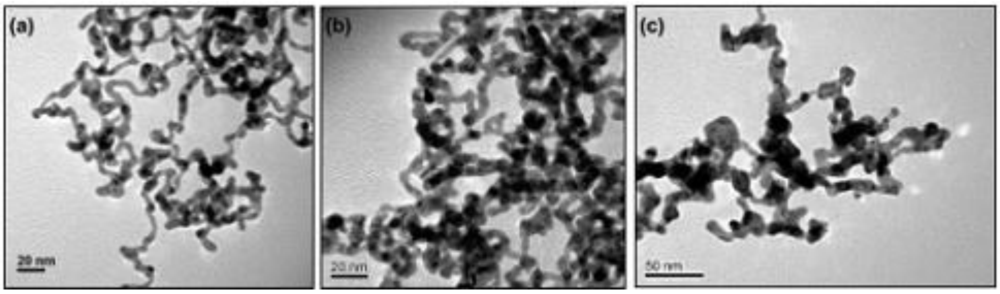

Figure 1.24. Similar nanowires were formed with different reaction conditions: (a) reaction temperature at 50 °C, R = 3.88; (b) reaction temperature at 100 °C, R = 5; (c) reaction temperature at 100 °C, R = 2. [$HAuCl_4$] = 0.91 mM in this study. Adapted from [176].

The proposed growth mechanism was schematically depicted by the authors (Figure 1.25) and was similar to the work by Pei et al. [174]. In summary, formed solid polycrystalline nanowires accounted for the purple/blue color during synthesis (mechanism (ii)). The breakdown of the nanowires to individual particles marked the transition to ruby-red color. The reasons behind nanowire formation and disintegration were also hypothesized (Figure 1.26). The formed ~5 nm AuNPs were adsorbed with $AuCl_4^-$, which induced an attractive interaction among the small particles, leading to the coalescence to form wire-like structures instead of other forms due to steric effects (geometrical constraints). Newly reduced gold atoms would firstly deposit onto the concave regions amorphously based on Kelvin equation of condensation, then onto the crystalline regions creating constriction sites. The amorphous region was depleted probably due to Ostwald ripening. With the consumption of $AuCl_4^-$ ions, citrate would adsorb to and cap the primary particles, increasing the electrostatic repulsion to finally cleave the particles off the nanowires.

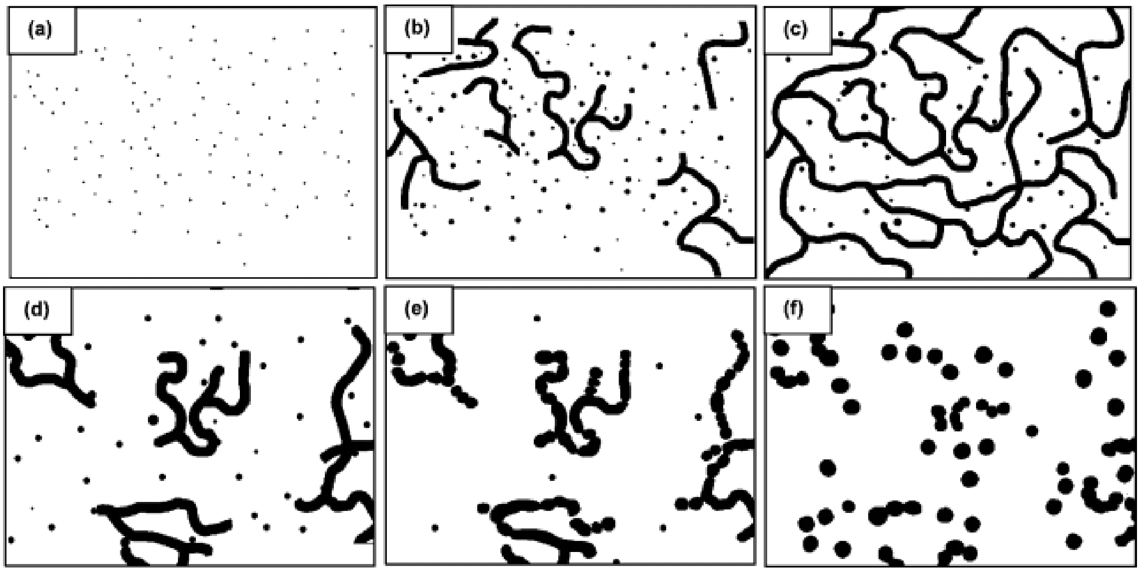

Figure 1.25. Schematic diagram showing the growth mechanism of Turkevich method. (a) Gold precursor $HAuCl_4$ was reduced by citrate to form Au atoms, which nucleated to form ~5 nm AuNPs. (b, c) The formed AuNPs self-assembled to form extensive nanowires. (d) More Au atoms were formed by reduction, and they adsorb onto the nanowires, increasing the nanowire diameter. At the same time, the wires were fragmented into smaller segments. (e, f) Further fragmentation to yield the final AuNPs. Adapted from [176].

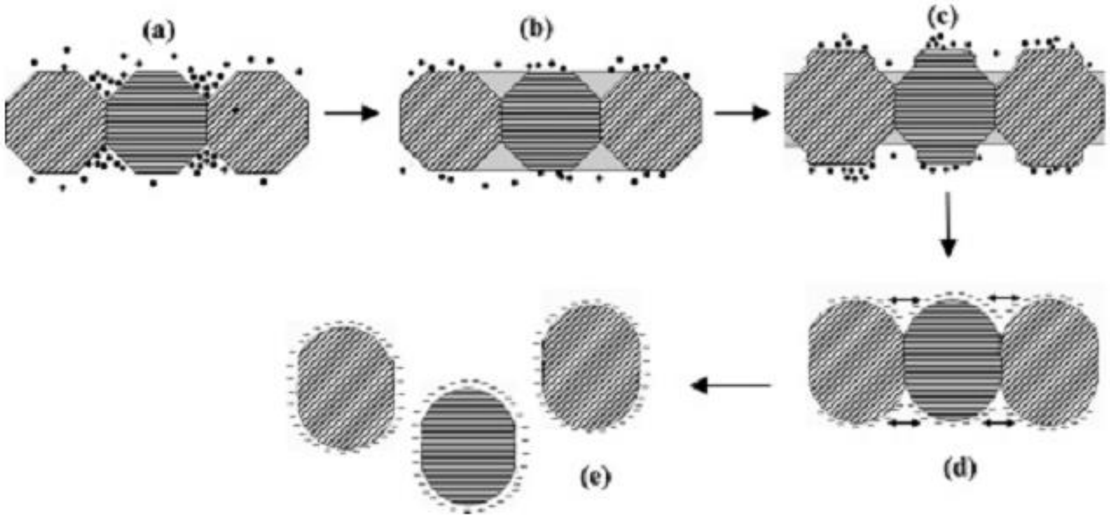

Figure 1.26. Schematic diagram showing the formation and disintegration of the nanowire structures. (a) Primary particles coalesced to form nanowires due to the adsorption of $AuCl_4^-$ ions. (b) Deposition of gold atoms to the concave region amorphously, smoothing the wire surface. (c) Further deposition of gold atoms to the crystalline regions on the particles, increasing the wire diameter. (d) Depletion of the amorphous region, and the particles were capped by citrate ions. (e) Individual particles cleaved from the wires, forming the final AuNP product. Adapted from [176].

(6) A systematic study on the third role of citrate in Turkevich synthesis was done by Ji et al. in 2007 [177]. Apart from functioning as reducing agent and capping agent, citrate was also found able to tune the reaction pH and thus affect the reaction pathway. In this piece of work, a threshold in R values (3.5) and thus pH (6.5) was identified, only below which the purple/blue color could appear. They monitored the reaction under different R values (0.7–28), and the color images and corresponding UV–vis absorption spectra of four R values are depicted in Figure 1.27. As can be seen, only lower R values had the purple/blue color stage. TEM images were taken for two

representative reactions, namely, R = 7 (pH 7.2) and R = 2 (pH 5.8). When R = 7, the reaction followed a pathway similar to the LaMer's nucleation-growth model, with the particle size continuously increasing (Figure 1.28, top row). When R = 2, faster nucleation occurred within 10 s, and the formed particles aggregated to form wire-like structures (mechanism (ii)), similar to those observed by Pei et al. [174] and Pong et al. [176]. The wire structures identified in this study were not uniform in diameter though (Figure 1.28, bottom row). HRTEM images of the formed wires with R = 2, shown in Figure 1.29, depict the solid and polycrystalline properties of the nanowires.

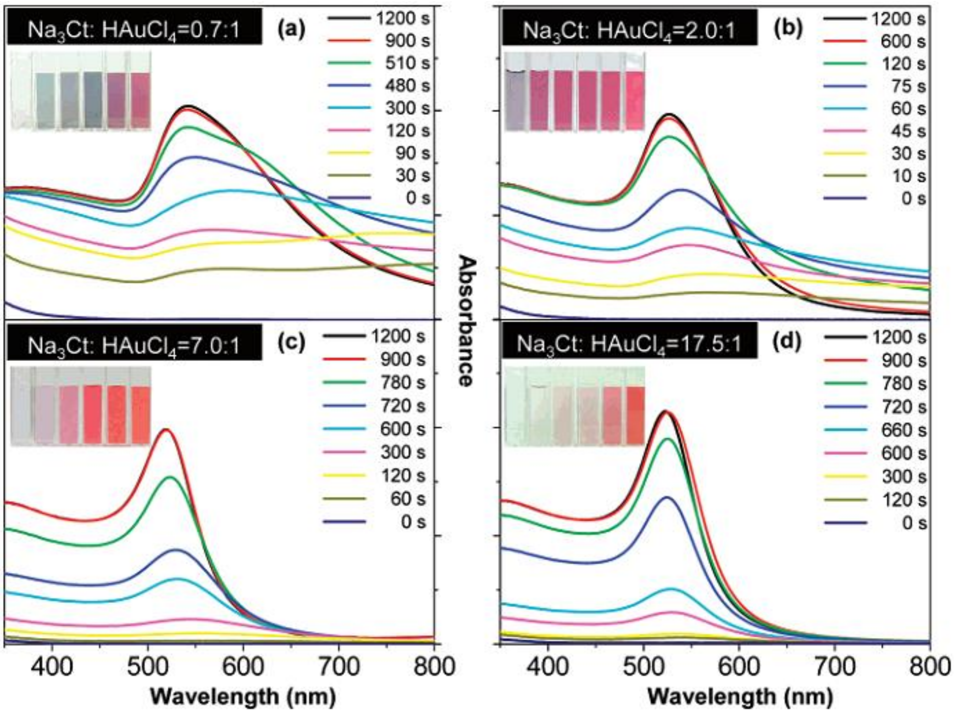

Figure 1.27. Color change and UV–vis spectrum change profile for (a) R = 0.7, (b) R = 2, (c) R = 7, and (d) R = 17.5. Adapted from [177].

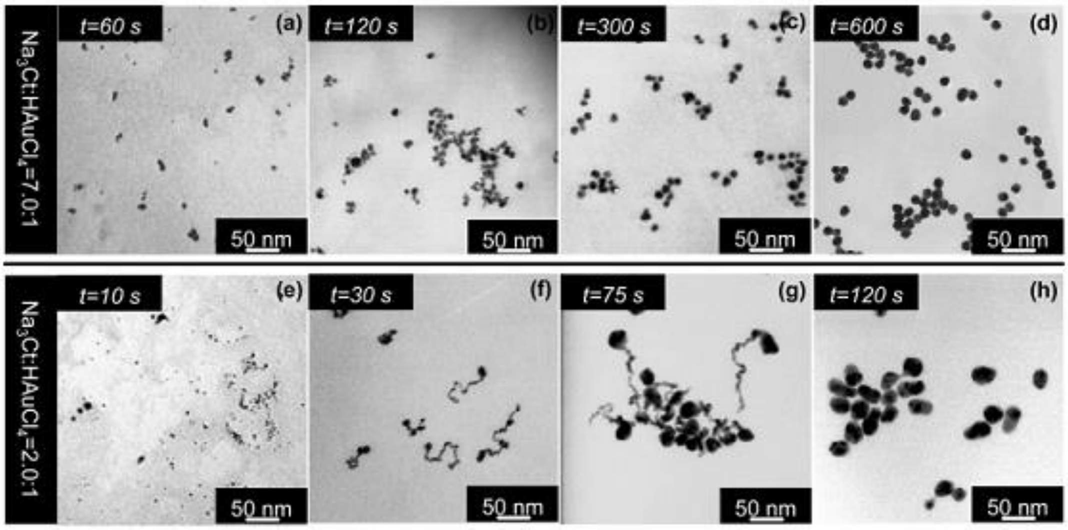

Figure 1.28. TEM images for two representative R values. (a–d) R = 7, the reaction proceeded in a nucleation-growth pathway. (e–h) R = 2, the reaction had faster nucleation, and nanowire structures formed as intermediate stage. Adapted from [177].

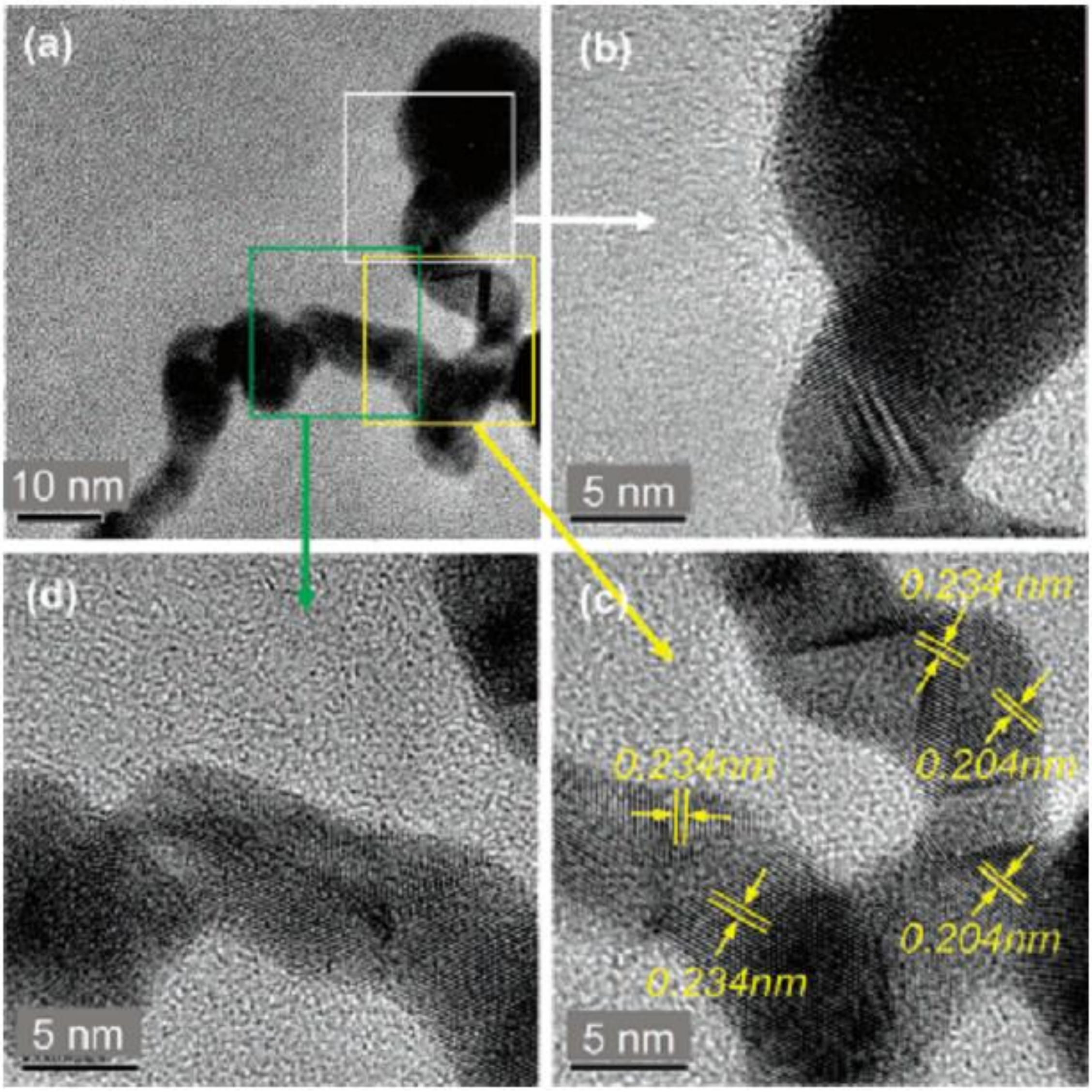

Figure 1.29. HRTEM images of the wires formed in reaction with R = 2. Enlargement of the selected regions shows the solid polycrystalline nature of the nanowires. Adapted from [177].

To further confirm the pH effects on reaction pathways, two more reaction conditions were monitored. One with R = 7 but pH adjusted to 5.8 (same as the unadjusted R = 2 case; Figure 1.30, top row). The other one with R = 2 but pH adjusted to 7.2 (same as the unadjusted R = 7 case; Figure 1.30, bottom row). After changing the pH, the pathways for the two R values were totally reversed.

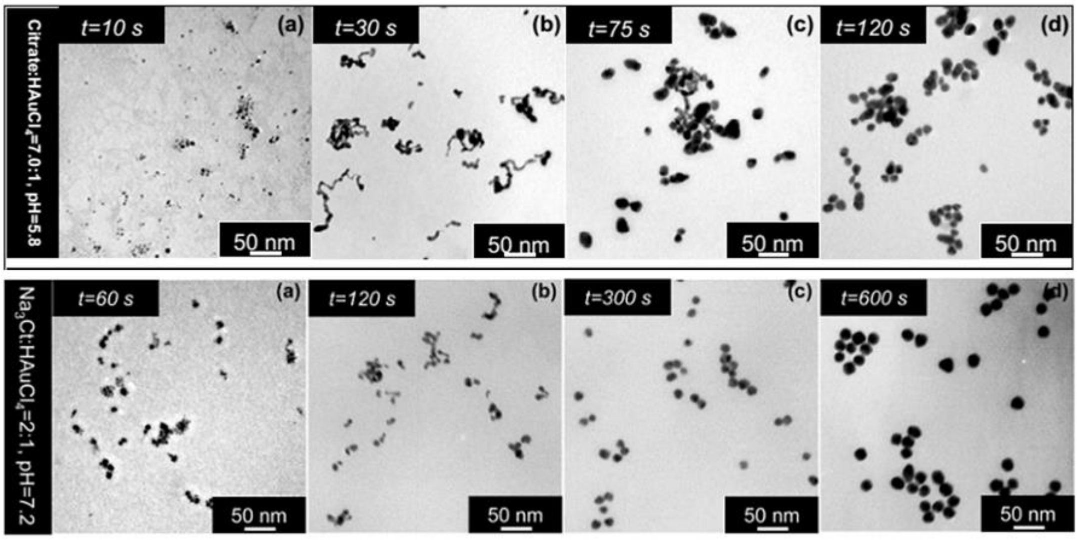

Figure 1.30. TEM images for the two R values with pH adjustment. Top row shows R = 7 with pH adjusted to 5.8. The nucleation occurred faster and wire-like structures appeared as intermediates. Bottom row shows R = 2 with pH adjusted to 7.2. The reaction proceeded in a nucleation-growth pathway. Adapted from [177].

pH values were measured across all the R values studied in this work and shown in Figure 1.31 together with the speciation and reactivity of Au(III) complexes dependence on pH. By manipulating the pH at a constant R value at 7, a pH threshold of 6.5 was established for the two reaction pathways shown in Figure 1.32.

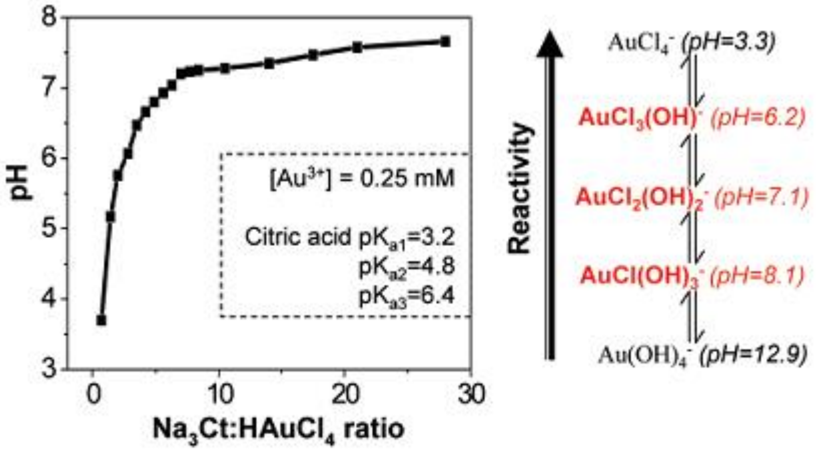

Figure 1.31. Measured pH values for different R ratio with [$AuCl_4^-$] at 0.25 mM. The speciation and reactivity of Au(III) complexes depend on pH. Adapted from [177].

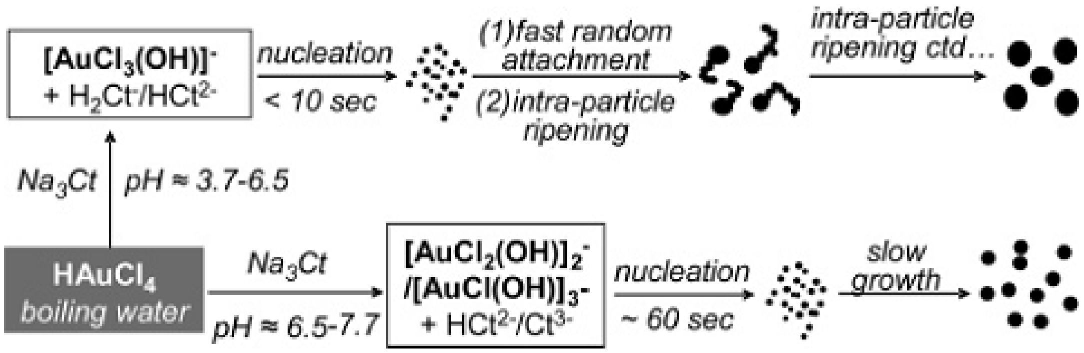

Figure 1.32. Schematic diagram showing the two pathways for AuNP synthesis under different pH, proposed by Ji et al. Adapted from [177].

In the pH range of 3.7–6.5, the Au(III) precursors would be reduced and undergo fast nucleation, then aggregate randomly to form nanowires, before intraparticle ripening to the final AuNPs. The researchers ruled out the possibility of cleavage of nanowires to form the final AuNPs, as suggested by previous literatures, due to their quantitative study on the concentration of Au(III) during reaction (Figure 1.33). As an example, for the case of R = 2, consumption of Au(III) was ~80% at 75 s and almost 100% at 2 min after the start of the reaction. If the color change was due to particles cleaving off the wire, there would be too many small particles originating from the thinner portion of the nanowires (Figure 1.28g). The remaining Au(III) wouldn't be sufficient to grow those small particles to their large size in Figure 1.28h. In the pH range of 6.5–7.7, a slow nucleation and growth pathway was involved and this pathway was exploited for monodisperse AuNP synthesis in this study.

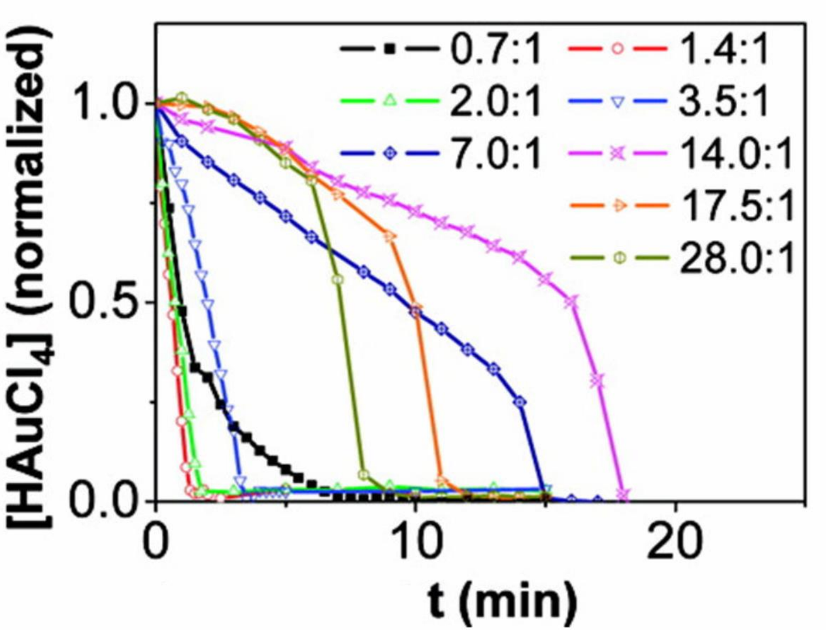

Figure 1.33. Quantification of $HAuCl_4$ concentration for different R values. Aliquots were taken from the reactions and immediately quenched in a mixture of 0.9 M NaCl and HCl (pH 1). Absorbance at 314 nm (due to ligand–metal transition of $AuCl_4^-$ complex at pH < 1.5) was measured and converted to concentration of $HAuCl_4$. Adapted from [177].

(7) Rodríguez-González et al. carried out Turkevich synthesis at R = 6.72 under boiling condition, and also observed the purple/blue color as the intermediate stage [178]. Correspondingly, the UV–vis absorption spectra displayed a blue shift of the peak

during the course of reaction (Figure 1.34). The purple/blue-to-red color transition was reported to occur at 10 min after reaction. The TEM images confirmed the appearance of fluffy large particles (~100 nm) which seemed to be composed of 5–10 nm smaller AuNPs at 1 min after reaction (Figure 1.35A; mechanism (i)). As reaction progressed, the size of aggregates decreased with the size of subunits increasing. Only individual separated AuNPs (~15 nm) could be observed after 10 min (Figure 1.35B).

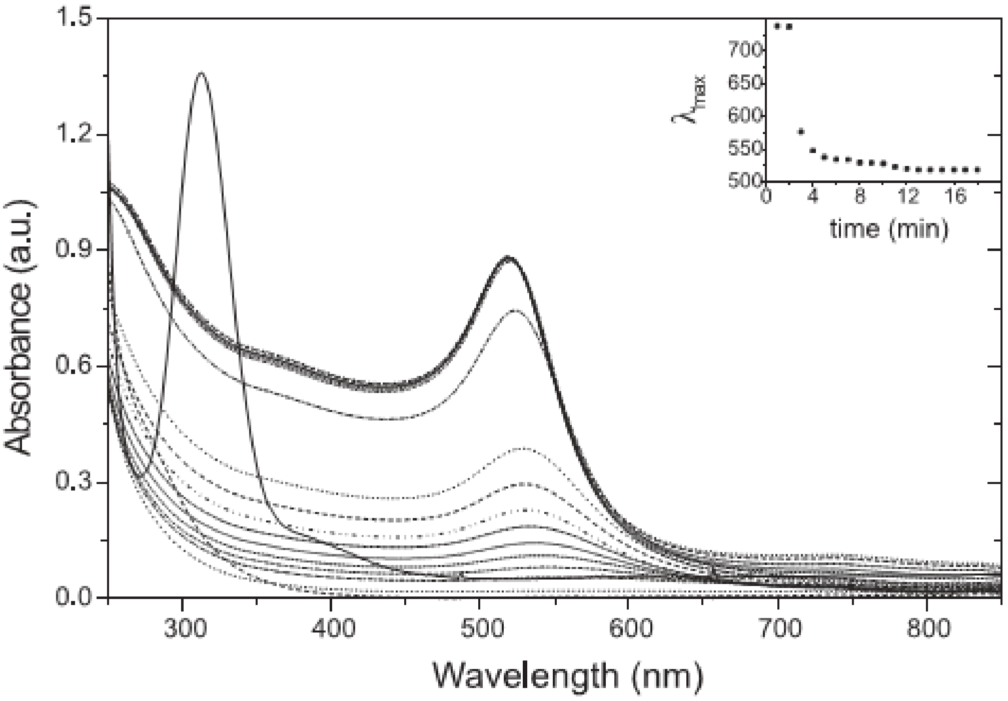

Figure 1.34. UV–vis absorption evolution of the reaction mixture with R = 6.72 under boiling condition, with 1 min interval between measurements. The inset shows the peak wavelength position of the spectra. Adapted from [178].

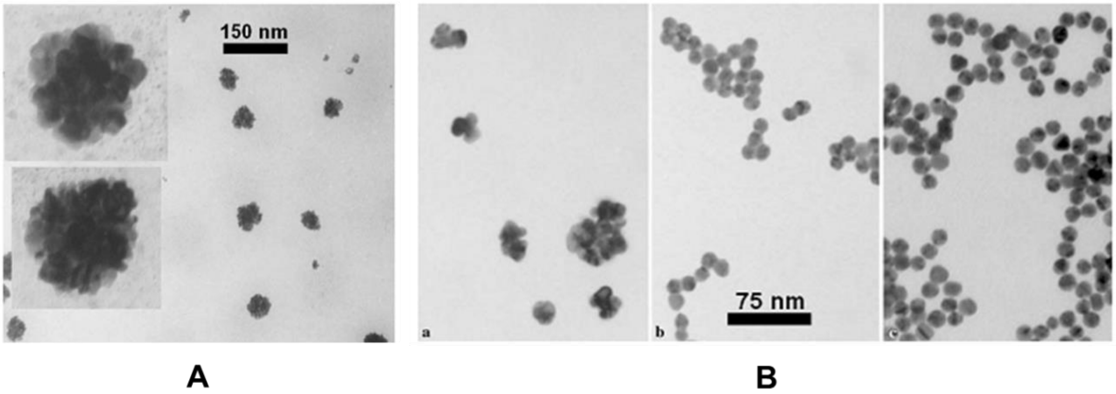

Figure 1.35. TEM images of the reaction mixture at (A) 1 min, (B) 5 min, 10 min, and 12 min after reaction. Adapted from [178].

The concentration of $AuCl_4^-$ was quantified and a precipitating drop was observed right before the purple/blue-to-red color change suddenly happened, which also manifested as a sudden increase of absorbance at 519 nm (Figure 1.36). A gold electrode was introduced into the boiling reaction to measure the open-circuit potential, offering semi-quantitative information of the redox potential and electrode potential of the AuNPs. As can be seen from Figure 1.37, a quick drop from +0.7 V to +0.1 V coincided with the color change. Actually such decrease in electrode potential should have rendered the AuNPs more prone to aggregation instead of the disintegration of aggregates. The authors attributed this observed unexpected color change to the specific adsorption of citrate. After the consumption of $AuCl_4^-$, the particle redox potential had the +0.6 V negative shift, which caused the preferred adsorption of citrate over the existing chloride ions. Although the gold surface became electrically neutral, the adsorbed citrate ions rendered a negative zeta potential. The net particle charge, which consists of electronic and ionic part, turned more negative and thus caused the disintegration to happen [178].

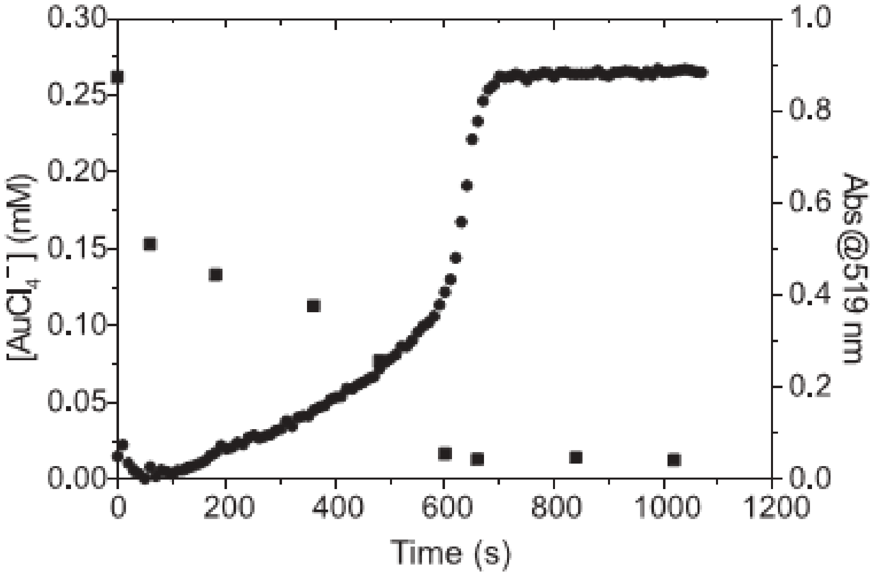

Figure 1.36. Concentration of AuCl$_4^-$ measured throughout reaction duration. Apart from the sudden drop at the beginning of reaction due to fast nucleation, another drop occurred right before the color change. The other set of data was the change of absorbance at plasmon peak (519 nm) of final AuNPs. Adapted from [178].

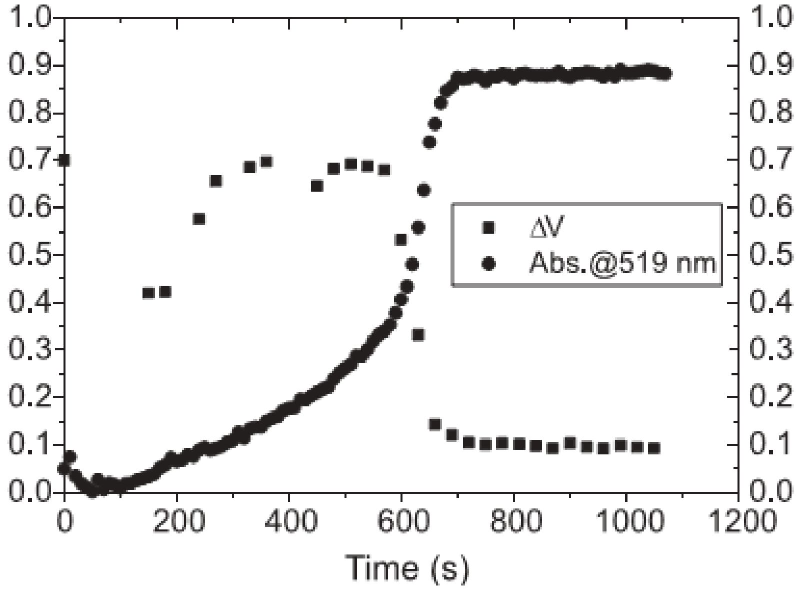

Figure 1.37. The measured open-circuit potential by a gold electrode (vs. Ag/AgCl) introduced to the boiling reaction. Adapted from [178].

(8) Polte et al. made use of SAXS and X-ray absorption near edge spectroscopy (XANES) to thoroughly inspect the Turkevich synthesis with R = 10 at 75 ℃ [179]. Figure 1.38 shows a part of their comprehensive data. As indicated by the arrow in Figure 1.38A inset, blue shift in their synthesis was observed although not that distinctive. Calculated from a time series of SAXS curves, the particle size was found exhibiting a monotonic increase trend throughout the whole reaction (Figure 1.38B). Similar results were obtained for R = 10 at 85 ℃ and R = 6.67 at 75 ℃. A detailed mechanism on Turkevich method was proposed by this group, and then refined by them later in another publication, as shown in Figure 1.39 [180]. Basically, the reduced gold atoms would form clusters, which would coalesce to primary particles due to their poor colloidal stability (phase 1 in Figure 1.38). The primary particles would then serve as seeds for further particle growth (phase 2 and 3 in Figure 1.38). No aggregate structures

were involved in their proposed mechanism, and they postulated that the slight purple color was due to the attachment of gold ions to the electric double layer of the seeds during particle growth stage (mechanism (v)) [180].

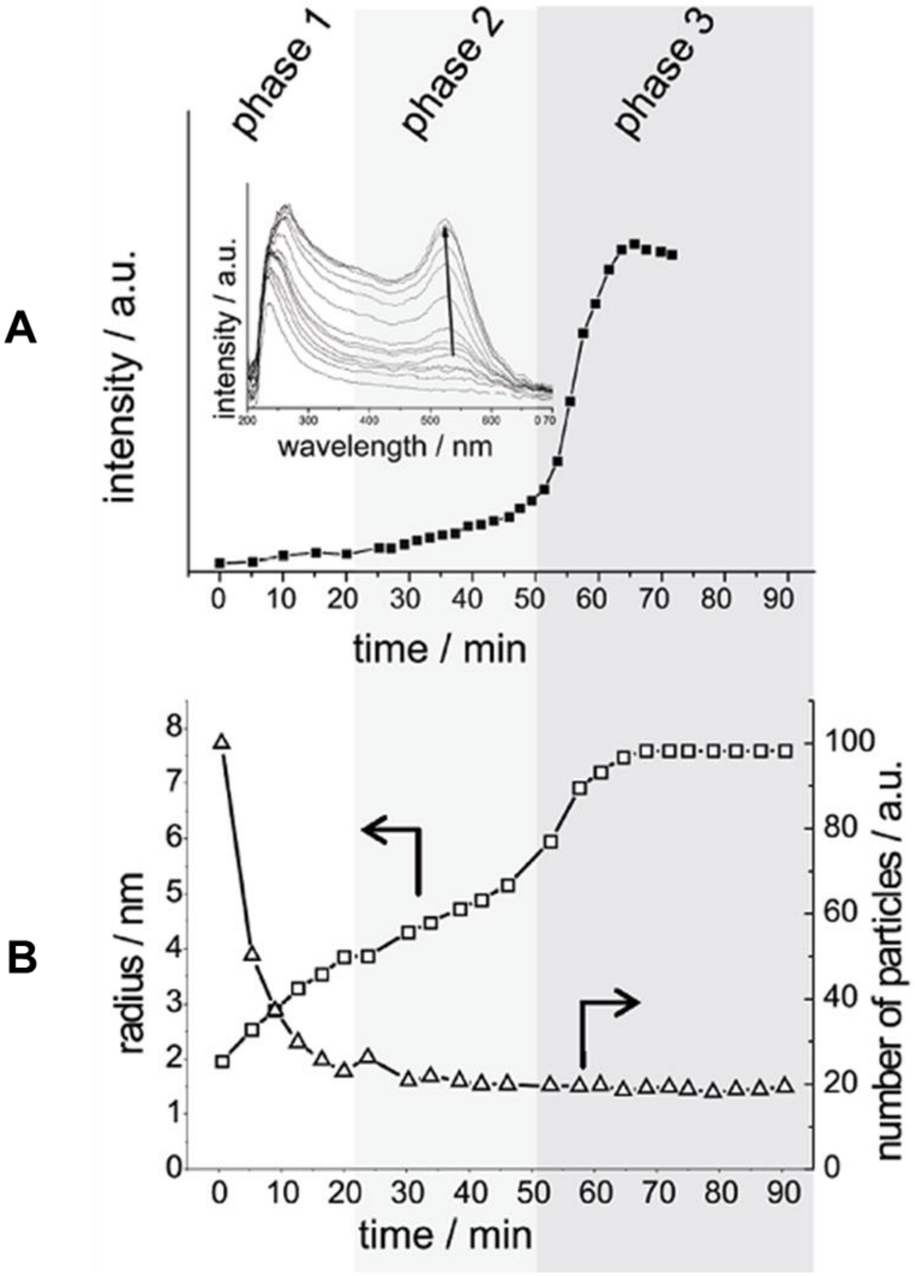

Figure 1.38. (A) Evolution of UV–vis spectra (inset) and absorbance at the peak wavelength during synthesis. (B) Particle mean radius and normalized number calculated from SAXS. Adapted from [179].

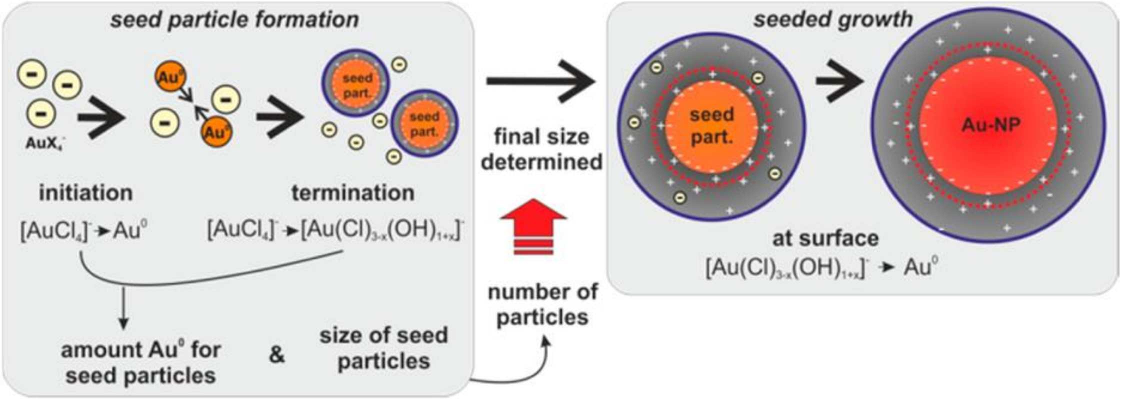

Figure 1.39. Schematic diagram showing the proposed mechanism for Turkevich synthesis of AuNPs by Polte et al., which can be considered as seed-mediated growth where the seeds are formed by coalescence of initially formed clusters due to their poor colloidal stability. Adapted from [180].

(9) Mikhlin et al. performed a modified version of Turkevich synthesis with R = 3 and R = 10 at room temperature [181]. They mixed $HAuCl_4$ and sodium citrate, with sodium hydroxide (NaOH), at 70 ℃ before cooling the reaction down for close monitoring at room temperature. The color progression still occurred at this lowered temperature (Figure 1.40), but the reaction time frame was much longer than at elevated temperature.

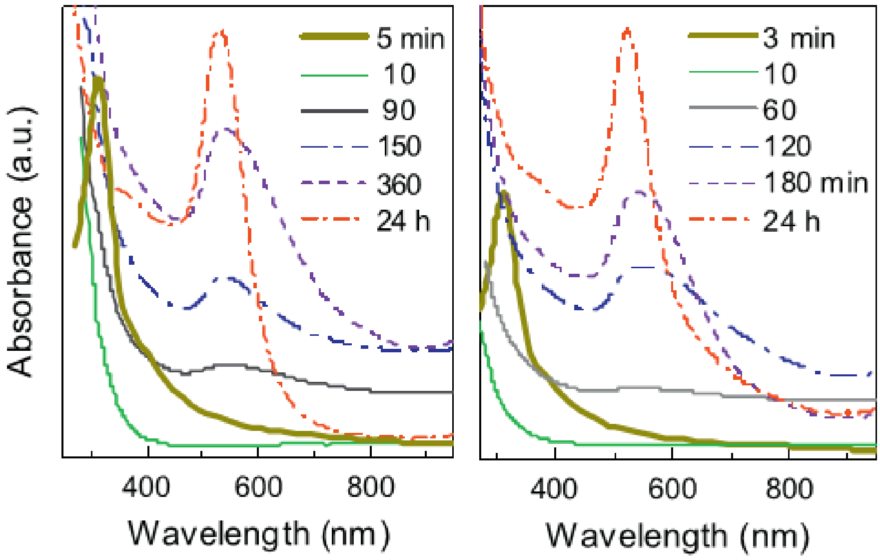

Figure 1.40. UV–vis absorption spectra of R = 3 (left panel) and R = 10 (right panel). The six curves represent pale yellow, colorless, gray, blue, purple, and red color phases during reaction for both R values. Adapted from [181].

Atomic force microscopy (AFM) was employed to probe the reaction *in situ*. For R = 3, the colorless state was populated with liquid domains, shown as the 200–300 nm long, 100 nm wide, and < 20 nm high droplets in Figure 1.41a. In the blue stage, aggregates of globules of 30–50 nm were visualized (Figure 1.41b). Their height increased with reaction time. Both the domains in colorless and globules in blue phases were found to be more of a liquid or soft matter, because they were easily stretchable by the AFM cantilever. Once the blue sample was dried, the *ex situ* AFM images showed ~100 nm solid structures in Figure 1.41c. The final red product contained only individual particles of size ~30 nm (Figure 1.41d). For R = 10, no submicrometer droplets were observed due to a faster reaction, but globules of 20–50 nm were identified in its gray and blue states, as shown in Figure 1.41e and 1.41f. The hydrodynamic diameter measured for R = 3 increased from ~70 nm to ~130 nm at 4 h (purple/blue stage) and then decreased afterwards till the end of reaction.

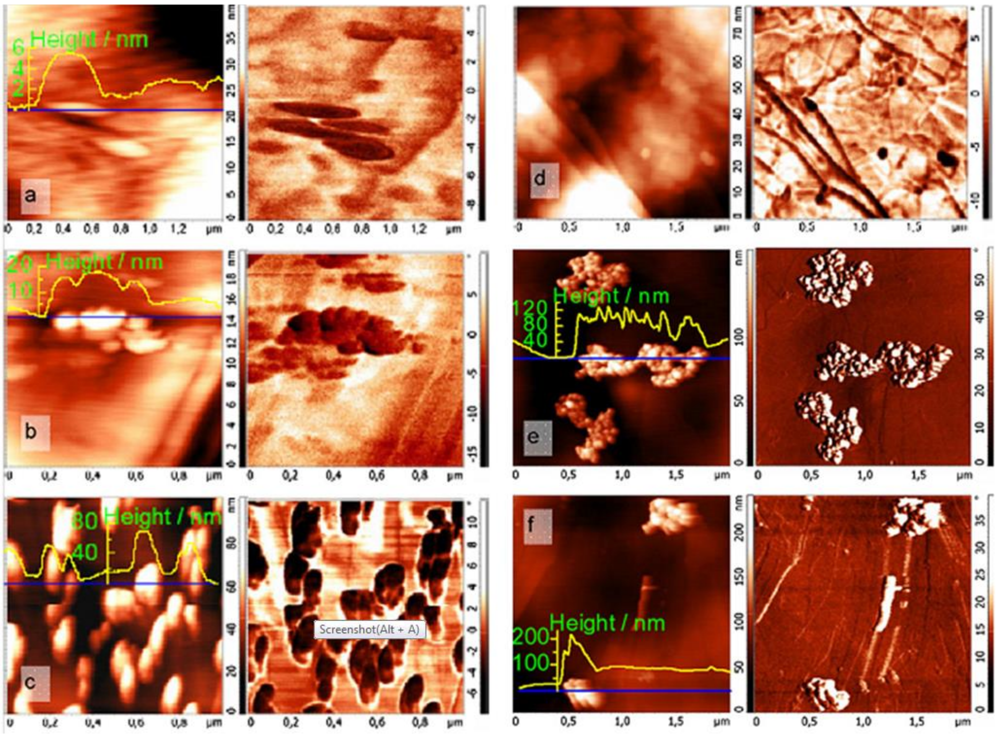

Figure 1.41. Tapping mode AFM images (left panel) and phase images (right panel) of the reactions at (a) colorless, (b) blue, and (d) red state of R = 3. (c) The dried sample at the blue stage of (b). (e) Gray and (f) blue state images of R = 10. Adapted from [181].

The acquired SAXS data in Figure 1.42 for R = 3, contrary to the DLS result, displays an increasing particle size throughout reaction. Although the introduced X-ray did accelerate the reaction and shorten the reaction time scale, the authors concluded that no larger particles/aggregates presented during reaction, consistent with the SAXS findings of Polte et al. [179-180].

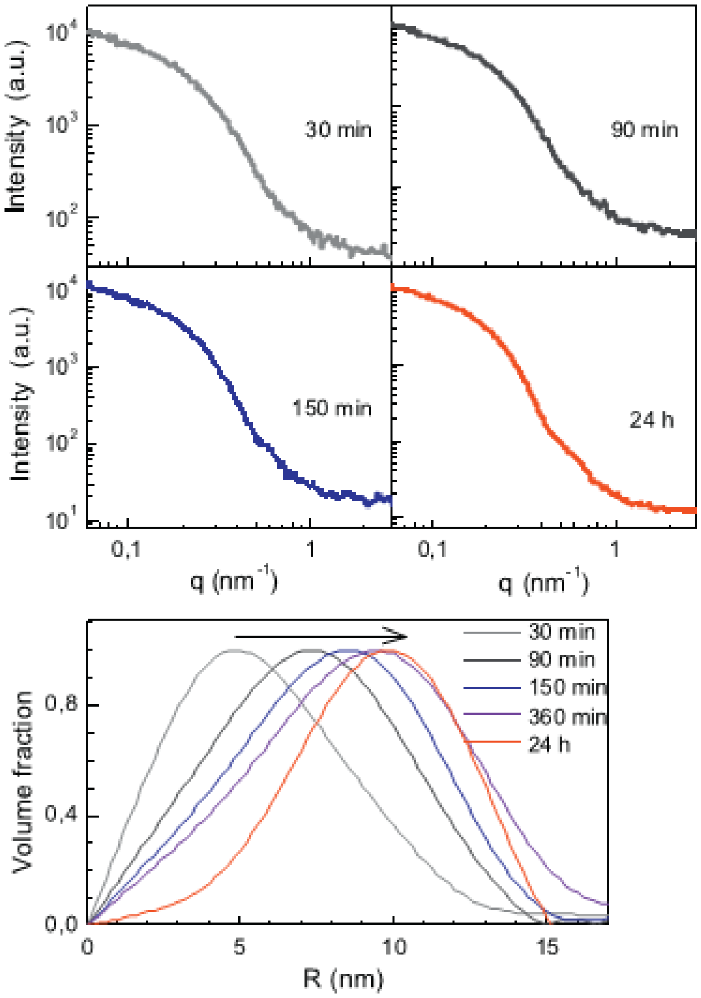

Figure 1.42. SAXS curves for R = 3 at different reaction times. Particle size distribution was extracted from the curves and shown in the bottom panel. Adapted from [181].

They proposed a reaction mechanism as in Figure 1.43. Basically, decomposition of supersaturated solution into some liquid domains precedes the globule formation, within which AuNPs grew to their final size. The color evolution was due to the aggregation of the globules and disintegration of globule aggregates (increase and then decrease in hydrodynamic size; mechanism (iii)) instead of AuNPs forming aggregates (monotonic size progression from SAXS data). The wire-like structures observed in their *ex situ* TEM images were claimed to result from reduction of gold ions in the globules during drying.

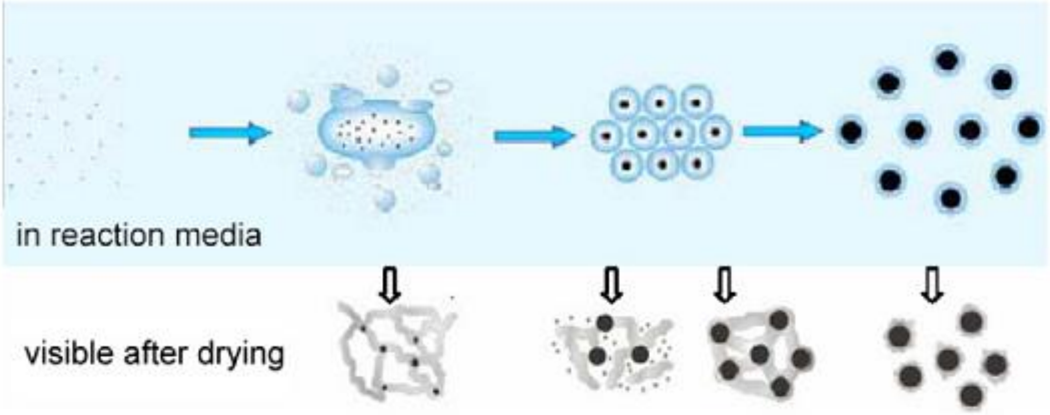

Figure 1.43. Proposed mechanism for AuNP formation. With the reduction of gold precursor, the solution decomposes to liquid domains. Then, globules form and aggregate to submicrometer aggregates. AuNPs form within each globule to their final size. Adapted from [181].

(10) Georgiev also utilized AFM to study the kinetics of Turkevich method with R = 7.75 at 70 and 90 ℃ [182]. Different from the *in situ* measurements of Mikhlin et al. [181], aliquots were taken from synthesis and spin-coated onto a mica support for drying. Although blue color appeared during the course of reaction (as indicated by the blue shift of peak wavelength shown in Figure 1.44), no large structures were observed in this work and particle size evolved monotonically till the final products were formed (Figure 1.45). Their DLS data showed similar trend. No mechanism for the intermediate purple/blue color was proposed in this work.

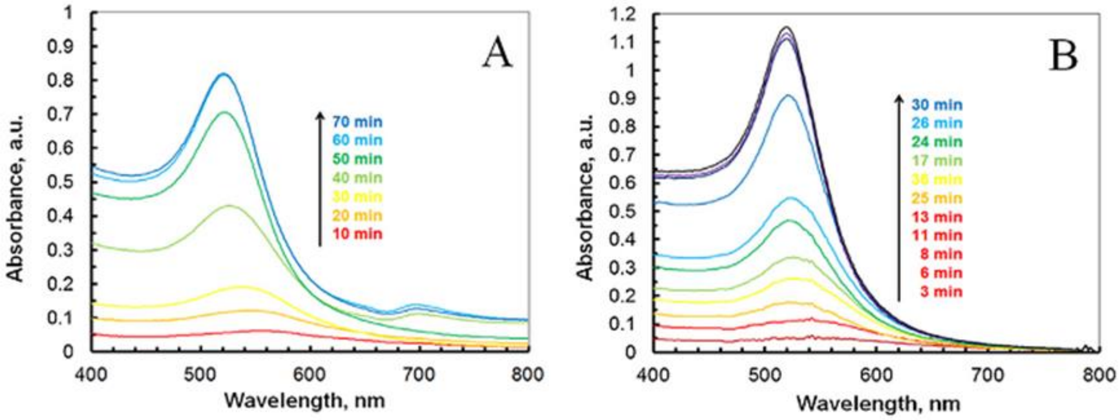

Figure 1.44. UV–vis spectra of reactions with R = 7.75 at (A) 70 ℃, and (B) 80 ℃. Adapted from [182].

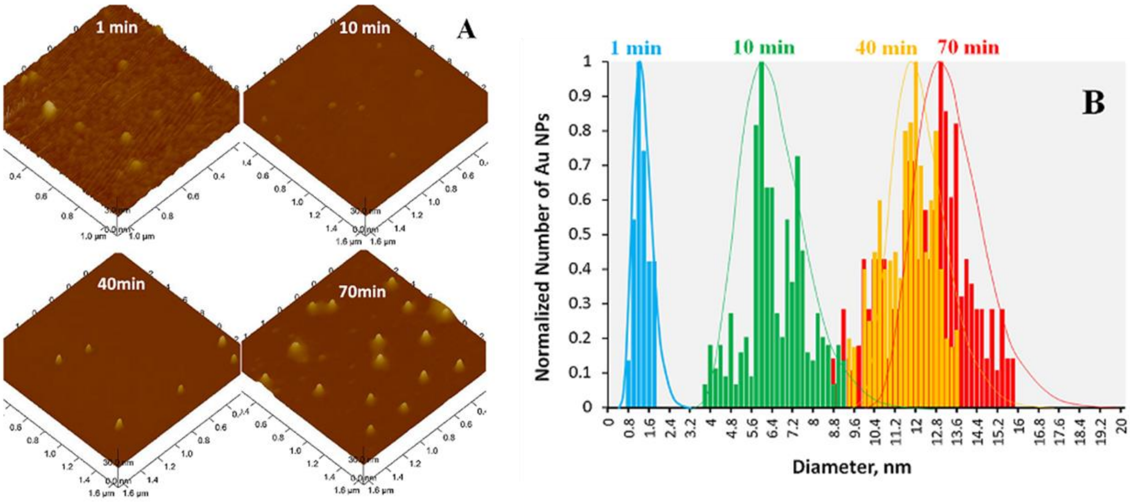

Figure 1.45. (A) 3D-AFM images of reaction with R = 7.75 at 70 ℃ of samples taken at different time after start of reaction. (B) Particle size and normalized number determined from the AFM images. Adapted from [182].

(11) Zhao et al. tried to investigate the effect of chloride ions on Turkevich synthesis with R = 5 under boiling condition [183]. For both without and with 10 mM sodium chloride (NaCl) addition, blue shift was detected (Figure 1.46a and 1.46b). They identified wire-like structures in their TEM results for both conditions and found the

transformation of wire-like structures to spherical AuNPs observed under TEM (Figure 1.47) well corresponded to the absorbance change (mechanism (ii)). They also proposed that chloride ions were able to promote the nanowire formation from particle aggregation due to reduced colloidal stability of the primary particles, causing a larger final AuNP size.

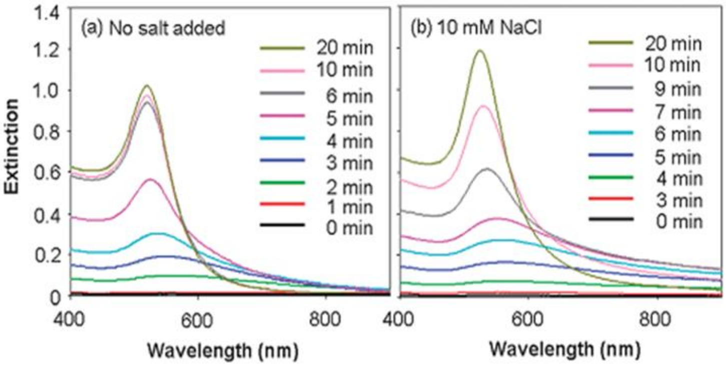

Figure 1.46. Absorption spectra of Turkevich synthesis (a) without and (b) with 10 mM NaCl. Adapted from [183].

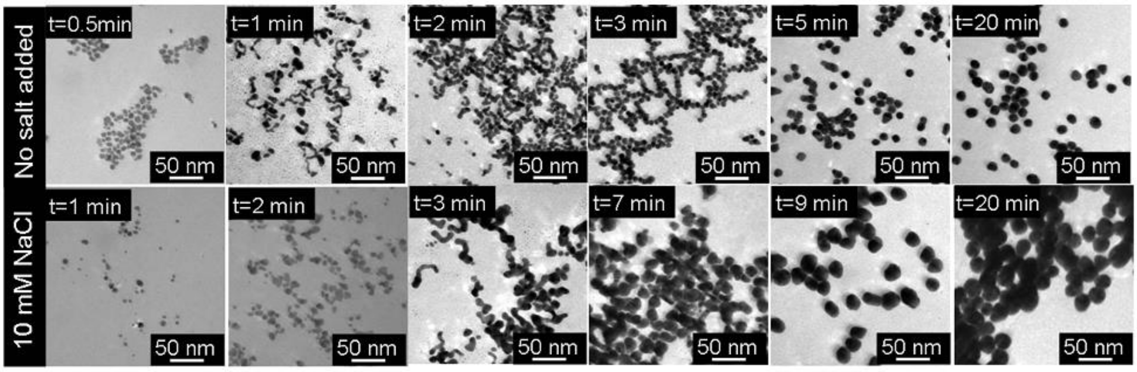

Figure 1.47. TEM images of reaction without (top panel) and with (bottom panel) 10 mM NaCl added to the synthesis. Adapted from [183].

(12) Xia et al. postulated a mechanism for AuNPs formation during Turkevich method, based on which high-quality gold particles in the range of 2–330 nm were synthesized [184].

The chemical reactions depicted in Figure 1.48a are efforts based on a lot of literature [136, 151-153, 185] and have been briefly elaborated in Section 1.3.2.1. Basically, when citrate is in stoichiometric excess (R > 1.5), citrate reduces Au(III) to Au(I) meanwhile being oxidized to sodium acetone dicarboxylate (SAD). Then Au(I) forms complex with SAD, inducing disproportionation of Au(I) to produce gold atoms for AuNP nucleation and growth. The hydrolysis and protonation of $AuCl_4^-$ and citrate ions are critical factors affecting the reaction kinetics.

Figure 1.48b illustrates the proposed particle interactions by the authors [184]. The formed large Au(I)/SAD particles (170 nm then decreased to 75 nm) aggregated to 1600 nm due to protonation of capped citrate, which increased the zeta potential to a less negative value. The citrate protonation was postulated to be caused by release of hydrogen chloride (HCl) from the Au(I)/SAD complex particle due to the disproportionation reaction of Au(I). Nucleation and growth of AuNPs took place exclusively within those little Au(I)/SAD particle reactors. Such aggregation brought the AuNPs closer to each other and rendered the solution a blue color. With the consumption of Au(I) and pH buffering by surrounding environment, capped citrate was deprotonated, giving rise to a more negative zeta potential and disintegrating the aggregates. This disintegration changed the color of solution from blue to purple and then finally to ruby red. The authors claimed that the color change was dependent solely on the interaction among Au(I)/SAD particles not AuNPs forming aggregates directly (mechanism (iii)). Adding another stabilizing chemical tris(hydroxymethyl) aminomethane (Tris) or increasing the concentration of citrate (R > 6.9) were able to stabilize the Au(I)/SAD complex particles and free the reactions from the appearance of blue/purple color.

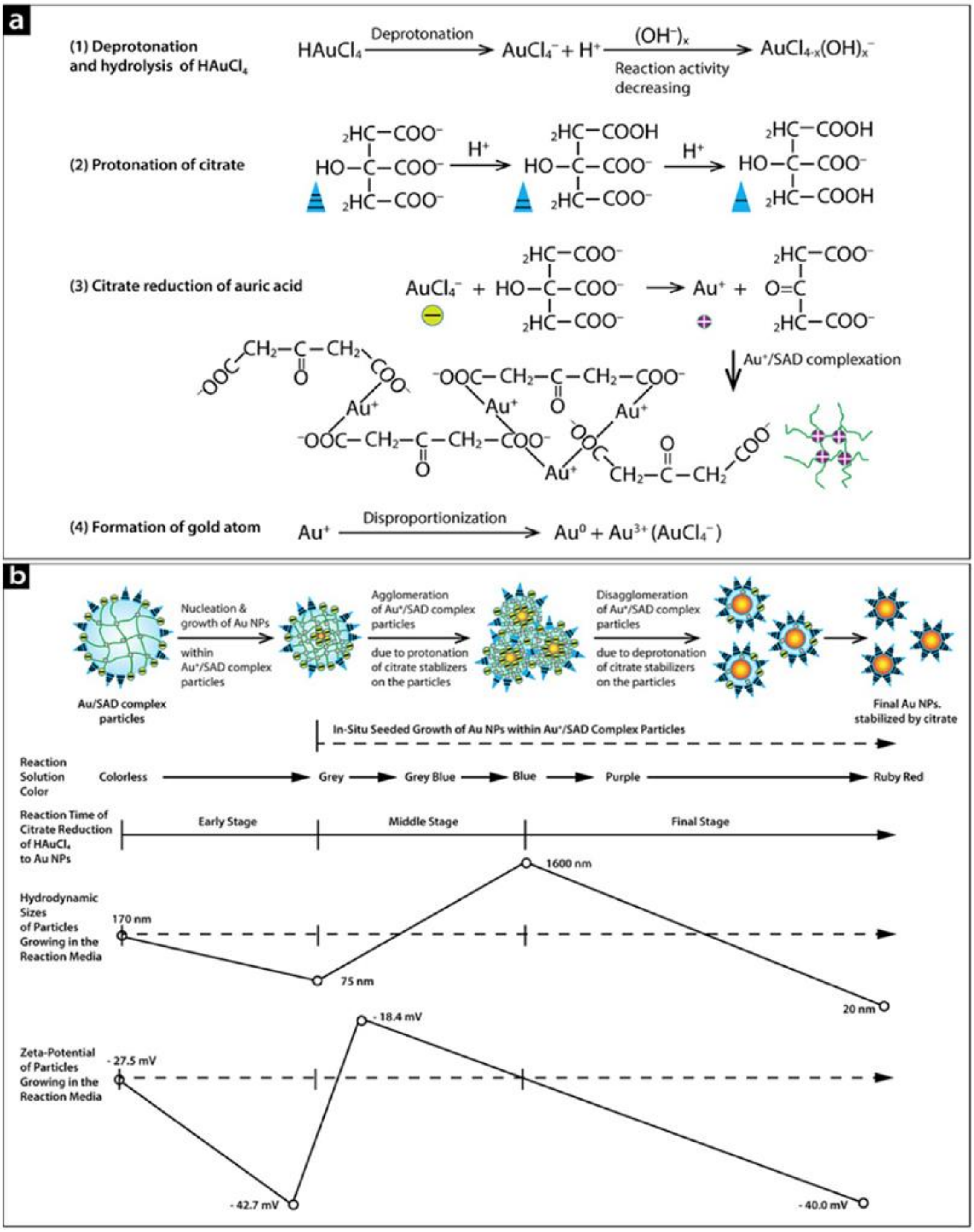

Figure 1.48. Schematic diagrams showing (a) the chemical reactions involved in Turkevich synthesis, and (b) the formation, agglomeration/aggregation, and disagglomeration/disintegration of Au(I)/SAD complex particles, within which nucleation and growth of AuNPs occur. Adapted from [184].

1.3.3.2. Seed-mediated method

The purple/blue-to-red color change, although not as distinctive as reported in Turkevich, was also studied in some seed-mediated growth of AuNPs with citrate as the reducing agent.

(13) Polte et al. performed seed-mediated growth on ~14 nm citrate-coated AuNPs synthesized by Turkevich method at 75 ℃ [186]. The growth solution, containing citrate and $HAuCl_4$, was added to the seeds with R = 10 (same ratio as for seeds preparation). To minimize further nucleation, the growth process was conducted at 65 ℃. As shown in Figure 1.49a, the color of solution changed a little bit from red to purple red upon the addition of growth solution to the seed solution, and then returned back to ruby red. Such slight color change was detectable in the peak shift of the absorbance spectra (Figure 1.49b and 1.49c).

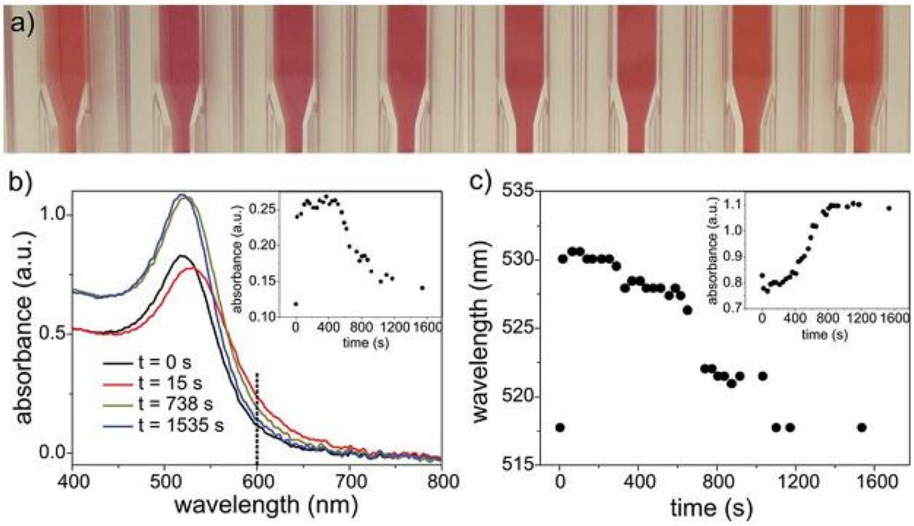

Figure 1.49. (a) Color images of the seed-mediated growth at different time after addition of growth solution to the seed solution. (b) Absorbance spectra progression during reaction. (c) Peak wavelength changed from 518 nm to 530 nm, and then back to 518 nm. Adapted from [186].

SAXS data on this seed-mediated growth with citrate as reducing agent proved that the red shift was not due to aggregates formation. The authors hypothesized that the pH change accompanying the addition of $HAuCl_4$ was the reason for such color transition (Figure 1.50). With the buffering of citrate, such red shift was reversed later. This hypothesis was revised by the authors in their later publications to the attachment of gold ions to the electric double layer of the AuNPs (mechanism (v)) [179-180].

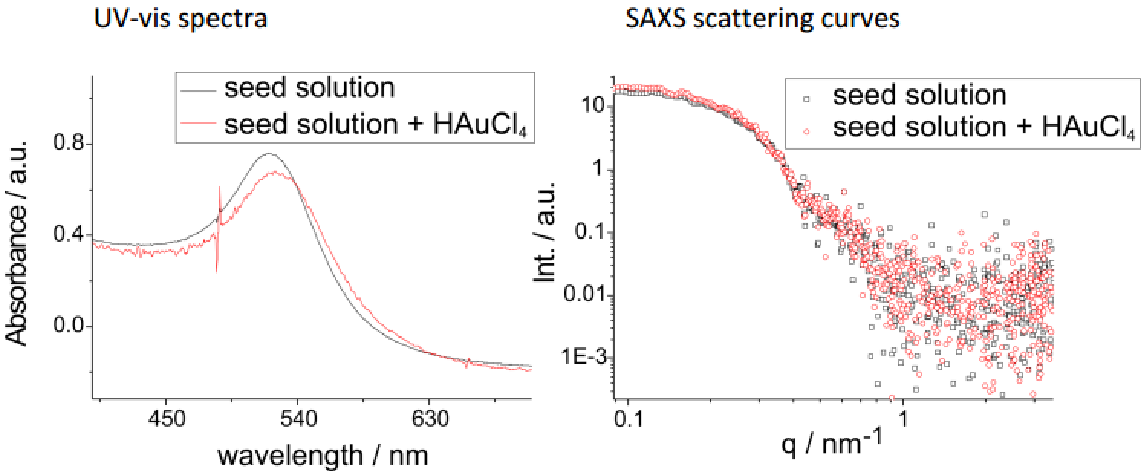

Figure 1.50. Absorbance and SAXS scattering curves change after addition of $HAuCl_4$ to seed solution. Adding $HAuCl_4$ shifted the absorption peak, but didn't induce any aggregates formation as indicated by the similar SAXS curves at low q values. Adapted from [186].

(14) Bastús et al. did a comprehensive study of seed-mediated growth of AuNPs with citrate as the reducing agent in a step-by-step manner at 90 ℃ to minimize nucleation [166]. The seed particles (~10 nm) were synthesized using inverse Turkevich method (adding $HAuCl_4$ to citrate) with R = 13.2 under boiling. The R value for growth was 2.4. The observed red shift (Figure 1.51B), right after adding growth components to the seed solution, was correlated with the observed aggregates found under TEM shown

in Figure 1.51A, disappearance of which coincided with a slight blue shift of the absorbance peak. No elaboration on this was made by the authors.

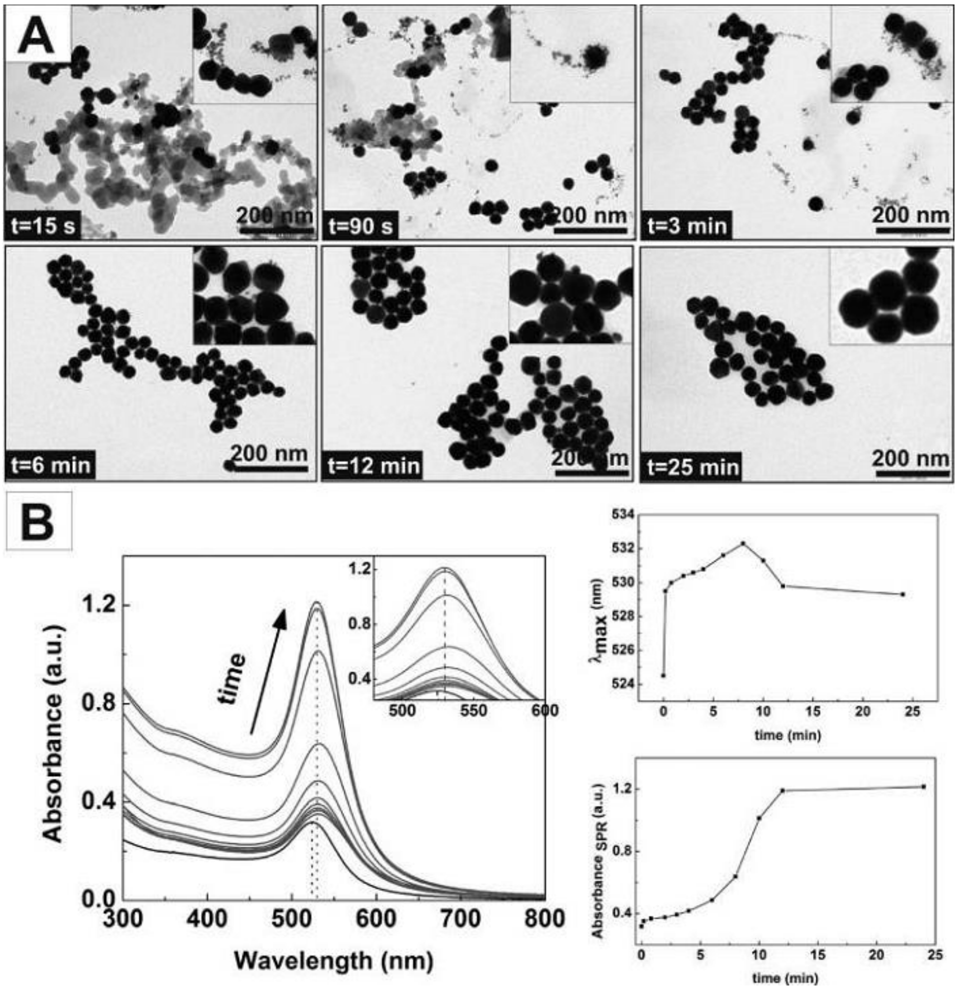

Figure 1.51. (A) TEM images of one step of the seed-mediated growth with seed size of 29.8 nm. (B) UV–vis absorbance spectrum, absorption peak wavelength, and peak absorbance during this step of growth. Adapted from [166].

(15) Wu et al. conducted seed-mediated growth on 25 nm citrate-coated AuNPs synthesized by Turkevich method with R = 7.76 under boiling condition [187]. The growth process was initialized by simply introducing $HAuCl_4$ to the seed solution without further adding citrate (R = 6.07; pH 5.5). The reaction temperature was set at

30 ℃ to suppress intraparticle ripening. UV–vis absorbance spectra and corresponding TEM images and Au(III) concentration are shown in Figure 1.52 and Figure 1.53, respectively. Although no color was reported in this study, the UV–vis data clearly indicates a red-to-purple/blue-to-red color change, evident from the peak shifts and absorbance changes in the 700–900 nm range. Such spectral changes correlated well with the morphology evolution of the gold nanostructures from spheres, to wires with non-uniform diameter, and finally to rods which can explain the two absorbance peaks after 150 min in Figure 1.52 (mechanism (ii)). HRTEM image of one nanowire shows continuous lattice fringes at the junction (Figure 1.54), and the authors attributed the formation of nanowires to the preferential growth of gold along certain facet of the seeds. Again, intraparticle ripening was considered as the mechanism for purple/blue-to-red change because all the Au(III) ions were depleted at 120 min (Figure 1.53j).

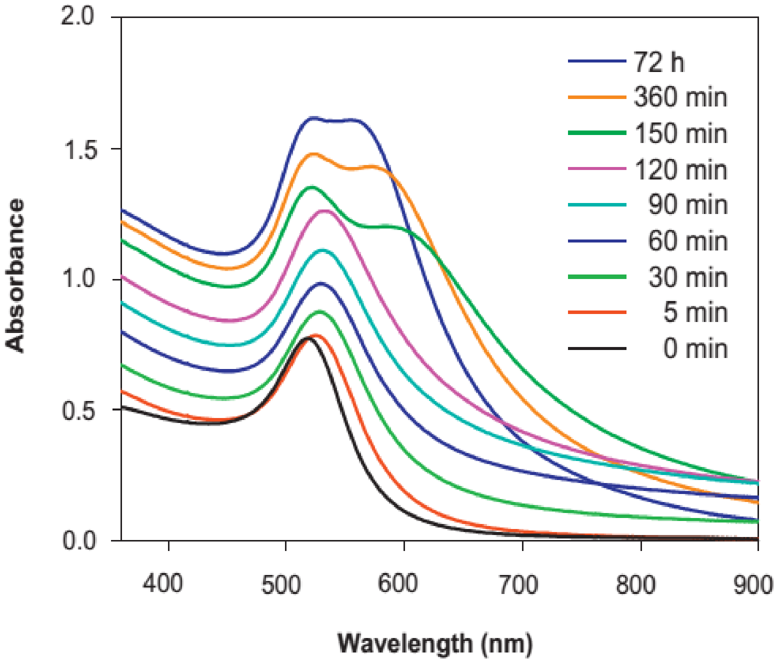

Figure 1.52. UV–vis absorbance spectra of the growth reaction conducted at 30 ℃. Peak shifts and absorbance changes in 700–900 nm range are detected. A second peak shows up at 30 min after reaction. Adapted from [187].

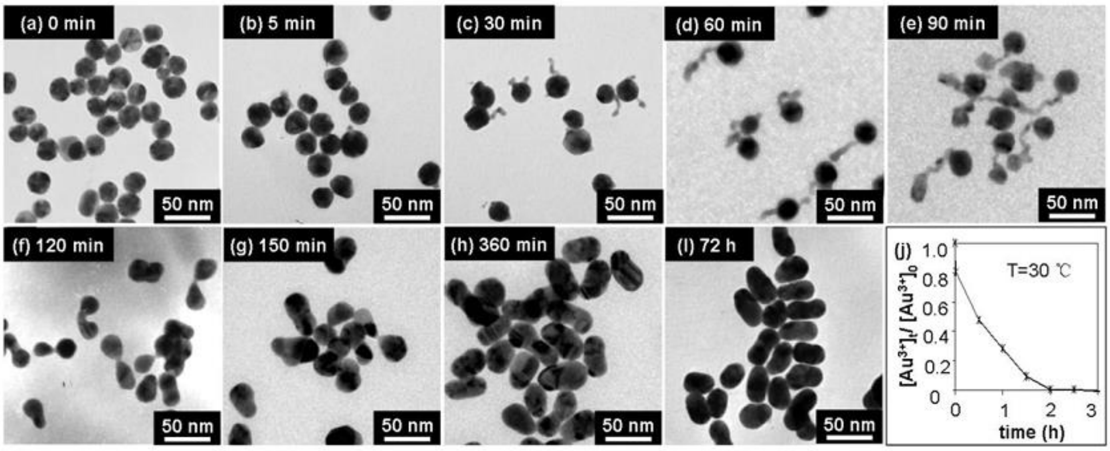

Figure 1.53. Corresponding TEM images (a–i) showing morphological change of the gold nanostructures at different time points after start of the growth reaction. (j) The concentration of Au(III) throughout reaction. Adapted from [187].

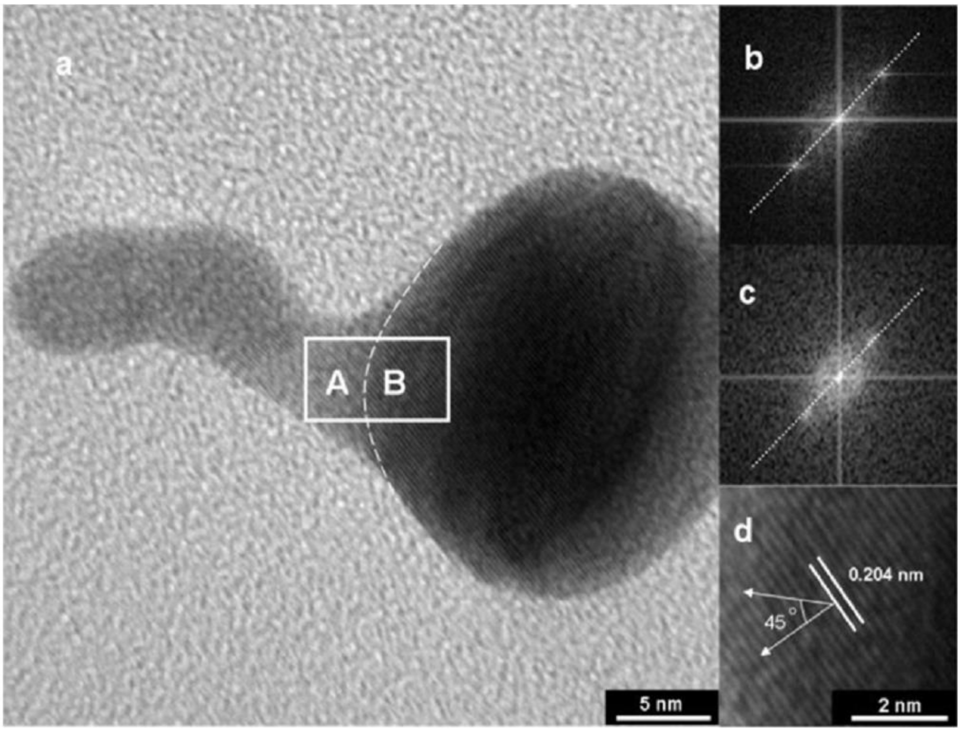

Figure 1.54. (a) HRTEM of one nanowire, and fast Fourier transformation of (b) region A and (c) region B at the junction. (d) Enlarged image of the junction showing continuous lattice fringes throughout the growth point. Adapted from [187].

(16) Leng et al. also performed seed-mediated growth on ~14 nm citrate-coated AuNPs prepared by Turkevich method (R = 3.88; boiling; with NaOH) [188]. Their seed-mediated growth was carried out under room temperature, and the growth solution consisted of citrate and $HAuCl_4$ with R = 0.67.

The authors attributed the light blue tint appeared at 30 min after reaction to the formation of nanowires and the purple-to-red color change to the cleavage of AuNPs off the wires from 2 h to 3 h (Figure 1.55; mechanism (ii)). The fluffy large particles (> 100 nm) observed under TEM (after washing the grids for three times) were not spotted using DLS shown in Figure 1.56A. Instead, the hydrodynamic diameter of the major peak continuously increased to ~57 nm at 3 h. Thus such fluffy large particles were attributed to the drying effects increasing the association between Au(III) and AuNPs by citrate both on the seed surface and in the growth medium (Figure 1.56B). The second peak below 10 nm in the DLS curves (after 1 h of reaction) was rationalized by the rotational diffusion of non-spherical particles.

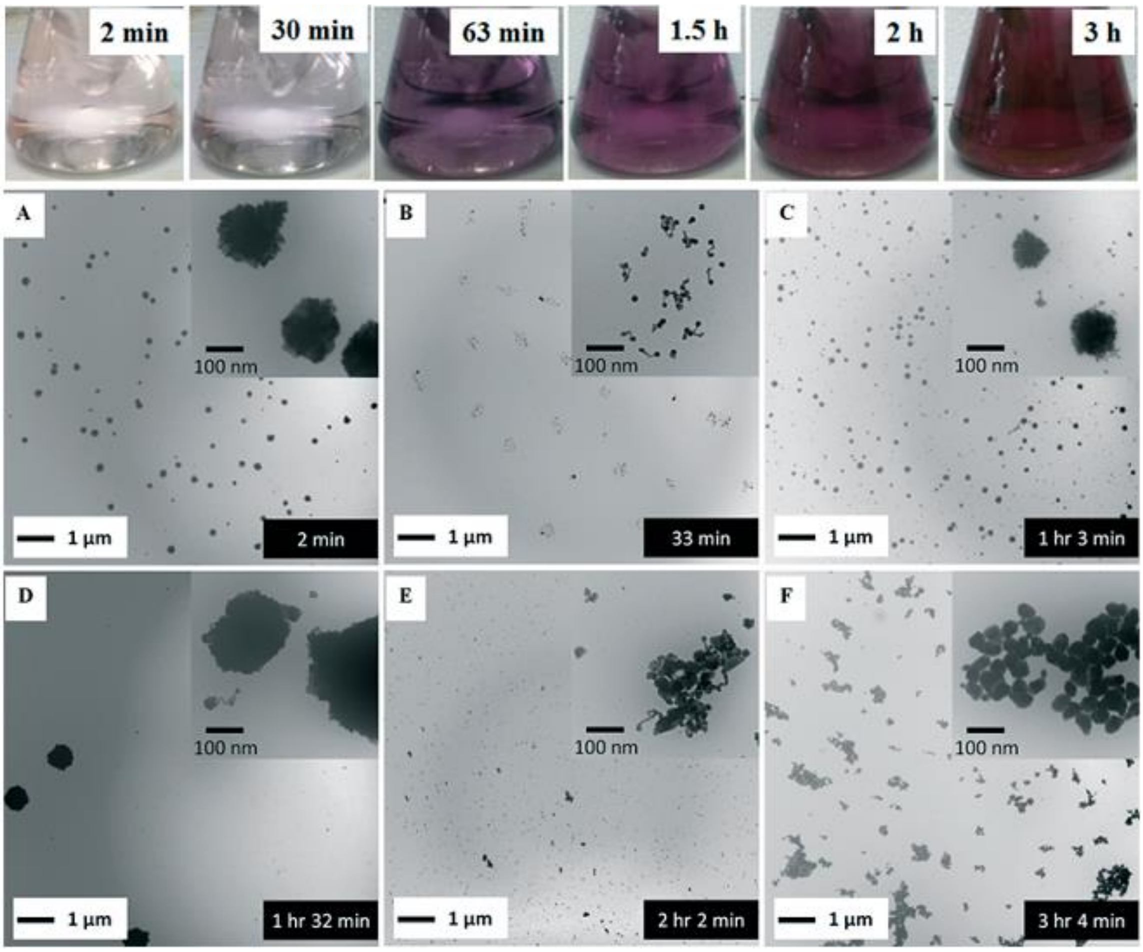

Figure 1.55. Color images and corresponding TEM images (A–F; after washing the grids for three times) of the seed-mediated growth of AuNPs under room temperature. Adapted from [188].

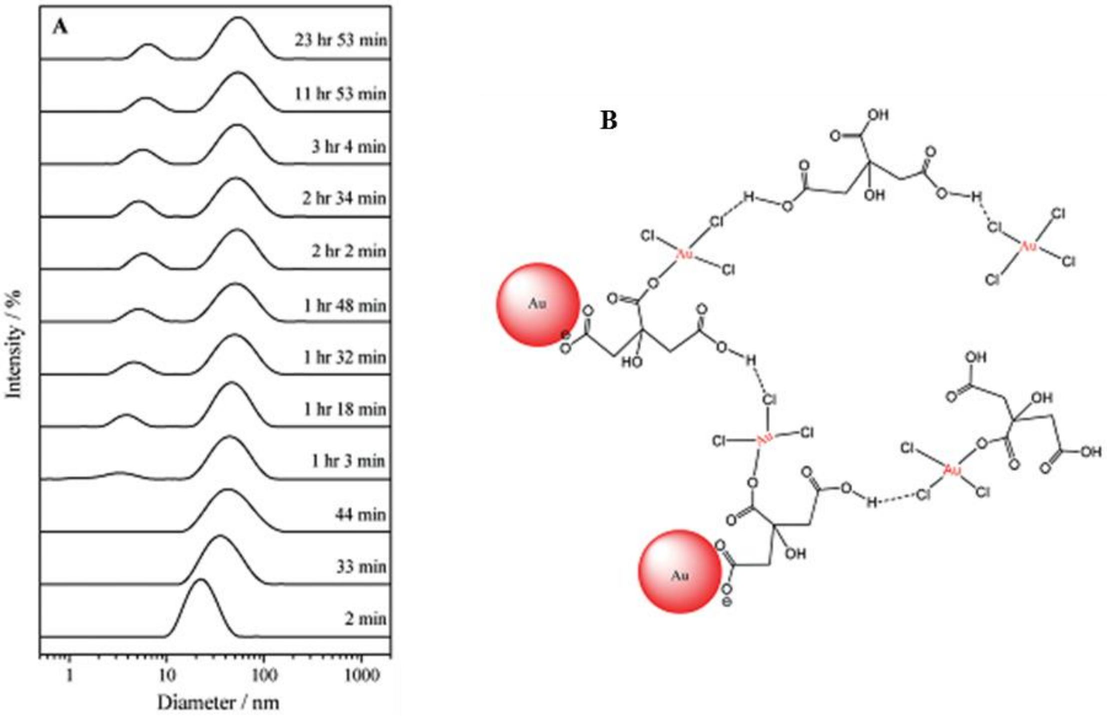

Figure 1.56. (A) DLS data of the seed-mediated growth of AuNPs under room temperature. The major peak continuously increased till ~57 nm at 3 h. A second peak below 10 nm started showing up after 1 h of reaction, which likely resulted from the rotational diffusion of non-spherical particles. (B) Schematic diagram showing the association between Au(III) and AuNPs by citrate both on the seed surface and in the growth medium. Adapted from [188].

1.3.3.3. Summary of the literature on the color change

The important findings for the papers introduced above are summarized and presented in the table below.

Table 1.1. Summary of the related papers introduced in Section 1.3.3.

	Synthesis methods	**Observed color change**	**Reaction condition**	**Important findings**	**Ref.**
1	Turkevich	black, blue, purple, deep red	$[HAuCl_4]$ = 0.24 mM; $[Na_3Ct]$ = 1.6 mM; R = 6.67; temp = 60/70/80 ℃	**(a)** UV–vis, TEM, and DLS all suggested shrinking particle size during reaction; **(b)** TEM identified fluffy large particles, which disappeared when final particles were formed; **(c)** $AuCl_4^-$ adsorption onto the primary particles were proposed to cause the formation of the fluffy large particles, which disintegrated when $AuCl_4^-$ ions were consumed; **(d)** The isolated structures giving rise to the blue/purple color contained little Au(III), and ~30% consumption of Au(III) ions were correlated with the abrupt purple-to-red color change; **(e)** The adsorbed ions sterically prevented irreversible aggregation of the fluffy large particles; **(f)** Mechanism (i).	[170]
2	Turkevich	Not applicable	$[HAuCl_4]$ = 0.1 mM; $[Na_3Ct]$ = 0.33 mM; R = 3.3; pH = 6.3; temp = room temperature	**(a)** When only sodium citrate existed in the solution, the force between two gold surfaces was repulsive; **(b)** When $HAuCl_4$ coexisted with sodium citrate, the force became attractive; **(c)** Despite the preferential adsorption of $AuCl_4^-$, citrate ions were forming a neutral deformable multilayer (possibly with counterions) on the gold surfaces; **(d)** $AuCl_4^-$ species probably adsorbed in their neutral form; **(e)** With consumption of $HAuCl_4$,	[173]

				the repulsive force restored; **(f)** No mechanism proposed.	
3	Turkevich	yellow, colorless, light blue, dark blue, red	[$NaAuCl_4$] = 0.25 mM; R = 0.4–2.7; temp = 80 ℃	**(a)** Blue color was due to the formation of solid polycrystalline nanowires; **(b)** From the quantification study, $AuCl_4^-$ played an important role in the formation and stabilization of nanowires; **(c)** With the consumption of $AuCl_4^-$ for larger R, such wire structures could no longer maintain and individual particles would form, causing blue-to-red color change; **(d)** The nanowires broke apart after treating the dried sample on TEM grid in H_2 for 1 h under room temperature; **(e)** Mechanism (ii).	[174]
		yellow, colorless, light blue, dark blue	[$NaAuCl_4$] = 0.25 mM; R = 0.1–0.3; temp = 80 ℃		
4	Turkevich	gray-blue tint, red within 2–3 s	[$HAuCl_4$] = 0–1.2 mM; R = 0.67–5; temp = 100 ℃	**(a)** SAXS results didn’t show any aggregates; **(b)** The blue color likely came from the plasmon excitation delocalization among the closely spaced clusters/particles (< 5 nm); **(c)** The kinetic intermediate only temporarily existed before the clusters/particles agglomerate and compact into AuNPs, causing the blue-to-red color change; **(d)** Mechanism (iv).	[149]
5	Turkevich	pale yellow, colorless, dark blue, purple, red	[$HAuCl_4$] = 0.91 mM; R = 2, 3.88, 5; temp = 50/100 ℃	**(a)** Colorless stage was populated with 3–5 nm small AuNPs and some wire-like structures; **(b)** Dark blue stage got extensive nanowire networks with diameter of ~5 nm; **(c)** The solid polycrystalline nanowires broke down to smaller network with diameter of ~8 nm in the purple stage; **(d)** Individual AuNPs (13–15 nm) cleaved off the wires in the red stage; **(e)** The adsorption of $AuCl_4^-$ onto formed ~5 nm AuNPs was	[176]

				hypothesized to induce attractive forces; **(f)** Steric effects were speculated to cause the formation of wires instead of other aggregates; **(g)** Further reduced gold atoms deposited to concave regions of wires amorphously and then crystalline regions; **(h)** The amorphous region was depleted probably due to Ostwald ripening; **(i)** With the consumption of $AuCl_4^-$ ions, citrate adsorption increased electrostatic repulsion, cleaving the particles off wires; **(j)** Mechanism (ii).	
6	Turkevich	colorless, blue, purple, red	$[HAuCl_4]$ = 0.25 mM; R = 0.7–3.5; temp = 100 ℃	**(a)** The third role of citrate was studied in this work; **(b)** The blue/purple color only appeared when R was smaller than 3.5 (corresponding to pH of 6.5) because of the formed solid polycrystalline nanowires, which were not uniform in diameter; **(c)** With pH adjustment, the authors were able to manipulate the reaction pathways, confirming the role of citrate as pH mediator; **(d)** In the pH range of 3.7–6.5, AuNP form via fast nucleation, fast random attachment, and slow intraparticle ripening; **(e)** The evolution from the wires to individual AuNPs, thus the blue/purple-to-red color change, was due to intraparticle ripening instead of wire cleavage; **(f)** In the pH range of 6.5–7.7, AuNP form via a slow nucleation and growth pathway; **(g)** Mechanism (ii).	[177]
		colorless, pink, red	$[HAuCl_4]$ = 0.25 mM; R = 3.5–28; temp = 100 ℃		
7	Turkevich	pale yellow, colorless, light blue, dark blue,	$[HAuCl_4]$ = 0.253 mM; $[Na_3Ct]$ = 1.7 mM; R = 6.72;	**(a)** Fluffy large particles (~100 nm) composed of 5–10 nm AuNPs were observed under TEM; **(b)** The size of aggregates decreased with increasing size of	[178]

		purple, red	temp = 100 ℃	the subunits increasing; **(c)** Only individual separated ~15 nm AuNPs existed when red color appeared; **(d)** The purple-to-red color change occurred at 10 min after reaction, before which a precipitating drop of [$AuCl_4^-$] was observed; **(e)** Such color change coincided with the decrease in electrode potential of the AuNPs, which caused the preferred adsorption of citrate over chloride ions; **(f)** Even though the gold surface became electrically neutral, the adsorbed citrate ions rendered a negative zeta potential, causing disintegration of the fluffy large particles to form AuNPs; **(g)** Mechanism (i).	
8	Turkevich	slight purple, red	[Na_3Ct] = 2.5 mM; R = 6.67, 10; temp = 75/85 ℃	**(a)** Plasmon band maximum only shifted slightly from 530 nm to 520 nm; **(b)** Particle size determined from SAXS increased monotonically throughout reaction; **(c)** No aggregates formed and the slight purple color was likely due to the attachment of gold ions to the electric double layer of the AuNPs during particle growth; **(d)** Mechanism (v).	[179-180]
9	Turkevich	pale yellow, colorless, gray, blue, violet, red	[$HAuCl_4$] = ~0.25 mM; R = 3, 10; [NaOH] = ~1.3 mM; mixing at 70 ℃; monitoring at room temperature	**(a)** Color progressing still occurred at room temperature, but with a much longer time frame; **(b)** *in situ* AFM found submicrometer liquid domains at colorless state; **(c)** Blue stage got aggregates of 30–50 nm liquid globules observed *in situ*, but ~100 nm solid structures when dried and examined *ex situ*; **(d)** Final red product contained only individual particles of ~30 nm examined both *in situ* and *ex situ*;	[181]

				(e) DLS result for R = 3 showed an increase to ~130 nm at blue stage and then decrease in hydrodynamic diameter till the end of reaction; **(f)** SAXS data for R = 3 indicated continuous increasing AuNP size. No larger particles/aggregates presented during reaction; **(g)** The color evolution was hypothesized to be caused by interaction of liquid globules not AuNPs forming aggregates; **(h)** The wire-like structures in ex situ TEM image were ascribed to the reduction of gold ions in the globules during drying; **(i)** Mechanism (iii).	
10	Turkevich	colorless, blue, cherry red, purple red	$[HAuCl_4]$ = 0.25 mM; $[Na_3Ct]$ = 1.94 mM; R = 7.75; temp = 70/90 ℃	**(a)** *ex situ* AFM found no aggregates throughout the synthesis; **(b)** Particle size evolved monotonically till the end of reaction from both AFM and DLS results; **(c)** No mechanism proposed.	[182]
11	Turkevich	no color reported; absorbance peak shift	$[HAuCl_4]$ = 0.25 mM; $[Na_3Ct]$ = 1.25 mM; R = 5; temp = 100 ℃	**(a)** Blue shift of the UV–vis curves was correlated with the transformation of nanowires to AuNPs; **(b)** Chloride ions were able to promote the nanowire formation from particle aggregation due to reduced colloidal stability of the primary particles, causing a larger final AuNP size; **(c)** Mechanism (ii).	[183]
12	Turkevich	light yellow, colorless, gray, gray blue, blue, purple, ruby red	$[HAuCl_4]$ = 0.294 mM; $[Na_3Ct]$ = 1.2 mM; R = 4.1; temp = 100 ℃	**(a)** The color change was due to aggregation and disintegration of Au(I)/SAD particles, within which nucleation and growth of AuNPs occurred; **(b)** Aggregation of Au(I)/SAD particles was caused by protonation of adsorbed citrate, whereas disintegration of these particles was due to deprotonation	[184]

				of adsorbed citrate; **(c)** Adding extra stabilizing chemical Tris or increasing R above 6.9 were able to get rid of the blue/purple color during reaction; **(d)** Mechanism (iii).	
13	seed-mediated growth	red, purple red, red	seeds : ~14 nm, citrate-coated; growth solution: R = 10; temp = 65 ℃	**(a)** SAXS didn't identify any aggregates formation for this seed-mediated growth of AuNPs; **(b)** The slight color change was ascribed to pH change upon addition of $HAuCl_4$, which was reversed upon the buffering of citrate; **(c)** The authors revised their explanation for the color change to the adsorption of gold ions at electric double layer of the AuNPs in their later publications as in #8 [179-180]; **(d)** Mechanism (v).	[186]
14	seed-mediated growth	no color reported; slight absorbance peak shift, similar to the previous one	seeds : ~10 nm, citrate-coated; growth solution: R = 2.4; temp = 90 ℃	**(a)** Aggregates of undefined morphology found under TEM were correlated with the red shift right after adding growth solution; **(b)** Disappearance of such aggregates coincided with the blue shift of absorbance peak; **(c)** No study or elaboration of the aggregates was made; **(d)** No mechanism proposed.	[166]
15	seed-mediated growth	no color reported; absorbance peak shift, absorbance change in 700–900 nm range	seeds : ~25 nm, citrate-coated; growth solution: R = 6.07; temp = 30 ℃	**(a)** Nanowire formation, due to preferential growth of gold along certain facet, accounted for the red shift and absorbance increase in 700–900 nm range; **(b)** Intraparticle ripening was responsible for the purple/blue-to-red change; **(c)** Mechanism (ii).	[187]
16	seed-mediated growth	pale pink, light blue, purple, red	seeds : ~14 nm, citrate-coated; growth solution:	**(a)** The blue tint was due to the formation of nanowires; **(b)** Purple-to-red color change resulted from the cleavage of AuNPs off the wires;	[188]

			R = 0.67; temp = room temperature	**(c)** Fluffy large particles observed under TEM were not detected using DLS; **(d)** Such structures were caused by drying effects, which increased the association between Au(III) and AuNPs; **(e)** Mechanism (ii).	

1.4. Gap of knowledge

Although the purple/blue-to-red color change was reported in Turkevich method and the red-to-purple/blue-to-red color reversal was reported in seed-mediated growth synthesis of AuNPs, no consensus has been reached on the underlying reason for the observed distinctive color transitions. There have been five main explanations for the purple/blue color appearance from the 16 papers in Section 1.3.3: **(i)** formation of fluffy large aggregates from AuNPs which are spherical in shape (#1 [170], #7 [178]); **(ii)** formation of solid polycrystalline nanowires via aggregation from AuNPs (#3 [174], #5 [176], #6 [177], #11 [183], #16 [188]) or deposition of gold along certain facet of AuNP seeds (#15 [187]); **(iii)** formation of spherical aggregates from "glue" particles (liquid globules #9 [181] or Au(I)/SAD complex #12 [184]) within which AuNPs nucleate and grow, without AuNPs directly interacting with each other; **(iv)** kinetic intermediate from closely spaced gold clusters/particles before compacting into AuNPs without any aggregates formation (#4 [149]); **(v)** attachment of gold ions at electric double layer of the AuNPs (#8 [179-180], #13 [186]) without any aggregates formation.

Since the purple/blue color appeared after the nucleation step, we believe it's the growth step of AuNP synthesis which contributes significantly to the color change phenomena for both Turkevich and seed-mediated growth methods (with citrate as reducing agent). Herein, we would like to understand more of the striking color changes by conducting seed-mediated growth of AuNPs (reduction by citrate) at room temperature. In this setup, the nucleation of AuNPs can be minimized and the growth process predominates. Via close monitoring and manipulation of the solution color change during seed-mediated growth of 5 nm AuNPs, we would like to propose a detailed mechanism for the red-to-purple/blue-to-red color reversal. Such mechanism will be validated with seed-mediated growth of 13 nm citrate-coated gold seeds (the size generally used for synthesizing larger AuNPs in this seed-mediated growth method). Since the reagents to be used in our study are basically the same as in Turkevich method, we believe our findings are able to offer more insights into the color change and AuNP growth mechanism in Turkevich synthesis as well.

1.5. Objectives of this study

- To study the red-to-purple/blue-to-red color reversal phenomenon in seed-mediated growth of citrate-coated AuNPs with seed size of 5 nm at room temperature and propose the underlying mechanism for the color reversal in seed-mediated growth of AuNPs.
- To study the red-to-purple/blue-to-red color reversal phenomenon in seed-mediated growth of citrate-coated AuNPs with seed size of 13 nm at room temperature and validate our proposed mechanism on 13 nm seeds.
- To study the purple/blue-to-red color change phenomenon in Turkevich method at both boiling and room temperature and validate our proposed mechanism on Turkevich method.

Chapter 2. Color reversal in seed-mediated growth of 5 nm AuNPs

2.1. Materials and methods

2.1.1. Materials and equipment

Hydrochloric acid (HCl), nitric acid (HNO_3), chloroauric acid ($HAuCl_4$, 30% wt. in diluted HCl), sodium borohydride ($NaBH_4$), sodium citrate tribasic dihydrate ($Na_3C_6H_5O_7 \cdot 2H_2O$), potassium hydroxide (KOH), sodium chloride (NaCl), 1,3-acetonedicarboxylic acid ($C_5H_6O_5$), sodium hydroxide (NaOH), gold(I) chloride (AuCl), formic acid (HCOOH), acetic acid (CH_3COOH), and acetone (C_3H_6O) were purchased from Sigma-Aldrich (St. Louis, MO, USA). All the chemicals were used as received without any further purification. Amicon® Ultra centrifugal filters (MWCO 10,000) were purchased from Millipore (Burlington, MA, USA). Mill-Q water was used throughout this work.

Centrifugation was performed using Eppendorf 5415 D centrifuge. UV–vis spectra were acquired using Amersham Biosciences UltrospecTM 2100 pro UV/visible spectrophotometer. DLS data were collected by Malvern Panalytical Zetasizer Nano ZS. TEM images were taken by field emission electron microscope (JEM-2100F, JEOL) with 200 kV field emission gun.

2.1.2. Synthesis of 5 nm AuNPs

The synthesis of 5 nm AuNPs was based on the reduction of $HAuCl_4$ with $NaBH_4$. Citrate was added to provide stability to the synthesized AuNPs. The protocol was adapted and modified from work by Grabar et al. [189] and Tam et al. [190].

Basically, after thorough washing of the glassware and magnetic stir bar with freshly prepared aqua regia (concentrated HCl:HNO_3 molar ratio of 3:1), Milli-Q water of 400 mL was heated to boiling. Then 4 mL of 25.4 mM $HAuCl_4$ was added and stirred for 1 min, after which 4 mL of 38.8 mM sodium citrate was introduced. Again after 1 min of stirring, 4 mL of 19.8 mM of $NaBH_4$ dissolved in 38.8 mM sodium citrate was added to the mixture. The solution was continuously stirred for another 5 min before cooled down in ice-cold water to room temperature.

To remove the formed unwanted larger particle impurities, centrifugation was carried out at 5,800 rpm for 45 min, and the supernatant was collected and used directly for the following studies without further treatment.

2.1.3. Characterization of synthesized 5 nm AuNPs

After centrifugation, the obtained supernatant was characterized by UV–vis spectroscopy and DLS. TEM was also performed for direct visualization of the synthesized AuNPs, after drop casting ~100 μL of the dispersion to a carbon-coated copper grid placed on a filter paper.

2.1.4. Preparation of growth solution

Growth solution was prepared by adding 5.7 mM of KOH to 0.87 mM $HAuCl_4$. The mixture would turn from pale yellow to colorless within minutes, indicating hydroxylation of the gold precursor. This growth solution was left overnight in dark at room temperature before use. The solution pH was ~5.5 after equilibration.

2.1.5. Seed-mediated growth of 5 nm AuNPs

The growth solution and the seed solution were mixed with volume ratio of 3:2, giving [$HAuCl_4$] = 0.52 mM, [Na_3Ct] = 0.31 mM, and [KOH] = 3.42 mM in the final mixture (R = 0.6). The growth process was monitored by UV–vis, DLS, and TEM.

2.1.6. Key components for color reversal in seed-mediated growth of 5 nm AuNPs

Concentration of Au(III) in the solution phase was quantified by measuring the absorbance at 314 nm due to ligand–metal charge transfer of $AuCl_4^-$, after taking aliquots from reaction and quenching them into 1 M NaCl (centrifugation at 13,200 rpm for 5 min to precipitate the nanostructures) and then adding the supernatant to 0.1 M HCl (to convert all Au(III) species to $AuCl_4^-$) [177, 185].

Then substitutions of Na_3Ct by its oxidation product SAD (mixing 1,3-acetonedicarboxylic acid with NaOH) and $HAuCl_4$ by its reduction product AuCl were performed to study the effects of these two important intermediate species of the redox reaction between Na_3Ct and $HAuCl_4$. Products of SAD oxidation (formic acid, acetic acid) and degradation (acetone) were added to replace SAD and their effects on the growth process were also inspected.

The effect of the four starting components in this seed-mediated growth (5 nm seeds, Na_3Ct, KOH, and $HAuCl_4$) on the growth process was studied by removing them from the mixture individually. Various other parameters (concentration of seeds, Na_3Ct, KOH, and $HAuCl_4$) were adjusted to examine their effects on the color change and growth process. Temperature effects were also studied by comparing the AuNP growth at room temperature and at elevated temperature (65 °C).

2.1.7. Manipulation of the growth at purple/blue stage

The purple/blue stage was arrested and was manipulated by adding 3.42 mM KOH/HCl. Besides, 500 μL of the mixture was added to a centrifugal filter device. This device was centrifuged at 14,000 rcf for 15 min to separate the structures giving rise to the purple/blue color from the solution medium. The concentrate was collected and redispersed in water for further manipulation, including increasing temperature and adding 3.42 mM HCl.

2.2. Results and discussion

2.2.1. Synthesis of 5 nm AuNPs

The UV–vis absorption spectrum of the synthesized 5 nm AuNPs is shown in Figure 2.1. The peak absorption wavelength of 514 nm corresponds to the LSPR of the synthesized AuNPs. According to the work by Haiss et al. [191], the diameter of the AuNPs is determined to be ~5 nm and the concentration is estimated to be ~59 nM. DLS data of the AuNPs before and after centrifugation are shown in Figure 2.2. Right after the completion of particle synthesis, the corresponding DLS curve has two peaks, indicating there being unwanted large particles. After centrifugation at 5,800 rpm for 45 min, only one peak exists, with an average hydrodynamic diameter of ~15 nm. TEM images in Figure 2.3 also confirm the successful synthesis of ~5 nm AuNPs.

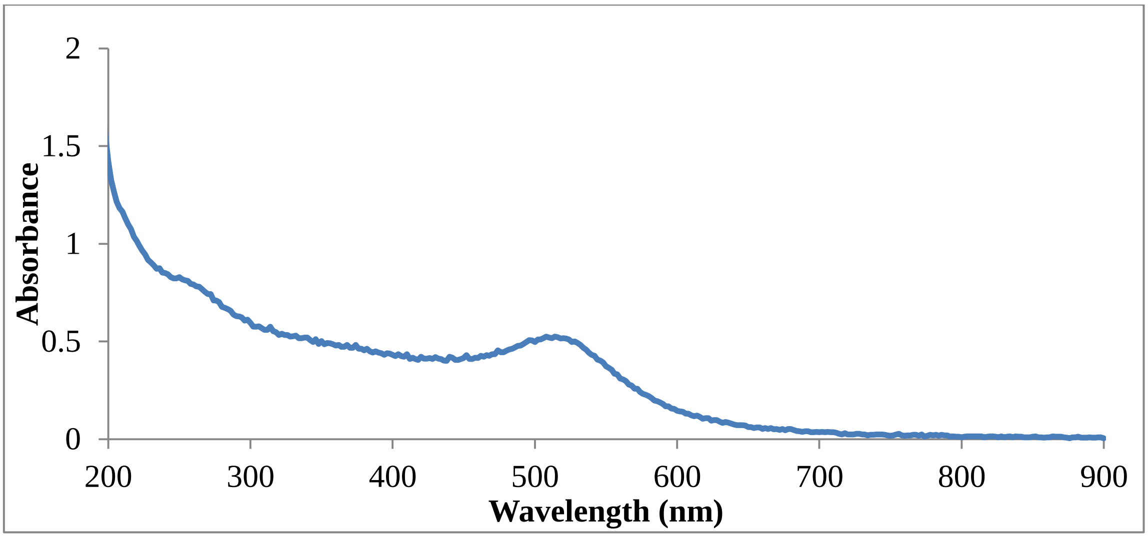

Figure 2.1. UV–vis spectrum of the synthesized AuNP solution after centrifugation. The LSPR position is at 514 nm, and A_{spr}/A_{450} ratio of ~1.27 gives particle size of ~5 nm. Concentration of the AuNPs is calculated to be ~59 nM from dividing A_{450} by the extinction coefficient at 450 nm of 5 nm AuNPs. The method was well reported by Haiss et al. from [191].

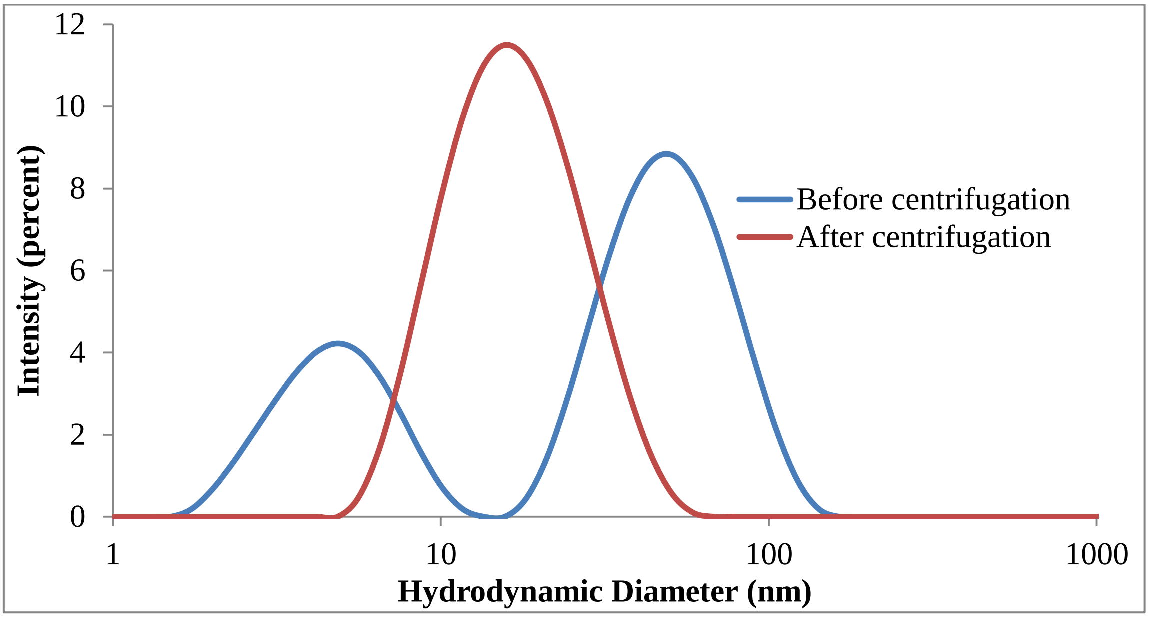

Figure 2.2. DLS curves of the synthesized AuNPs before (blue) and after (red) centrifugation. The unwanted larger impurities have been successfully removed as indicated by the single peak in red.

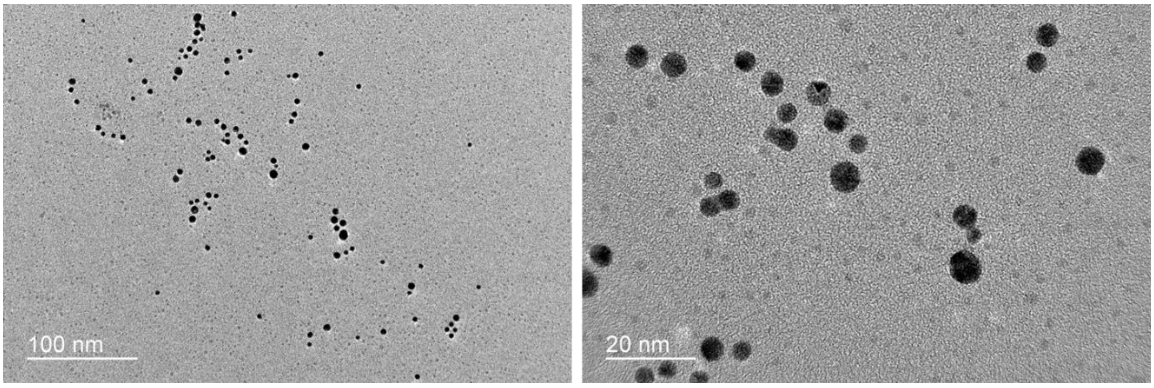

Figure 2.3. TEM images of the synthesized AuNPs. The size is not uniform but is averaged around 5 nm, consistent with the UV–vis calculation.

2.2.2. Seed-mediated growth of 5 nm AuNPs

The general color progression in the growth process at room temperature consists of the following stages: light pink (from the seeds), light gray, dark grayish blue, purple, and purple red, then finally red (Figure 2.4). This color change is striking because it manifests the dark intermediate color reported by many literatures studying Turkevich method, while the four papers studying on seed-mediated growth of AuNPs with citrate as reducing agent failed to achieve. By controlling the reaction conditions, the color change time frame can be manipulated within 24 h, although there were minor variations between batches, which we will elaborate more in Section 2.2.3 (on p. 123). For a different batch, the color images and corresponding UV–vis curves are shown in Figure 2.5. The color images are similar to those in Figure 2.4. Red shift of the LSPR peak occurred within the first 6 h (from 531 nm to 553 nm; Figure 2.6A) with increase of absorbance in NIR region (700–900 nm) within the first 10 h (from 0.141 to 0.623 of absorbance at 700 nm as a representative; Figure 2.6B). Then, blue shift followed (from 553 nm back to 524 nm; Figure 2.6A) with decrease in NIR absorption (from 0.623 to 0.067 of absorbance at 700 nm as a representative; Figure 2.6B) until the final red color was attained. Right after mixing growth solution with the 5 nm seeds, the absorbance peak shifted from 514 nm (Figure 2.1) to 531 nm (Figure 2.5, 0 h) without any change in the NIR absorbance, similar to the study of Polte et al. (#8 [179-180], #13 [186]). They didn't observe the further red shift after that, therefore their hypothesis of the adsorption of gold ions to the electric double layer (mechanism (v); Section 1.4; p. 79) may not hold for the observed dark grayish blue color of seed-mediated growth in this thesis. This change in absorption spectra is indicative of either a large intermediate particle size (Section 1.2.1.2), or transient anisotropic morphology (Section 1.2.1.3; nanowire formation discussed in Section 1.3.3, mechanism (ii)), or reversible changes in AuNP interparticle distance (Section 1.2.1.4) via temporary aggregates formation (mechanism (i), (ii), (iii)). The aggregates can be formed from AuNPs directly interacting with each other (mechanism (i) and (ii)) or from “glue” particle (within which AuNP nucleate and grow) aggregation into spherical shape (mechanism (iii)). Change of interparticle distance is also attainable by mechanism (iv) where kinetic intermediate of closely spaced gold cluters/particles (< 5 nm) exist before compacting to form AuNPs.

DLS evolution of this batch is depicted in Figure 2.7 and Figure 2.8, exhibiting a monotonic increase in hydrodynamic size till 10 h followed by a plateau. This trend rules out the formation of large spherical aggregates, from either AuNPs directly interacting with each other (mechanism (i)) or “glue” particles bringing the interior AuNPs close to each other (mechanism (iii)), in the purple/blue stage as suggested in the literatures. For both scenarios, a large hydrodynamic size exceeding 100 nm is expected, and a decrease of the size should follow till the red color reappears. Mechanism (ii) can also be excluded because the formation of solid nanowires should also render a large peak in the DLS curve, and the cleavage or intraparticle ripening of wires to AuNPs is also expected to correlate with decreasing hydrodynamic size. Therefore, only mechanism (iv) seems reasonable to explain the color changes in our seed-mediated growth of 5 nm citrate-coated AuNPs after analyzing the UV–vis and DLS data.

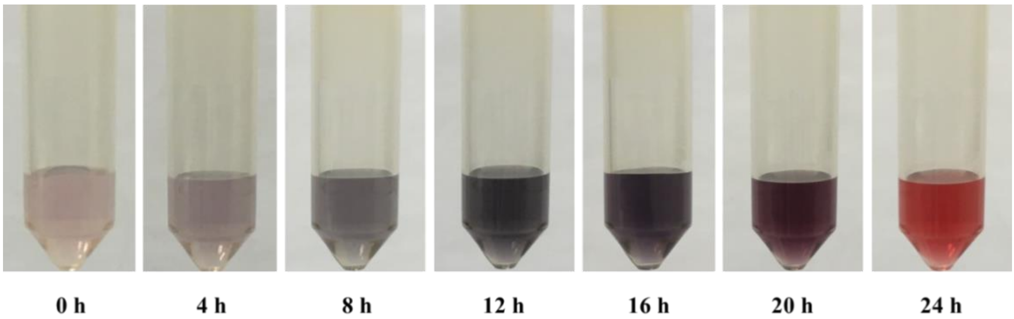

Figure 2.4. Color progression in seed-mediated growth process of 5 nm citrate-capped AuNPs at room temperature. The darkest color (grayish blue) occurred at 12–16 h for this batch.

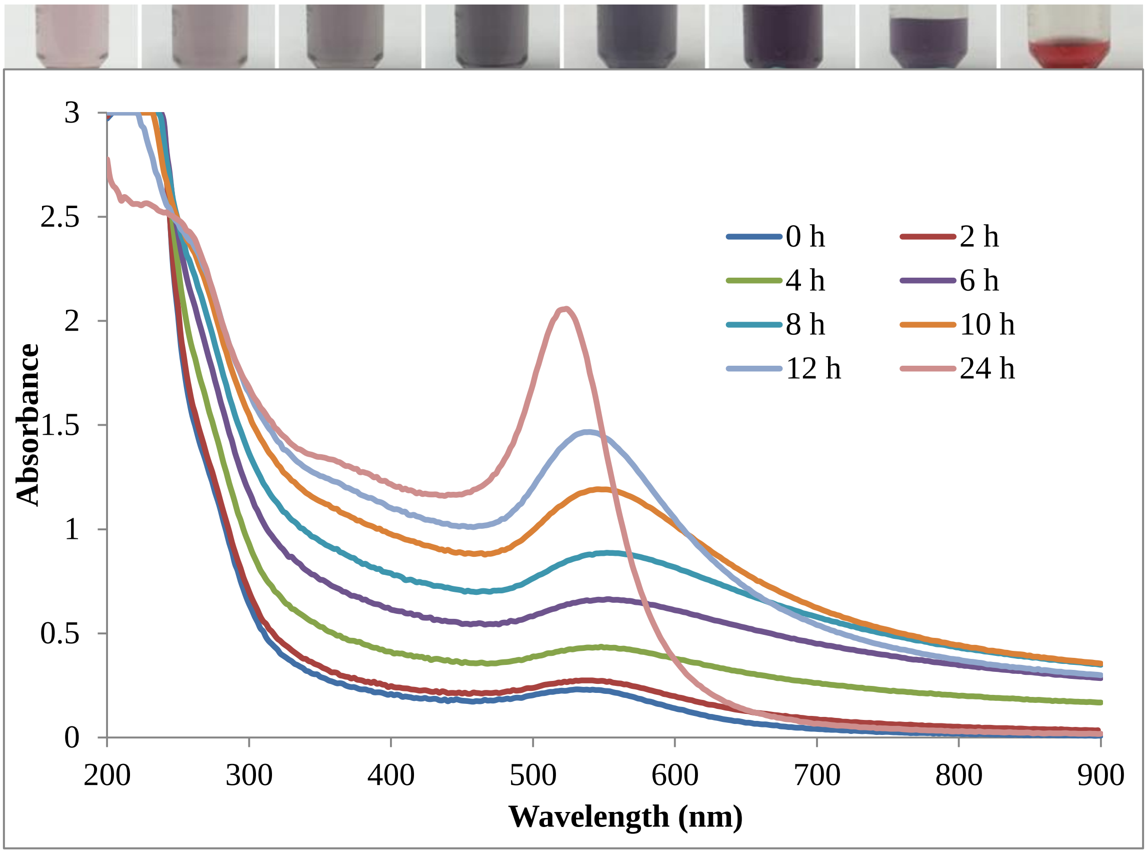

Figure 2.5. UV–vis spectra of another batch throughout the growth process. A clear red shift and increase in NIR absorption were observed in the first 8–10 h for this batch. Then the LSPR peak blue shifted and NIR absorption decreased till the color images above turned red. The size of the final AuNPs in the red dispersion was calculated to be ~22 nm, according to Haiss et al. [191].

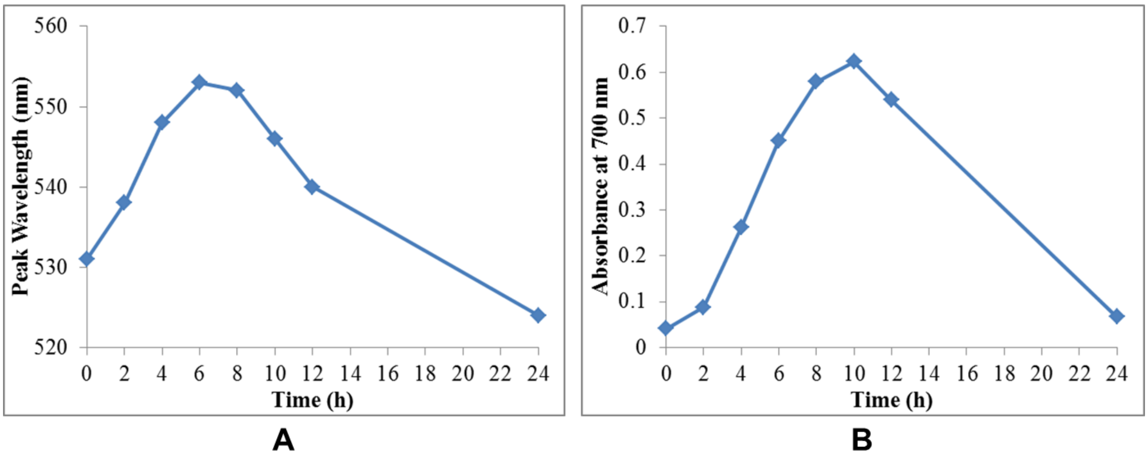

Figure 2.6. (A) Absorbance peak wavelength and (B) absorbance at 700 nm of spectra in Figure 2.5.

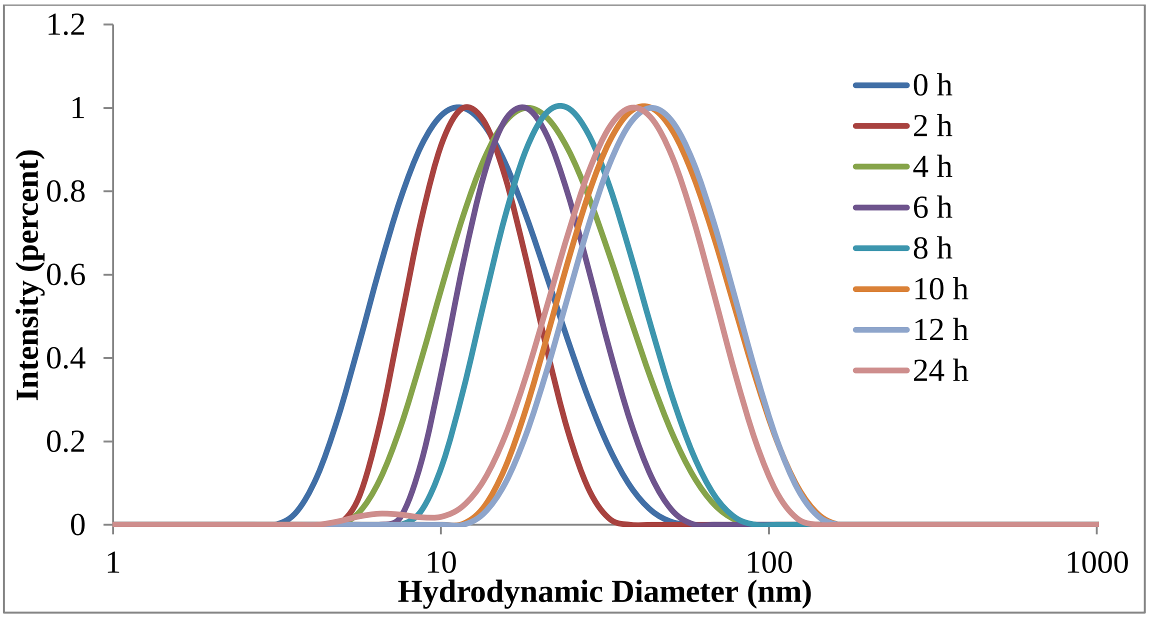

Figure 2.7. DLS curves (normalized) corresponding to Figure 2.5, indicating a monotonic size enlargement till 10 h followed by nearly constant size until the final red color appeared. No large structures were detected at the dark grayish blue color (8–10 h).

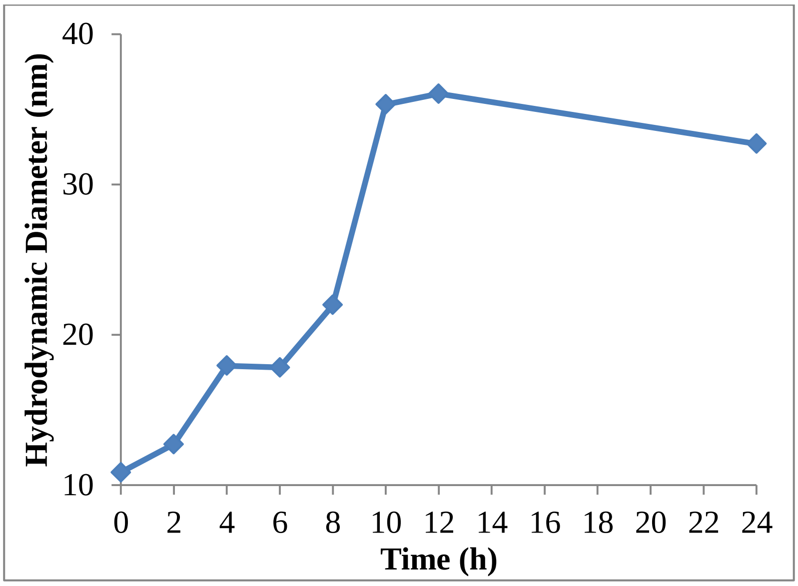

Figure 2.8. The intensity-averaged hydrodynamic diameters of the DLS curves depicted in Figure 2.7.

To have direct visualization of the structures giving rise to the different colors in the growth process, TEM images were taken for this batch and are shown in Figure 2.9–16. For the time series of TEM, the appearance and disappearance of wire-like structures well correlated with the color changes shown in Figure 2.5. However, different from the reported solid long continuous nanowires as in mechanism (ii), the wire-like structures observed in this reaction are shorter in length. The observed structures disproved the mechanism (iv) for the intermediate purple/blue color, since there were no clusters/particles (< 5 nm) compacting into larger particles during the purple/blue-to-red color progression. Thus till now, all the five schools of explanation for the purple/blue color failed to account for the striking color change in our seed-mediated growth of 5 nm citrate-coated AuNPs. Taking all the UV–vis, DLS, and TEM data together, small nanowires which are not continuous solid structures (otherwise will be picked up by

DLS) are causing the purple/blue color in this reaction. ***We would like to propose that some soft "glue" is bringing AuNPs to close proximity in chain-like form.*** The term chain-like is to distinguish our flexible structures with the solid nanowires in mechanism (ii). Because of the flexibility of "glue" and the chain configuration, it's possible that DLS cannot detect the larger intermediate structures (liquid "glue" particles forming aggregates in spherical shape will also be detected by DLS [181]). In the chain form, LSPR peak red shift and NIR absorbance increase are also explainable by referencing to other chain-like structures from linked AuNPs [192]. Therefore, such chain-like structures bridged by soft "glue" are the most reasonable explanation for the characterization results presented above.

Actually the paper by Leng et al. (#16 [188]) proposing mechanism (ii) also found no large structures in their DLS results, even though they claimed nanowire formation in their study. To have a more consistent terminology, we would also consider such structures as chain-like rather than wire-like in their seed-mediated growth of ~14 nm citrate-coated AuNPs at room temperature. For the remaining literatures in support of solid nanowire formation in mechanism (ii), no DLS data were included in their papers and the possibility of chain-like structures cannot be completely ruled out because their HRTEM images didn't show continuous lattice fringes (#3 [174], #6 [177], #15 [187]). Another point worth mentioning from #3 is that the claimed nanowires disintegrated to individual AuNPs after putting the TEM grid carrying the structures in H_2 atmosphere at room temperature for 1 h (Figure 1.22), more supportive of our chain-like configuration instead of their solid nanowires [174].

For Figure 2.9 (right after mixing the seeds and growth solution) and Figure 2.12 (6 h after mixing), fluffy large particles similar to those reported in mechanism (i) in the range of 50–500 nm were observed. They were not present in TEM images of other time points and were likely formed from the drying artefacts of gold precursor in the growth solution, as similar structures were detected in the TEM images of growth solution (Figure 2.17). By depleting the medium (mainly containing sodium citrate, gold precursor $HAuCl_4$, and KOH) and isolating the nanostructure in water using centrifugal filter devices, such large spherical aggregates were not detected while the other features well retained (Figure 2.18–24).

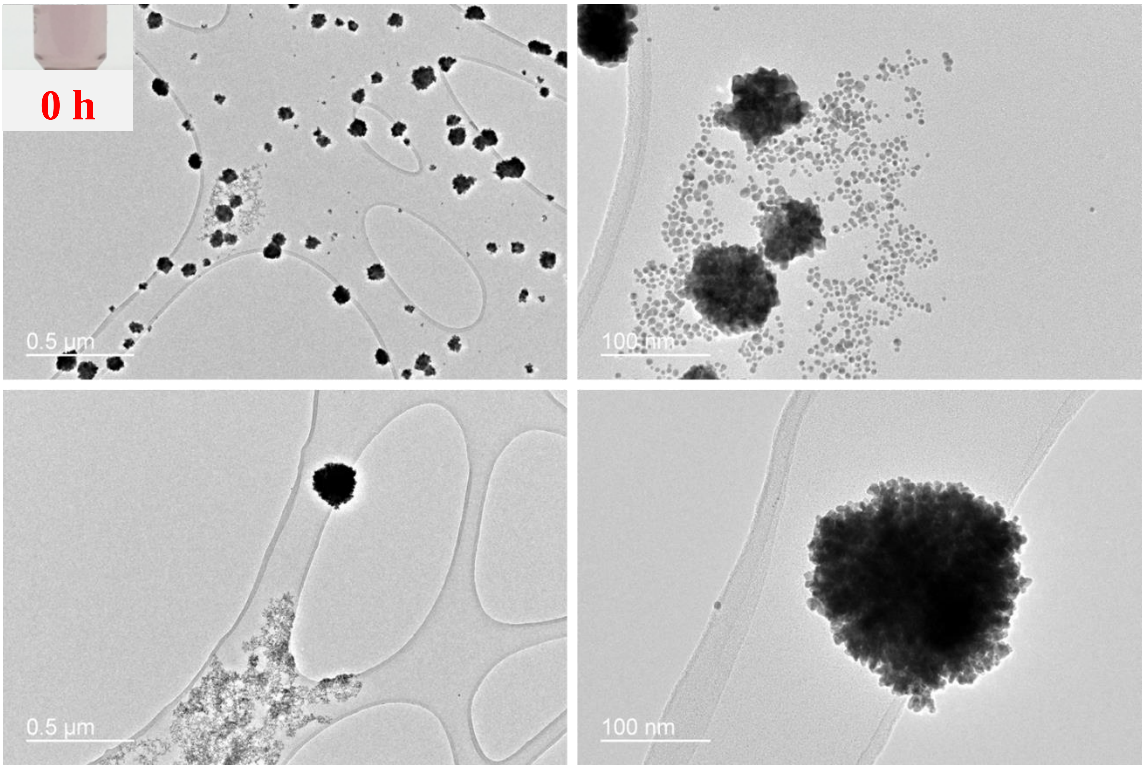

Figure 2.9. TEM images of seed-mediated growth of 5 nm AuNPs, right after mixing seed solution with growth solution. The left images have the same scale bar of 0.5 µm and the right images have the same scale bar of 100 nm. Fluffy large particles in the range of 50–500 nm coexisted with the ~5 nm AuNP seeds.

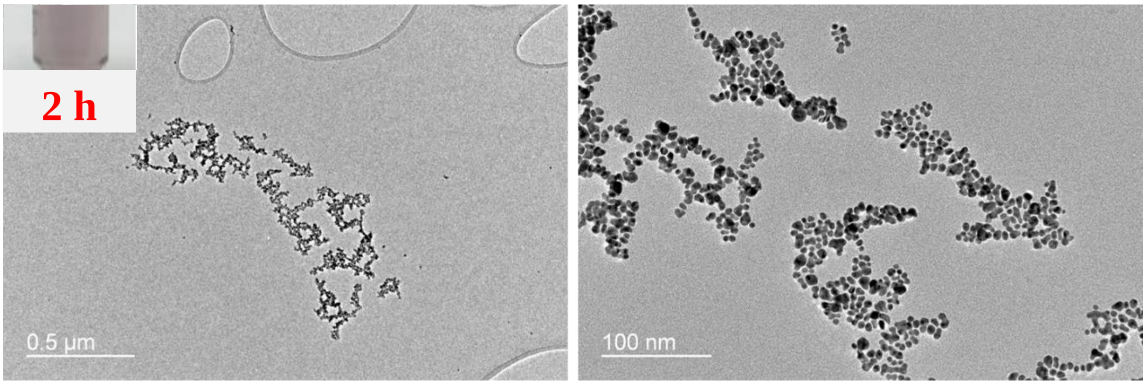

Figure 2.10. TEM images of seed-mediated growth of 5 nm AuNPs, 2 h after mixing seed solution with growth solution. The left image has scale bar of 0.5 µm and the right image has scale bar of 100 nm. The seeds got larger size than the 0 h sample in Figure 2.9.

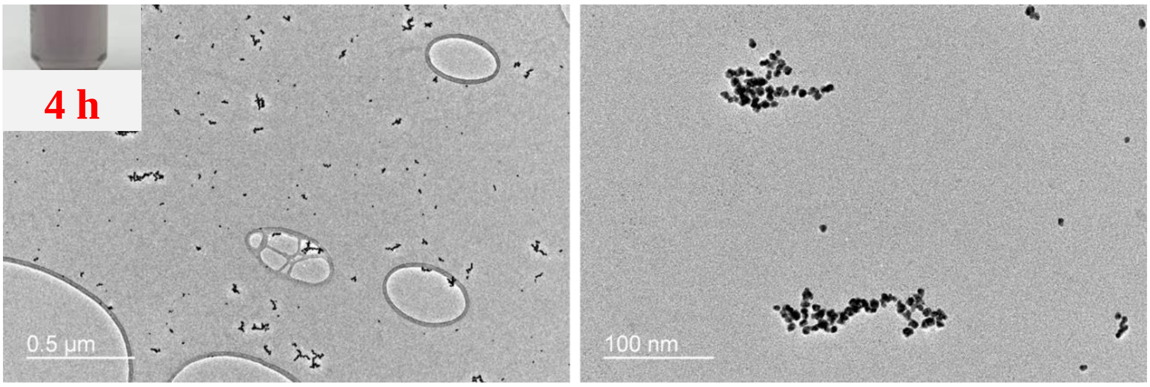

Figure 2.11. TEM images of seed-mediated growth of 5 nm AuNPs, 4 h after mixing seed solution with growth solution. The left image has scale bar of 0.5 µm and the right image has scale bar of 100 nm. Diameter of the seeds further increased and the seeds started to form chain-like structures.

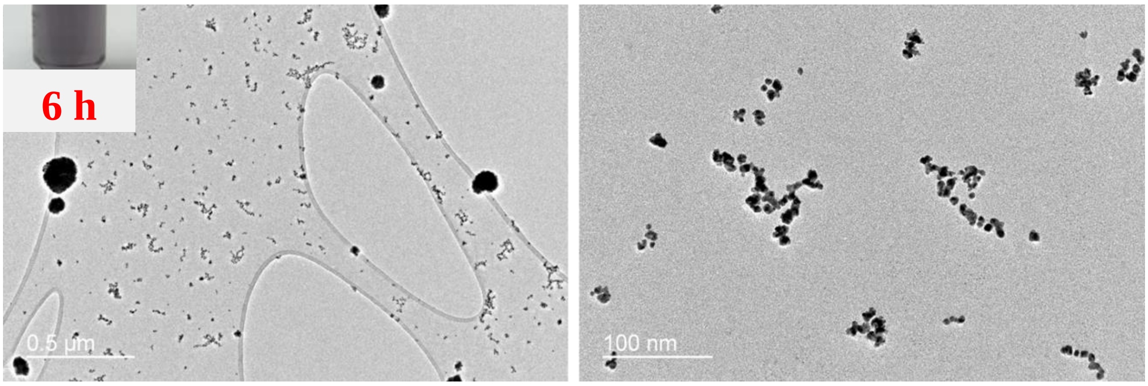

Figure 2.12. TEM images of seed-mediated growth of 5 nm AuNPs, 6 h after mixing seed solution with growth solution. The left image has scale bar of 0.5 µm and the right image has scale bar of 100 nm. Increase in seed size continued and more seeds were associating to form chain-like structures. Fluffy large particles in the range of 50–500 nm were identified.

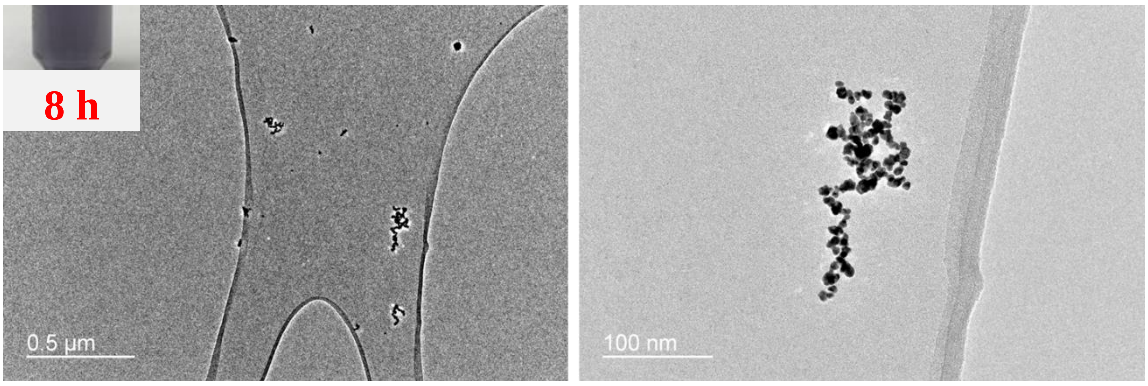

Figure 2.13. TEM images of seed-mediated growth of 5 nm AuNPs, 8 h after mixing seed solution with growth solution. The left image has scale bar of 0.5 µm and the right image has scale bar of 100 nm. Even more seeds were forming chain-like structures.

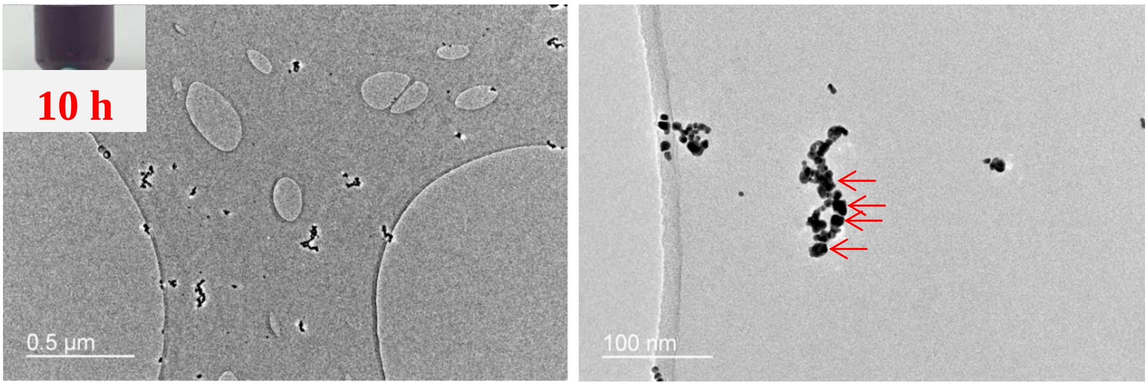

Figure 2.14. TEM images of seed-mediated growth of 5 nm AuNPs, 10 h after mixing seed solution with growth solution. The left image has scale bar of 0.5 µm and the right image has scale bar of 100 nm. Size increase was obvious in some parts of the chains (indicated by red arrows).

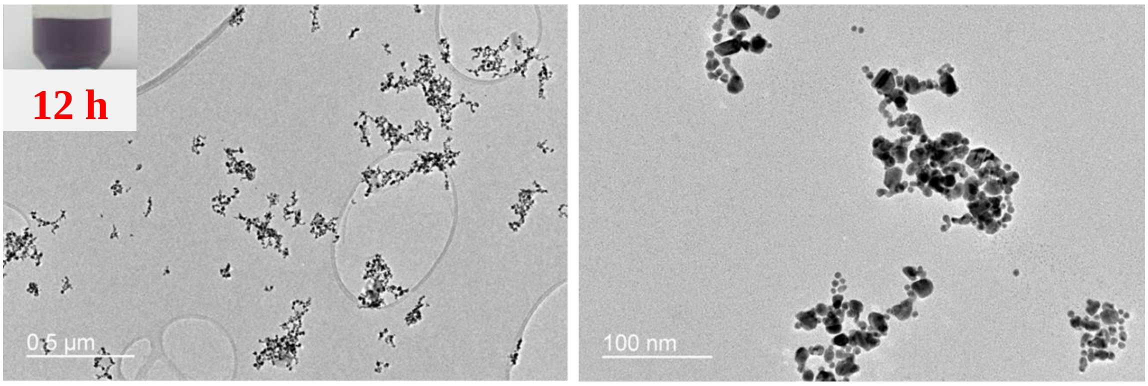

Figure 2.15. TEM images of seed-mediated growth of 5 nm AuNPs, 12 h after mixing seed solution with growth solution. The left image has scale bar of 0.5 µm and the right image has scale bar of 100 nm. The diameter of the chains became more non-uniform. Individual particles started dissociating off the chains.

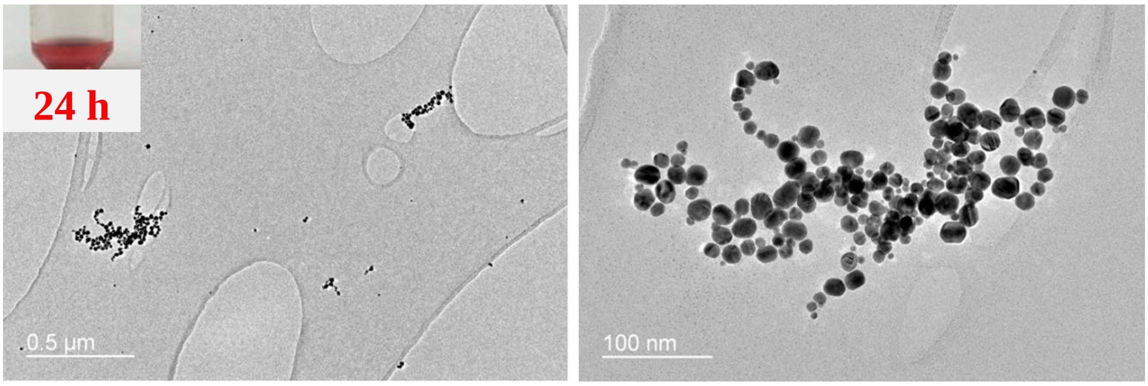

Figure 2.16. TEM images of seed-mediated growth of 5 nm AuNPs, 24 h after mixing seed solution with growth solution. The left image has scale bar of 0.5 μm and the right image has scale bar of 100 nm. No chains were observed and the final individual particles were polydisperse and spherical in shape.

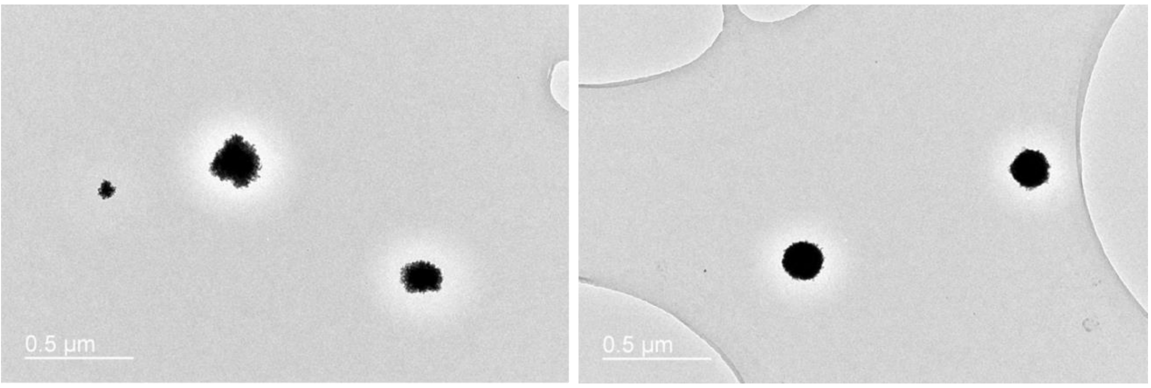

Figure 2.17. TEM images of as-prepared growth solution. Both images have the same scale bar of 0.5 μm. Similar fluffy large particles in the range of 50–500 nm were observed.

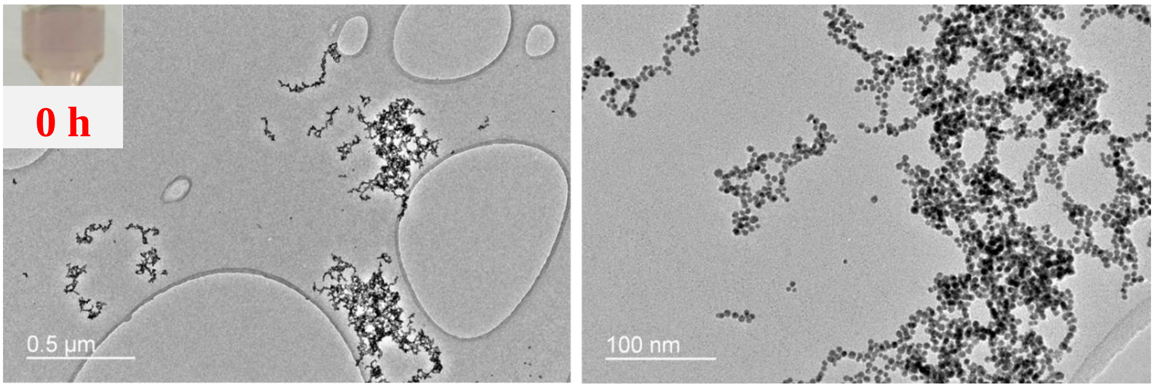

Figure 2.18. TEM images of seed-mediated growth of 5 nm AuNPs, right after mixing seed solution with growth solution. The left image has scale bar of 0.5 μm and the right image has scale bar of 100 nm. The mixture was filtered off the solutes using centrifugal filtration and the concentrate was redispersed in water. Fluffy large particles were not detected.

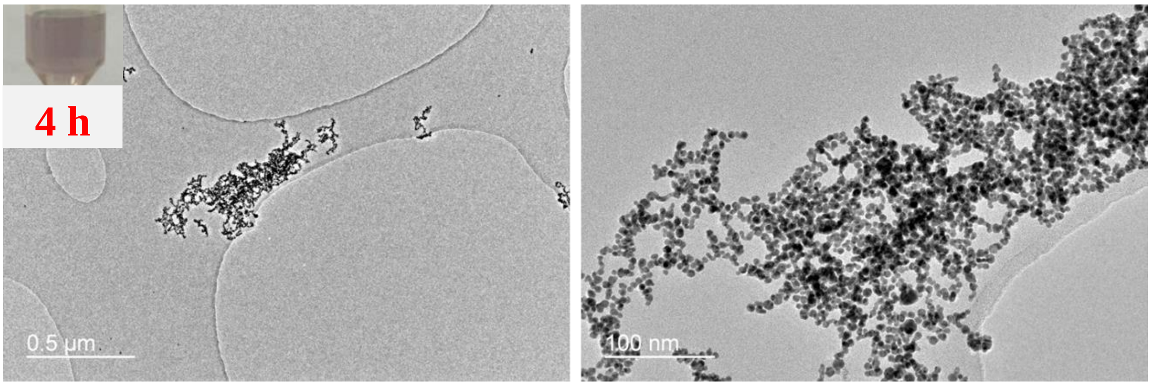

Figure 2.19. TEM images of seed-mediated growth of 5 nm AuNPs, 4 h after mixing seed solution with growth solution. The left image has scale bar of 0.5 μm and the right image has scale bar of 100 nm. The mixture was filtered off the solutes using centrifugal filtration and the concentrate was redispersed in water.

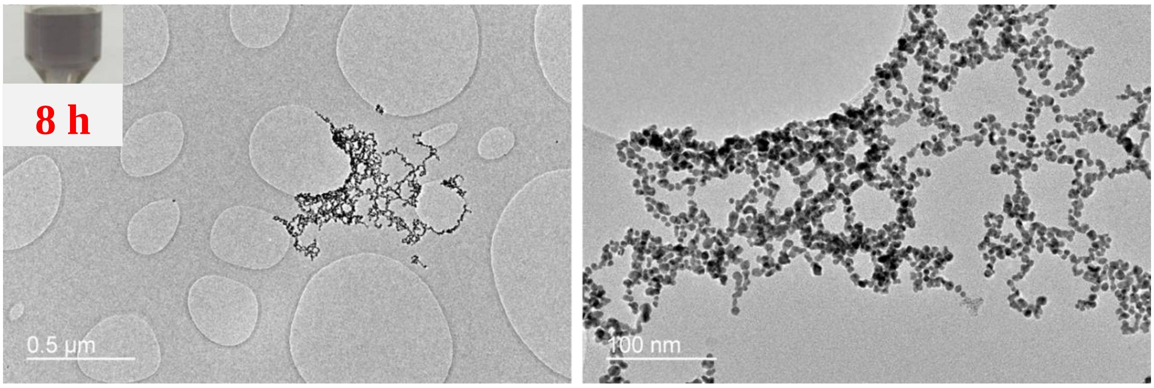

Figure 2.20. TEM images of seed-mediated growth of 5 nm AuNPs, 8 h after mixing seed solution with growth solution. The left image has scale bar of 0.5 µm and the right image has scale bar of 100 nm. The mixture was filtered off the solutes using centrifugal filtration and the concentrate was redispersed in water.

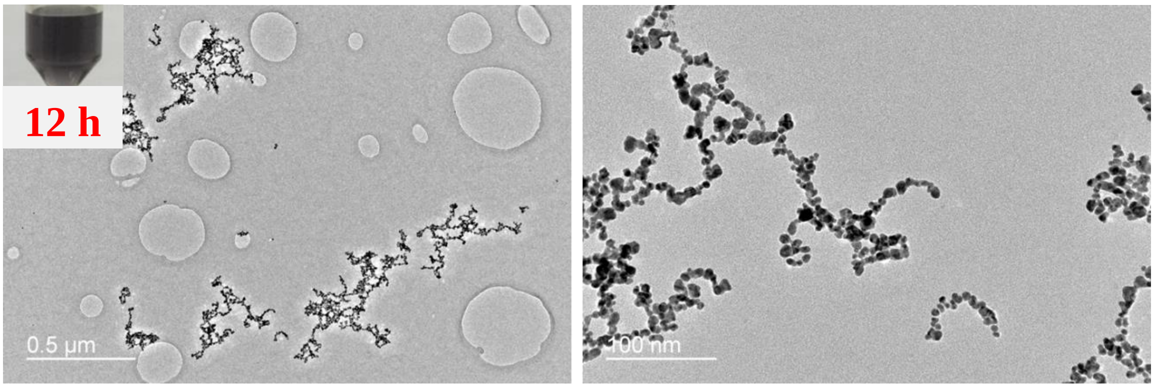

Figure 2.21. TEM images of seed-mediated growth of 5 nm AuNPs, 12 h (the darkest color) after mixing seed solution with growth solution. The left image has scale bar of 0.5 µm and the right image has scale bar of 100 nm. The mixture was filtered off the solutes using centrifugal filtration and the concentrate was redispersed in water. Size increase was obvious in some parts of the chains, rendering them non-uniform diameters.

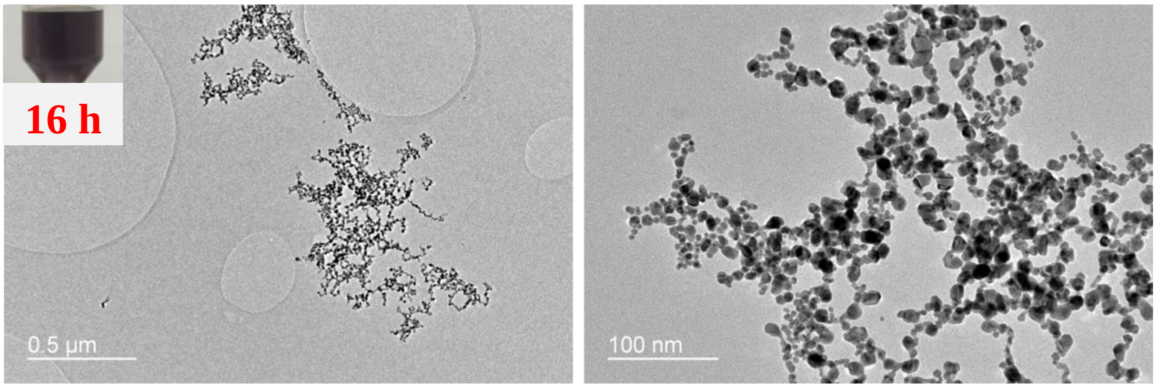

Figure 2.22. TEM images of seed-mediated growth of 5 nm AuNPs, 16 h (purple in color) after mixing seed solution with growth solution. The left image has scale bar of 0.5 µm and the right image has scale bar of 100 nm. The mixture was filtered off the solutes using centrifugal filtration and the concentrate was redispersed in water. The diameter of the chains became more non-uniform. Individual particles started dissociating off the chains.

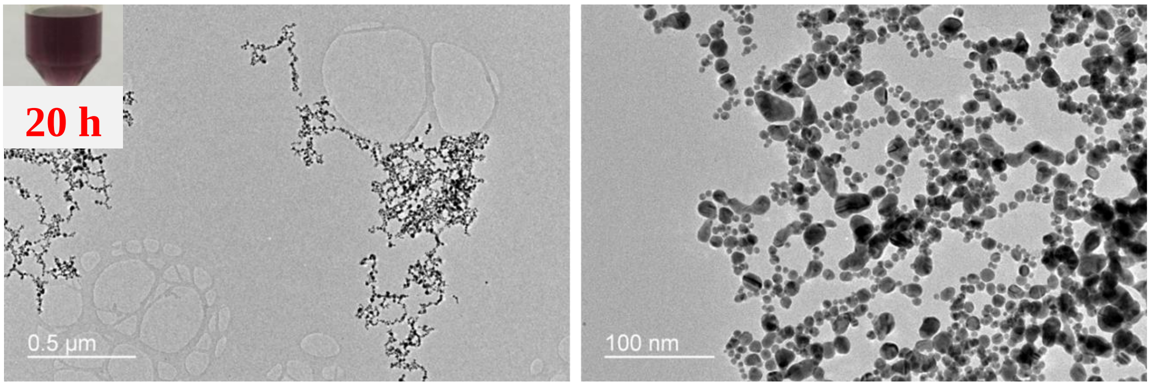

Figure 2.23. TEM images of seed-mediated growth of 5 nm AuNPs, 20 h (turning red in color) after mixing seed solution with growth solution. The left image has scale bar of 0.5 µm and the right image has scale bar of 100 nm. The mixture was filtered off the solutes using centrifugal filtration and the concentrate was redispersed in water. More individual particles dissociated off the chains.

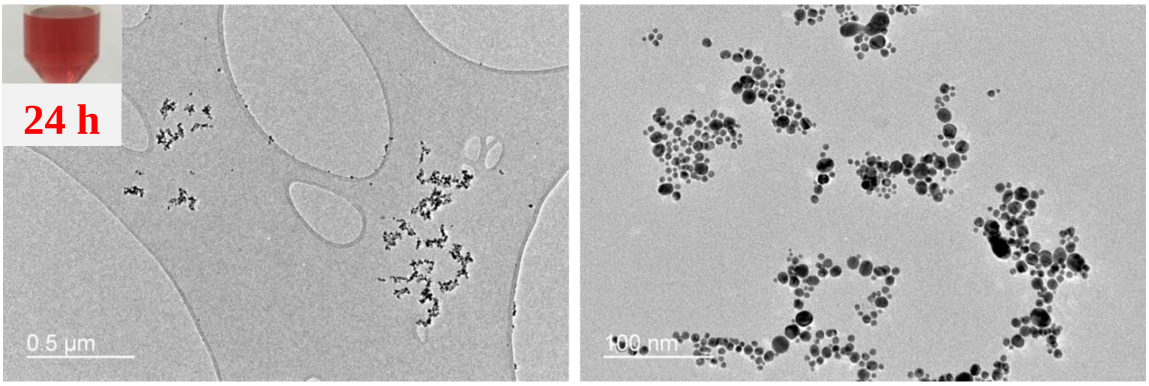

Figure 2.24. TEM images of seed-mediated growth of 5 nm AuNPs, 24 h (final red color) after mixing seed solution with growth solution. The left image has scale bar of 0.5 µm and the right image has scale bar of 100 nm. The mixture was filtered off the solutes using centrifugal filtration and the concentrate was redispersed in water. Most of the particles were discrete and spherical in shape, with polydisperse size distribution.

Schematic diagram of the structural evolution of gold nanostructures during the seed-mediated growth of 5 nm citrate-coated AuNPs is shown in Figure 2.25. Basically, the dispersed seeds, with increasing size, would be brought in chain-like form by the liquid “glue”. Plasmon coupling among these closely located AuNPs would red shift the LSPR peak and increase the NIR absorbance, causing red-to-purple/blue color changes. As for the favored formation of one-dimensional chain-like structures instead of three-dimensional agglomerates, one possible reason is the limited amount of “glue” material. In a study on the formation of chain-like ensemble from pyrrole-functionalized AuNPs, the authors found the amount of pyrrole linkers dictated the morphology of ensemble. Below a certain threshold, one-dimensional chain-like structures were formed, whereas more pyrroles induced fast aggregation and disordered precipitates [192]. Another possible explanation for the chain-like morphology can be steric effects (from geometrical restriction [176] or charge density, etc.). As the growth process continues, the liquid "glue" is consumed with AuNPs are further enlarged. The complete depletion of "glue" marks the transition of the structures from chain-like form to individual polydisperse AuNPs and the reversal of color from purple/blue to ruby red. The polydispersity of the final AuNPs shown in the TEM images (Figure 2.16 and 2.24) is likely due to Ostwald ripening, during which the smaller particles dissolve for the growth of their larger counterparts when the precursor concentration is lowered [166]. These size changes may contribute to the non-uniform diameter of the chain-like structures (indicated by red arrows in Figure 2.14). However, the size distribution is not the focus of this thesis and therefore not emphasized in the Scheme (Figure 2.25).

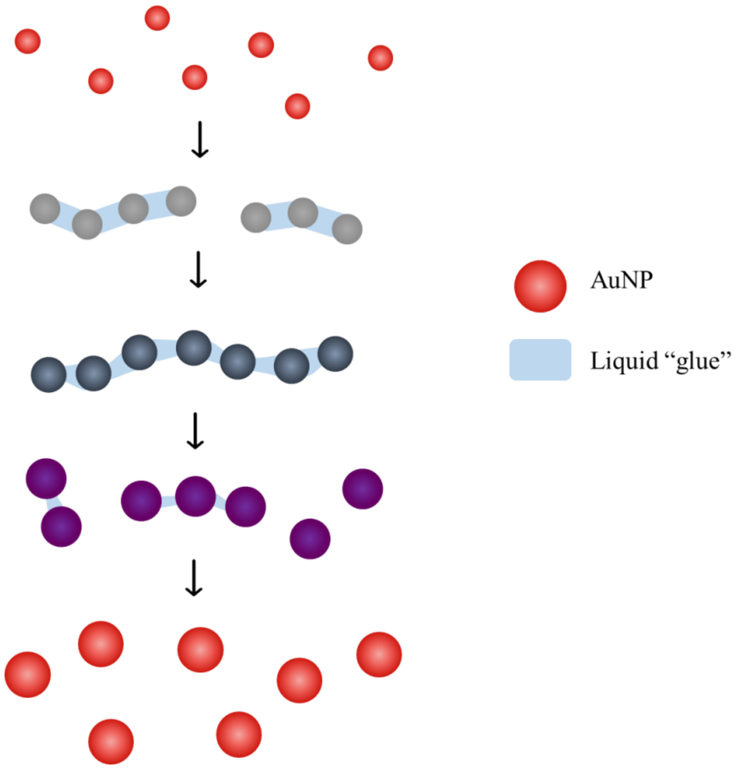

Figure 2.25. Schematic diagram showing the structural changes of gold nanostructures during the seed-mediated growth of 5 nm citrate-coated AuNPs.

2.2.3. Key components for color reversal in seed-mediated growth of 5 nm AuNPs

This section serves to study the key components involved in the red-to-purple/blue-to-red color reversal in this seed-mediated growth. To start with, the following experiments were conducted to provide more information about the liquid “glue” composition. Such “glue” can only be the components in the mixture (Na_3Ct, $HAuCl_4$, and the intermediate species from the redox reaction between Na_3Ct and $HAuCl_4$ as well as the oxidation and degradation reactions of SAD; discussed in Section 1.3.2.1; shown in Figure 2.26).

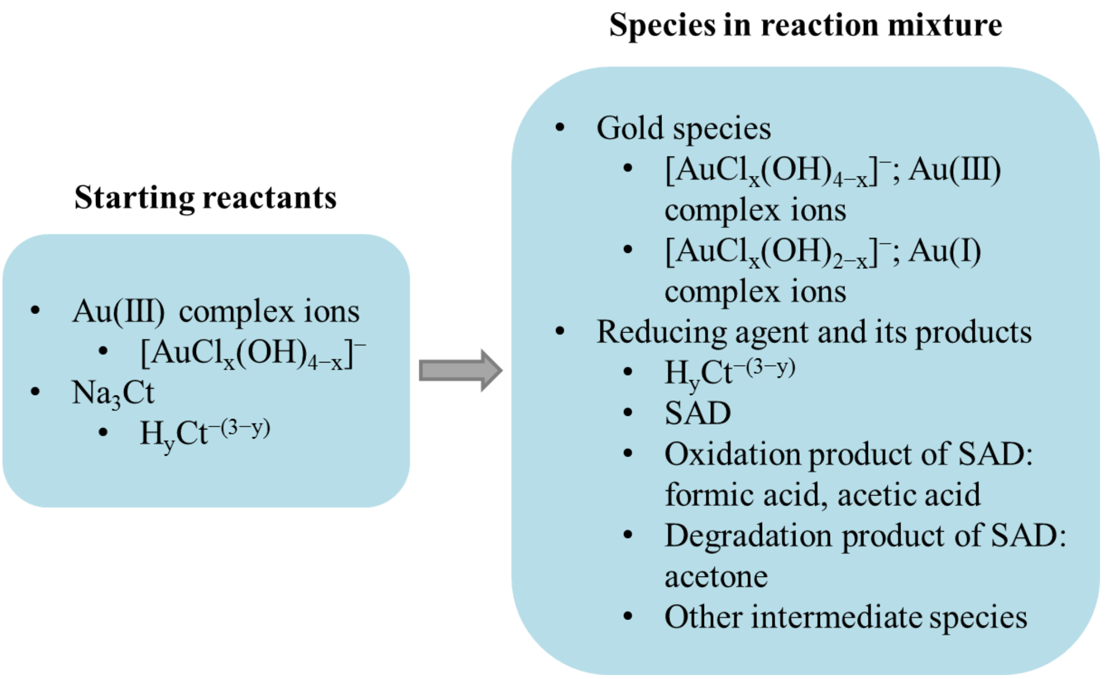

Figure 2.26. Possible components in the liquid “glue” for the chain-like structure formation.

Concentration of total Au(III) in solution phase (Au(III) only exist in complex ion form of $[AuCl_x(OH)_{4-x}]^-$ with x = 0, 1, 2, 3, 4 depending on solution pH [185, 193]) during reaction was monitored by measuring the absorbance at 314 nm due to ligand–

metal charge transfer of $AuCl_4^-$, after taking aliquots from reaction and quenching them into 1 M NaCl (providing ionic strength to precipitate the nanostructures) and then adding the supernatant to 0.1 M HCl (to convert all Au(III) complex ions to $AuCl_4^-$) [177, 185]. The absorbance spectrum of diluted growth solution ($HAuCl_4$ and KOH) after such treatment is shown in Figure 2.27. A calibration curve is displayed in Figure 2.28, covering Au(III) concentration range relevant in this thesis. The Au(III) concentration, denoted as $[Au^{3+}]$, during the whole growth process is depicted in Figure 2.29. The vertical axis shows the relative amount of $[Au^{3+}]$ over the added total Au(III) in the growth solution (denoted as $[Au^{3+}]_{t=0}$). At the dark grayish blue stage, there were ~20% of the Au(III) complex ions coexisting with the chain-like structures. When the color changed to red, all Au(III) complex ions were completely consumed. These results indicate that Au(III) complex ions may play an essential role in maintaining the chain-like structures, consistent with the results from Pei et al. [174]. This hypothesis is also supported by the findings that Au(III) complex ions preferentially adsorb onto gold surface and would induce attractive forces even in excess amount of citrate ions within minutes after addition [172-173]. ***Therefore Au(III) complex ions are very likely involved in the chain-like structure formation and constitute an important component in the liquid "glue".*** The depletion of Au(III) leads to readsorption of other chemicals onto the gold surface, endowing repulsive forces large enough to redisperse and stabilize the AuNPs. Such chemicals can be citrate, SAD, and acetone, all of which have been reported the capability to reduce $HAuCl_4$ to produce stable AuNPs [136-137, 156-157].

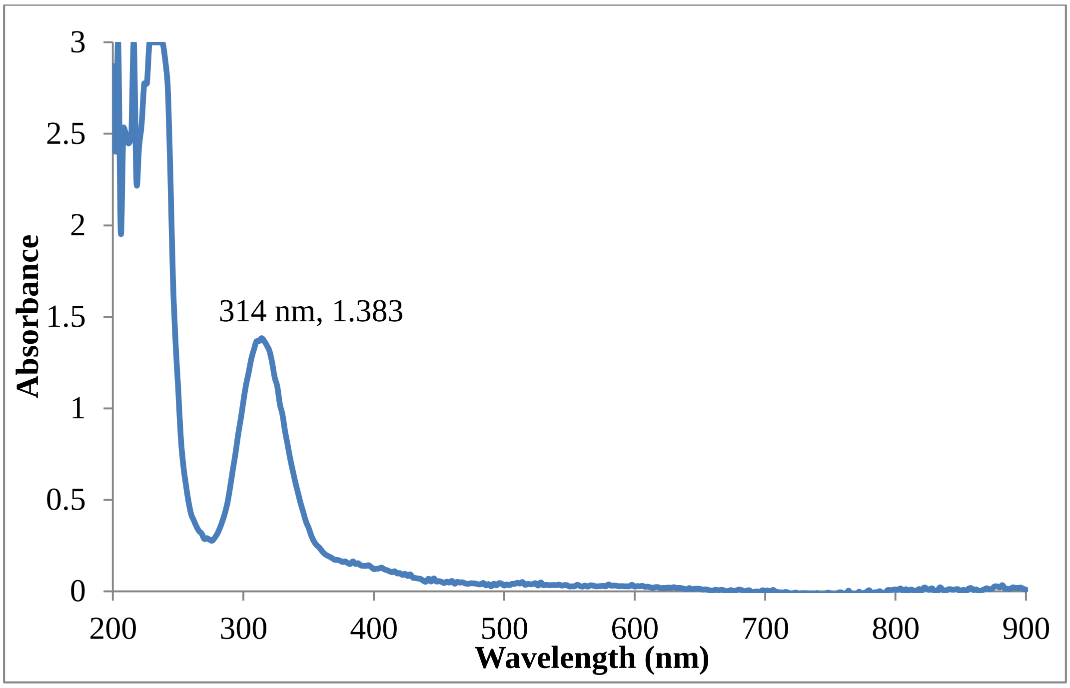

Figure 2.27. Absorption spectrum of prepared growth solution (0.52 mM Au(III)) in the mixture of 1 M NaCl and 0.1 M HCl. The peak absorbance at 314 nm results from ligand–metal charge transfer of $AuCl_4^-$.

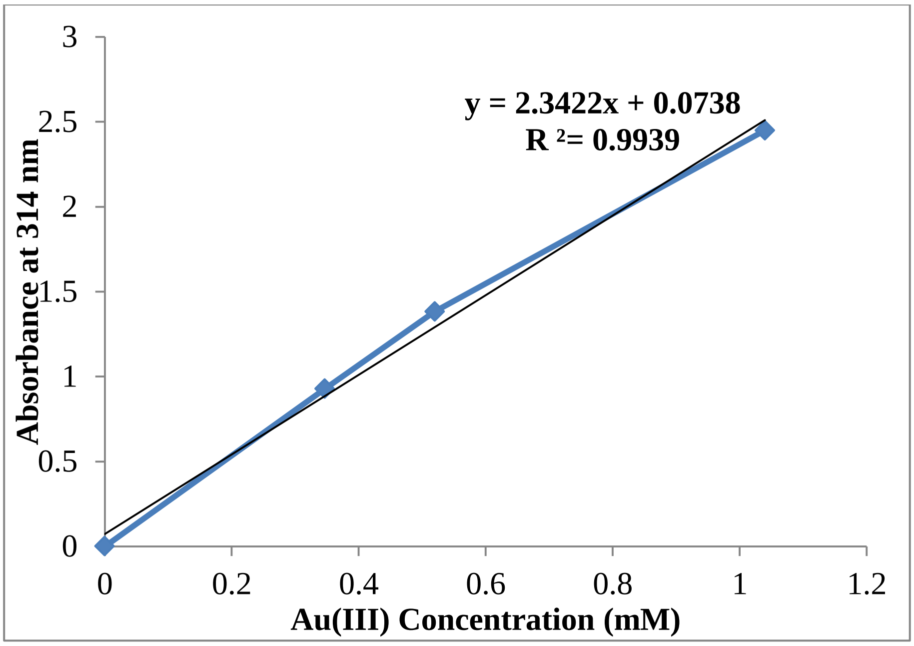

Figure 2.28. Calibration curve of absorbance at 314 nm with respect to Au(III) concentration in the mixture of 1 M NaCl and 0.1 M HCl.

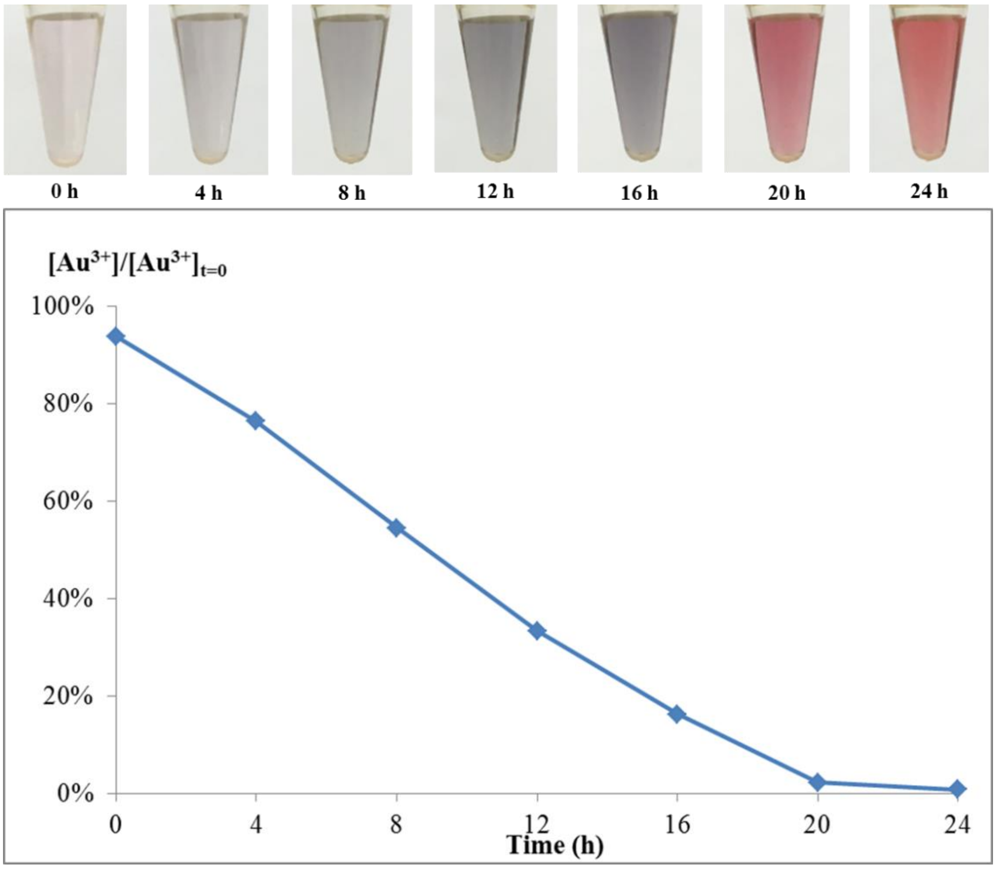

Figure 2.29. Quantification of Au(III) concentration (denoted as [Au^{3+}]) during the color change process. [Au^{3+}]$_{t=0}$ represents the added Au(III) amount in the growth solution. When the color turned red at 20 h, all the Au(III) complex ions were consumed.

Another key component for the "glue" can be deduced as follows: in order to bridge the AuNPs together, this component is expected to associate with adsorbed Au(III) and the Au(III) complex ions within the "glue". In this reaction with limited species of starting reactants, citrate ions are possible polydentate candidate to coordinate with Au(III) because of their three carboxylate groups. However, if citrate is the key component in the "glue" then such chain-like structures should have formed very soon after mixing growth solution and AuNP seeds. The gradual development of the purple/blue appearance could be well explained by the oxidation product of sodium citrate, sodium acetone dicarboxylate (SAD), which also contains more than one carboxylate groups and can form polymer structures with gold ions [136, 194]. SAD complexation with Au(I) was also proposed as the "glue" material in the study by Xia et al. (#12 [184]), but the aggregates formed were not chain-like and showed large hydrodynamic size in their DLS results (~1600 nm).

To provide some experimental evidence on the importance of SAD in the color change of our seed-mediated growth, Na_3Ct was replaced with SAD in Tube (d) in Figure 2.30. This tube was much faster in developing the purple/blue color as compared with Tube (e). Tube (f), with half Na_3Ct being replaced by SAD, got the color change profile between those of Tube (d) and (e). Purple/blue stage of Tube (d) at 8 h was characterized by TEM and similar chain-like structures were identified (Figure 2.31). These results suggest that ***SAD is more powerful than citrate in forming chain-like structures and is another key component in the liquid "glue"***. Comparing Tube (a)–(c) with (d)–(f) further supports the first claim that Au(III) is a key component in the liquid "glue". Au(I) may not be as prominent as Au(III) in forming the liquid "glue" by comparing Tube (g)–(i) with Tube (d)–(f). Solubility of AuCl is very low, and Au(I) complex ions are metastable and would readily disproportionate to form Au(III) complex ions and gold atoms in aqueous solutions [151]. The revised key components for the liquid "glue" are highlighted in red in Figure 2.32. Another insight from Figure 2.30 is that citrate may not be the only chemical capable of stabilizing AuNPs when purple/blue-to-red color change occurs.

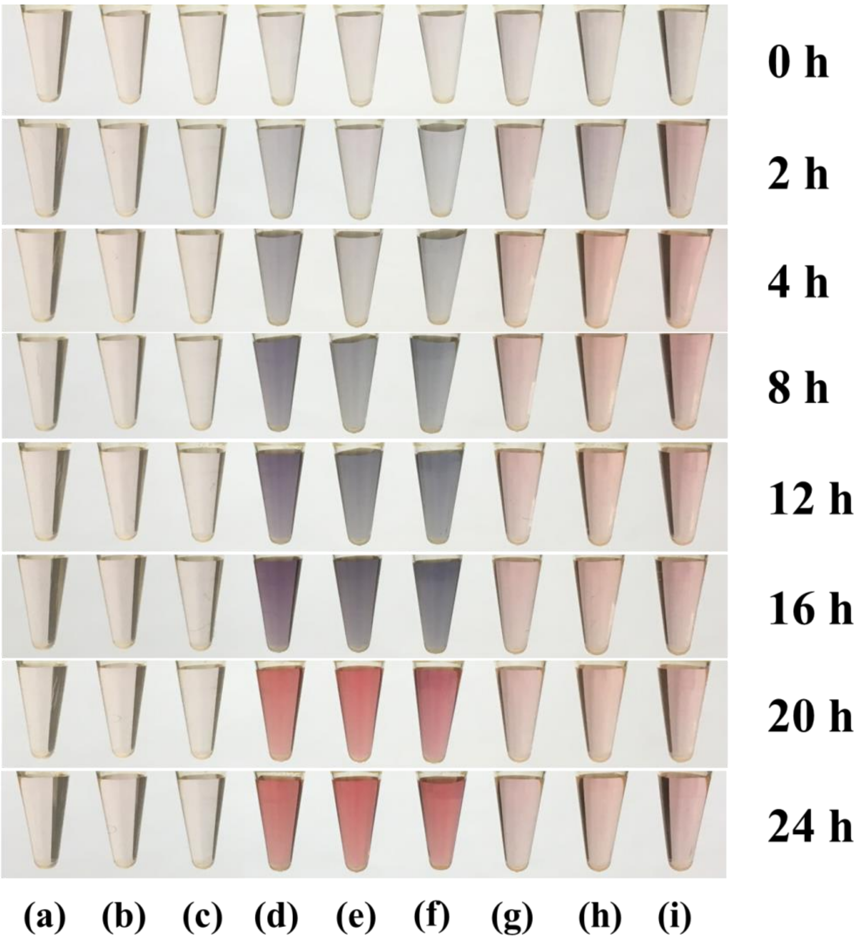

(a) 5 nm seeds + SAD
(b) 5 nm seeds + Na_3Ct
(c) 5 nm seeds + SAD + Na_3Ct
(d) 5 nm seeds + SAD + growth (KOH+$HAuCl_4$)
(e) 5 nm seeds + Na_3Ct + growth (KOH+$HAuCl_4$)
(f) 5 nm seeds + SAD + Na_3Ct + growth (KOH+$HAuCl_4$)
(g) 5 nm seeds + SAD + AuCl
(h) 5 nm seeds + Na_3Ct + AuCl
(i) 5 nm seeds + SAD + Na_3Ct + AuCl

Figure 2.30. Color change profile of tubes added with different starting chemicals. Tube (e) is the standard protocol performed in the seed-mediated growth of 5 nm citrate-capped AuNPs.

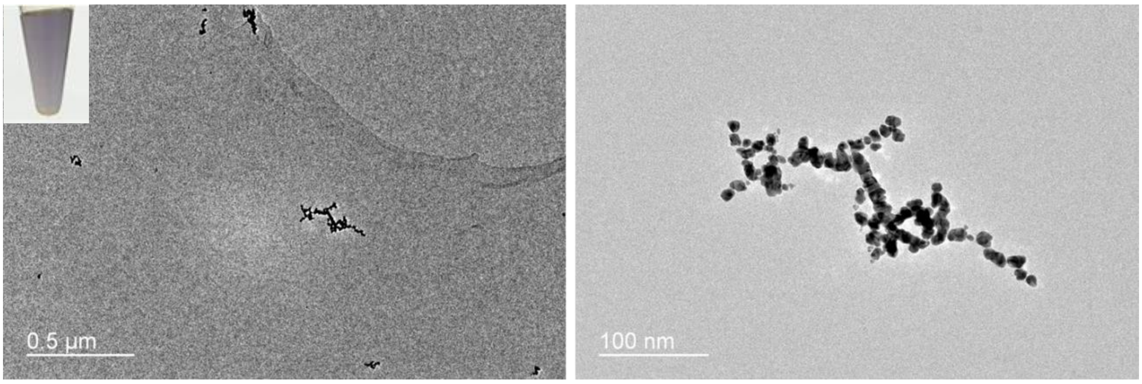

Figure 2.31. TEM images of Tube (d) in Figure 2.30, 8 h after mixing. The left image has scale bar of 0.5 µm and the right image has scale bar of 100 nm. Similar chain-like structures were identified.

- Gold species
  - $[AuCl_x(OH)_{4-x}]^-$; Au(III) complex ions
  - $[AuCl_x(OH)_{2-x}]^-$; Au(I) complex ions
- Reducing agent and its products
  - $H_yCt^{-(3-y)}$
  - SAD
  - Oxidation product of SAD: formic acid, acetic acid
  - Degradation product of SAD: acetone
  - Other intermediate species

Figure 2.32. Refined "glue" composition, with key components highlighted in red and less important chemicals in gray color. The other species in the mixture were studied in the coming experiment.

SAD was further substituted by its oxidation products (formic acid and acetic acid) and degradation product (acetone). The color progression results are displayed in

Figure 2.33. No purple/blue color appeared for the three tubes, implying less important role in the liquid “glue” formation. The key components in the liquid “glue” can be further revised in Figure 2.34.

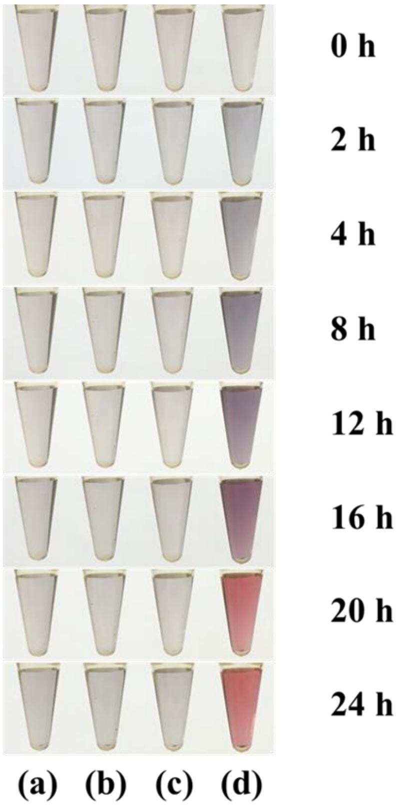

(a) 5 nm seeds + formic acid + growth (KOH+$HAuCl_4$)
(b) 5 nm seeds + acetic acid + growth (KOH+$HAuCl_4$)
(c) 5 nm seeds + acetone + growth (KOH+$HAuCl_4$)
(d) 5 nm seeds + SAD + growth (KOH+$HAuCl_4$)

Figure 2.33. Substituting SAD with its oxidation products and degradation product yielded no such red-to-purple/blue-to-red color reversal.

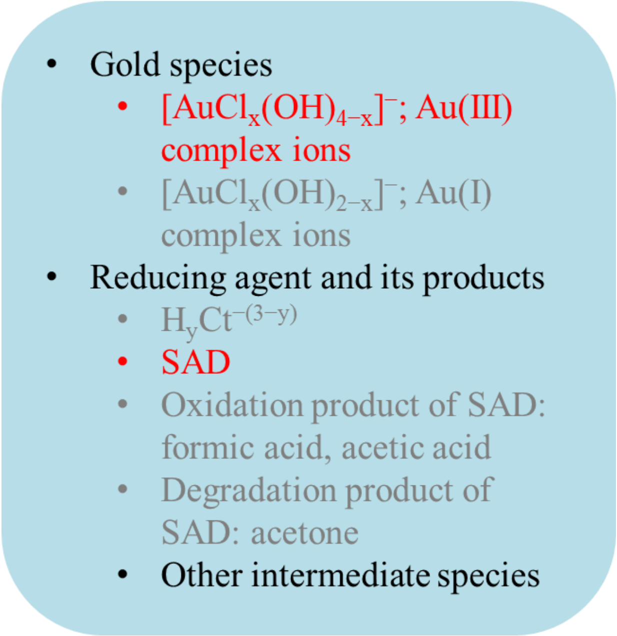

- Gold species
  - $[AuCl_x(OH)_{4-x}]^-$; Au(III) complex ions
  - $[AuCl_x(OH)_{2-x}]^-$; Au(I) complex ions
- Reducing agent and its products
  - $H_yCt^{-(3-y)}$
  - SAD
  - Oxidation product of SAD: formic acid, acetic acid
  - Degradation product of SAD: acetone
  - Other intermediate species

Figure 2.34. Further refined “glue” composition, with key components highlighted in red and less important chemicals in gray color.

In summary, a mechanism on the purple/blue coloration during seed-mediated growth of 5 nm citrate-capped AuNPs (with citrate as reducing agent) is proposed after detailed characterization using UV–vis, DLS, and TEM. With the enlargement of individual AuNPs in this growth process, the formation and disintegration of chain-like structures, which are composed of AuNPs interconnected by some liquid “glue”, are the underlying causes for such transient purple/blue color appearance and disappearance. After adding the growth solution ($HAuCl_4$, KOH) to the 5 nm citrate-coated AuNP seeds, the adsorbed citrate would be replaced rapidly with Au(III) complex ions, rendering attractive forces between AuNPs to facilitate such chain-like structure formation. The quantification of Au(III) during the growth process identified full consumption of Au(III) when the red color reappears, suggesting Au(III) can be an important component for the liquid “glue”. With the reduction of Au(III) by citrate, another key component for the liquid “glue”, SAD, is gradually produced. The interaction between the two components results such chain-like structure formation. With the depletion of Au(III), chain-like structures could no longer maintain and the readsorption of other stabilization chemicals (e.g., citrate, SAD, and acetone) onto AuNP surface can redisperse the particles to form final stable red colloid. One point worth noting is the involvement of other possible intermediate species (from the redox and degradation reactions) in the liquid “glue” formation and color change process. Our proposed model only includes the well-established species in our studied reaction system (Figure 2.35).

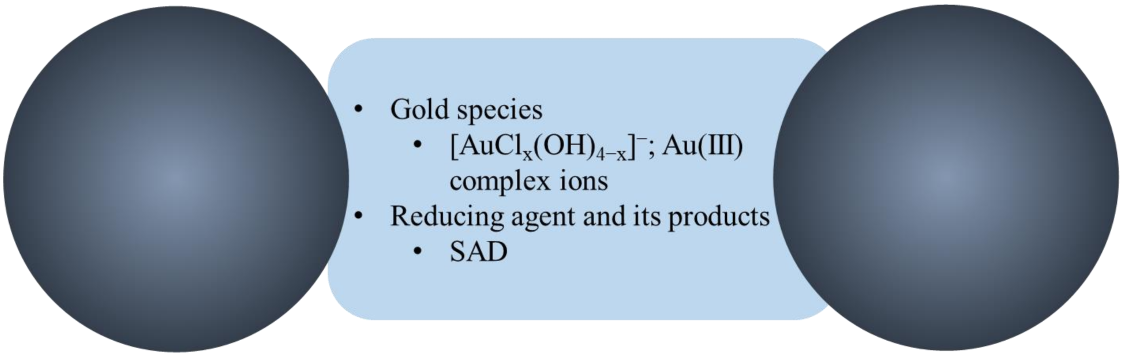

Figure 2.35. Proposed mechanism for the purple/blue coloration during our seed-mediated growth with citrate as reducing agent. Formation of reversible chain-like structures from gold seeds (denoted as dark grayish blue spheres) is mediated by liquid “glue”, with key components of Au(III) complex ions and SAD.

The following experiments were conducted to validate and refine the proposed mechanism. In this studied reaction, there are four starting components (5 nm seeds, Na_3Ct, KOH, and $HAuCl_4$), without any one of them such red-to-purple/blue-to-red color change wouldn’t have been possible. As shown in Figure 2.36, only Tube (b) with all the four components had the complete color progression. Without seeds in Tube (c), the purple/blue color would appear, but the final red homogeneous product was not obtained. Instead, precipitation occurred after 2 days of reaction. This could be due to the *in situ* generation of seeds, delaying the purple/blue color appearance and depleting the mixture of enough other chemicals (e.g., citrate, SAD, and acetone) to redisperse the final AuNPs. When citrate was removed from the system, as shown in Tube (d), a light purple/blue color appeared and no further change was observed even after 1 week. In this tube, only a very limited amount of citrate capped on the 5 nm seeds. Thus, the formation of “glue” was not enough to bring about the dark grayish blue color. Again, similar to Tube (c), not enough chemicals remained to achieve the purple/blue-to-red color transition. Without KOH in Tube (e), red color darkened quite rapidly and red precipitates formed within hours. No purple/blue hue was produced throughout the color changes. As the reactivity of Au(III) complex ions increases rapidly with decreasing pH [185, 195], fast reduction of Au(III) would produce burst supply of gold atoms for deposition onto the seeds. The fast reaction kinetics quickly consumes Au(III) and does not favor the “glue” formation thus the purple/blue coloration. When $HAuCl_4$ was depleted from the reaction, no color change was observed at all in Tube (f). This is because Au(III) complex ions play essential role in capping the gold seeds and oxidizing citrate to form SAD, both are indispensable for the liquid “glue” and thus chain-like structure formation.

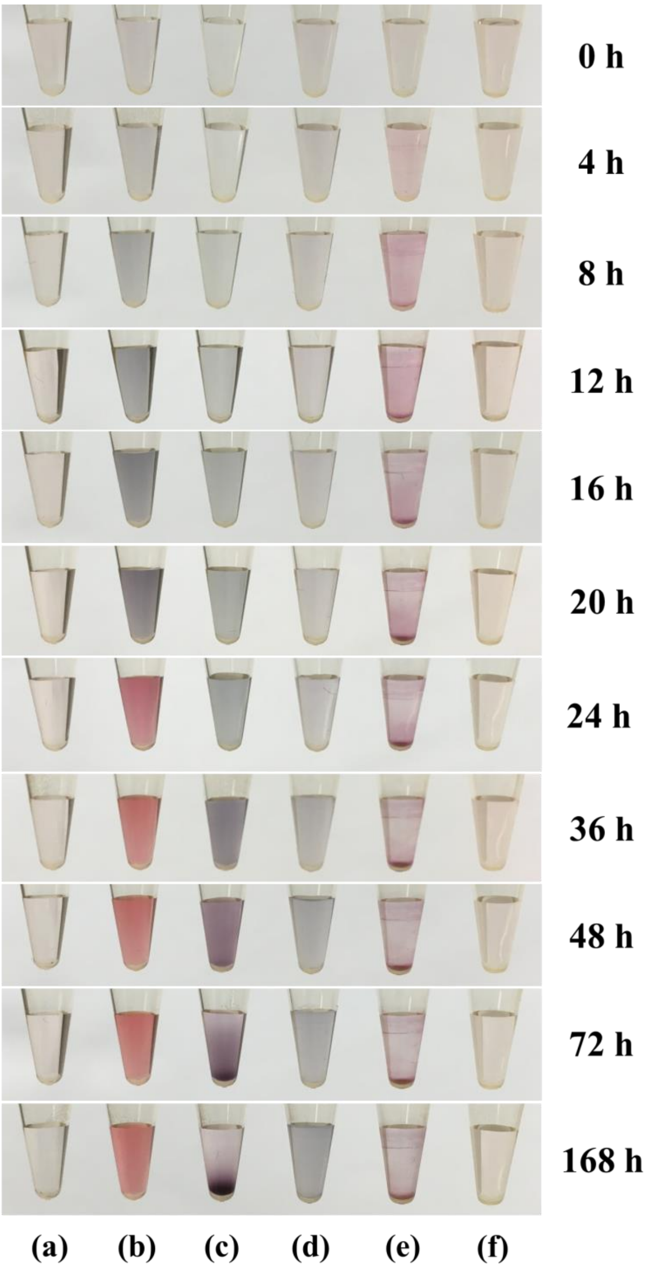

(a) Control: seeds (with Na_3Ct) only
(b) Full recipe: seeds (with Na_3Ct) + growth (KOH+$HAuCl_4$)
(c) No seeds: Na_3Ct + growth (KOH+$HAuCl_4$)
(d) No Na_3Ct: seeds (washed; no Na_3Ct) + growth (KOH+$HAuCl_4$)
(e) No KOH: seeds (with Na_3Ct) + $HAuCl_4$
(f) No $HAuCl_4$: seeds (with Na_3Ct) + KOH

Figure 2.36. Color progression with and without the four starting reactants. Only the second tube (b) with all the components had such red-to-purple/blue-to-red color change.

Concentrations of these four starting reactants were adjusted to examine their effects on the color change and growth process. Figure 2.37 shows that decreasing the seed number caused a delay in the color change time frame while maintaining similar color change profiles as long as seeds presented. Such delay can be explained by the reduced gold surface, which can catalyze the redox reaction between Au(III) and citrate for “glue” formation. A lower number of seeds also corresponded to a lighter grayish blue color, because there were fewer particles for plasmon coupling. Actually, when the seeds concentration is too low, secondary nucleation is also possible [166]. Therefore, similar to the tube with no seeds addition, such *in situ* generation of seeds can also postpone the appearance of purple/blue color.

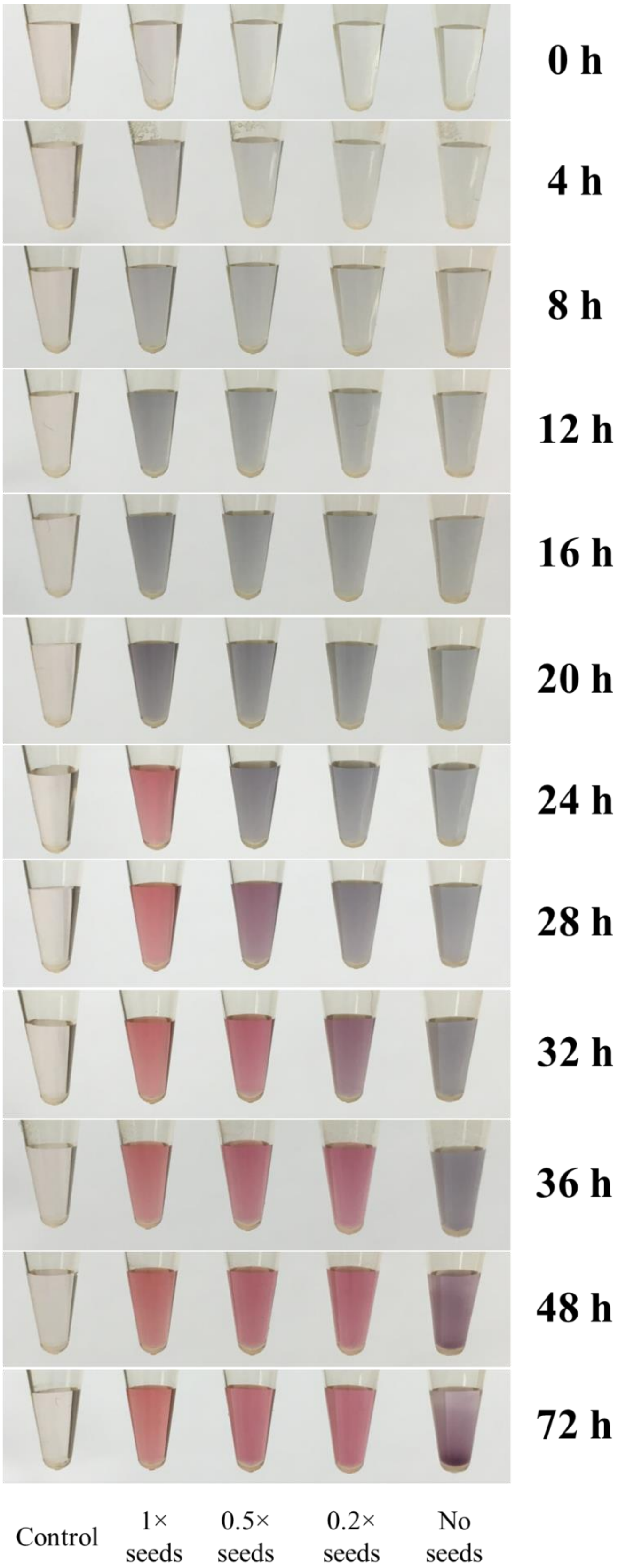
0 h
4 h
8 h
12 h
16 h
20 h
24 h
28 h
32 h
36 h
48 h
72 h
Control
1× seeds
0.5× seeds
0.2× seeds
No seeds

Figure 2.37. Variation of the number of seeds on the color change profile. With decrease in seed number, the color change happened in a longer time frame. When no seeds presented, the dark grayish blue color appeared but the final dispersion was not red and got precipitates (same as Tube (c) in Figure 2.36).

The second key reactant, sodium citrate, is quite special in our studied system. We didn’t introduce any extra Na_3Ct, but the citrate from the 5 nm AuNP seed synthesis was found enough to enable this color change process. Concentration of citrate was varied by adding 0.5× and 1× more of the original amount in the seed solution (increasing R from 0.6 to 0.9 and 1.2), and the color change process was almost identical (Figure 2.38). From the redox reaction point of view, increasing concentration of one reagent should have expedited the kinetics and thus a faster color change process was expected. However, apart from being a reducing agent and capping agent, sodium citrate is also a pH mediator [177]. We will elaborate the pH effect on the color change in the coming set of experiment. For Figure 2.38, the effect from citrate concentration increase was probably offset by the change in accompanying pH.

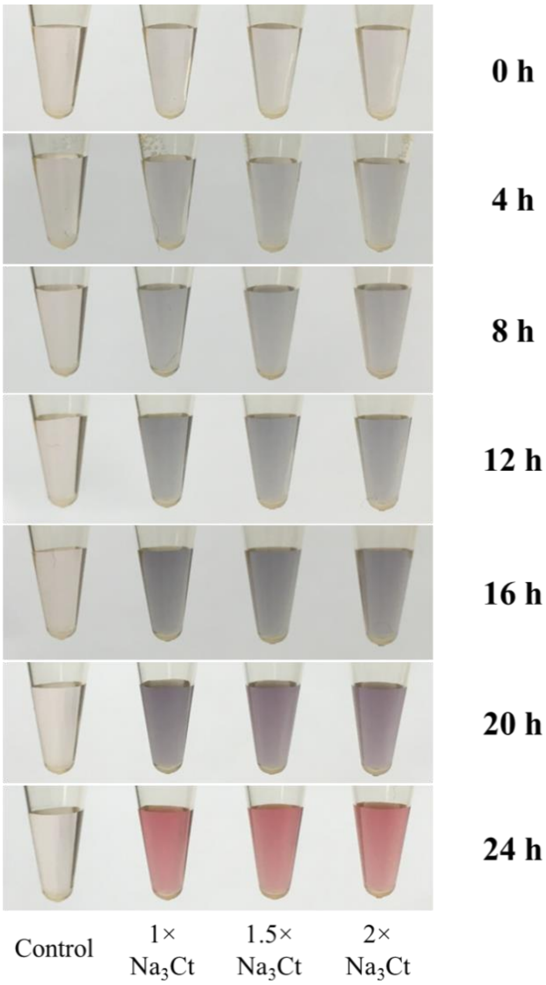

Figure 2.38. Variation of the citrate concentration on the color change profile. Adding extra citrate (thus increasing R) showed almost identical color change profile as the 1× tube.

Amount of added KOH was also varied, and the pH effects were not simply on the time frame of color change (Figure 2.39). When less than 0.8 times of the original KOH was added (pH ~4), no purple/blue color appeared and the reaction progressed fast with some red precipitation, similar to the case when no KOH was added shown in Figure 2.36 Tube (e). However, when more than 2 times of the original KOH (pH ~8) was introduced, no red color appeared, and purple/blue precipitates were formed and attached to the tubes. Only two tubes with 1× (pH ~5) and 1.2× KOH (pH ~6) went through the red-to-purple/blue-to-red color reversal, with the latter one having a much longer color change time frame and less intense intermediate color. The corresponding pH range of the mixture which allows for such color change was found to be roughly 4.5–6.0, similar to the pH range identified in the work by Ji et al. (3.7–6.5) for intermediate purple/blue color appearance in Turkevich method at boiling condition [177].

Another set of experiment with 1× and 1.1× KOH was monitored and the concentration of Au(III) was measured. As can be seed in Figure 2.40, the 1.1× tube (pH ~5.2) experienced a much slower color change than the 1× tube (pH ~5) and took 48 h to complete the whole red-to-purple/blue-to-red color reversal.

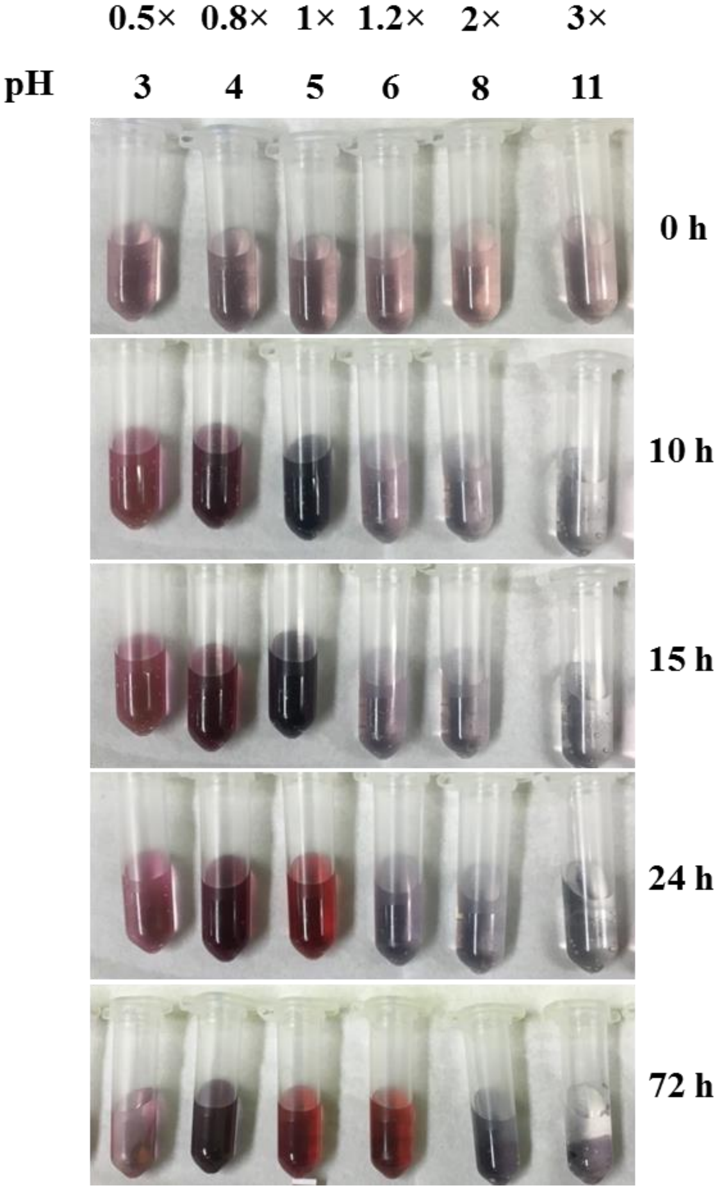

Figure 2.39. Variation of KOH concentration on the color change process. Only the two tubes with 1 × (pH ~5) and 1.2 × (pH ~6) of the original KOH got the color reversal with the final red dispersion.

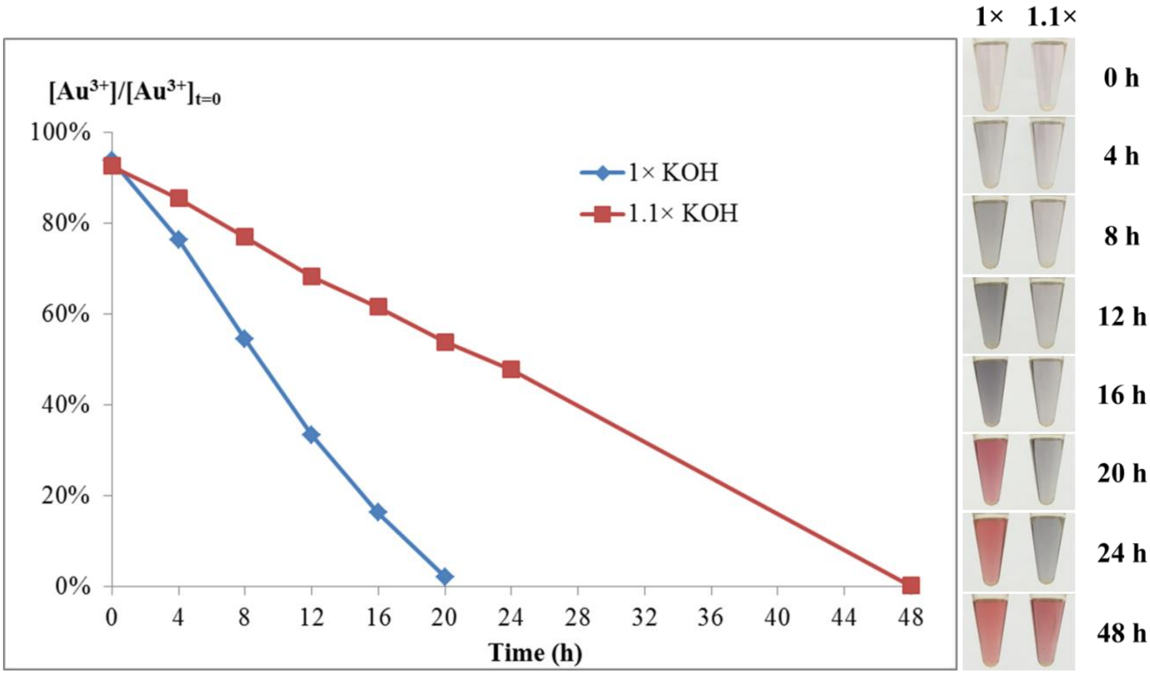

Figure 2.40. Variation of KOH concentration on the color change process. The more alkaline tube (1.1×, pH ~5.2) experienced a much slower color change profile.

For pH smaller than 4.5, the dominant species of Au(III) complex is $AuCl_4^-$ (Figure 2.41), which has the highest reactivity and thus depletes Au(III) rapidly [185, 195], hindering the “glue” formation for the purple/blue coloration. For pH larger than 6.0, $AuCl_4^-$ speciation is almost negligible and more hydroxylated species predominate. Only in the pH region of interest from 4.5–6.0, $AuCl_4^-$ and $[AuCl_3(OH)]^-$ coexist in enough amount for the red-to-purple/blue-to-red color reversal. Thus these two species are important for the “glue” formation and development of reversible chain-like structures in our studied reaction. It’s reasonable to propose here that ***$AuCl_3(OH)^-$ form is the key speciation of Au(III) complex ion in the liquid “glue”.*** Acetone dicarboxylate ions from SAD are mainly in their fully deprotonated form because of their low pKa values below 4 [196]. The $AuCl_4^-$ species ensures enough SAD production for the “glue” formation. Within the pH range of 4.5–6.0, even a minor increase in pH corresponds to slower generation of SAD and therefore the purple/blue color would develop in a longer time frame. This can explain the batch-to-batch variation of the color change under same reaction conditions mentioned in Section 2.2.2 (on p. 88). When pH approaches 6.0, the observed purple/blue color is not as intense, probably associated with the limited SAD production as well. For pH above 6.0, only the hydroxylated species prevails. The production of SAD is even slower and does not favor the reversible chain-like structure formation. The multiple hydroxyl groups might cross-link AuNPs to form irreversible aggregates, giving purple precipitates for the 2 × (pH ~8) and 3 × (pH ~11) tubes in Figure 2.38. The speciation of citrate ions is also pH-dependent and the relevant citrate species in the pH range of interest are in the form of H_2Cit^- and $HCit^{2-}$ [139, 152, 197]. However, changes in the protonation state of citrate have much lower effect on the energetics of the redox reaction than Au(III) complexes [152], therefore the speciation of Au(III) complexes are more emphasized throughout this thesis.

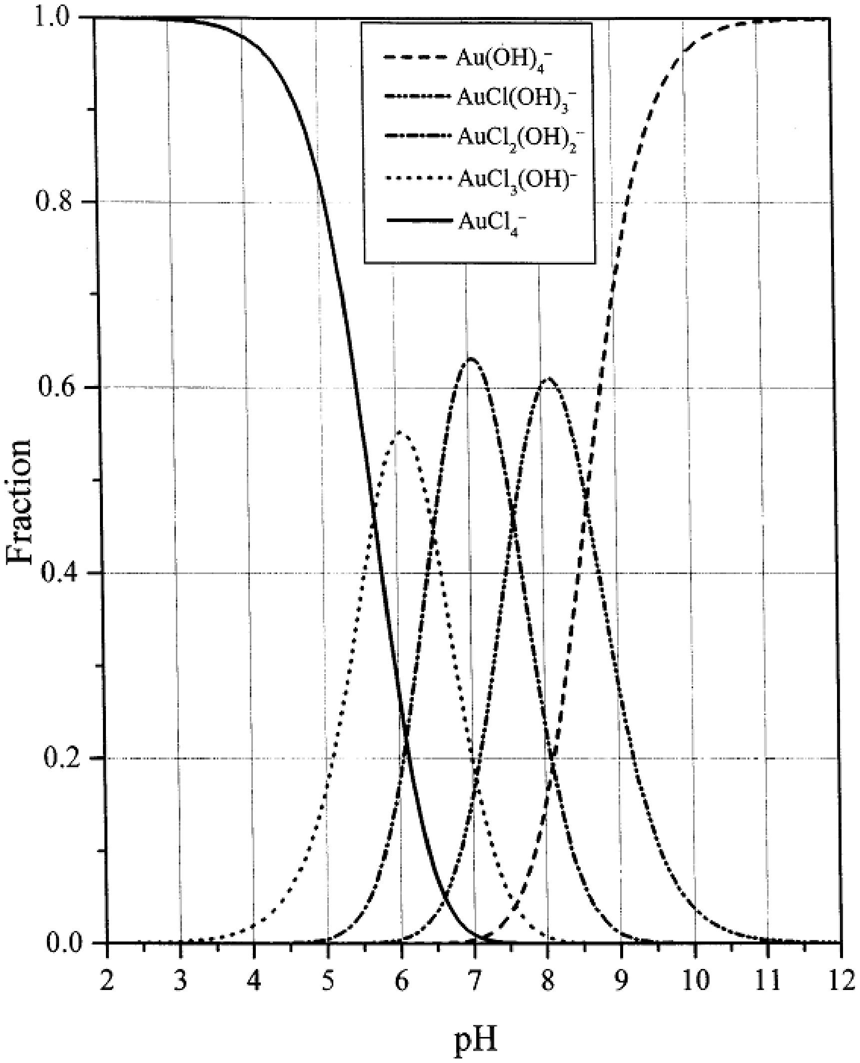

Figure 2.41. The fraction of Au(III) complex ion speciation at different pH values. Adapted from [195].

Replacing KOH with another two pH mediators (K_2CO_3 and $K_4P_2O_7$) but maintaining the pH at ~5 showed similar color changes and similar chain-like structures at the purple/blue state (Figure 2.42). Shown in Figure 2.43, the concentration of K_2CO_3 was varied and similar effects were observed, providing further evidence for the effects of pH. The liquid "glue" composition can be further refined in Figure 2.44.

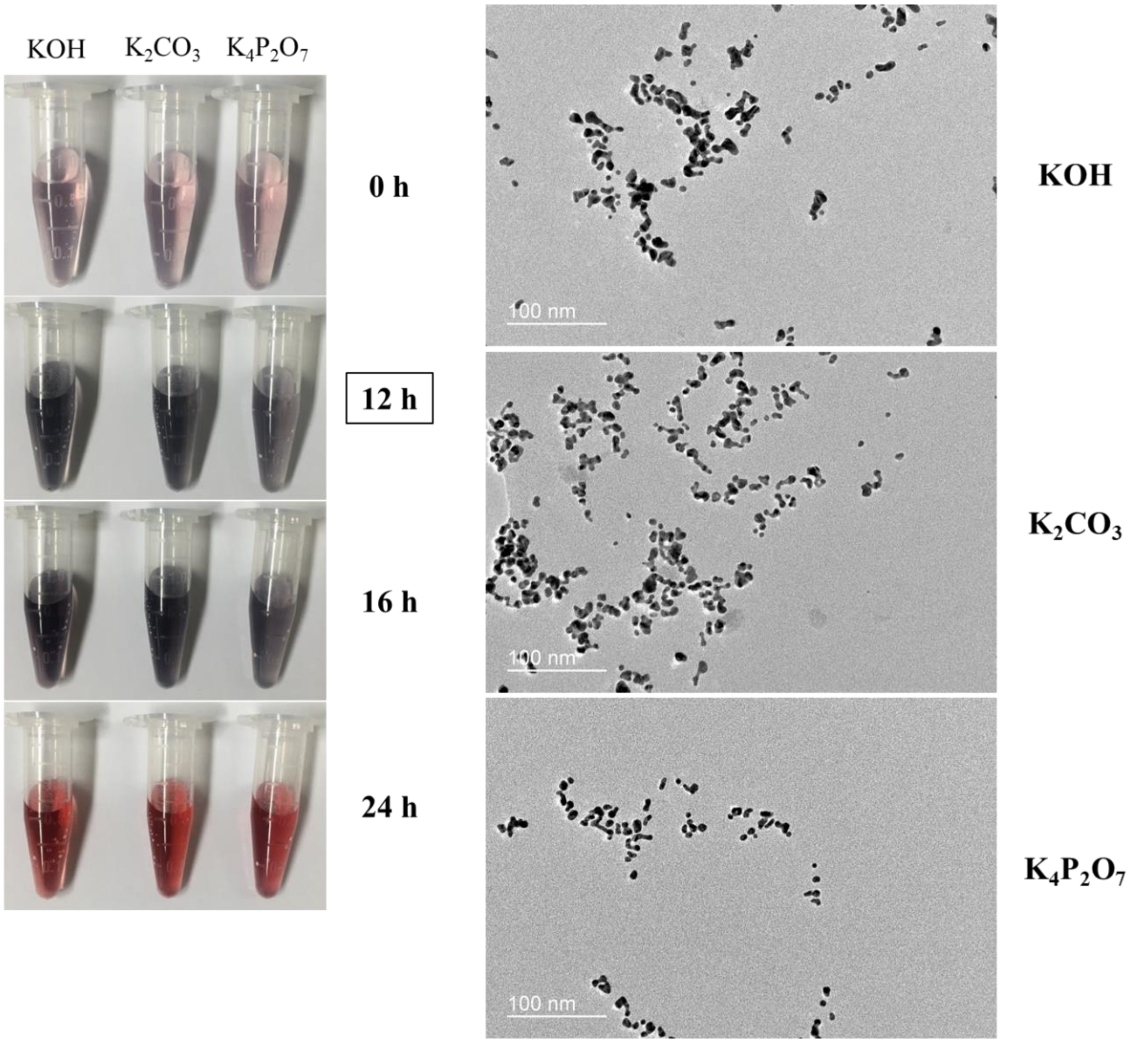

Figure 2.42. Replacing KOH (3.42 mM) with another two pH mediators (K_2CO_3 and $K_4P_2O_7$; both 2.17 mM to achieve pH ~5) yielded similar color change process. The TEM images taken at 12 h show similar chain-like structures at the purple/blue state of the three tubes.

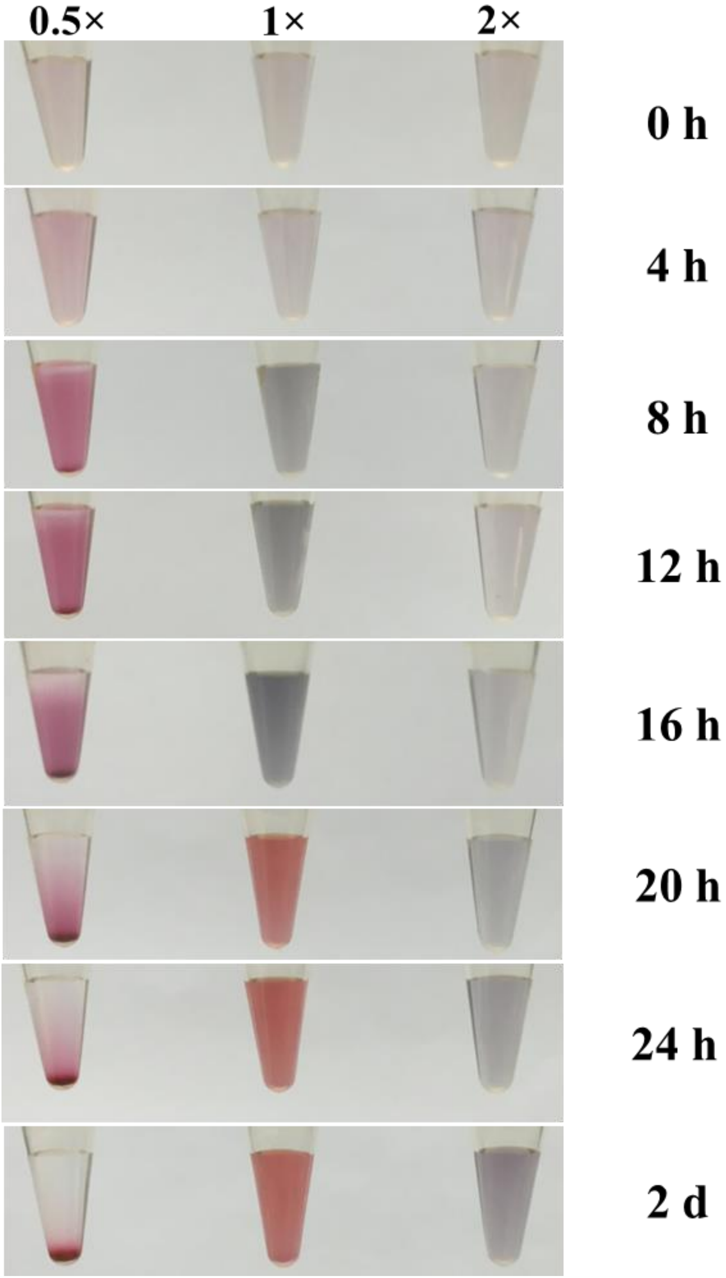

Figure 2.43. Variation of K_2CO_3 concentration on the color change process. The trend is similar to the KOH concentration effect shown in Figure 2.39–40.

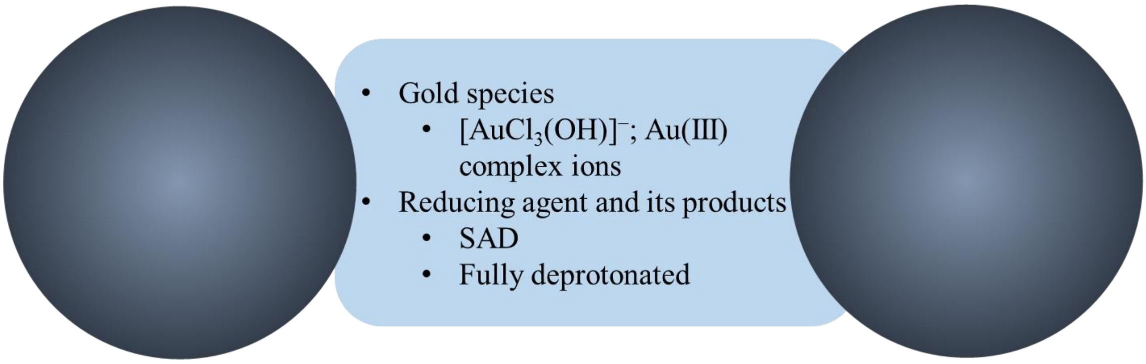

Figure 2.44. Further refined “glue” composition after the discussion of pH effects on the color change.

Higher temperature at 65 ℃ was found able to accelerate the color change process, shortening the time frame from 24 h to 1 h for reaction at pH ~5 (Figure 2.45). This is reasonable considering the increased reaction kinetics. One little observation when examining the temperature effect (data not shown) is that 65 ℃ can shift the pH range with red-to-purple/blue-to-red color reversal to slightly more acid values, approximating 4.0–5.5. This shift can be rationalized by the increased hydroxylation of gold precursor under elevated temperature [180], resembling the effects from increasing pH of the mixture.

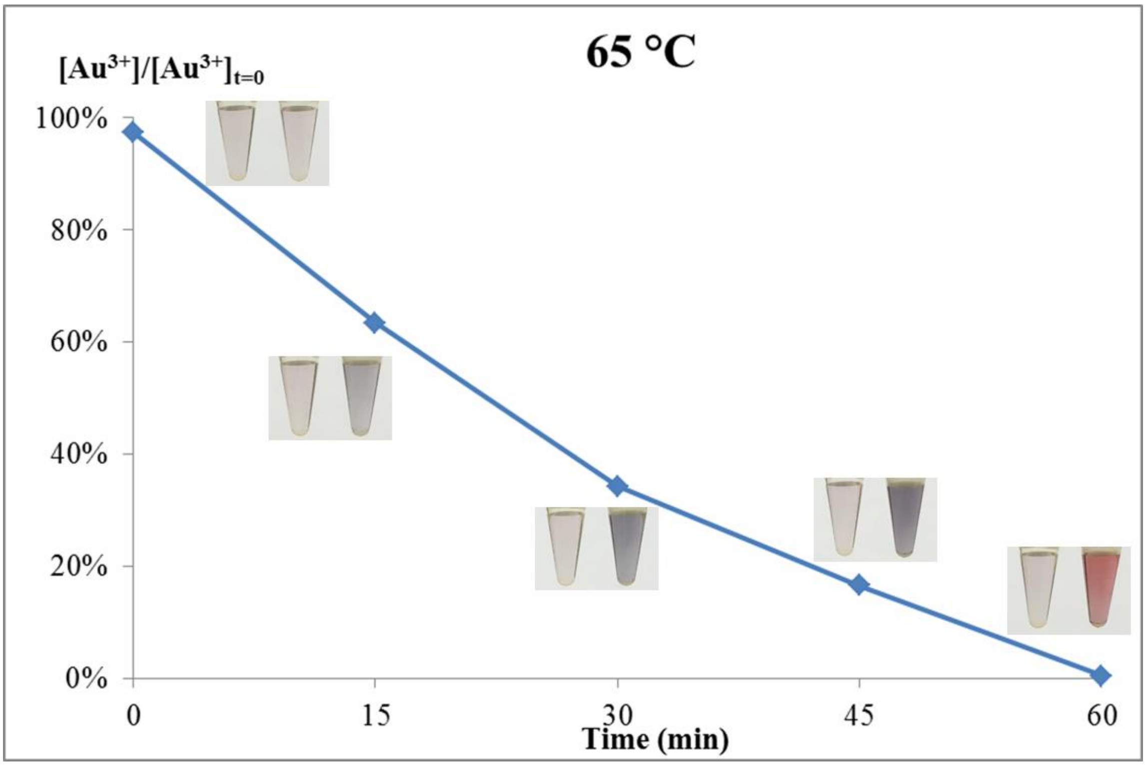

Figure 2.45. Higher temperature at 65 ℃ was found able to accelerate this color change process and complete the whole reaction within 60 min. The color images at each time point were shown with the left tube as control at room temperature.

Concentration of the last key component, gold precursor $HAuCl_4$, was varied at 65 ℃. The $HAuCl_4$ concentrations of 2×, 1× and 0.67× corresponded to R values of 0.3, 0.6 and 0.9, respectively. The pH of this set of experiment was controlled at ~5 for the three tubes to minimize pH effects. Shown in Figure 2.46, with increasing $HAuCl_4$ concentration, the color change process was faster and the intermediate purple/blue color was more intense. Interestingly, the purple/blue-to-red color changes occurred once the relative concentration of Au(III) complex ions reached ~20% and the final red color correlated with full consumption of Au(III) for all the three tubes, further substantiating that Au(III) ions are essential in the liquid "glue" to maintain the chain-like structures thus the purple/blue color as proposed at the beginning of this section. UV–vis absorption spectra were taken for the final red samples (data not shown) and the final sizes were calculated to be 40 nm, 12 nm, and 8.5 nm by Haiss method [191]. The magic ~20% relative amount of added Au(III) indicates that more Au(III) complex ions are needed to maintain the chain-like structures for the 2× sample. This is reasonable because the AuNPs during seed-mediated growth for this sample are larger in size (final size of 40 nm), requiring more "glue" to hold the particles together.

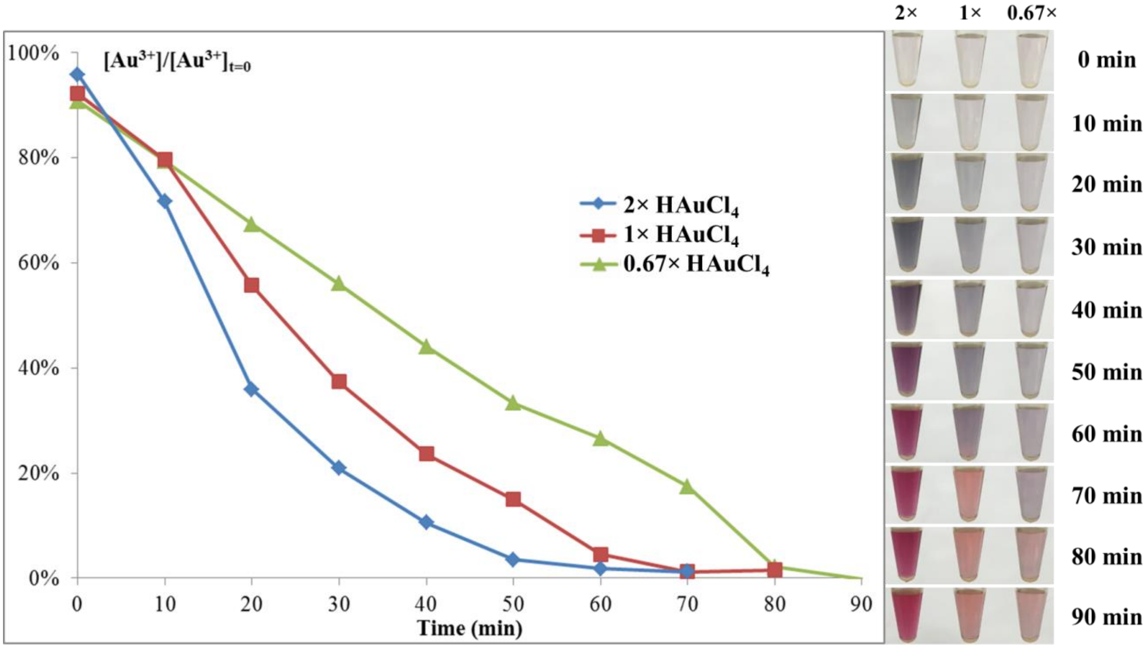

Figure 2.46. Variation of the concentration of added gold precursor $HAuCl_4$ in the growth solution on the color change process. The three tubes shown in the color images (from left to right) corresponded to decreasing concentrations of $HAuCl_4$. With lower concentration of $HAuCl_4$ thus larger R value under the same pH, the color change was slower, consistent with the quantitative curves.

To summarize, the four starting components (5 nm seeds, Na_3Ct, KOH, and $HAuCl_4$) are all necessary to obtain the red-to-purple/blue-to-red color reversal. Higher concentrations of seeds and $HAuCl_4$ can expedite such color change, whereas the concentration effects of Na_3Ct and KOH are more complicated because pH effects are involved. Only within a specific concentration range thus pH range (4.5–6.0) can the color reversal be observed. Within this range, higher KOH concentration thus higher pH, is associated with slower color reversal profile, and the intermediate purple/blue color is less intense when the pH approaches 6.0. Elevating temperature to 65 ℃ and 100 ℃ (data not shown) is also capable of accelerating the color change progress. At pH ~5, the higher the temperature, the faster the color reversal was observed. All these manipulation results are complying with the proposed red-to-purple/blue-to-red color change mechanism in seed-mediated growth of AuNPs.

2.2.4. Manipulation of the growth at purple/blue stage

To further validate and refine the proposed mechanism, the purple/blue stage was manipulated by adding extra KOH (Figure 2.47) and HCl (Figure 2.48–49). A general trend was observed: higher pH could lengthen the purple/blue-to-red time frame, whereas lower pH could speed up such color change. This could also be supported by our proposed mechanism, because at higher pH the redox reaction between Au(III) and reducing agents (e.g., citrate, SAD, and acetone) is slower due to pH-dependent reactivity of Au(III) complex ions, delaying the consumption of Au(III) which is a key component in the “glue”. On the contrary, when pH is lowered by adding acid, Au(III) is converted from its hydroxylated $[AuCl_3(OH)]^-$ form to $AuCl_4^-$. Two things can happen from this. One is fast consumption of Au(III) depleting the “glue”. The other one is direct sabotage of the liquid “glue” by changing the Au(III) speciation. Both scenarios can explain the fast red color appearance within minutes. The relative concentration of Au(III) to growth solution after adding HCl to the purple/blue state (12 h) was measured and displayed in Table 2.1. There were still ~31% Au(III) at 10 min after HCl addition when the dispersion color turned red, supporting the second scenario that the liquid “glue” is sabotaged due to speciation change of the Au(III) complex ions. This can further substantiate the hypothesis that $[AuCl_3(OH)]^-$ is the key speciation in the liquid “glue”.

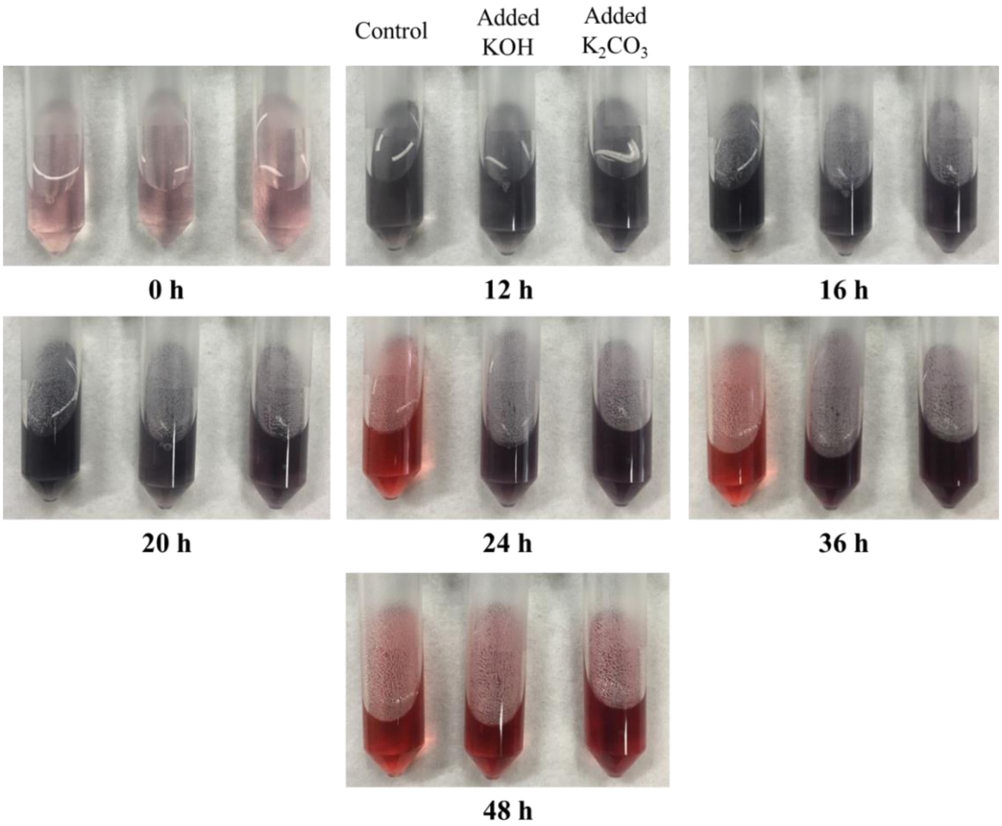

Figure 2.47. Extra KOH (3.42 mM, middle tube) and K_2CO_3 (2.17 mM, right tube) were added to the reaction mixture at the dark grayish blue stage (not the darkest color) at 12 h. The added KOH and K_2CO_3 amount were the same as those in Figure 2.42. This manipulation lengthened the time needed for the final red color to appear.

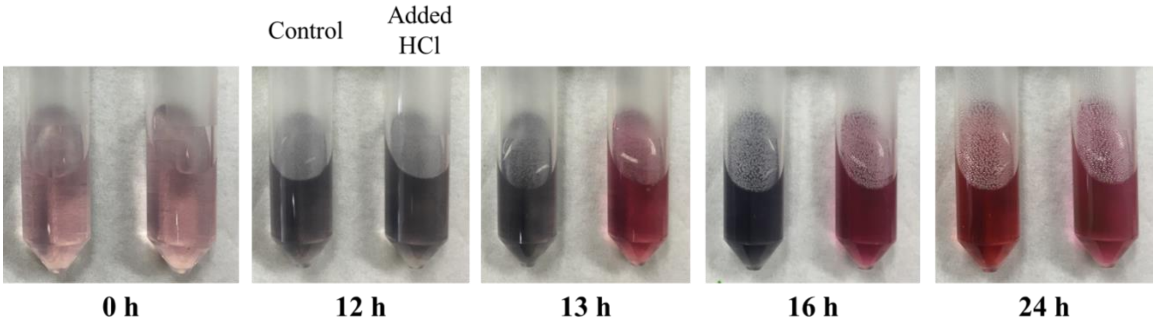

Figure 2.48. HCl (3.42 mM, similar to the KOH case) was added to the reaction mixture at dark grayish blue stage (not the darkest color) at 12 h (right tube). Red color appeared within minutes after adding HCl, which can be inferred from Figure 2.49. This tube got red precipitates at 24 h.

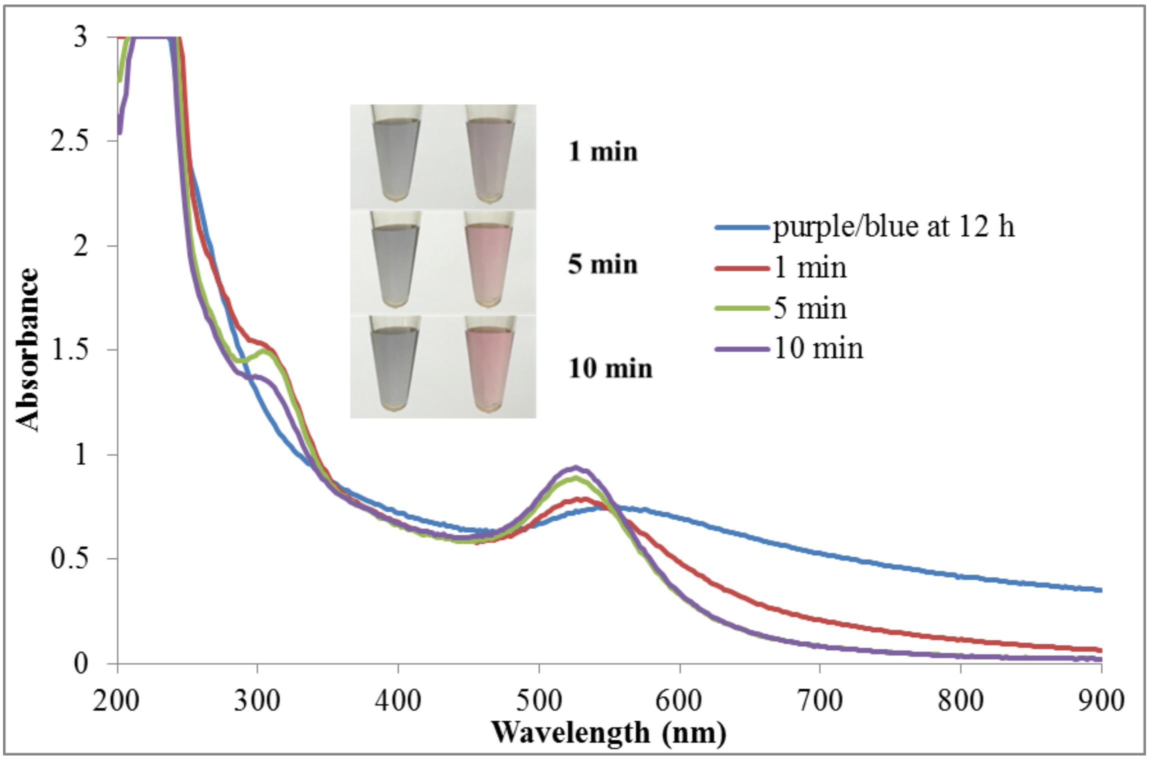

Figure 2.49. UV–vis spectra of the reaction at dark purple/blue state, and right after adding 3.42 mM HCl. The LSPR peak and NIR absorbance changed instantly after adding HCl.

Table 2.1. Quantification of Au(III) concentration (denoted as $[Au^{3+}]$) after adding 3.42 mM HCl to the purple/blue state at 12 h in Figure 2.48–49. $[Au^{3+}]_{t=0}$ represents the added Au(III) amount in the growth solution.

	$[Au^{3+}]/[Au^{3+}]_{t=0}$
Growth solution	100%
0 h	95.4%
12 h	39.6%
1 min after adding HCl	31.8%
5 min after adding HCl	31.8%
10 min after adding HCl	30.9%

To further isolate the structures giving rise to the purple/blue color, centrifugal filtration was employed to the reaction at purple/blue state to get rid of the solution medium. As depicted in Figure 2.50, the absorbance at visible range was lower in value but the LSPR feature was maintained after the filtration, indicating that the structures were well retained without any significant changes. Such little change was also consistent with the similar TEM images between samples with and without centrifugal filtration shown in Section 2.2.2.

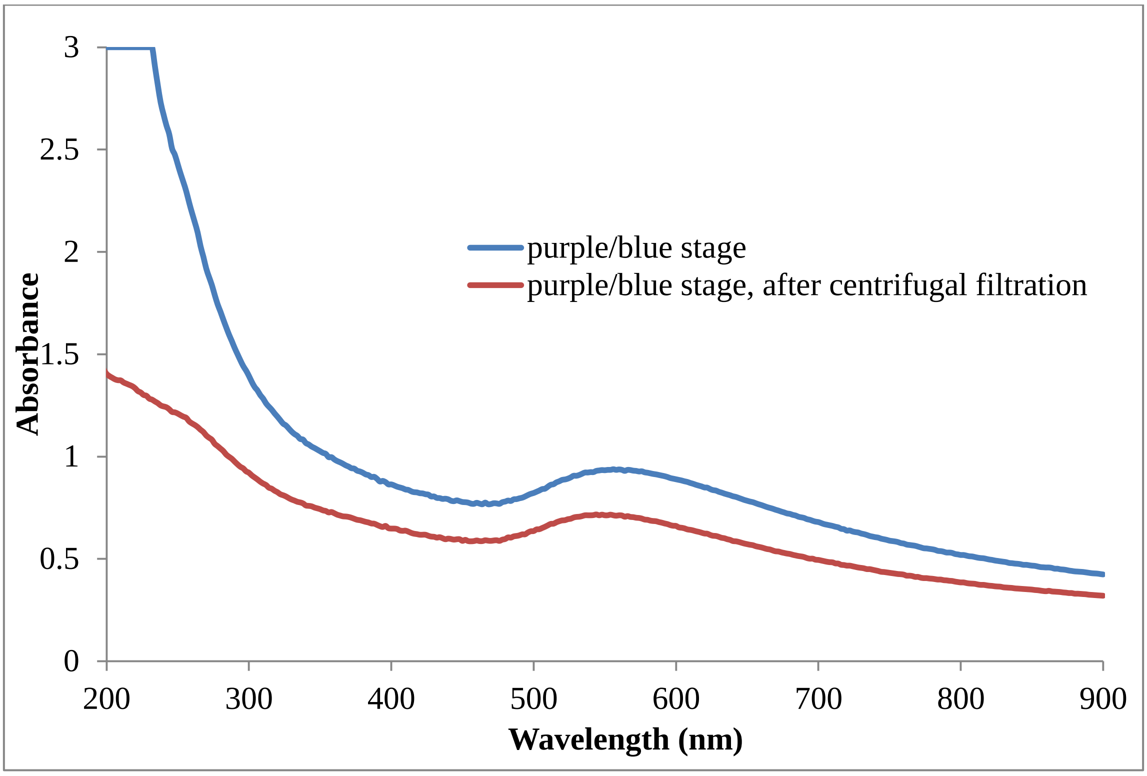

Figure 2.50. UV–vis spectra of the reaction at purple/blue stage before and after centrifugal filtration. The absorbance at visible range after centrifugal filtration was similar but with a lower value likely due to material loss in the procedure.

One important finding from centrifugal filtration is that the purple/blue-to-red color change was not inhibited by depleting the solutes, but progressed even faster with more solutes washed off. Figure 2.51 shows the filtered purple/blue structures at 12 h. The left tube is control without any centrifugal filtration, and the right six tubes were filtered for once (n = 3) and twice (n = 3). Faster color evolution was observed for the Filtration for Twice tubes. The corresponding UV–vis spectra in Figure 2.52 and TEM images in Figure 2.53 are consistent with these color changes, further substantiating that Au(III) may be of utmost importance in maintaining the purple/blue state chain-like structures. Another important insight is, after washing off all the solutes in the medium, the chain-like structures can still evolve to spherical individual AuNPs. This suggests that enough reducing and stabilizing agents (e.g., citrate, SAD, and acetone) exist within the chain-like structures to deplete the Au(III) in the “glue” and readsorb onto the AuNPs to bring them apart to individual particles.

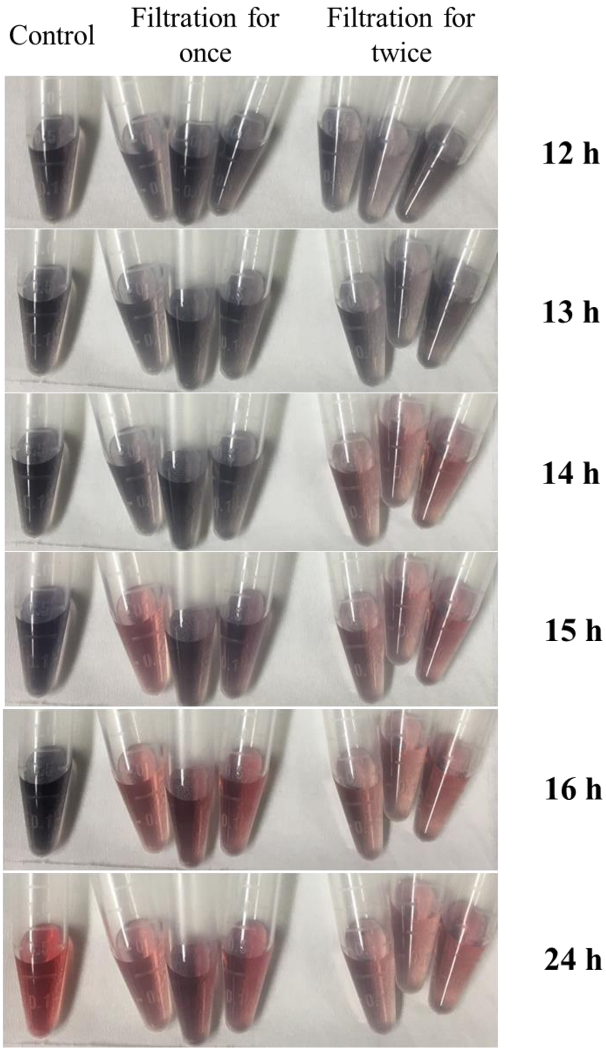

Figure 2.51. Effects of centrifugal filtration on the color change. With more solutes washed off, the purple/blue structures were no longer maintained and red color appeared faster with more rounds of filtration.

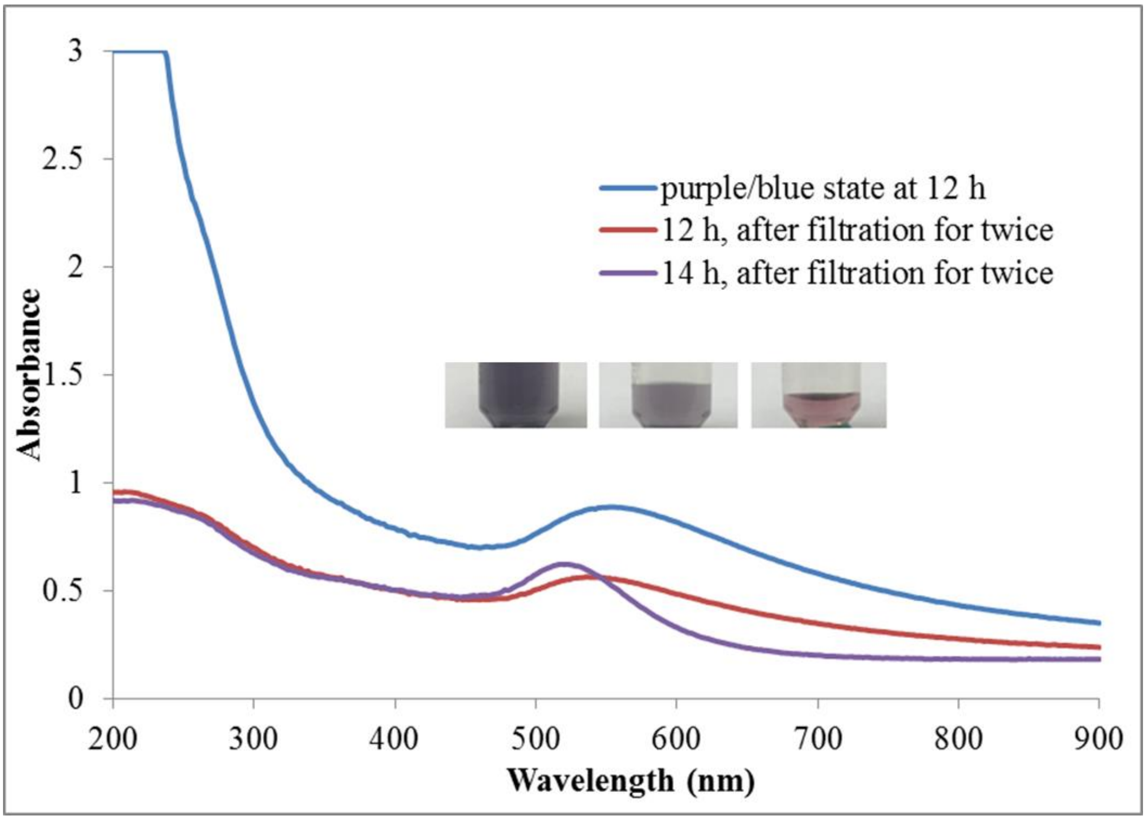

Figure 2.52. UV–vis spectra of the purple/blue state (at 12 h) before and after centrifugal filtration for twice, and 2 h after the filtration. LSPR peak shift and NIR absorbance decrease corresponded with the observed purple/blue-to-red color change after centrifugal filtration.

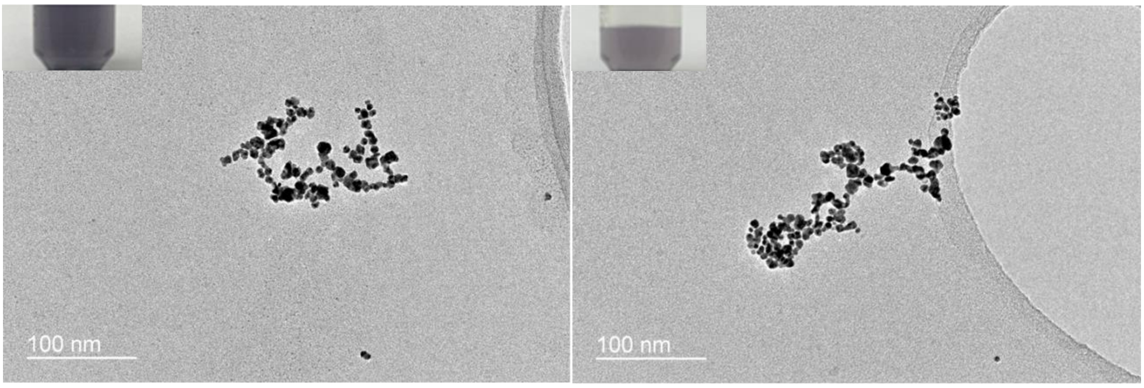

12 h, purple/blue state **12 h, after filtration for twice**

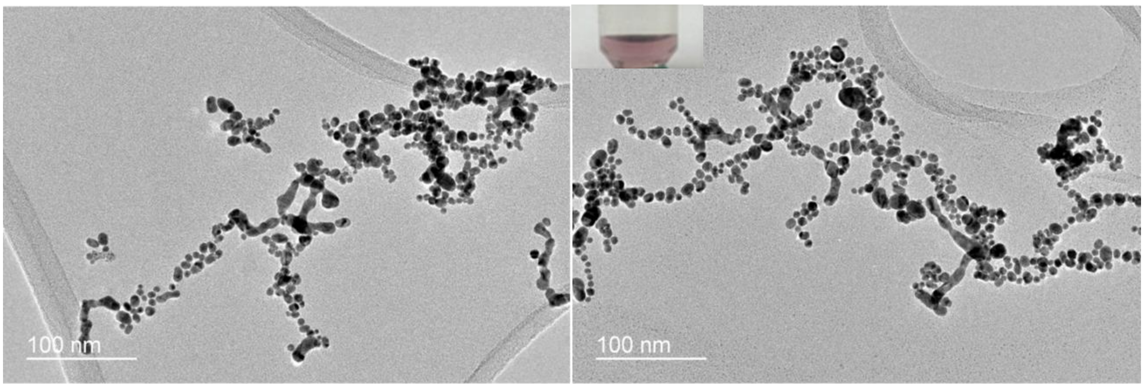

13 h, after filtration for twice **14 h, after filtration for twice**

Figure 2.53. TEM images corresponding to samples in Figure 2.52. At the purple/blue state, chain-like structures were observed. These structures were well retained after centrifugal filtration for twice, and then evolved to dissociate spherical AuNPs. Some larger chain-like or wire-like structures were formed and coexisted with the spherical AuNPs, likely due to the concentration effect during centrifugal filtration.

After centrifugal filtration at purple/blue state and redispersing the concentrate in water for once, the dispersion was put into boiling water and the color changed abruptly to red, as shown in the middle tube of Figure 2.54. Similar trend was observed when HCl was added to the washed purple/blue structures (right tube). The left tube is the control without any manipulation after the centrifugal filtration. These results proved that both heating and lowering pH were able to disrupt the “glue” and thus chain-like structures, due to either increased reduction of Au(III) or changing speciation of Au(III) complex ions within the liquid “glue”.

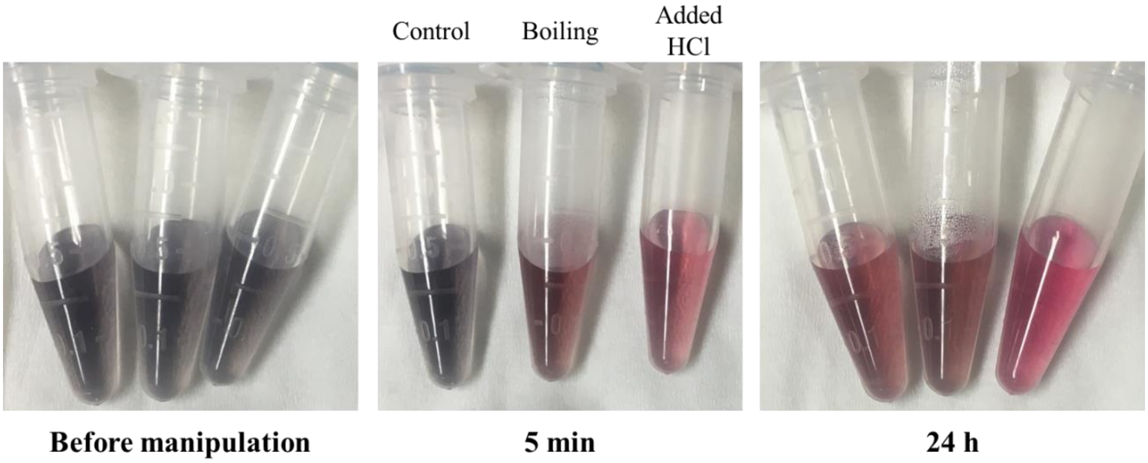

Figure 2.54. Manipulation of the purple/blue structures after centrifugal filtration. The left tube is the control without any manipulation after the centrifugal filtration for once. Both boiling and HCl addition caused the red color appearance immediately.

To summarize on the manipulation findings at the purple/blue state, higher pH delayed the process for red color appearance. Lower pH, however, accelerated the purple/blue-to-red color transition. When the solutes in the medium were depleted, such color change was faster than the tube without any centrifugal filtration. Applying high temperature and adding HCl to the washed purple/blue structures brought even faster color change to the dispersion. Again, these results are supportive of the proposed mechanism.

2.2.5. Proposed mechanism for color reversal in seed-mediated growth of 5 nm AuNPs

Based on all the information from characterizing the growth process and manipulation results, a new mechanism for the red-to-purple/blue-to-red color reversal phenomenon in seed-mediated growth of 5 nm citrate-coated AuNPs (with citrate as reducing agent) is proposed as follows.

Firstly, right after mixing the seeds with the growth solution, the citrate-capped AuNPs would be adsorbed with Au(III) complex ions. The preferential binding of the Au(III) over citrate was well established by previous literatures [171-172]. This ligand exchange would endow an attractive force among the seeds, bringing them in close proximity. Majority of the seeds are discretely located at this stage, probably because of the presence of citrate ions near the particle surface, providing steric/electrostatic stabilization [173].

Secondly, the reducing agent citrate near the surface/in the medium would reduce the Au(III) complex ions to Au(I) complex ions, which would disproportionate to form Au(III) complex ions and gold atoms. These newly produced gold atoms would then attach to the seeds, enlarging the seed particles.

Thirdly, the oxidation product of citrate, SAD, would form a liquid “glue” with Au(III) complex ions (in the form of $[AuCl_3(OH)]^-$). This “glue” can bridge adjacent Au(III)-coated seeds into chain-like configuration, allowing plasmon coupling of the AuNPs and causing LSPR peak red shift and NIR absorbance increase. Such changes in absorbance correspond to the red-to-purple/blue color change. The liquid “glue” instead of solid linkers and the chain configuration can explain the monotonic increase of measured hydrodynamic size and absence of large peaks in DLS results, in accordance with the lack of large structures under SAXS in those literatures introduced in Section 1.3.3 (#4 [149], #8 [179], #9 [181], and #13 [186]). Apart from SAD and Au(III) complex ions, other chemical species involved in this reaction (including citrate, Au(I) complex ions, formic acid, acetic acid, acetone, and other possible intermediate species) can also exist in the chain-like structures, either as less important components in the "glue" or as capping agents on the AuNPs (this is possible with more Au(III) consumed during the growth process, freeing gold surface space for adsorption of other species).

Lastly, with the continuous consumption of Au(III) complex ions, the "glue" will be used up and the chain-like structures can no longer maintain. During this process, the AuNP surface will be mainly coated with other stabilizing ions/molecules (e.g., citrate, SAD, and acetone), which render enough colloidal stability to bring the individual AuNPs apart [172-173]. The breakdown of chain-like structures corresponds to the purple/blue-to-red color change.

Therefore, the red-to-purple/blue-to-red color reversal can be viewed as a dynamic process between formation of chain-like structures (by Au(III) adsorption and liquid "glue" production) and disintegration of chain-like structures (by depletion of liquid "glue" and readsorption of stabilizing species onto AuNP surface). All the manipulation results in Section 2.2.3 and 2.2.4 are affecting this dynamics and thus influencing the color changes.

2.3. Summary

Color reversal in seed-mediated growth of 5 nm citrate-coated AuNPs with citrate as reducing agent is examined and manipulated in this chapter. A mechanism is proposed to explain the observed red-to-purple/blue-to-red color reversal: a dynamic process between formation and disintegration of chain-like structures mediated by liquid “glue”. The key components in the liquid “glue” are SAD and Au(III) complex ions (in the form of [AuCl$_3$(OH)]$^-$). The molecular interactions between them can be briefly hypothesized as shown in Figure 2.55. One possible interaction between SAD and [AuCl$_3$(OH)]$^-$ in the liquid “glue” is drawn based on the molecular mechanism of redox reaction between citrate and Au(III) complex ions, where ligand replacement of one chloride ion in the Au(III) complex by one carboxylate group of citrate is the first step calculated by density function theory [152]. Since the hydroxylation state of Au(III) complex ion is very critical, the other possible interaction between SAD and [AuCl$_3$(OH)]$^-$ can be in the form of hydrogen bond. This can also help explain the less powerfulness of citrate in forming such liquid “glue” because the hydroxyl groups within citrate would likely compete with hydroxyl groups inside [AuCl$_3$(OH)]$^-$ in forming hydrogen bonds.

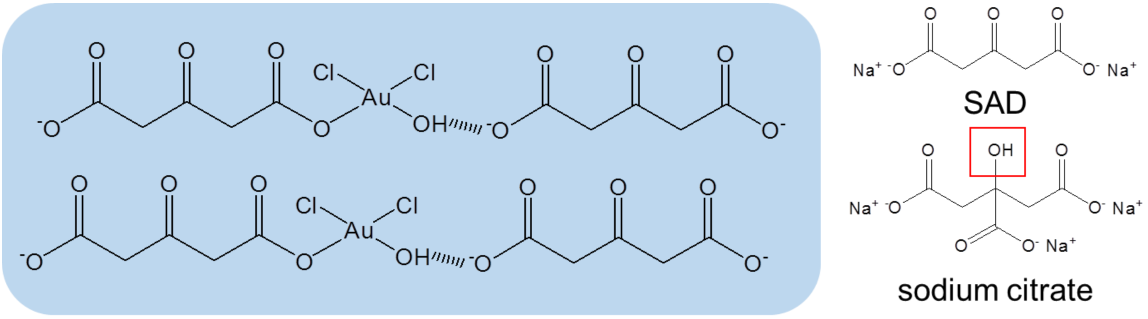

Figure 2.55. Hypothesized molecular interactions between Au(III) complex ions (in the form of [AuCl$_3$(OH)]$^-$) and SAD within the liquid “glue” at the purple/blue stage.

Chapter 3. Color reversal in seed-mediated growth of 13 nm AuNPs

3.1. Materials and methods

3.1.1. Materials and equipment

Hydrochloric acid (HCl), nitric acid (HNO_3), chloroauric acid ($HAuCl_4$, 30% wt. in diluted HCl), sodium citrate tribasic dihydrate ($Na_3C_6H_5O_7\ 2H_2O$), and potassium hydroxide (KOH) were purchased from Sigma-Aldrich (St. Louis, MO, USA). All the chemicals were used as received without any further purification. Amicon® Ultra centrifugal filters (MWCO 10,000) were purchased from Millipore (Burlington, MA, USA). Mill-Q water was used throughout this work.

Centrifugation was performed using Eppendorf 5415 D centrifuge. UV–vis spectra were acquired using Amersham Biosciences UltrospecTM 2100 pro UV/visible spectrophotometer. DLS data were collected by Malvern Panalytical Zetasizer Nano ZS. TEM images were taken by field emission electron microscope (JEM-2100F, JEOL) with 200 kV field emission gun.

3.1.2. Synthesis of 13 nm AuNPs

The synthesis of 13 nm AuNPs is based on Turkevich method, reducing $HAuCl_4$ with $Na_3C_6H_5O_7$, with minor modifications from reported literatures [136-137, 198]. Basically, the glassware and stir bar were washed with freshly prepared aqua regia (concentrated HCl:HNO_3 volume ratio of 3:1). Then 10 µL of 30% $HAuCl_4$ was added to 29.99 mL water, boiled with vigorous stirring and refluxing for 30 mins. Afterwards, 3 mL of 1% $Na_3C_6H_5O_7$ was quickly introduced to the gold precursor. The final concentrations of $HAuCl_4$ and $Na_3C_6H_5O_7$ were 0.48 mM and 3.87 mM (R = 8.03), respectively. The final ruby red color appeared within 5 min of mixing. Then the mixture was cooled to room temperature for characterization and seed-mediated growth, without further purification.

3.1.3. Characterization of synthesized 13 nm AuNPs

Right after synthesis, the as-synthesized 13 nm AuNP dispersion was characterized by UV–vis spectroscopy and DLS. TEM was also performed for direct visualization of the synthesized AuNPs, after drop casting ~100 µL of the dispersion to a carbon-coated copper grid placed on a filter paper.

3.1.4. Preparation of growth solution

The same growth solution was prepared by adding 5.7 mM of KOH to 0.87 mM $HAuCl_4$. The mixture would turn from pale yellow to colorless within minutes, indicating hydroxylation of the gold precursor. This growth solution was left overnight in dark at room temperature before use. The solution pH was ~5.5 after equilibration.

3.1.5. Seed-mediated growth of 13 nm AuNPs

Similarly, the growth solution and the seed solution were mixed with volume ratio of 3:2, giving $[HAuCl_4] = 0.522$ mM, $[Na_3Ct] \approx 1.26$ mM (calculated from 1.5:1 stoichiometry of Na_3Ct: $HAuCl_4$ in the synthesis of 13 nm AuNP seeds), and [KOH] = 3.42 mM in the final mixture ($R \approx 2.4$). The growth process was monitored by UV–vis, DLS, and TEM.

3.2. Results and discussion

3.2.1. Synthesis of 13 nm AuNPs

The UV–vis spectrum of as-synthesized AuNPs is shown in Figure 3.1. The peak absorption wavelength of 520 nm corresponds to the LSPR of the synthesized AuNPs. According to the work by Haiss et al. [191], the diameter of the AuNPs is determined to be ~13 nm, and the concentration is estimated to be ~6.5 nM. DLS data of the AuNPs is shown in Figure 3.2. The hydrodynamic diameter is ~19 nm. TEM images in Figure 3.3 also confirm the successful synthesis of ~13 nm AuNPs.

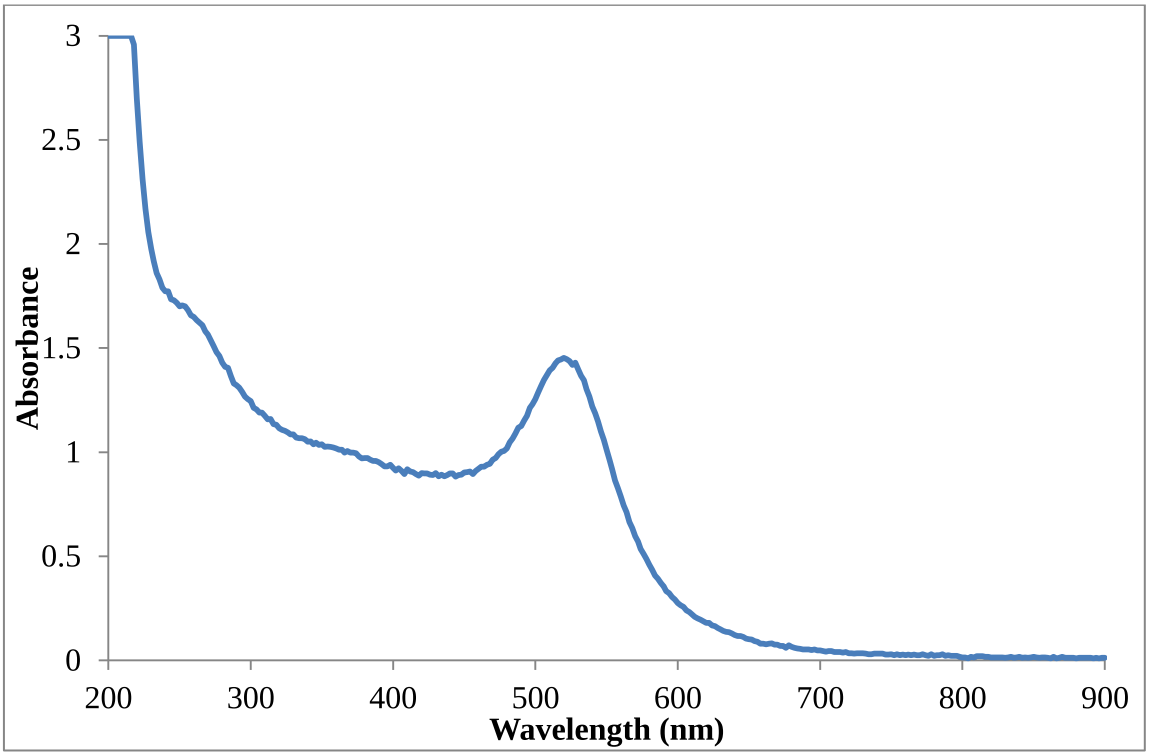

Figure 3.1. UV–vis spectrum of the as-synthesized AuNP solution. The LSPR position is at 520 nm, and A_{spr}/A_{450} ratio of ~1.59 gives particle size of ~13 nm. Concentration of the AuNPs is calculated to be ~6.5 nM form dividing A_{450} by the extinction coefficient at 450 nm of 13 nm AuNPs. The method was well reported by Haiss et al. from [191].

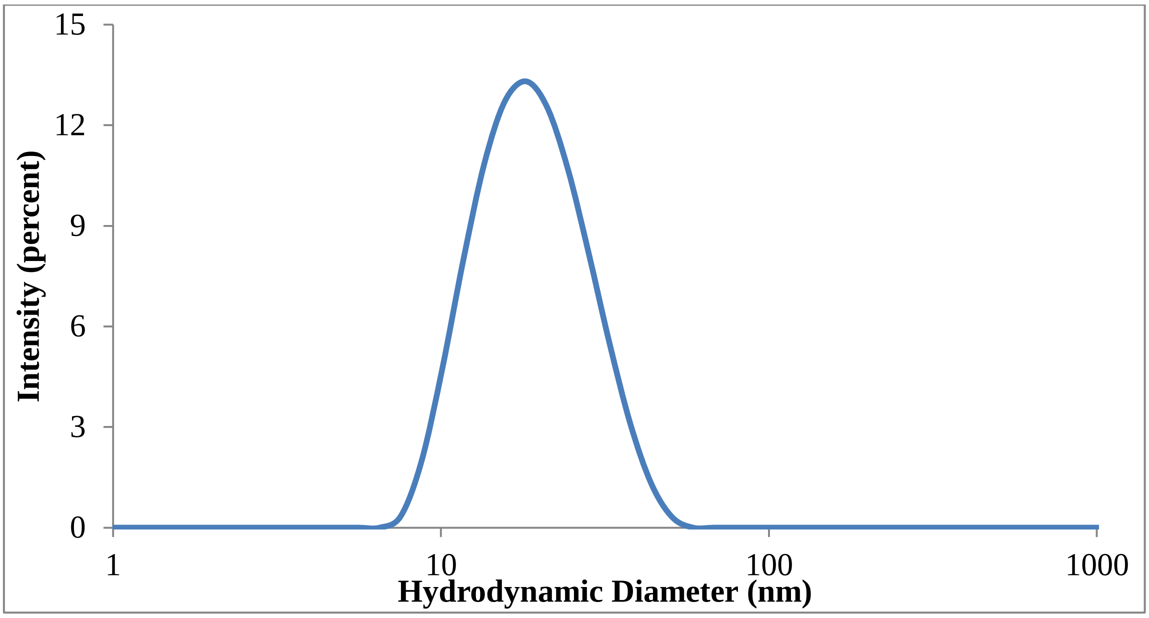

Figure 3.2. DLS curve of the as-synthesized 13 nm AuNP dispersion, showing single peak with average hydrodynamic diameter of ~19 nm.

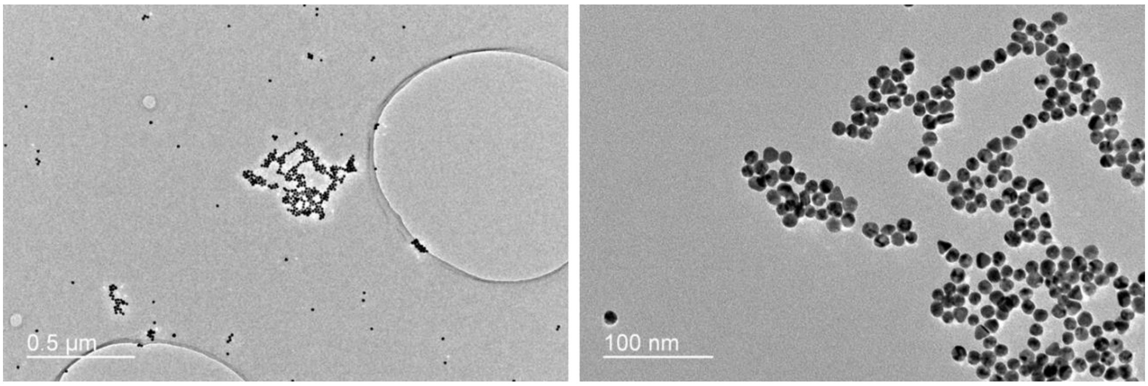

Figure 3.3. TEM images of the synthesized AuNPs. The size is not uniform but is averaged around 13 nm, consistent with the UV–vis calculation.

3.2.2. Seed-mediated growth of 13 nm AuNPs

The growth of the 13 nm citrate-capped AuNPs, after mixing with the same growth solution as in Chapter 2, showed similar red-to-purple/blue-to-red color reversal.

The intermediate purple/blue color was not as intense or blue as the growth of 5 nm AuNPs in previous chapter, but the trend was similar as evidenced from the color images in Figure 3.4 and UV–vis spectra in Figure 3.5. DLS data shows no large structures above 100 nm even in the most purple/blue stage at 10 h, disproving solid aggregates formation. Instead, when the color started turning red at 12 h, a small peak below 1 nm appeared and maintained till the end of color reversal process.

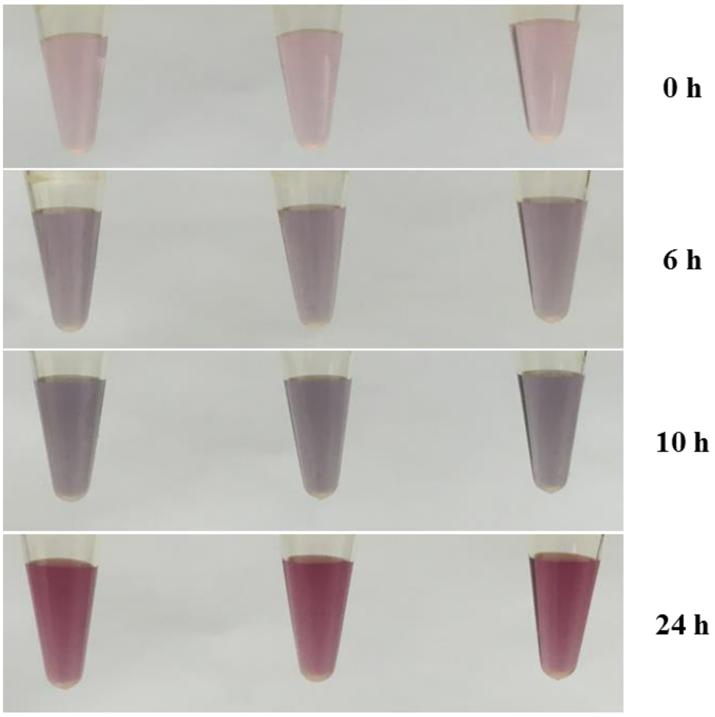

Figure 3.4. Color progression in the growth process of as-synthesized 13 nm citrate-capped AuNPs at room temperature. Even though the mixture had pH ~6, the color reversal was complete within 24 h, in a comparable time frame as the growth of 5 nm AuNPs in Chapter 2 with pH ~5.

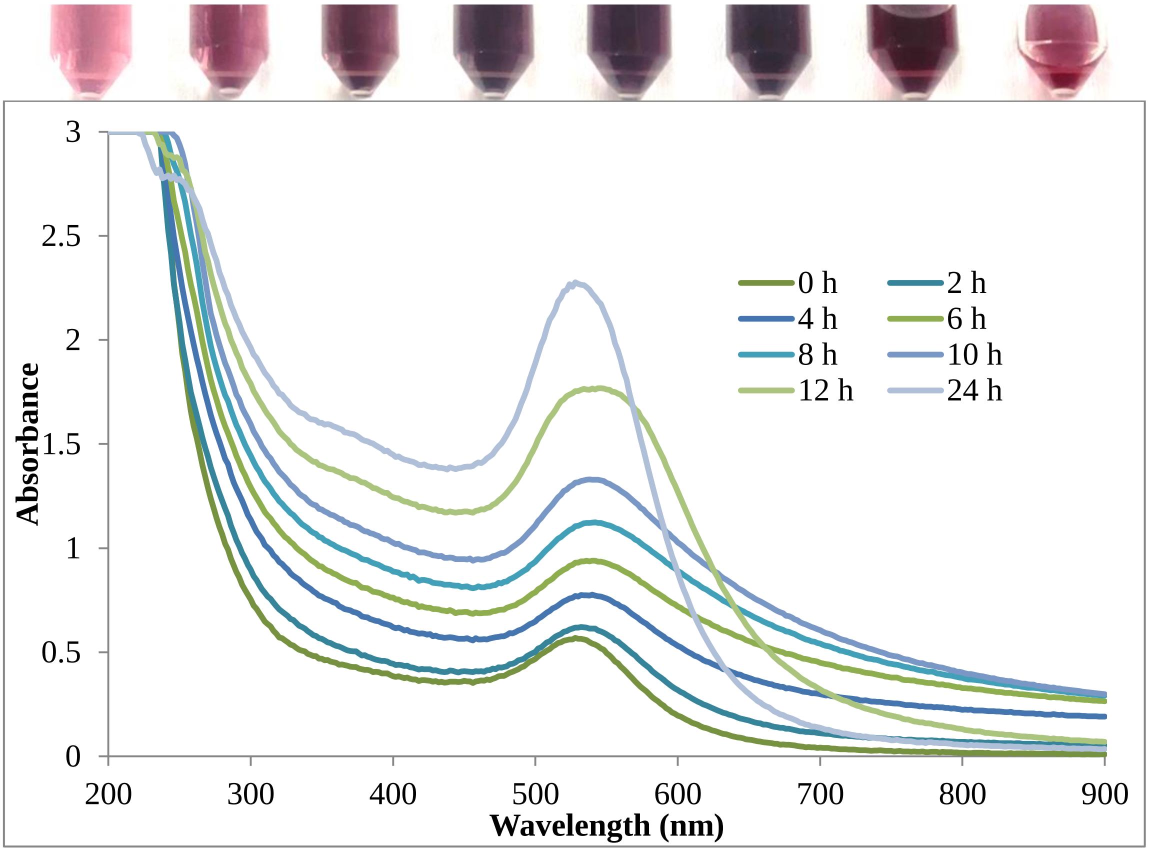

Figure 3.5. UV–vis spectra throughout the growth process of 13 nm AuNPs. A clear red shift and increase in NIR absorption were observed in the first 10 h for this batch. Then the LSPR peak blue shifted and NIR absorption decreased till the color images above turned red.

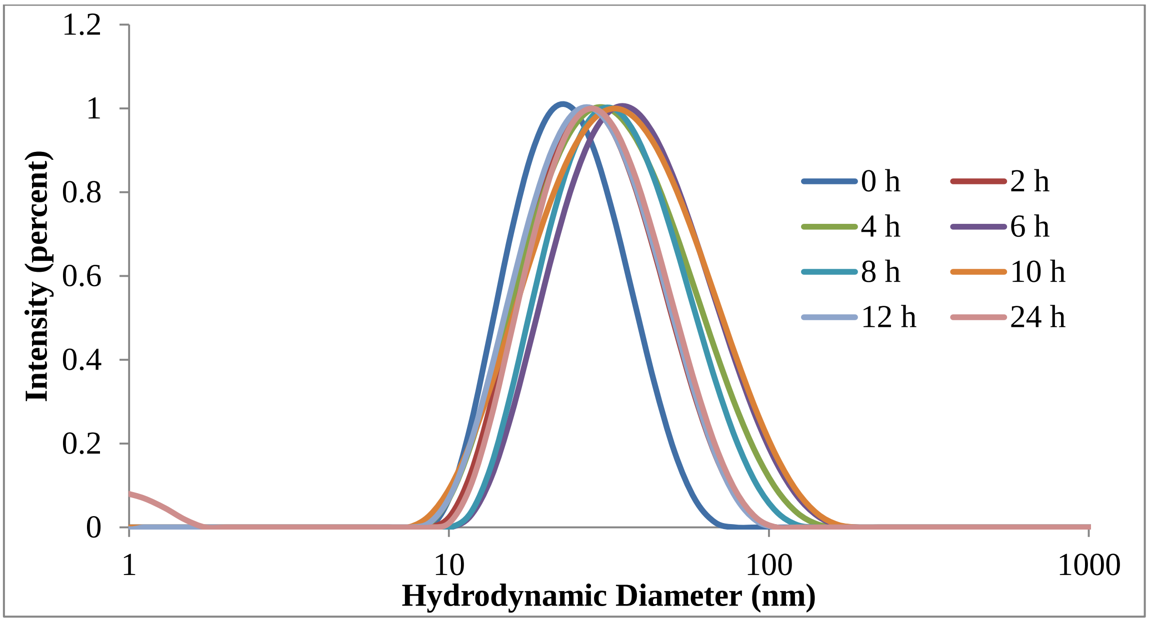

Figure 3.6. DLS curves (normalized) corresponding to Figure 3.5. No large structures observed even at the most purple/blue stage at 10 h.

TEM images were also taken for direct visualization of the nanostructures during growth of the synthesized 13 nm AuNPs. Right after mixing the seeds with the growth solution, fluffy large particles in the range of 50–500 nm coexisted with the 13 nm seeds. The observed large structures are similar to the ones in the growth process of 5 nm AuNPs (Figure 2.9 and 2.12), and are believed to be caused by the gold precursor in the growth solution (Figure 2.17). Depleting the solutes using centrifugal filtration was capable of eliminating those structures (Figure 3.8). The purple stage of the growth of 13 nm AuNPs is also populated with chain-like structures with non-uniform diameter (Figure 3.9), which dissociated to form the final discrete and elliptical AuNPs in Figure 3.10.

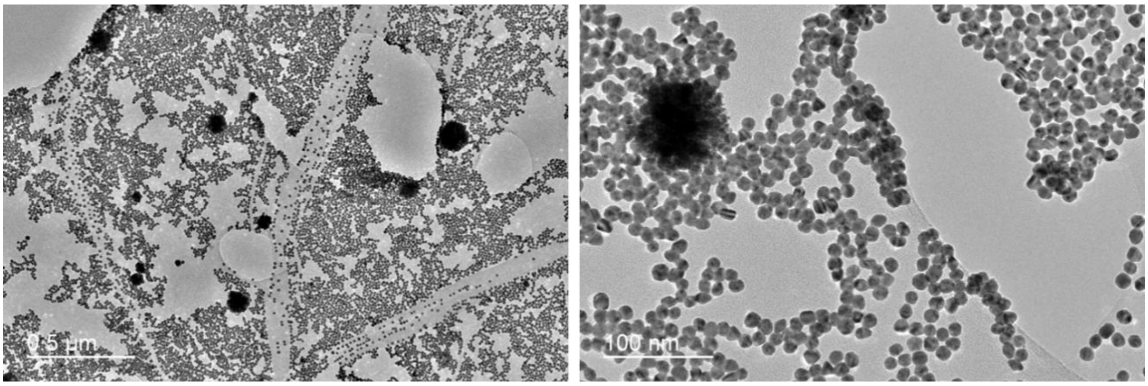

Figure 3.7. TEM images of seed-mediated growth of 13 nm AuNPs, right after mixing seed solution with growth solution. The left image has scale bar of 0.5 µm and the right image has scale bar of 100 nm. Fluffy large particles in the range of 50–500 nm were identified together with the individual seeds.

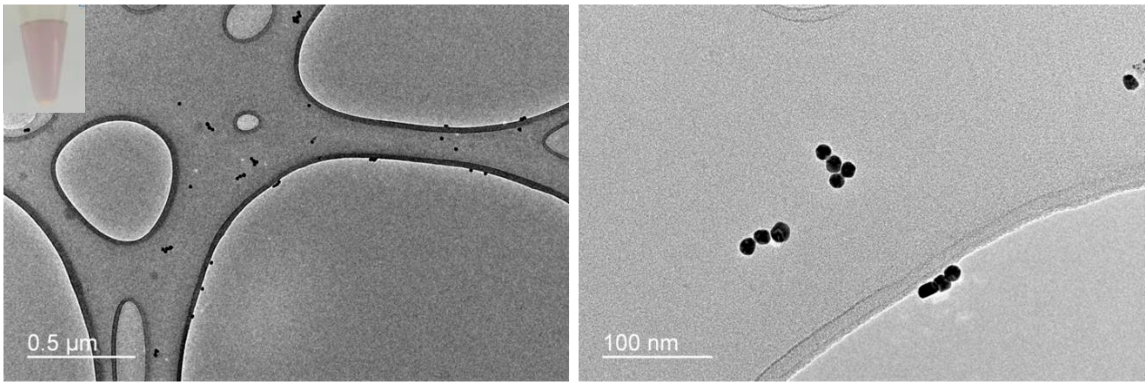

Figure 3.8. TEM images of seed-mediated growth of 13 nm AuNPs, right after mixing seed solution with growth solution. The left image has scale bar of 0.5 µm and the right image has scale bar of 100 nm. This mixture was filtered off the solutes using centrifugal filtration and the concentrate was redispersed in water. Fluffy large particles were not detected.

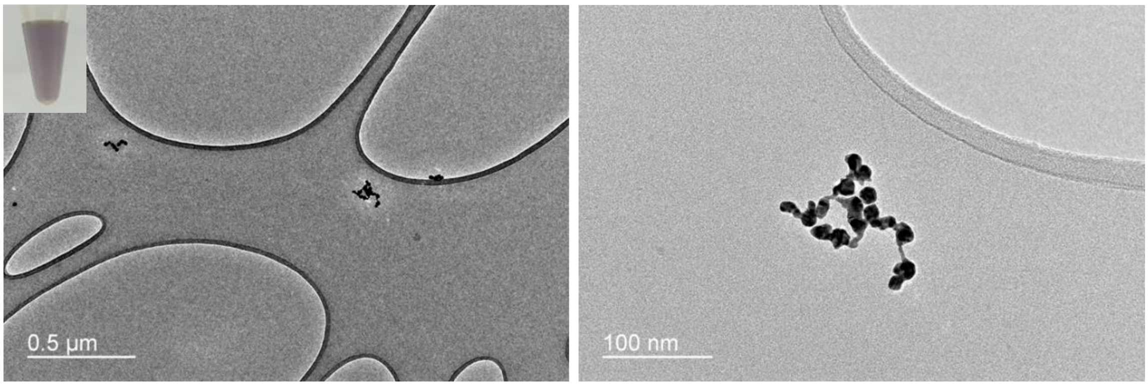

Figure 3.9. TEM images of seed-mediated growth of 13 nm AuNPs, 10 h after mixing seed solution with growth solution. The left image has scale bar of 0.5 μm and the right image has scale bar of 100 nm. This mixture was filtered off the solutes using centrifugal filtration and the concentrate was redispersed in water. Chain-like structures with non-uniform diameter were observed.

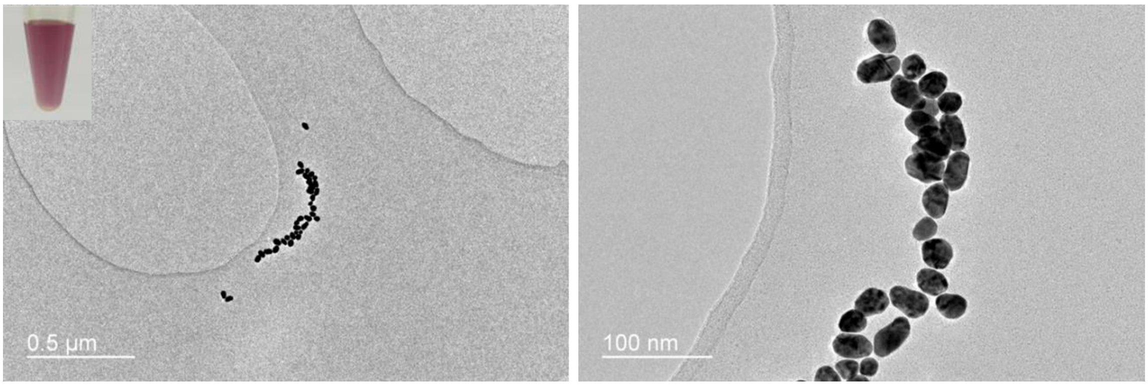

Figure 3.10. TEM images of seed-mediated growth of 13 nm AuNPs, 24 h (final red color) after mixing seed solution with growth solution. The left image has scale bar of 0.5 μm and the right image has scale bar of 100 nm. This mixture was filtered off the solutes using centrifugal filtration and the concentrate was redispersed in water. Most of the particles were discrete but elliptical in shape (different from the final products of 5 nm AuNP growth).

3.3. Summary

Similar to the growth of 5 nm AuNPs, the purple/blue state in the seed-mediated growth of 13 nm AuNPs is also related to the formation and disintegration of chain-like structures. AuNPs interconnected by liquid “glue” is the most appropriate mechanism that can concord all the UV–vis, DLS, and TEM results. The mechanism proposed in Chapter 2 is also applicable to elucidate the growth of 13 nm AuNPs. The elliptical shape of the final particles is interesting but is out of the scope of this thesis. This could result from the readsorbed citrate (from larger R value for this seed-mediated growth as compared to growth in Chapter 2) limiting the intraparticle ripening of the individual particles to more spherical shape under our reaction conditions.

Chapter 4. Color change in Turkevich method

4.1. Materials and methods

4.1.1. Materials and equipment

Chloroauric acid ($HAuCl_4$, 30% wt. in diluted HCl), and sodium citrate tribasic dihydrate ($Na_3C_6H_5O_7 \cdot 2H_2O$) were purchased from Sigma-Aldrich (St. Louis, MO, USA). All the chemicals were used as received without any further purification. Mill-Q water was used throughout this work.

TEM images were taken by field emission electron microscope (JEM-2100F, JEOL) with 200 kV field emission gun.

4.1.2. Turkevich method at boiling temperature

This Turkevich synthesis is the similar to the protocol in Section 3.1.2, reducing $HAuCl_4$ with $Na_3C_6H_5O_7$, with minor modifications from reported literatures [136-137, 198]. Basically, 1.67 μL of 30% $HAuCl_4$ was added to 5 mL water in a centrifugal tube under boiling. Afterwards, 0.5 mL of 1% $Na_3C_6H_5O_7$ was quickly introduced to the gold precursor. The final concentrations of $HAuCl_4$ and $Na_3C_6H_5O_7$ were 0.48 mM and 3.87 mM (R = 8.03), respectively. The final ruby red color appeared within 5 min of mixing in this setup.

Another set of Turkevich synthesis was conducted with concentrations of $HAuCl_4$ and $Na_3C_6H_5O_7$ being 0.48 mM and 1.59 mM (R = 3.29). The final ruby red color appeared within 3 min of mixing and boiling.

4.1.3. Turkevich method at room temperature

This synthesis is similar to the protocol above, but conducted at room temperature instead of boiling. Basically, $HAuCl_4$ and $Na_3C_6H_5O_7$ were mixed with R = 8.03 (pH 5.8) and R = 3.29 (pH 4.2). The final ruby red color appeared within 12 h and 2 h after mixing for the two R ratios, respectively.

4.1.4. Characterization of Turkevich method at room temperature

TEM was performed for direct visualization of the structures responsible for the color change in Turkevich method conducted at room temperature, after drop casting ~100 µL of the dispersion to a carbon-coated copper grid placed on a filter paper.

4.2. Results and discussion

4.2.1. Color change in Turkevich method at boiling temperature

The color images of Turkevich syntheses at boiling temperature with two R values are shown in Figure 4.1. After the mixtures of Na_3Ct and $HAuCl_4$ were put into the boiling water bath, the R = 8.03 tube went through gradual color change with a light purple/blue phase. On the other hand, for the R = 3.29 tube, a distinct dark grayish blue stage was observed at 2.5 min. It took less time for the final red color to appear for the low R tube, probably stemming from the higher reactivity of gold precursors at lower pH condition [185, 195].

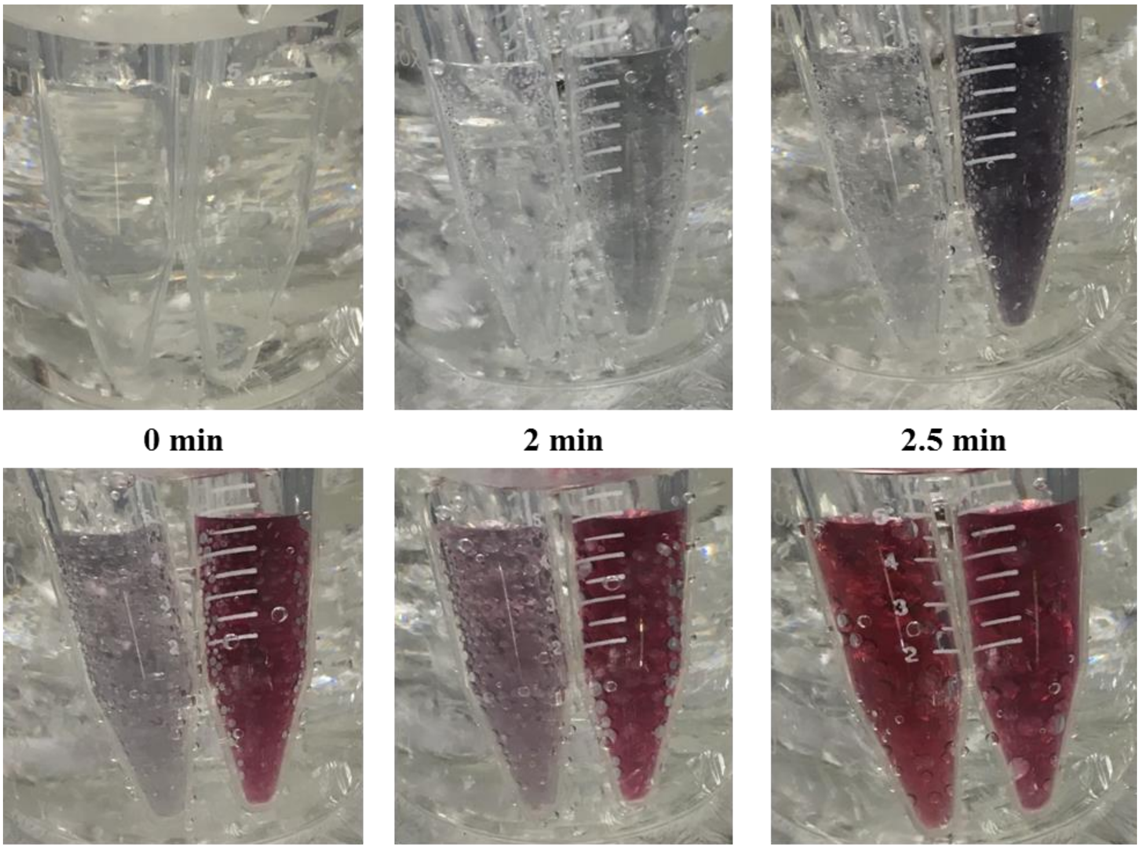

0 min 2 min 2.5 min

3 min 4 min 5 min

Figure 4.1. Turkevich syntheses of AuNPs under boiling conditions. The left tube has R value of 8.03 (pH 5.8 measured at room temperature) and the right tube has R value of 3.29 (pH 4.2 measured at room temperature).

4.2.2. Color change in Turkevich method at room temperature

The color images of Turkevich syntheses at room temperature with the two R values are shown in Figure 4.2. Different from the boiling case, the R = 8.03 (pH 5.8) tube got the dark grayish blue stage, whereas the R = 3.29 (pH 4.2) tube only experienced a light purple/blue color before the final red color appeared. Similar to the boiling condition, the R = 3.29 tube had faster reaction, evidenced from the faster red color appearance than the R = 8.03 tube on the left. Since the R = 8.03 tube has pH value of 5.8, the speciation of gold precursor ($AuCl_4^-$ and $[AuCl_3(OH)]^-$) at this pH [185, 195] and the associated SAD production may explain the dark color appearance at room temperature as the case for the seed-mediated growth of 5 nm and 13 nm AuNPs. The standard Turkevich synthesis has similar R value at 7.63, but conducted at elevated temperature [136]. The lack of such dark coloration at high temperature may be attributed to the increased hydroxylation of gold precursor [180]. This can also explain the dark color observed for R = 3.29 (pH 4.2) at high temperature. Increasing the temperature has similar effects as shifting the pH to a higher value. To provide further evidence that the proposed mechanism in Chapter 2 may be related to the commonly adopted Turkevich method for AuNP synthesis, TEM images were taken on the 0 min, 3 h, and 12 h samples aliquoted from the R = 8.03 tube (Figure 4.3–5). The chain-like structures for the 3 h sample (dark grayish blue) are similar to the chain-like structures observed before, especially the purple/blue stage of seed-mediated growth of 13 nm AuNPs in Figure 3.9. The final red dispersion also has similar elliptical AuNPs as the final product of seed-mediated growth of 13 nm AuNPs in Figure 3.10, but different from the final product at elevated temperature with the same reagent concentrations in Figure 3.3. The spherical shape at elevated temperature may be attributed to the promoted intraparticle ripening with increasing temperature.

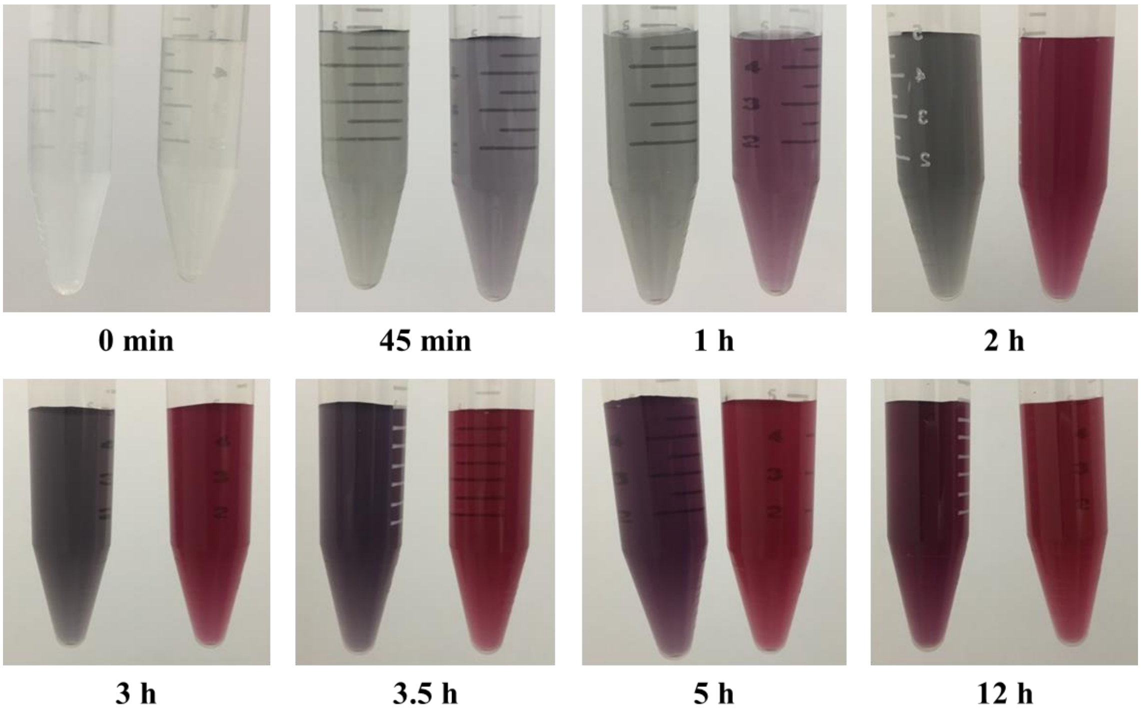

Figure 4.2. Turkevich syntheses of AuNPs under room temperature. The left tube had R value of 8.03 (pH 5.8) and the right tube had R value of 3.29 (pH 4.2).

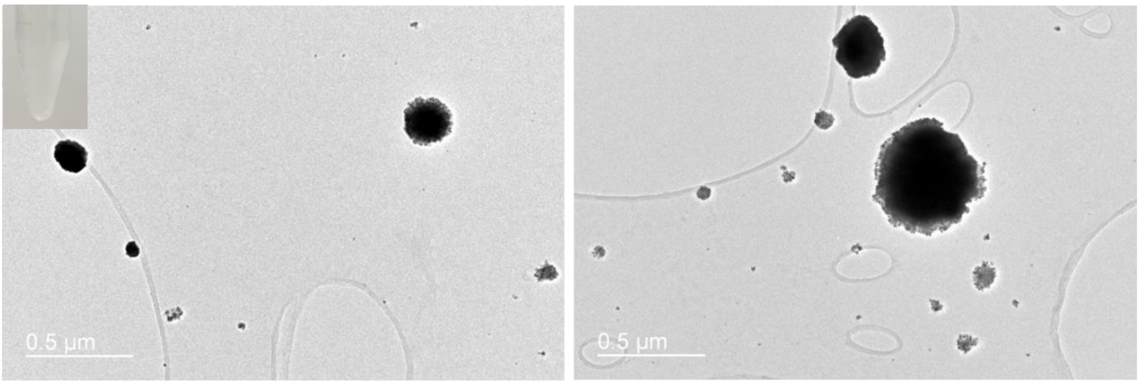

Figure 4.3. TEM images of Turkevich synthesis of AuNPs, right after mixing citrate with gold precursor (R = 8.03; pH 5.8; room temperature). Both images have the same scale bar of 0.5 μm. Large structures in the range of 50–500 nm were identified, similar to the structures observed for the growth solution in Figure 2.17.

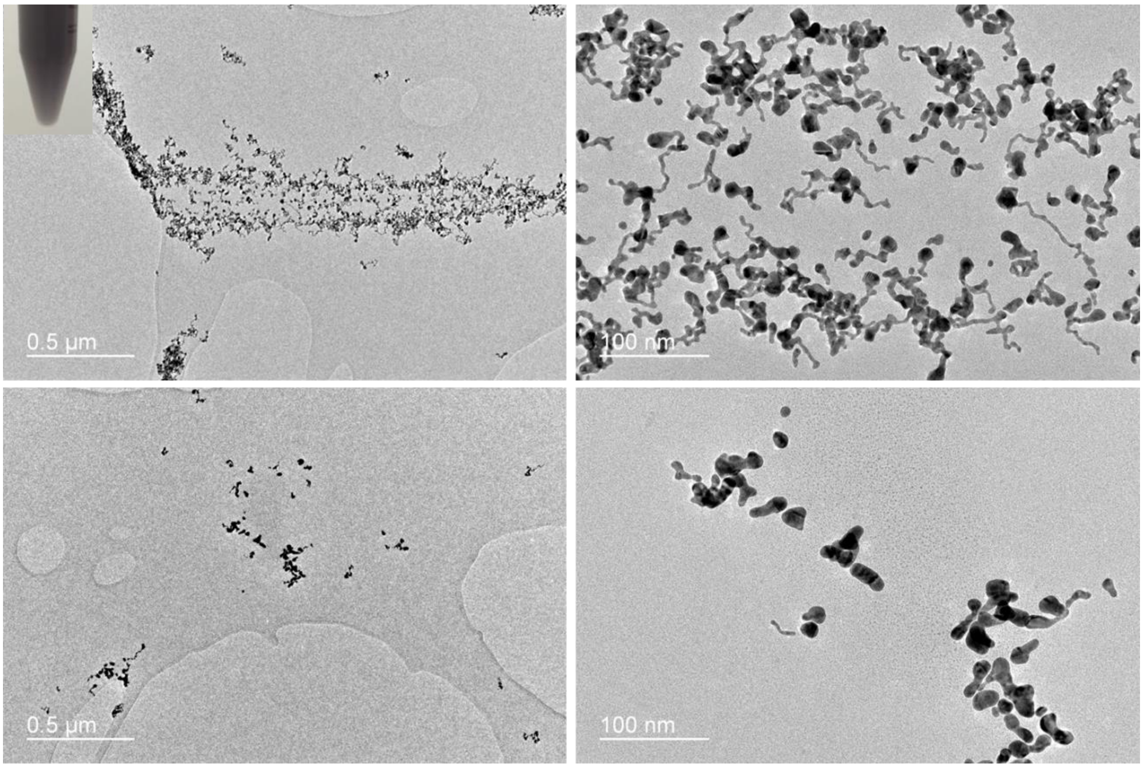

Figure 4.4. TEM images of Turkevich synthesis of AuNPs, 3 h after mixing citrate with gold pre cursor (R = 8.03; pH 5.8; room temperature). The left images have the same scale bar of 0.5 µm and the right images have the same scale bar of 100 nm. Chain-like structures with non-uniform diameter were observed.

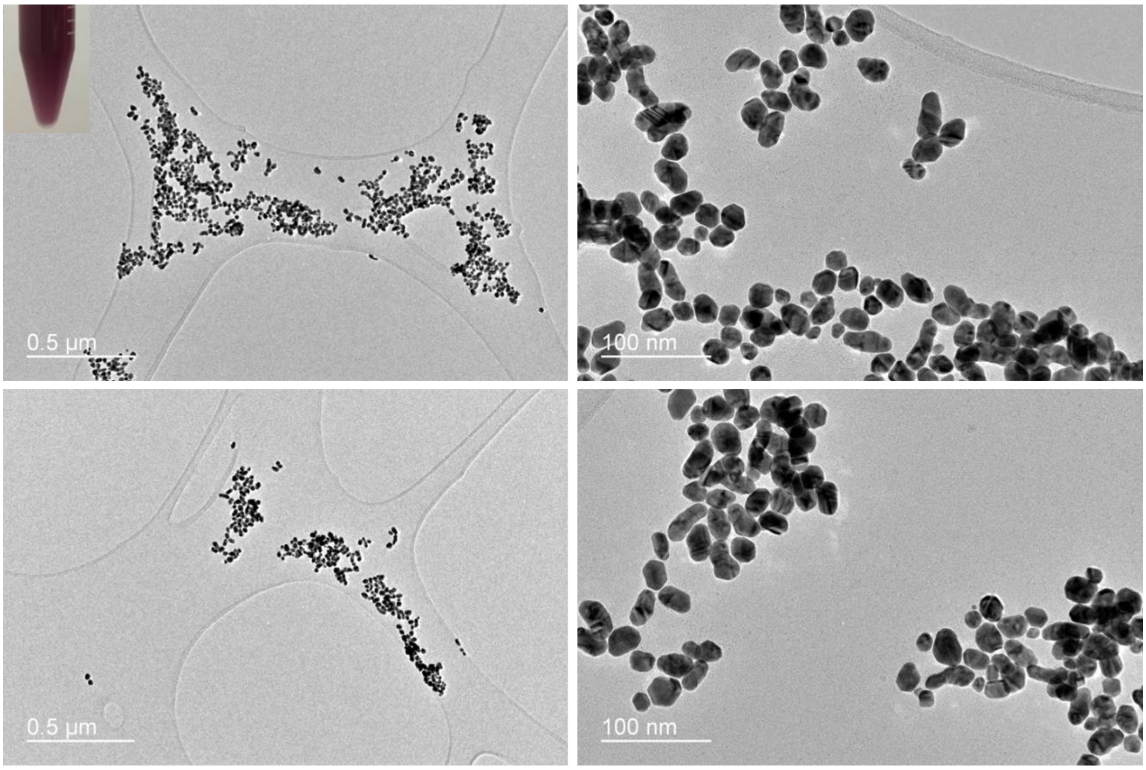

Figure 4.5. TEM images of Turkevich synthesis of AuNPs, 12 h after mixing citrate with gold precursor (R = 8.03; pH 5.8; room temperature). The left images have the same scale bar of 0.5 µm and the right images have the same scale bar of 100 nm. Most of the particles were discrete but elliptical in shape (similar to the final products of seed-mediated growth of 13 nm AuNPs).

4.3. Summary

Similar to the seed-mediated growth of 5 nm and 13 nm AuNPs, the purple/blue stage in the Turkevich method (both at elevated temperature and at room temperature) can also be explained by the proposed mechanism in Chapter 2. Without added seeds, the first step involved in the Turkevich method could be the formation of seeds *in situ* from Na_3Ct reduction of $HAuCl_4$, which are then adsorbed with Au(III) precursor. The subsequent events can be illustrated by the mechanism with particle growth, particle interaction with each other to form chain-like structures mediated by liquid “glue” from SAD and $[AuCl_3(OH)]^-$, and disintegration of the chains by “glue” depletion.

Conclusions

A mechanism on the red-to-purple/blue-to-red color reversal in the seed-mediated growth of AuNPs (with citrate as reducing agent) was proposed as formation and disintegration of chain-like structures formed from AuNPs mediated by some liquid "glue" (with key components of Au(III) complex ions and SAD). After adding growth solution to the AuNPs, the following events take place: (a) Au(III) complex ions adsorb more preferentially onto the seeds than citrate ions, bringing AuNPs in close proximity; (b) citrate converts Au(III) complex ions to Au(I) complex ions, which disproportionate to form Au(III) complex ions and gold atoms, enlarging the AuNP size; (c) at the same time, SAD is produced as the oxidation product of citrate, forming a liquid "glue" with Au(III) complex ions (in the form of $[AuCl_3(OH)]^-$) possibly via hydrogen bonds and ligand replacement of chloride ions by carboxylate groups in SAD. Such "glue" cross-links AuNPs into chain-like structures. The close proximity of the connected AuNPs results in red shift of the localized surface plasmon resonance peak and increase in the near-infrared absorption; (d) with further consumption of Au(III) by reducing agents (e.g., citrate, SAD, and acetone), the "glue" is depleted and such chain-like structures can no longer maintain. The readsorption of some stabilizing agents (e.g., citrate, SAD, and acetone) onto the gold surface causes disintegration of the chain-like structures, producing dispersed spherical AuNPs. These steps can well explain the red-to-purple/blue color change from (a) to (c) and the purple/blue-to-red color change from (c) to (d). The red-to-purple/blue-to-red color reversal can be viewed as the dynamic process between chain-like structure formation (facilitated by liquid "glue" formation) and chain-like structure disintegration (induced by depletion of liquid "glue"). This proposed mechanism is also applicable to illustrate the red-to-purple/blue-to-red color reversal in seed-mediated growth of 13 nm citrate-coated AuNPs as well as the purple/blue-to-red color change in Turkevich method, offering new insights into the underlying physicochemical processes for the two widely adopted AuNP synthesis methods.

Future Work

- Understanding more of the interaction between “glue” components via adding hydrogen bond denaturants (e.g., urea) and carboxyl-containing molecules (e.g., formic acid, and acetic acid) to the reaction mixture.
- Providing more direct proof of the molecular nature of the “glue” after isolating the “glue” from the purple/blue nanostructures and dissociating the “glue” components for more characterization (e.g., NMR, FTIR, and HPLC–MS/UV–vis).
- Validating the proposed mechanism for other sizes of AuNP seeds in seed-mediated growth.
- Validating the proposed mechanism for other reaction conditions in Turkevich method (e.g., different R values, different temperatures, different pH, etc.).

References

1. Astruc, D.; Lu, F.; Aranzaes, J. R., Nanoparticles as Recyclable Catalysts: The Frontier between Homogeneous and Heterogeneous Catalysis. *Angew. Chem.-Int. Edit.* **2005**, *44*, 7852-7872.
2. Zhou, Z. Y.; Tian, N.; Li, J. T.; Broadwell, I.; Sun, S. G., Nanomaterials of High Surface Energy with Exceptional Properties in Catalysis and Energy Storage. *Chem. Soc. Rev.* **2011**, *40*, 4167-4185.
3. Arico, A. S.; Bruce, P.; Scrosati, B.; Tarascon, J. M.; Van Schalkwijk, W., Nanostructured Materials for Advanced Energy Conversion and Storage Devices. *Nature Materials* **2005**, *4*, 366-377.
4. Bruce, P. G.; Scrosati, B.; Tarascon, J. M., Nanomaterials for Rechargeable Lithium Batteries. *Angew. Chem.-Int. Edit.* **2008**, *47*, 2930-2946.
5. Zhang, S.; Geryak, R.; Geldmeier, J.; Kim, S.; Tsukruk, V. V., Synthesis, Assembly, and Applications of Hybrid Nanostructures for Biosensing. *Chemical Reviews* **2017**, *117*, 12942-13038.
6. Zhang, A.; Lieber, C. M., Nano-Bioelectronics. *Chemical Reviews* **2016**, *116*, 215-257.
7. Farka, Z.; Juřík, T.; Kovář, D.; Trnková, L.; Skládal, P., Nanoparticle-Based Immunochemical Biosensors and Assays: Recent Advances and Challenges. *Chemical Reviews* **2017**, *117*, 9973-10042.
8. Rosi, N. L.; Mirkin, C. A., Nanostructures in Biodiagnostics. *Chemical Reviews* **2005**, *105*, 1547-1562.

9. Smith, B. R.; Gambhir, S. S., Nanomaterials for In Vivo Imaging. *Chemical Reviews* **2017**, *117*, 901-986.

10. Lavik, E.; von Recum, H., The Role of Nanomaterials in Translational Medicine. *ACS Nano* **2011**, *5*, 3419-3424.

11. Pansare, V. J.; Hejazi, S.; Faenza, W. J.; Prud'homme, R. K., Review of Long-Wavelength Optical and NIR Imaging Materials: Contrast Agents, Fluorophores, and Multifunctional Nano Carriers. *Chemistry of Materials* **2012**, *24*, 812-827.

12. Barreto J. A.; O'Malley, W.; Kubeil, M.; Graham, B.; Stephan, H.; Spiccia, L., Nanomaterials: Applications in Cancer Imaging and Therapy. *Advanced Materials* **2011**, *23*, H18-H40.

13. Soppimath, K. S.; Aminabhavi, T. M.; Kulkarni, A. R.; Rudzinski, W. E., Biodegradable Polymeric Nanoparticles as Drug Delivery Devices. *Journal of Controlled Release* **2001**, *70*, 1-20.

14. Owens, D. E.; Peppas, N. A., Opsonization, Biodistribution, and Pharmacokinetics of Polymeric Nanoparticles. *International Journal of Pharmaceutics* **2006**, *307*, 93-102.

15. Paul, D. R.; Robeson, L. M., Polymer Nanotechnology: Nanocomposites. *Polymer* **2008**, *49*, 3187-3204.

16. Jiang, Y.; McNeill, J., Light-Harvesting and Amplified Energy Transfer in Conjugated Polymer Nanoparticles. *Chemical Reviews* **2017**, *117*, 838-859.

17. Grimaldi, N.; Andrade, F.; Segovia, N.; Ferrer-Tasies, L.; Sala, S.; Veciana, J.; Ventosa, N., Lipid-Based Nanovesicles for Nanomedicine. *Chem. Soc. Rev.* **2016**, *45*, 6520-6545.

18. Jesorka, A.; Orwar, O., Liposomes: Technologies and Analytical Applications. In *Annual Review of Analytical Chemistry*, 2008; Vol. 1, pp 801-832.

19. Lee, C. C.; MacKay, J. A.; Frechet, J. M. J.; Szoka, F. C., Designing Dendrimers for Biological Applications. *Nat. Biotechnol.* **2005**, *23*, 1517-1526.

20. Li, W.-S.; Aida, T., Dendrimer Porphyrins and Phthalocyanines. *Chemical Reviews* **2009**, *109*, 6047-6076.

21. Mignani, S.; El Kazzouli, S.; Bousmina, M. M.; Majoral, J.-P., Dendrimer Space Exploration: An Assessment of Dendrimers/Dendritic Scaffolding as Inhibitors of Protein–Protein Interactions, a Potential New Area of Pharmaceutical Development. *Chemical Reviews* **2014**, *114*, 1327-1342.

22. Thompson, B. C.; Frechet, J. M. J., Organic Photovoltaics - Polymer-Fullerene Composite Solar Cells. *Angew. Chem.-Int. Edit.* **2008**, *47*, 58-77.

23. Dennler, G.; Scharber, M. C.; Brabec, C. J., Polymer-Fullerene Bulk-Heterojunction Solar Cells. *Advanced Materials* **2009**, *21*, 1323-1338.

24. Zieleniewska, A.; Lodermeyer, F.; Roth, A.; Guldi, D. M., Fullerenes - How 25 Years of Charge Transfer Chemistry Have Shaped Our Understanding of (Interfacial) Interactions. *Chem. Soc. Rev.* **2018**, *47*, 702-714.

25. Tasis, D.; Tagmatarchis, N.; Bianco, A.; Prato, M., Chemistry of Carbon Nanotubes. *Chemical Reviews* **2006**, *106*, 1105-1136.

26. Hu, L.; Hecht, D. S.; Grüner, G., Carbon Nanotube Thin Films: Fabrication, Properties, and Applications. *Chemical Reviews* **2010**, *110*, 5790-5844.

27. Yu, L.; Shearer, C.; Shapter, J., Recent Development of Carbon Nanotube Transparent Conductive Films. *Chemical Reviews* **2016**, *116*, 13413-13453.

28. Farrera, C.; Torres Andón, F.; Feliu, N., Carbon Nanotubes as Optical Sensors in Biomedicine. *ACS Nano* **2017**, *11*, 10637-10643.

29. Navalon, S.; Dhakshinamoorthy, A.; Alvaro, M.; Garcia, H., Carbocatalysis by Graphene-Based Materials. *Chemical Reviews* **2014**, *114*, 6179-6212.

30. Ambrosi, A.; Chua, C. K.; Bonanni, A.; Pumera, M., Electrochemistry of Graphene and Related Materials. *Chemical Reviews* **2014**, *114*, 7150-7188.

31. Mao, H. Y.; Laurent, S.; Chen, W.; Akhavan, O.; Imani, M.; Ashkarran, A. A.; Mahmoudi, M., Graphene: Promises, Facts, Opportunities, and Challenges in Nanomedicine. *Chemical Reviews* **2013**, *113*, 3407-3424.

32. Spicer, C. D.; Jumeaux, C.; Gupta, B.; Stevens, M. M., Peptide and Protein Nanoparticle Conjugates: Versatile Platforms for Biomedical Applications. *Chem. Soc. Rev.* **2018**, *47*, 3574-3620.

33. Dreaden, E. C.; Alkilany, A. M.; Huang, X.; Murphy, C. J.; El-Sayed, M. A., The Golden Age: Gold Nanoparticles for Biomedicine. *Chem. Soc. Rev.* **2012**, *41*, 2740-2779.

34. Saha, K.; Agasti, S. S.; Kim, C.; Li, X.; Rotello, V. M., Gold Nanoparticles in Chemical and Biological Sensing. *Chemical Reviews* **2012**, *112*, 2739-2779.

35. Caltagirone, C.; Bettoschi, A.; Garau, A.; Montis, R., Silica-Based Nanoparticles: A Versatile Tool for the Development of Efficient Imaging Agents. *Chem. Soc. Rev.* **2015**, *44*, 4645-4671.

36. Wegner, K. D.; Hildebrandt, N., Quantum Dots: Bright and Versatile In Vitro and In Vivo Fluorescence Imaging Biosensors. *Chem. Soc. Rev.* **2015**, *44*, 4792-4834.

37. Lu, A. H.; Salabas, E. L.; Schuth, F., Magnetic Nanoparticles: Synthesis, Protection, Functionalization, and Application. *Angew. Chem.-Int. Edit.* **2007**, *46*, 1222-1244.

38. Yang, X.; Yang, M.; Pang, B.; Vara, M.; Xia, Y., Gold Nanomaterials at Work in Biomedicine. *Chemical Reviews* **2015**, *115*, 10410-10488.

39. Daniel, M.-C.; Astruc, D., Gold Nanoparticles: Assembly, Supramolecular Chemistry, Quantum-Size-Related Properties, and Applications toward Biology, Catalysis, and Nanotechnology. *Chemical Reviews* **2004**, *104*, 293-346.

40. Faraday, M., Experimental Relations of Gold (and Other Metals) to Light. *Philosophical Transactions of the Royal Society of London* **1857**, *147*, 145-181.

41. Gustav, M., Beiträge Zur Optik Trüber Medien, Speziell Kolloidaler Metallösungen. *Annalen der Physik* **1908**, *330*, 377-445.

42. Huang, X.; El-Sayed, M. A., Gold Nanoparticles: Optical Properties and Implementations in Cancer Diagnosis and Photothermal Therapy. *Journal of Advanced Research* **2010**, *1*, 13-28.

43. Huang, X.; Jain, P. K.; El-Sayed, I. H.; El-Sayed, M. A., Plasmonic Photothermal Therapy (PPTT) Using Gold Nanoparticles. *Lasers in Medical Science* **2007**, *23*, 217.

44. Willets, K. A.; Van Duyne, R. P., Localized Surface Plasmon Resonance Spectroscopy and Sensing. *Annual Review of Physical Chemistry* **2007**, *58*, 267-297.

45. R., G., Über Die Form Ultramikroskopischer Silberteilchen. *Annalen der Physik* **1915**, *352*, 270-284.

46. Link, S.; Mohamed, M. B.; El-Sayed, M. A., Simulation of the Optical Absorption Spectra of Gold Nanorods as a Function of Their Aspect Ratio and the Effect of the Medium Dielectric Constant. *The Journal of Physical Chemistry B* **1999**, *103*, 3073-3077.

47. Neeves, A. E.; Birnboim, M. H., Composite Structures for the Enhancement of Nonlinear-Optical Susceptibility. *J. Opt. Soc. Am. B* **1989**, *6*, 787-796.

48. Averitt, R. D.; Westcott, S. L.; Halas, N. J., Linear Optical Properties of Gold Nanoshells. *J. Opt. Soc. Am. B* **1999**, *16*, 1824-1832.

49. Skrabalak, S. E.; Chen, J.; Sun, Y.; Lu, X.; Au, L.; Cobley, C. M.; Xia, Y., Gold Nanocages: Synthesis, Properties, and Applications. *Accounts of Chemical Research* **2008**, *41*, 1587-1595.

50. Jones, M. R.; Osberg, K. D.; Macfarlane, R. J.; Langille, M. R.; Mirkin, C. A., Templated Techniques for the Synthesis and Assembly of Plasmonic Nanostructures. *Chemical Reviews* **2011**, *111*, 3736-3827.

51. Su, K. H.; Wei, Q. H.; Zhang, X.; Mock, J. J.; Smith, D. R.; Schultz, S., Interparticle Coupling Effects on Plasmon Resonances of Nanogold Particles. *Nano Letters* **2003**, *3*, 1087-1090.

52. Hao, E.; Schatz, G. C., Electromagnetic Fields around Silver Nanoparticles and Dimers. *The Journal of Chemical Physics* **2004**, *120*, 357-366.

53. Mirkin, C. A.; Letsinger, R. L.; Mucic, R. C.; Storhoff, J. J., A DNA-Based Method for Rationally Assembling Nanoparticles into Macroscopic Materials. *Nature* **1996**, *382*, 607.

54. Kneipp, J.; Kneipp, H.; Kneipp, K., SERS-A Single-Molecule and Nanoscale Tool for Bioanalytics. *Chem. Soc. Rev.* **2008**, *37*, 1052-1060.

55. Haes, A. J.; Haynes, C. L.; McFarland, A. D.; Schatz, G. C.; Van Duyne, R. P.; Zou, S., Plasmonic Materials for Surface-Enhanced Sensing and Spectroscopy. *MRS Bulletin* **2005**, *30*, 368-375.

56. Linic, S.; Christopher, P.; Ingram, D. B., Plasmonic-Metal Nanostructures for Efficient Conversion of Solar to Chemical Energy. *Nature Materials* **2011**, *10*, 911.

57. Navalon, S.; de Miguel, M.; Martin, R.; Alvaro, M.; Garcia, H., Enhancement of the Catalytic Activity of Supported Gold Nanoparticles for the Fenton Reaction by Light. *Journal of the American Chemical Society* **2011**, *133*, 2218-2226.

58. Huaiyong, Z.; Xuebin, K.; Xuzhuang, Y.; Sarina, S.; Hongwei, L., Reduction of Nitroaromatic Compounds on Supported Gold Nanoparticles by Visible and Ultraviolet Light. *Angewandte Chemie International Edition* **2010**, *49*, 9657-9661.

59. Ma, T.; Yang, W.; Liu, S.; Zhang, H.; Liang, F., A Comparison Reduction of 4-Nitrophenol by Gold Nanospheres and Gold Nanostars. *Catalysts* **2017**, *7*, 38.

60. Xi, C.; Huai-Yong, Z.; Jin-Cai, Z.; Zhan-Feng, Z.; Xue-Ping, G., Visible-Light-Driven Oxidation of Organic Contaminants in Air with Gold Nanoparticle Catalysts on Oxide Supports. *Angewandte Chemie* **2008**, *120*, 5433-5436.

61. Zhu, H.; Chen, X.; Zheng, Z.; Ke, X.; Jaatinen, E.; Zhao, J.; Guo, C.; Xie, T.; Wang, D., Mechanism of Supported Gold Nanoparticles as Photocatalysts under Ultraviolet and Visible Light Irradiation. *Chemical Communications* **2009**, 7524-7526.

62. Jeanmaire, D. L.; Van Duyne, R. P., Surface Raman Spectroelectrochemistry: Part I. Heterocyclic, Aromatic, and Aliphatic Amines Adsorbed on the Anodized

Silver Electrode. *Journal of Electroanalytical Chemistry and Interfacial Electrochemistry* **1977**, *84*, 1-20.

63. Albrecht, M. G.; Creighton, J. A., Anomalously Intense Raman Spectra of Pyridine at a Silver Electrode. *Journal of the American Chemical Society* **1977**, *99*, 5215-5217.

64. Lane, L. A.; Xue, R.; Nie, S., Emergence of Two Near-Infrared Windows for In Vivo and Intraoperative SERS. *Current Opinion in Chemical Biology* **2018**, *45*, 95-103.

65. Emmanuel, F.; Samuel, G., Surface Enhanced Fluorescence. *Journal of Physics D: Applied Physics* **2008**, *41*, 013001.

66. Li, J.-F.; Li, C.-Y.; Aroca, R. F., Plasmon-Enhanced Fluorescence Spectroscopy. *Chem. Soc. Rev.* **2017**, *46*, 3962-3979.

67. Lakowicz, J. R., Radiative Decay Engineering 5: Metal-Enhanced Fluorescence and Plasmon Emission. *Analytical Biochemistry* **2005**, *337*, 171-194.

68. Ray, K.; Badugu, R.; Lakowicz, J. R., Polyelectrolyte Layer-by-Layer Assembly to Control the Distance between Fluorophores and Plasmonic Nanostructures. *Chemistry of Materials* **2007**, *19*, 5902-5909.

69. Aslan, K.; Malyn, S. N.; Geddes, C. D., Metal-Enhanced Fluorescence from Gold Surfaces: Angular Dependent Emission. *Journal of Fluorescence* **2007**, *17*, 7-13.

70. Dulkeith, E.; Morteani, A. C.; Niedereichholz, T.; Klar, T. A.; Feldmann, J.; Levi, S. A.; van Veggel, F. C. J. M.; Reinhoudt, D. N.; Möller, M.; Gittins, D. I., Fluorescence Quenching of Dye Molecules Near Gold Nanoparticles: Radiative and Nonradiative Effects. *Physical Review Letters* **2002**, *89*, 203002.

71. Aslan, K.; Pérez-Luna, V. H., Quenched Emission of Fluorescence by Ligand Functionalized Gold Nanoparticles. *Journal of Fluorescence* **2004**, *14*, 401-405.

72. Dulkeith, E.; Ringler, M.; Klar, T. A.; Feldmann, J.; Muñoz Javier, A.; Parak, W. J., Gold Nanoparticles Quench Fluorescence by Phase Induced Radiative Rate Suppression. *Nano Letters* **2005**, *5*, 585-589.

73. Xia, X.; Yang, M.; Oetjen, L. K.; Zhang, Y.; Li, Q.; Chen, J.; Xia, Y., An Enzyme-Sensitive Probe for Photoacoustic Imaging and Fluorescence Detection of Protease Activity. *Nanoscale* **2011**, *3*, 950-953.

74. Elghanian, R.; Storhoff, J. J.; Mucic, R. C.; Letsinger, R. L.; Mirkin, C. A., Selective Colorimetric Detection of Polynucleotides Based on the Distance-Dependent Optical Properties of Gold Nanoparticles. *Science* **1997**, *277*, 1078-1081.

75. Li, H.; Rothberg, L., Colorimetric Detection of DNA Sequences Based on Electrostatic Interactions with Unmodified Gold Nanoparticles. *Proceedings of the National Academy of Sciences of the United States of America* **2004**, *101*, 14036-14039.

76. Wang, L.; Liu, X.; Hu, X.; Song, S.; Fan, C., Unmodified Gold Nanoparticles as a Colorimetric Probe for Potassium DNA Aptamers. *Chemical Communications* **2006**, 3780-3782.

77. Juan, Z.; Lihua, W.; Dun, P.; Shiping, S.; C., B. F. Y.; Hua, Z.; Chunhai, F., Visual Cocaine Detection with Gold Nanoparticles and Rationally Engineered Aptamer Structures. *Small* **2008**, *4*, 1196-1200.

78. Wei, H.; Li, B.; Li, J.; Wang, E.; Dong, S., Simple and Sensitive Aptamer-Based Colorimetric Sensing of Protein Using Unmodified Gold Nanoparticle Probes. *Chemical Communications* **2007**, 3735-3737.

79. Link, S.; El-Sayed, M. A., Spectral Properties and Relaxation Dynamics of Surface Plasmon Electronic Oscillations in Gold and Silver Nanodots and Nanorods. *The Journal of Physical Chemistry B* **1999**, *103*, 8410-8426.

80. Dreaden, E. C.; Mackey, M. A.; Huang, X.; Kang, B.; El-Sayed, M. A., Beating Cancer in Multiple Ways Using Nanogold. *Chem. Soc. Rev.* **2011**, *40,* 3391-3404.

81. Weissleder, R., A Clearer Vision for In Vivo Imaging. *Nat. Biotechnol.* **2001**, *19*, 316.

82. Hirsch, L. R.; Stafford, R. J.; Bankson, J. A.; Sershen, S. R.; Rivera, B.; Price, R. E.; Hazle, J. D.; Halas, N. J.; West, J. L., Nanoshell-Mediated Near-Infrared Thermal Therapy of Tumors under Magnetic Resonance Guidance. *Proceedings of the National Academy of Sciences* **2003**, *100*, 13549-13554.

83. O'Neal, D. P.; Hirsch, L. R.; Halas, N. J.; Payne, J. D.; West, J. L., Photo-Thermal Tumor Ablation in Mice Using Near Infrared-Absorbing Nanoparticles. *Cancer Letters* **2004**, *209*, 171-176.

84. Huang, X.; El-Sayed, I. H.; Qian, W.; El-Sayed, M. A., Cancer Cell Imaging and Photothermal Therapy in the Near-Infrared Region by Using Gold Nanorods. *Journal of the American Chemical Society* **2006**, *128*, 2115-2120.

85. Jingyi, C.; Charles, G.; Richard, L.; Qiang, Z.; Miaoxian, Y.; Michael, G.; J., W. M.; Younan, X., Gold Nanocages as Photothermal Transducers for Cancer Treatment. *Small* **2010**, *6*, 811-817.

86. He, J.; Huang, X.; Li, Y.-C.; Liu, Y.; Babu, T.; Aronova, M. A.; Wang, S.; Lu, Z.; Chen, X.; Nie, Z., Self-Assembly of Amphiphilic Plasmonic Micelle-Like Nanoparticles in Selective Solvents. *Journal of the American Chemical Society* **2013**, *135*, 7974-7984.

87. Huanjun, C.; Lei, S.; Tian, M.; Zhenhua, S.; Chunmei, Z.; Baocheng, Y.; Jianfang, W., Understanding the Photothermal Conversion Efficiency of Gold Nanocrystals. *Small* **2010**, *6*, 2272-2280.

88. Sigrist, M. W., Laser Generation of Acoustic Waves in Liquids and Gases. *Journal of Applied Physics* **1986**, *60,* R83-R122.

89. Kim, C.; Favazza, C.; Wang, L. V., In Vivo Photoacoustic Tomography of Chemicals: High-Resolution Functional and Molecular Optical Imaging at New Depths. *Chemical Reviews* **2010**, *110*, 2756-2782.

90. Copland, J. A.; Eghtedari, M.; Popov, V. L.; Kotov, N.; Mamedova, N.; Motamedi, M.; Oraevsky, A. A., Bioconjugated Gold Nanoparticles as a Molecular Based Contrast Agent: Implications for Imaging of Deep Tumors Using Optoacoustic Tomography. *Molecular Imaging & Biology* **2004**, *6*, 341-349.

91. Wang, Y.; Xie, X.; Wang, X.; Ku, G.; Gill, K. L.; O'Neal, D. P.; Stoica, G.; Wang, L. V., Photoacoustic Tomography of a Nanoshell Contrast Agent in the In Vivo Rat Brain. *Nano Letters* **2004**, *4*, 1689-1692.

92. Yang, X.; Skrabalak, S. E.; Li, Z.-Y.; Xia, Y.; Wang, L. V., Photoacoustic Tomography of a Rat Cerebral Cortex In Vivo with Au Nanocages as an Optical Contrast Agent. *Nano Letters* **2007**, *7*, 3798-3802.

93. James, F. H.; Daniel, N. S.; Henry, M. S., The Use of Gold Nanoparticles to Enhance Radiotherapy in Mice. *Physics in Medicine & Biology* **2004**, *49,* N309.

94. Hainfeld, J. F.; Slatkin, D. N.; Focella, T. M.; Smilowitz, H. M., Gold Nanoparticles: A New X-Ray Contrast Agent. *The British Journal of Radiology* **2006**, *79*, 248-253.

95. Chien, C. C.; Wang, C. H.; Hua, T. E.; Tseng, P. Y.; Yang, T. Y.; Hwu, Y.; Chen, Y. J.; Chung, K. H.; Je, J. H.; Margaritondo, G., Synchrotron X-Ray Synthesized Gold Nanoparticles for Tumor Therapy. *AIP Conference Proceedings* **2007**, *879*, 1908-1911.

96. Maeda, H.; Wu, J.; Sawa, T.; Matsumura, Y.; Hori, K., Tumor Vascular Permeability and the EPR Effect in Macromolecular Therapeutics: A Review. *Journal of Controlled Release* **2000**, *65*, 271-284.

97. Iyer, A. K.; Khaled, G.; Fang, J.; Maeda, H., Exploiting the Enhanced Permeability and Retention Effect for Tumor Targeting. *Drug Discovery Today* **2006**, *11*, 812-818.

98. F., P. G.; G.I., K. D.; Lawrence, T., Colloidal Gold Nanoparticles: A Novel Nanoparticle Platform for Developing Multifunctional Tumor-Targeted Drug Delivery Vectors. *Drug Development Research* **2006**, *67*, 47-54.

99. Cheng, Y.; Samia, A. C.; Li, J.; Kenney, M. E.; Resnick, A.; Burda, C., Delivery and Efficacy of a Cancer Drug as a Function of the Bond to the Gold Nanoparticle Surface. *Langmuir* **2010**, *26*, 2248-2255.

100. Jin, R., Quantum Sized, Thiolate-Protected Gold Nanoclusters. *Nanoscale* **2010**, *2*, 343-362.

101. Lu, Y.; Chen, W., Sub-Nanometre Sized Metal Clusters: From Synthetic Challenges to the Unique Property Discoveries. *Chem. Soc. Rev.* **2012**, *41*, 3594-3623.

102. Fedrigo, S.; Harbich, W.; Buttet, J., Optical Response of Ag_2, Ag_3, Au_2, and Au_3 in Argon Matrices. *The Journal of Chemical Physics* **1993**, *99*, 5712-5717.

103. Taylor, K. J.; Pettiette-Hall, C. L.; Cheshnovsky, O.; Smalley, R. E., Ultraviolet Photoelectron Spectra of Coinage Metal Clusters. *The Journal of Chemical Physics* **1992**, *96*, 3319-3329.

104. Schmid, G.; Pfeil, R.; Boese, R.; Bandermann, F.; Meyer, S.; Calis Gijs, H. M.; van der Velden Jan, W. A., $Au_{55}[P(C_6H_5)_3]_{12}Cl_6$ — Ein Goldcluster Ungewöhnlicher Größe. *Chemische Berichte* **1981**, *114*, 3634-3642.

105. Brust, M.; Walker, M.; Bethell, D.; Schiffrin, D. J.; Whyman, R., Synthesis of Thiol-Derivatised Gold Nanoparticles in a Two-Phase Liquid-Liquid System. *Journal of the Chemical Society, Chemical Communications* **1994**, 801-802.

106. Brust, M.; Fink, J.; Bethell, D.; Schiffrin, D. J.; Kiely, C., Synthesis and Reactions of Functionalised Gold Nanoparticles. *Journal of the Chemical Society, Chemical Communications* **1995**, 1655-1656.

107. Hostetler, M. J.; Wingate, J. E.; Zhong, C.-J.; Harris, J. E.; Vachet, R. W.; Clark, M. R.; Londono, J. D.; Green, S. J.; Stokes, J. J.; Wignall, G. D.; Glish, G. L.; Porter, M. D.; Evans, N. D.; Murray, R. W., Alkanethiolate Gold Cluster Molecules with Core Diameters from 1.5 to 5.2 nm: Core and Monolayer Properties as a Function of Core Size. *Langmuir* **1998**, *14*, 17-30.

108. Price, R. C.; Whetten, R. L., All-Aromatic, Nanometer-Scale, Gold-Cluster Thiolate Complexes. *Journal of the American Chemical Society* **2005**, *127*, 13750-13751.

109. Zhu, M.; Lanni, E.; Garg, N.; Bier, M. E.; Jin, R., Kinetically Controlled, High-Yield Synthesis of Au_{25} Clusters. *Journal of the American Chemical Society* **2008**, *130*, 1138-1139.

110. Jin, R.; Egusa, S.; Scherer, N. F., Thermally-Induced Formation of Atomic Au Clusters and Conversion into Nanocubes. *Journal of the American Chemical Society* **2004**, *126*, 9900-9901.

111. Duan, H.; Nie, S., Etching Colloidal Gold Nanocrystals with Hyperbranched and Multivalent Polymers: A New Route to Fluorescent and Water-Soluble Atomic Clusters. *Journal of the American Chemical Society* **2007**, *129*, 2412-2413.

112. Lin, C.-A. J.; Yang, T.-Y.; Lee, C.-H.; Huang, S. H.; Sperling, R. A.; Zanella, M.; Li, J. K.; Shen, J.-L.; Wang, H.-H.; Yeh, H.-I.; Parak, W. J.; Chang, W. H., Synthesis, Characterization, and Bioconjugation of Fluorescent Gold Nanoclusters toward Biological Labeling Applications. *ACS Nano* **2009**, *3*, 395-401.

113. Martin, C. R., Membrane-Based Synthesis of Nanomaterials. *Chemistry of Materials* **1996**, *8*, 1739-1746.

114. Yu; Chang, S.-S.; Lee, C.-L.; Wang, C. R. C., Gold Nanorods: Electrochemical Synthesis and Optical Properties. *The Journal of Physical Chemistry B* **1997**, *101*, 6661-6664.

115. R., J. N.; L., G.; J., M. C., Seed-Mediated Growth Approach for Shape-Controlled Synthesis of Spheroidal and Rod-Like Gold Nanoparticles Using a Surfactant Template. *Advanced Materials* **2001**, *13,* 1389-1393.

116. Jana, N. R.; Gearheart, L.; Murphy, C. J., Wet Chemical Synthesis of High Aspect Ratio Cylindrical Gold Nanorods. *The Journal of Physical Chemistry B* **2001**, *105*, 4065-4067.

117. B.D., B.; S.O., O.; C.J., M., An Improved Synthesis of High-Aspect-Ratio Gold Nanorods. *Advanced Materials* **2003**, *15,* 414-416.

118. Nikoobakht, B.; El-Sayed, M. A., Preparation and Growth Mechanism of Gold Nanorods (NRs) Using Seed-Mediated Growth Method. *Chemistry of Materials* **2003**, *15*, 1957-1962.

119. Johnson, C. J.; Dujardin, E.; Davis, S. A.; Murphy, C. J.; Mann, S., Growth and Form of Gold Nanorods Prepared by Seed-Mediated, Surfactant-Directed Synthesis. *Journal of Materials Chemistry* **2002**, *12*, 1765-1770.

120. J., P. J.; M., L. M. L.; S., C.; C., C. D. Y.; P., M., Electric-Field-Directed Growth of Gold Nanorods in Aqueous Surfactant Solutions. *Advanced Functional Materials* **2004**, *14,* 571-579.

121. R., J. N., Gram-Scale Synthesis of Soluble, Near-Monodisperse Gold Nanorods and Other Anisotropic Nanoparticles. *Small* **2005**, *1*, 875-882.

122. Ali, M. R. K.; Snyder, B.; El-Sayed, M. A., Synthesis and Optical Properties of Small Au Nanorods Using a Seedless Growth Technique. *Langmuir* **2012**, *28*, 9807-9815.

123. Chen, H.; Shao, L.; Li, Q.; Wang, J., Gold Nanorods and Their Plasmonic Properties. *Chem. Soc. Rev.* **2013**, *42*, 2679-2724.

124. Oldenburg, S. J.; Averitt, R. D.; Westcott, S. L.; Halas, N. J., Nanoengineering of Optical Resonances. *Chemical Physics Letters* **1998**, *288*, 243-247.

125. Brinson, B. E.; Lassiter, J. B.; Levin, C. S.; Bardhan, R.; Mirin, N.; Halas, N. J., Nanoshells Made Easy: Improving Au Layer Growth on Nanoparticle Surfaces. *Langmuir* **2008**, *24*, 14166-14171.

126. Jin, Y.; Gao, X., Plasmonic Fluorescent Quantum Dots. *Nature Nanotechnology* **2009**, *4*, 571.

127. Jin, Y.; Gao, X., Spectrally Tunable Leakage-Free Gold Nanocontainers. *Journal of the American Chemical Society* **2009**, *131*, 17774-17776.

128. Shi, W.; Sahoo, Y.; Swihart, M. T.; Prasad, P. N., Gold Nanoshells on Polystyrene Cores for Control of Surface Plasmon Resonance. *Langmuir* **2005**, *21*, 1610-1617.

129. Stöber, W.; Fink, A.; Bohn, E., Controlled Growth of Monodisperse Silica Spheres in the Micron Size Range. *Journal of Colloid and Interface Science* **1968**, *26*, 62-69.

130. Duff, D. G.; Baiker, A.; Edwards, P. P., A New Hydrosol of Gold Clusters. 1. Formation and Particle Size Variation. *Langmuir* **1993**, *9*, 2301-2309.

131. Leff, D. V.; Brandt, L.; Heath, J. R., Synthesis and Characterization of Hydrophobic, Organically-Soluble Gold Nanocrystals Functionalized with Primary Amines. *Langmuir* **1996**, *12*, 4723-4730.

132. Sun, Y.; Xia, Y., Shape-Controlled Synthesis of Gold and Silver Nanoparticles. *Science* **2002**, *298*, 2176-2179.

133. Sun, Y.; Xia, Y., Alloying and Dealloying Processes Involved in the Preparation of Metal Nanoshells through a Galvanic Replacement Reaction. *Nano Letters* **2003**, *3*, 1569-1572.

134. Cobley, C. M.; Xia, Y., Engineering the Properties of Metal Nanostructures via Galvanic Replacement Reactions. *Materials Science and Engineering: R: Reports* **2010**, *70*, 44-62.

135. Zhao, P.; Li, N.; Astruc, D., State of the Art in Gold Nanoparticle Synthesis. *Coordination Chemistry Reviews* **2013**, *257*, 638-665.

136. Turkevich, J.; Stevenson, P. C.; Hillier, J., A Study of the Nucleation and Growth Processes in the Synthesis of Colloidal Gold. *Discussions of the Faraday Society* **1951**, *11*, 55-75.

137. Frens, G., Controlled Nucleation for the Regulation of the Particle Size in Monodisperse Gold Suspensions. *Nature Physical Science* **1973**, *241*, 20.

138. Xia, H.; Bai, S.; Hartmann, J.; Wang, D., Synthesis of Monodisperse Quasi-Spherical Gold Nanoparticles in Water via Silver(I)-Assisted Citrate Reduction. *Langmuir* **2010**, *26*, 3585-9.

139. Patungwasa, W.; Hodak, J. H., pH Tunable Morphology of the Gold Nanoparticles Produced by Citrate Reduction. *Materials Chemistry and Physics* **2008**, *108*, 45-54.

140. Li, C.; Li, D.; Wan, G.; Xu, J.; Hou, W., Facile Synthesis of Concentrated Gold Nanoparticles with Low Size-Distribution in Water: Temperature and pH Controls. *Nanoscale Research Letters* **2011**, *6*, 440.

141. Zabetakis, K.; Ghann, W. E.; Kumar, S.; Daniel, M.-C., Effect of High Gold Salt Concentrations on the Size and Polydispersity of Gold Nanoparticles Prepared by an Extended Turkevich–Frens Method. *Gold Bulletin* **2012**, *45*, 203-211.

142. Ojea-Jiménez, I.; Bastús, N. G.; Puntes, V., Influence of the Sequence of the Reagents Addition in the Citrate-Mediated Synthesis of Gold Nanoparticles. *The Journal of Physical Chemistry C* **2011**, *115*, 15752-15757.

143. Schulz, F.; Homolka, T.; Bastus, N. G.; Puntes, V.; Weller, H.; Vossmeyer, T., Little Adjustments Significantly Improve the Turkevich Synthesis of Gold Nanoparticles. *Langmuir* **2014**, *30*, 10779-84.

144. Chakraborty, A.; Chakraborty, S.; Chaudhuri, B.; Bhattacharjee, S., Process Engineering Studies on Gold Nanoparticle Formation via Dynamic Spectroscopic Approach. *Gold Bulletin* **2016**, *49*, 75-85.

145. Shiba, F., Size Control of Monodisperse Au Nanoparticles Synthesized via a Citrate Reduction Process Associated with a pH-Shifting Procedure. *CrystEngComm* **2013**, *15*.

146. Tran, M.; DePenning, R.; Turner, M.; Padalkar, S., Effect of Citrate Ratio and Temperature on Gold Nanoparticle Size and Morphology. *Materials Research Express* **2016**, *3*.

147. Rohiman, A.; Anshori, I.; Surawijaya, A.; Idris, I., Study of Colloidal Gold Synthesis Using Turkevich Method. *AIP Conference Proceedings* **2011**, *1415*, 39-42.

148. Sivaraman, S. K.; Kumar, S.; Santhanam, V., Monodisperse Sub-10 nm Gold Nanoparticles by Reversing the Order of Addition in Turkevich Method--The Role of Chloroauric Acid. *J Colloid Interface Sci* **2011**, *361*, 543-7.

149. Kimling, J.; Maier, M.; Okenve, B.; Kotaidis, V.; Ballot, H.; Plech, A., Turkevich Method for Gold Nanoparticle Synthesis Revisited. *The Journal of Physical Chemistry B* **2006**, *110*, 15700-15707.

150. Thanh, N. T. K.; Maclean, N.; Mahiddine, S., Mechanisms of Nucleation and Growth of Nanoparticles in Solution. *Chemical Reviews* **2014**, *114*, 7610-7630.

151. Gammons, C. H.; Yu, Y.; Williams-Jones, A. E., The Disproportionation of Gold(I) Chloride Complexes at 25 to 200 ℃. *Geochimica et Cosmochimica Acta* **1997**, *61*, 1971-1983.

152. Ojea-Jiménez, I.; Campanera, J. M., Molecular Modeling of the Reduction Mechanism in the Citrate-Mediated Synthesis of Gold Nanoparticles. *The Journal of Physical Chemistry C* **2012**, *116*, 23682-23691.

153. Kumar, S.; Gandhi, K. S.; Kumar, R., Modeling of Formation of Gold Nanoparticles by Citrate Method. *Industrial & Engineering Chemistry Research* **2007**, *46*, 3128-3136.

154. Wiig, E. O., Carbon Dioxide Cleavage from Acetone Dicarboxylic Acid. *The Journal of Physical Chemistry* **1927**, *32*, 961-981.

155. Wiig, E. O., Temperature Coefficients of the Decomposition of Acetone Dicarboxylic Acid in Water. *The Journal of Physical Chemistry* **1929**, *34*, 596-597.

156. Davies, A. E., The Kinetics of the Coagulation of Gold Sols. An Investigation of the "Thermo-Senescence Effect" Exhibited at Elevated Temperatures. *The Journal of Physical Chemistry* **1928**, *33*, 274-284.

157. Doyen, M.; Bartik, K.; Bruylants, G., UV–Vis and NMR Study of the Formation of Gold Nanoparticles by Citrate Reduction: Observation of Gold–Citrate Aggregates. *Journal of Colloid and Interface Science* **2013**, *399*, 1-5.

158. Leff, D. V.; Ohara, P. C.; Heath, J. R.; Gelbart, W. M., Thermodynamic Control of Gold Nanocrystal Size: Experiment and Theory. *The Journal of Physical Chemistry* **1995**, *99*, 7036-7041.

159. Brown, K. R.; Natan, M. J., Hydroxylamine Seeding of Colloidal Au Nanoparticles in Solution and on Surfaces. *Langmuir* **1998**, *14*, 726-728.

160. Brown, K. R.; Walter, D. G.; Natan, M. J., Seeding of Colloidal Au Nanoparticle Solutions. 2. Improved Control of Particle Size and Shape. *Chemistry of Materials* **2000**, *12*, 306-313.

161. Brown, K. R.; Lyon, L. A.; Fox, A. P.; Reiss, B. D.; Natan, M. J., Hydroxylamine Seeding of Colloidal Au Nanoparticles. 3. Controlled Formation of Conductive Au Films. *Chemistry of Materials* **2000**, *12*, 314-323.

162. Jana, N. R.; Gearheart, L.; Murphy, C. J., Seeding Growth for Size Control of 5−40 nm Diameter Gold Nanoparticles. *Langmuir* **2001**, *17*, 6782-6786.

163. Rodríguez-Fernández, J.; Pérez-Juste, J.; García de Abajo, F. J.; Liz-Marzán, L. M., Seeded Growth of Submicron Au Colloids with Quadrupole Plasmon Resonance Modes. *Langmuir* **2006**, *22*, 7007-7010.

164. Perrault, S. D.; Chan, W. C. W., Synthesis and Surface Modification of Highly Monodispersed, Spherical Gold Nanoparticles of 50−200 nm. *Journal of the American Chemical Society* **2009**, *131*, 17042-17043.

165. Ziegler, C.; Eychmüller, A., Seeded Growth Synthesis of Uniform Gold Nanoparticles with Diameters of 15−300 nm. *The Journal of Physical Chemistry C* **2011**, *115*, 4502-4506.

166. Bastús, N. G.; Comenge, J.; Puntes, V., Kinetically Controlled Seeded Growth Synthesis of Citrate-Stabilized Gold Nanoparticles of up to 200 nm: Size Focusing versus Ostwald Ripening. *Langmuir* **2011**, *27*, 11098-11105.

167. Volkert, A. A.; Subramaniam, V.; Haes, A. J., Implications of Citrate Concentration During the Seeded Growth Synthesis of Gold Nanoparticles. *Chemical Communications* **2011**, *47*, 478-480.

168. LaMer, V. K.; Dinegar, R. H., Theory, Production and Mechanism of Formation of Monodispersed Hydrosols. *Journal of the American Chemical Society* **1950**, *72*, 4847-4854.

169. LaMer, V. K., Nucleation in Phase Transitions. *Industrial & Engineering Chemistry* **1952**, *44*, 1270-1277.

170. Chow, M. K.; Zukoski, C. F., Gold Sol Formation Mechanisms: Role of Colloidal Stability. *Journal of Colloid and Interface Science* **1994**, *165*, 97-109.

171. Biggs, S.; Chow, M. K.; Zukoski, C. F.; Grieser, F., The Role of Colloidal Stability in the Formation of Gold Sols. *Journal of Colloid and Interface Science* **1993**, *160*, 511-513.

172. Biggs, S.; Mulvaney, P.; Zukoski, C. F.; Grieser, F., Study of Anion Adsorption at the Gold-Aqueous Solution Interface by Atomic Force Microscopy. *Journal of the American Chemical Society* **1994**, *116*, 9150-9157.

173. Wall, J. F.; Grieser, F.; Zukoski, C. F., Monitoring Chemical Reactions at the Gold/Solution Interface Using Atomic Force Microscopy. *Journal of the Chemical Society, Faraday Transactions* **1997**, *93*, 4017-4020.

174. Pei, L.; Mori, K.; Adachi, M., Formation Process of Two-Dimensional Networked Gold Nanowires by Citrate Reduction of $AuCl_4^-$ and the Shape Stabilization. *Langmuir* **2004**, *20*, 7837-7843.

175. Adachi, M.; Mori, K.; Sato, Y.; Pei, L., Gold Nanowire Formation of 2-Dimensional Network Structure with Electric Conductivity. *Journal of Chemical Engineering of Japan* **2004**, *37*, 604-608.

176. Pong, B.-K.; Elim, H. I.; Chong, J.-X.; Ji, W.; Trout, B. L.; Lee, J.-Y., New Insights on the Nanoparticle Growth Mechanism in the Citrate Reduction of Gold(III) Salt: Formation of the Au Nanowire Intermediate and Its Nonlinear Optical Properties. *The Journal of Physical Chemistry C* **2007**, *111*, 6281-6287.

177. Ji, X.; Song, X.; Li, J.; Bai, Y.; Yang, W.; Peng, X., Size Control of Gold Nanocrystals in Citrate Reduction: The Third Role of Citrate. *Journal of the American Chemical Society* **2007**, *129*, 13939-13948.

178. Rodríguez-González, B.; Mulvaney, P.; Liz-Marzán Luis, M., An Electrochemical Model for Gold Colloid Formation via Citrate Reduction. In *Zeitschrift für Physikalische Chemie*, 2007; Vol. 221, p 415.

179. Polte, J.; Ahner, T. T.; Delissen, F.; Sokolov, S.; Emmerling, F.; Thünemann, A. F.; Kraehnert, R., Mechanism of Gold Nanoparticle Formation in the Classical Citrate Synthesis Method Derived from Coupled In Situ XANES and SAXS Evaluation. *Journal of the American Chemical Society* **2010**, *132*, 1296-1301.

180. Wuithschick, M.; Birnbaum, A.; Witte, S.; Sztucki, M.; Vainio, U.; Pinna, N.; Rademann, K.; Emmerling, F.; Kraehnert, R.; Polte, J., Turkevich in New Robes: Key Questions Answered for the Most Common Gold Nanoparticle Synthesis. *ACS Nano* **2015**, *9*, 7052-7071.

181. Mikhlin, Y.; Karacharov, A.; Likhatski, M.; Podlipskaya, T.; Zubavichus, Y.; Veligzhanin, A.; Zaikovski, V., Submicrometer Intermediates in the Citrate Synthesis of Gold Nanoparticles: New Insights into the Nucleation and Crystal Growth Mechanisms. *Journal of Colloid and Interface Science* **2011**, *362*, 330-336.

182. Georgiev, P.; Bojinova, A.; Kostova, B.; Momekova, D.; Bjornholm, T.; Balashev, K., Implementing Atomic Force Microscopy (AFM) for Studying Kinetics of Gold Nanoparticle's Growth. *Colloids and Surfaces A: Physicochemical and Engineering Aspects* **2013**, *434*, 154-163.

183. Zhao, L.; Jiang, D.; Cai, Y.; Ji, X.; Xie, R.; Yang, W., Tuning the Size of Gold Nanoparticles in the Citrate Reduction by Chloride Ions. *Nanoscale* **2012**, *4*, 5071-5076.

184. Xia, H.; Xiahou, Y.; Zhang, P.; Ding, W.; Wang, D., Revitalizing the Frens Method to Synthesize Uniform, Quasi-Spherical Gold Nanoparticles with Deliberately Regulated Sizes from 2 to 330 nm. *Langmuir* **2016**, *32*, 5870-5880.

185. Peck, J. A.; Tait, C. D.; Swanson, B. I.; Brown, G. E., Speciation of Aqueous Gold(III) Chlorides from Ultraviolet/Visible Absorption and Raman/Resonance Raman Spectroscopies. *Geochimica et Cosmochimica Acta* **1991**, *55*, 671-676.

186. Polte, J.; Herder, M.; Erler, R.; Rolf, S.; Fischer, A.; Wurth, C.; Thunemann, A. F.; Kraehnert, R.; Emmerling, F., Mechanistic Insights into Seeded Growth Processes of Gold Nanoparticles. *Nanoscale* **2010**, *2*, 2463-2469.

187. Wu, H.; Ji, X.; Zhao, L.; Yang, S.; Xie, R.; Yang, W., Shape Evolution of Citrate Capped Gold Nanoparticles in Seeding Approach. *Colloids and Surfaces A: Physicochemical and Engineering Aspects* **2012**, *415*, 174-179.

188. Leng, W.; Pati, P.; Vikesland, P. J., Room Temperature Seed Mediated Growth of Gold Nanoparticles: Mechanistic Investigations and Life Cycle Assesment. *Environmental Science: Nano* **2015**, *2*, 440-453.

189. Grabar, K. C.; Allison, K. J.; Baker, B. E.; Bright, R. M.; Brown, K. R.; Freeman, R. G.; Fox, A. P.; Keating, C. D.; Musick, M. D.; Natan, M. J., Two-Dimensional Arrays of Colloidal Gold Particles: A Flexible Approach to Macroscopic Metal Surfaces. *Langmuir* **1996**, *12*, 2353-2361.

190. Tam, J. M.; Tam, J. O.; Murthy, A.; Ingram, D. R.; Ma, L. L.; Travis, K.; Johnston, K. P.; Sokolov, K. V., Controlled Assembly of Biodegradable Plasmonic Nanoclusters for Near-Infrared Imaging and Therapeutic Applications. *ACS Nano* **2010**, *4*, 2178-2184.

191. Haiss, W.; Thanh, N. T. K.; Aveyard, J.; Fernig, D. G., Determination of Size and Concentration of Gold Nanoparticles from UV−Vis Spectra. *Analytical Chemistry* **2007**, *79*, 4215-4221.

192. Wang, T.; Zhang, D.; Xu, W.; Li, S.; Zhu, D., New Approach to the Assembly of Gold Nanoparticles: Formation of Stable Gold Nanoparticle Ensemble with Chainlike Structures by Chemical Oxidation in Solution. *Langmuir* **2002**, *18*, 8655-8659.

193. Wang, S.; Qian, K.; Bi, X.; Huang, W., Influence of Speciation of Aqueous $HAuCl_4$ on the Synthesis, Structure, and Property of Au Colloids. *The Journal of Physical Chemistry C* **2009**, *113*, 6505-6510.

194. Turkevich, J., Colloidal Gold. Part I. *Gold Bulletin* **1985**, *18*, 86-91.

195. Goia, D.; Matijević, E., Tailoring the Particle Size of Monodispersed Colloidal Gold. *Colloids and Surfaces A: Physicochemical and Engineering Aspects* **1999**, *146*, 139-152.

196. Larson, D. W.; Lister, M. W., Catalytic Decomposition of Acetonedicarboxylic Acid. *Canadian Journal of Chemistry* **1968**, *46*, 823-832.

197. Kettemann, F.; Birnbaum, A.; Witte, S.; Wuithschick, M.; Pinna, N.; Kraehnert, R.; Rademann, K.; Polte, J., Missing Piece of the Mechanism of the Turkevich Method: The Critical Role of Citrate Protonation. *Chemistry of Materials* **2016**, *28*, 4072-4081.

198. Grabar, K. C.; Freeman, R. G.; Hommer, M. B.; Natan, M. J., Preparation and Characterization of Au Colloid Monolayers. *Analytical Chemistry* **1995**, *67*, 735-743.